Universidade de Lisboa

Faculdade de Medicina de Lisboa

CELLULAR RESPONSES TO TOPOISOMERASE II-MEDIATED DNA LESIONS

Pedro Martins Didelet Pereira

Orientador

Prof. Doutor João António Augusto Ferreira

Tese especialmente elaborada para obtenção do grau de Doutor em Ciências Biomédicas, especialidade de Biologia Celular e Molecular

2017

Universidade de Lisboa

Faculdade de Medicina de Lisboa

CELLULAR RESPONSES TO TOPOISOMERASE II-MEDIATED DNA LESIONS

Pedro Martins Didelet Pereira

Orientador: Prof. Doutor João António Augusto Ferreira

Tese especialmente elaborada para obtenção do grau de Doutor em Ciências Biomédicas, especialidade de Biologia Celular e Molecular

Júri

Presidente: Doutor José Luís Bliebernicht Ducla Soares, Professor Catedrático em regime de *tenure* e Vice-Presidente do Conselho Científico da Faculdade de Medicina da Universidade de Lisboa

Vogais: - Doutor Hélder José Martins Maiato, Professor Auxiliar Convidado da Faculdade de Medicina da Universidade do Porto;

- Doutor Álvaro Augusto Marques Tavares, Professor Auxiliar, Departamento de Ciências Biomédicas e Medicina da Universidade do Algarve;

- Doutora Ana Cristina Gomes Espada de Sousa, Investigadora Coordenadora, Professora Associada Convidada com Agregação da Faculdade de Medicina da Universidade de Lisboa;

- Doutor João António Augusto Ferreira, Professor Associado da Faculdade de Medicina da Universidade de Lisboa; *(Orientador)*

- Doutor Domingos Manuel Pinto Henrique, Investigador Auxiliar, Professor Auxiliar Convidado da Faculdade de Medicina da Universidade de Lisboa;

- Doutor Sérgio Alexandre Fernandes de Almeida, Professor Auxiliar da Faculdade de Medicina da Universidade de Lisboa.

Instituições Financiadoras

Fundação para a Ciência e Tecnologia (SFRH/BD/45502/2008)

Fundação Calouste Gulbenkian (96526)

2017

A impressão desta tese foi aprovada pelo Conselho Científico da Faculdade de Medicina de Lisboa na reunião de 18 de Julho de 2017.

As opiniões expressas nesta publicação são da exclusiva responsabilidade do seu autor.

Table of Contents

Figures and Table Index

1. General Introduction

3. Results

4. Quantification of cell cycle kinetics by EdU (5-ethynyl-2'-deoxyuridine) - Coupled-Fluorescence-Intensity analysis

Summary

DNA Topoisomerases are an important family of enzymes that catalyze the introduction of topological changes at the level of the DNA molecule and are required for several vital cellular processes such as replication, transcription, DNA recombination and chromosome segregation. The activity of Topoisomerases type II (Topo2) relies on the introduction of a transient DSB in the DNA strand by formation of a covalent bond between the enzyme and the nucleic acid molecule. This reversible covalent interaction promotes unwinding of topological events by allowing the passage of another strand through the formed gap, followed by ligation of DNA ends. The ability of Topo2 to relax positively supercoiled DNA defines its role as a determinant factor in both replication and transcription. Topo2 is the target for several clinically relevant anti-cancer drugs, such as Etoposide and Idarubicin, commonly referred to as Topo2 poisons, which stabilize the cleavage complex formed between the enzyme and DNA during its catalytic activity, thus preventing religation of broken DNA ends. When a DNA-tracking system, such as replication and transcription complexes, collides with the cleavage complex they leave a permanent double-strand break (DSB) in its place. If these breaks are not properly repaired, they can lead to chromosome translocations, increased genomic instability and even trigger apoptotic cell death. Most studies focusing on DSB repair have used ionizing radiation (IR) as the lesion inducing agent. However, DSBs introduced by IR are intrinsically more complex to repair because of the base modifications and sequence deletions that they often involve, whereas Topo2-mediated DSBs are stabilized by an enzyme and cleavage is performed in a precise manner, allowing for DNA end homology to be preserved.

It is known from studies using irradiation that heterochromatin (HC) and euchromatin (EC) represent separate entities with respect to both damage sensitivity and repair. The high degree of compaction present in heterochromatin is thought to protect DNA from damage although, when lesions do occur, this compaction further restricts the capability of DNA damage response proteins to access the site to properly signal and mediate repair. Indeed, DNA damage introduced by IR in HC has been shown to be refractory to repair and resolved with slower kinetics than in EC. However, not much is

known about how these repair kinetics are affected by the particular nature of Topo2-induced lesions and the restrictions imposed by chromatin structure on its enzymatic activity.

Eukaryotic cells have evolved two major conserved pathways to repair DSBs in order to prevent transmission of genomic defects to their offspring: Non-Homologous End Joining (NHEJ) and Homologous Recombination (HR). HR only functions in later S or G2 phases of the cell cycle since it requires an available sister chromatid to use as template for faithful repair. NHEJ is active throughout the entire cell cycle and is the only DSB repair pathway available in G1 when there are no twin templates for HR. However, since it joins broken DNA ends regardless of sequence homology, there is a risk of introducing sequence errors during repair, such as deletions and translocations.

In the present thesis we aimed to characterize how each of the two main DSB repair pathways, NHEJ and HR, contributes to repair of Topo2-mediated DSBs. This was done for separate cell cycle phases using a protocol for cell cycle synchronization based on a double-thymidine block. Cells with DSBs introduced by a short pulse of the Topo2 poison Etoposide were monitored for their cell cycle progression and usage of repair factors over a period of 24h after Etoposide exposure. We found a diverging pattern of DSB repair system usage between lesions introduced in different cell cycle stages. We also used cell lines deficient for either BRCA1, the major determinant of HR pathway initiation, or DNAPKcs, the catalytic core unit of the complex that initiates NHEJ, to investigate whether behavior of DNA damage checkpoints is dependent on the choice of repair system. Loss of DNAPKcs dramatically sensitized HCT116 cells to Topo2-mediated DSBs, whereas similar loss of BRCA1 did not induce a dose-dependent cell viability decline much beyond spontaneous levels, highlighting the importance of NHEJ as the system that handles the bulk of these lesions.

Overall, our results highlight G2 as a critical “workstation” phase for DSB repair, particularly for lesions introduced in heterochromatin. These lesions were predominantly repaired by HR, therefore leading to an increase in Chk1 recruitment and prolongation of G2/M arrest. DSBs introduced in G2, by contrast, did not induce sufficient activation of HR to sustain a stable checkpoint arrest, leading to slippage of cells with unrepaired DSBs into mitosis which is associated with an increased risk of genomic instability. We also found that cells damaged in late S phase, when heterochromatin is the preferential target

for Topo2, trigger a strong HR activation, whereas for cells damaged in early S, when Topo2 is focused on euchromatin, this was not observed. We conclude therefore that HR in G2 preferentially targets a specific subset of DSBs that are located in heterochromatin regions.

We propose a model where slippage through checkpoint arrest is also a major determinant of repair system usage, particularly for DSBs arising in G1 and G2 phases since escaping arrest and passing to the following cell cycle phase will change the availability of repair pathways. Because of intrinsic limitations of the checkpoints operating at these stages, we conclude that a significant number of DSBs introduced in G1 are repaired by HR in S and G2 phases, while DSBs induced in G2 are mostly repaired by NHEJ in both G2 and G1.

In this thesis we also provide evidence that generalized disruption of heterochromatin epigenetic marks sensitizes cells to the DNA damaging action of Etoposide-bound Topo2. By using an inhibitor of histone methylation, DZNep, prior to Etoposide, we could robustly determine synergistic interactions between these two drugs. This highlights the potential for use of DZNep in combination with existing drugs targeting Topo2 in the chemotherapy of cancer.

Finally, we also present a new published methodology for accurate quantification of cell cycle dynamics by flow cytometry yielding absolute values (in units of time) based on the unique stoichiometric properties of the thymidine analogue EdU (5-ethynyl-2'-deoxyuridine).

Resumo

DNA Topoisomerases são uma importante família de enzimas que catalizam a resolução de problemas topológicos ao nível da molécula de DNA e a sua actuação é necessária em processos celulares essenciais, como por exemplo, na replicação, na transcrição, na recombinação de DNA e na segregação dos cromossomas. A actividade das Topoisomerases de tipo II (Topo2) é baseada na introdução de uma quebra na dupla cadeia (double strand break; DSB) de DNA através da formação de uma ligação covalente entre o enzima e o ácido nucleico. Esta interacção reversível promove o desembaraçamento de problemas topológicos ao permitir a passagem de outra cadeia de DNA pela quebra que é formada, seguida da ligação das extremidades de DNA. A capacidade da Topo2 de relaxar DNA na conformação supercoiled positiva define o seu papel como factor determinante na replicação e na transcrição. A Topo2 é alvo de várias drogas anti-cancro clinicamente relevantes, tais como Etoposido e Idarrubicina, vulgarmente designadas de venenos de Topo2, que estabilizam o complexo de clivagem formado entre o enzima e o DNA durante a actividade catalítica, impedindo a religação das extremidades de DNA quebradas. Quando um sistema que percorre o DNA, tais como os complexos de replicação ou transcrição, encontra o complexo de clivagem, a resultante excisão da enzima deixa no seu lugar um DSB permanente. Se estas quebras não forem propriamente reparadas podem levar a translocações cromossómicas, aumento da instabilidade genética e até desencadear a morte celular por apoptose. A maioria dos estudos realizados sobre reparação de DNA usaram radiação ionizante como o agente indutor de lesões. Contudo, os DSBs introduzidos por IR são intrinsecamente mais complexos de reparar devido às bases modificadas e à deleção de sequências que eles normalmente envolvem, enquanto que DSBs mediados por Topo2 são estabilizados por um enzima e a clivagem é realizada de maneira precisa, permitindo que a homologia entre as extremidades seja preservada.

Estudos usando radiação permitiram estabelecer que a heterocromatina (HC) e a eucromatina (EC) representam entidades separadas no que diz respeito à sua sensibilidade a danos e capacidade de reparação. Pensa-se que o elevado grau de compactação da heterocromatina proteja o DNA da ocorrência de lesões mas, quando

elas acontecem, esta compactação restringe o acesso de factores de reparação de DNA ao local da lesão para sinalizarem e mediarem a reparação. De facto, já foi demonstrado que danos de DNA introduzidos em HC por radiação ionizante (IR) são reparados com uma cinética mais lenta que em EC. No entanto, ainda não é conhecido como esta cinética de reparação é afectada pela natureza particular das lesões mediadas por Topo2 e pelas restrições impostas pela estrutura da cromatina sobre a sua actividade enzimática.

As células eucariontes desenvolveram dois mecanismos principais de reparação de DSBs de modo a prevenirem a transmissão de defeitos genéticos à sua descendência: a ligação de extremidades não homólogas (Non-Homologous End Joining; NHEJ) e a recombinação homóloga (Homologous Recombination; HR). A HR só pode funcionar no fim da fase S ou na fase G2 do ciclo celular uma vez que requer que esteja disponível um cromatidio irmão para ser usado como base para uma reparação fidedigna. A NHEJ está activa ao longo de todo o ciclo celular e é a única via de reparação de DSBs disponível em G1 pois nesta fase ainda não existem cromatidios irmãos para a HR. No entanto, como esta via simplesmente faz a junção directa de extremidades de DNA partidas sem se importar com a homologia das sequências, existe o risco de introduzir erros na sequência de DNA durante a reparação, tais como deleções e translocações.

Na presente tese procurou-se caracterizar como cada um dos dois sistemas de reparação de DSBs, NHEJ e HR, contribui para a reparação de DSBs mediados por Topo2. Isto foi feito separadamente para cada uma das fases do ciclo através do uso de um protocolo de sincronização de ciclo celular baseado num duplo bloqueio com timidina. Células com DSBs introduzidos por um curto pulso com o veneno de Topo2 Etoposido foram monitorizadas quanto à sua progressão no ciclo e ao uso de factores de reparação, durante um período de 24h após exposição ao Etoposido. Verificou-se a existência de um padrão divergente quanto ao uso de sistemas de reparação entre lesões introduzidas em diferentes fases do ciclo. Foram também usadas linhas celulares com deficiência em BRCA1, o principal determinador do início da HR, ou em DNAPKcs, a subunidade catalítica do complexo que inicia a NHEJ, para investigar se o comportamento dos checkpoints de danos de DNA é dependente da escolha de sistema de reparação. A perda de DNAPKcs sensibilizou dramaticamente células de cancro do cólon HCT116 a DSBs mediados por Topo2, enquanto que a perda de BRCA1 não induziu uma perda de viabilidade celular

dependente da dose de Etoposido muito acima dos níveis espontâneos, realçando a importância da NHEJ como sistema que se encarrega da maioria destas lesões.

Acima de tudo, os nossos resultados indicam que a fase G2 é uma "oficina" para reparação de DSBs, particularmente para lesões introduzidas em heterocromatina. Estas lesões foram predominantemente reparadas por HR, levando consequentemente a um aumento no recrutamento de Chk1 e prolongamento da paragem em G2/M. DSBs introduzidos em G2, por contrário, não induziram activação de HR suficiente para manter uma paragem por checkpoint, levando a passagem de células com lesão por reparar para mitose, o que está associado com um aumento do risco de instabilidade genómica. Também verificámos que células cujo DNA é danificado mais tarde dentro da fase S, quando a heterocromatina é o alvo preferencial da Topo2, despoletam uma forte activação da HR, enquanto que em células danificadas no início de S, quando a Topo2 está focada na eucromatina, isto não foi observado. Concluímos assim que a HR em G2 visa uma fracção específica de DSBs que está localizada em regiões de heterocromatina.

Propomos então um modelo onde a fuga à paragem por checkpoint é também um factor que determina a escolha de sistema de reparação, particularmente para DSBs que surjam nas fases G1 e G2, uma vez que ao evitar a paragem e passando para a fase celular seguinte a disponibilidade dos factores de reparação é alterada. Devido às limitações intrínsecas dos checkpoints que operam nestas fases, concluímos que um número significante de DSBs introduzidos em G1 são reparados por HR nas fases S e G2, enquanto que DSBs introduzidos em G2 são reparados pela NHEJ tanto em G2 como em G1.

Nesta tese também mostramos evidências que a disrupção generalizada de marcas epigenéticas de heterocromatina sensibiliza o DNA das células à acção danificadora da Topo2 quando esta se liga ao Etoposido. Através do uso de um inibidor de metilação de histonas, DZNep, antes da adição de Etoposido, conseguimos determinar interacções sinergéticas entre estas duas drogas. Isto realça o potencial para o uso de DZNep em combinação com drogas já existentes, cujo alvo é a Topo2, na terapia do cancro.

Finalmente, apresentamos ainda uma nova metodologia, já em publicação, que permite a quantificação precisa da cinética do ciclo celular por citometria de fluxo, fornecendo valores absolutos (em unidades de tempo) baseada nas propriedades particulares do análogo de timidina EdU (5-ethynyl-2'-deoxyuridine).

Acknowledgements

I would like to begin by deeply thanking my supervisor João Ferreira for giving me the chance to be his Ph.D student and work in his group. Over the years I became aware of how much I learned and grew as a researcher and a person thanks to him. He was a true fountain of knowledge and of ideas for this work but he also made sure I thought for myself and came to my own solutions. I hope a little of that wisdom has brushed off on me.

I want to thank Joana Cardoso and Inês Alves for helping me give the first steps in the lab so I could start working by myself, especially to Joana that also helped a lot with the bioinformatics. I wish you two all the best! A very big thank you to all the members of Prof. Luís Costa group with whom I shared the lab for so long and that provided such a great work environment: Sandra Casimiro, Irina Alho, Teresa Raquel (thank you so much for advising me and being in my thesis committee), Ricardo Pires (never a boring moment with you around my friend) and, most of all, Joana Tato who was such a great lab partner besides being an amazing friend, through the good and the bad times. I will really miss our time in the lab! I also cannot forget Sérgio Almeida's group that became our lab neighbours later on. Really loved working next to you guys. Thanks to Sérgio Almeida, Ana Raposo, Filipa Martins, Alexandra Vítor, S Sree Rama Chaitanya for all the energy and help you provided. A special thank you to a special friend, Sílvia Carvalho, who helped me more times than I can remember and always managed to make me smile.

I also want to thank all the amazing people from IMM and other institutes who I got to know and work with throughout all these years: Ana Serra Caetano, Ana Espada de Sousa, Ana Leitão, Francisco Enguita, João Barata, Lars Jansen, Marisa Cabrita, Sérgio Marinho, Dinora Levy, Joana Desterro, Ângelo Chora, Catarina Moita, Nadja Pejanovic, Célia Carvalho, Noélia Custódio, Sandra Martins, Teresa Carvalho, Ana Neves Costa, Nuno Figueiredo, Helena Raquel, Susana Gonçalves, Rita Cascão e Rita Drago. A special thanks also to Andreia Pinto for all the good and fun moments we shared at IMM and outside.

A special thanks to the amazing people of IMM's Bioimmaging group for all their patience with me and for helping me incredibly with their knowledge and advice: José Rino, António Temudo e Ana Nascimento.

Ackowledgements

A big thank you to my friends outside of work who were a big help for me to forget the worries of the moment and always ready with a word of support when I needed. Inês Fragata, Carlos Almeida, Ana Fragata, João Taveira, Francisco Pina, Ana Barata, João Máximo, Hugo Rodrigues. We always have the best of times together!

I wouldn´t have been able to embark on this journey if it not for the help and love from my parents. I am forever in their debt for raising me the way I am and for never stopping believing in me for a second. Thank you so much and I hope to make you proud! A big thank you to my sister that also supported me in any way she could, and to my brother-in-law.

And last, but definitely not least, a heartfelt thank you to my best friend and partner in life, who always pushed me forward when I was unsure and was my guiding light through the storm. Thank you for all the patience and support, and sorry for taking so long! Avec tout l'amour, merci Laetitia.

Abbreviations

γH2AX	Histone 2A variant X phosphorylated in serine 139
53BP1	p53-binding protein 1
ATM	Ataxia telangiectasia mutated
ATR	Ataxia telangiectasia and Rad3 related
ATP	adenosine triphosphate
BRCA1	Breast cancer type 1 susceptibility factor
BrdU	5-bromo-2'-deoxyuridine
Cdc	Cell division cycle
Cdk	Cyclin-dependent kinase
Chk	Checkpoint kinase
CK2	Casein kinase 2
CPT	Camptothecin
CT	chromosome territories
CtIP	C-terminal binding protein (CTBP)-interacting protein
DAPI	4',6-diamidino-2-phenylindole
DDR	DNA damage response
D/J/F	Dean/Jett/Fox algorithm
DNA	Deoxyribonucleic acid
DNAPK	DNA-dependent protein kinase
DNAPKcs	DNA-dependent protein kinase, catalytic subunit
DSB	double-strand break
DZNep	3-deazaneplanocin A
EC	Euchromatin
E-CFI	EdU-coupled Fluorescence Intensity analysis
EdU	5-ethynyl-2'-deoxyuridine
Etop	Etoposide
EZH2	Enhancer of zeste homologue 2
FLM	Fraction-of-labelled mitosis
GDP	guanoside triphosphate

H3K9me2	Histone 3 dimethylated in lysine 9
H3K9me3	Histone 3 trimethylated in lysine 9
H3K27me3	Histone 3 trimethylated in lysine 27
H4K20me3	Histone 4 trimethylated in lysine 20
HAT	Histone acethyltransferase
HC	Heterochromatin
HDAC	Histone deacethylase
HDM	Histone demethylase
HEPES	4-(2-hydroxyethyl)-1-piperazineethanesulfonic acid
HMT	Histone methyltransferase
HP1	Heterochromatin protein 1
HR	Homologous Recombination
JAK2	Janus kinase 2
K	lysine
KAP1	KRAB domain associated protein 1
MDC1	Mediator of DNA damage checkpoint protein 1
MEFs	mouse embryonic fibroblasts
mESCs	mouse embryonic stem cells
MFI	mean fluorescence intensity
mRNA	messenger RNA
MRN	Mre11, Rad50 and NBS1 complex
NHEJ	Non-Homologous End Joining
PCNA	Proliferating cell nuclear antigene
PI	propidium iodide
Plk	Polo-like kinase
pRb	phosphorylated Retinoblastoma protein
PRC	Polycomb Repressor Complex
PTIP	Pax transactivation-domain interacting protein
RIF1	Regulation timing regulatory factor 1
RING	Really interesting new gene
RNA	Ribonucleic acid
RNase	Ribonuclease

RNF	Ring finger protein
RPA2	Replication protein A 2
S	serine
SAHA	suberoylanilide hydroxamic acid
shEZH2	small hairpin RNA targeting EZH2
shRNA	small hairpin RNA
SMARCAD1	SWI/SNF-related matrix-associated actin-dependent regulator of chromatin subfamily A containing DEAD/H box 1
ssDNA	single-strand DNA
SUMO	Small ubiquitin-like modifier
SUV39	Suppressor of variegation 3-9
SWI/SNF	Switch/sucrose non-fermentable
T	threonine
Tip60	Tat interactive protein 60 kDa, also called KAT5
Topo2	Topoisomerase II
WP	Watson Pragmatic algorithm
XLF	XRCC4-like factor
XRCC4	X-ray repair cross-complementing protein 4
Y	tyrosine

Chapter 1

General Introduction

1. General Introduction

1.1. Chromatin structure and histone modifications

In all eukaryotes, the genetic information that comprises the genome is stored in the cell nucleus. Yet the entire length of genomic DNA of an organism would not be able be packed inside its nucleus if it was randomly folded. DNA-binding proteins called histones must coordinate the folding of genomic DNA into an extremely condensed DNA-protein complex known as chromatin, which is basically a repetition of units formed by histones and DNA called “nucleosomes”, first described by Kornberg in 1974 (Kornberg, 1974). Each nucleosome is an octamer of four core histones (two copies each of histones H2A, H2B, H3 and H4) around which are coiled approximately 146 DNA base pairs. Another histone, H1, acts as a physical link, along with “linker” DNA, between adjacent nucleosome core particles. These evolutionally conserved proteins are globular except for their N-terminal domains, commonly designated as histone “tails”, which are unstructured and protrude from the nucleosome core. A particular characteristic of the tails is the vast number of post-translational covalent modifications their amino acids can acquire, the most common being phosphorylation, acetylation, methylation, ubiquitination and sumoylation. These modifications or “marks” are reversible, allowing cells to adjust their occurrence in chromatin by means of specific histone modifying enzymes (Santos-Rosa & Caldas, 2005).

Some of the modifications to nucleosomal histone tails, particularly methylation and acetylation, can affect the chromatin condensation state by changing the affinity of histones for DNA or adjacent nucleosomes. This allows chromatin regions to be remodelled into two different configurations: a loosely coiled or “open” state when the interactions between DNA and histones are weakened that facilitates access for transcription factors, referred to as euchromatin (EC), and a tightly coiled or “closed” state when interactions are strengthened that suppresses transcription, referred to as heterochromatin (HC) (**Fig.1**). While all known histone acetylations are associated with relaxing chromatin structure, their presence being notably enriched at promoter regions

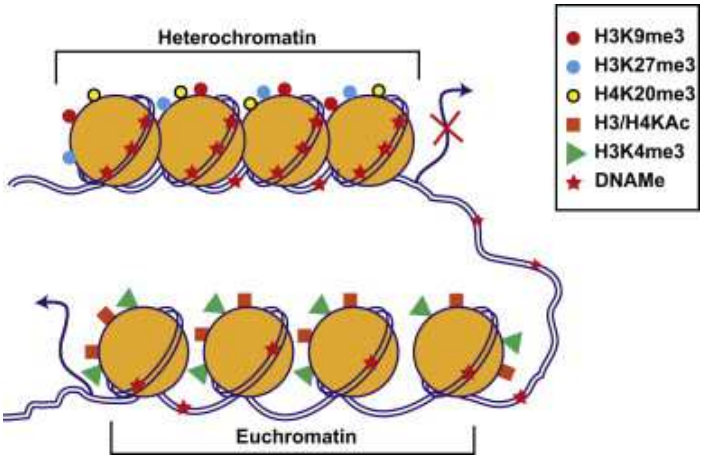

Figure 1. Chromatin structure and function. Chromatin is made up of repeating units of nucleosomes consisting of 146 base pairs of DNA wrapped around dimers of four histone proteins (H2A, H2B, H3, and H4). The exposed amino-terminal tails of nucleosomal histones are subjected to post-translational modifications. Combinatorial effects of histone modifications and DNA methylation regulate the chromatin structure between transcriptionally silent "heterochromatin" and active "euchromatin." Enrichment of DNA methylation in promoters and histone modifications such as H3K9me3, H3K27me3, and H4K20me3 promote nucleosome condensation to repress transcription (heterochromatin). On the other hand, histone modifications H3 or H4KAc and H3K4me promote open chromatin formation and increase accessibility to the transcription machinery, leading to active transcription (euchromatin). Other histone modifications such as Ser/Thr phosphorylation, ubiquitination and SUMOylation, and non-coding RNAs including microRNAs also regulate chromatin structure and function (not shown). Genome-wide patterns of DNA methylation and histone modifications are referred to as the "epigenome." Its response to internal and external signals regulates gene expression involved in diverse biological processes and disease conditions. KAc, lysine acetylation. From Reddy, Park, & Natarajan, 2012.

and at the 5'-end of genes, methylations can have competing effects according to the number of methyl groups added (either one, two or three), the amino acid residue targeted and internal cell signalling conditions (Kouzarides, 2007). As examples, di- and trimethylated histone H3 at lysine 9 (H3K9me2 and me3) and trimethylated histone H3 at lysine 27 (H3K27me3) are hallmarks of transcriptionally silent genes, whereas active genes display di- and trimethylated histone H3 at lysine 4 (H3K4me2 and me3) along with methylations in lysine 36 (H3K36) (Bach & Hegde, 2016). Other modifications can also have an impact on gene expression by stabilizing or weakening binding sites for regulatory proteins, either repressors or activators of transcription (e.g. sumoylations are typically repressive and phosphorylations activating; cf. **Table 1**) (Choudhuri, 2011).

Covalent histone modifications are precisely regulated epigenetic events in which a vast number of enzymes can participate and great efforts have been made since the beginning of the 21st century to characterize these modifications on a genome-wide scale, partly thanks to the development of new technologies such as chromatin immunoprecipitation (ChIP) that allow to globally assess the incidence of these marks (Barski et al., 2007). The combination of these studies led researchers to propose that multiple histone marks could occur sequentially to form a combination or "code" for distinct downstream responses, such as chromosome condensation, DNA repair and transcription activation or repression (Strahl & Allis, 2000). Phosphorylation of histone 3 at serine 10 (H3S10), for example, stimulates acetylation of histone 3 lysine 14 (H3K14), while ubiquitination of histone H2B at lysine 120 (H2BK120) stimulates methylation of histone H3 at lysine 4 (H3K4), both cases contributing to transcription activation (Choudhuri, 2011). Understanding if there is an underlying histone code in critical epigenetic events and how to read it is still one of the major focuses of epigenetics to this day, particularly for diseases that arise due to deregulation of gene expression in relation to abnormal histone modification patterns. A key example is the silencing of tumor suppressor genes by disturbances in histone methylation and acetylation as a result of mutations in histone modifying enzymes and chromatin remodelers, which consequently elevates chromatin structure to a decidedly relevant topic for cancer research and potential target for therapeutic strategies (Kelly & Issa, 2017).

Table 1. Histone modifications and their known effects on activating or repressing transcription

	Methylation	Acetylation	Phosphorylation	Sumoylation	Ubiquitination
Activating Modifications	H3:K4,K36,K79 H3:R17,R23 H4:R3	H2A:K5,K9,K13 H2B:K5,K12,K15,K20 H3:K9,K14,K18,K23,K56 H4:K5,K8,K13,K16	H3:T3 H3:S10,S28 H3:Y41 H2AX:S139		H2B:K120 H2B:K123
Repressing Modifications	H3:K9,K27 H4:K20			H2A:K126 H2B:K6,K7 H4:K5,K8,K12,K16,K20	H2A:K119

(K)- lysine, (R)- arginine, (S)- serine, (Y)- tyrosine, (T)- threonine

Adapted from Choudhuri, 2011

1.2. Chromatin modifying enzymes and cancer

Normal histone modification states in cells are maintained through a combination of enzymes that place or remove those particular marks in histone tails. Alterations in the activity or expression of these enzymes have been associated with a variety of human diseases, namely many oncologic disorders (cf. **Table 2**) (Ma & Zhang, 2016).

Acetylation is controlled by means of histone acetyltransferases (HATs) and histone deacetylases (HDACs). These classes of enzymes are considered major chromatin remodelling factors due to the capability of acetyl groups to neutralize the natural positive charge of lysine residues in nucleosomes. This reduces their electrostatic attraction to negatively charged DNA, resulting in the unfolding of chromatin (Kouzarides, 2007). HDAC inhibitors are currently the largest group of epigenetic drugs being developed for clinical use in cancer therapy by virtue of their confirmed anti-tumor

Table 2. Alterations in histone modifying enzymes in human diseases

Enzymes	Associated disease
Histone acetyltransferases (HATs)	
General control of amino-acid synteshis 5 (GcN5)	Spinocerebellar ataxia
CREB binding protein (CBP)	Lung cancer
Histone acetyltransferase binding to origin recognition complex 1 (HBO1)	Multiple primary cancers
Histone deacetylases (HDACs)	
HDAC1, 2 and 3	Prostate cancer
Sirtuin type 1 (SIRT1)	Prostate cancer
Sirtuin type 4 (SIRT4)	Acute myeloid leukaemia
Histone methyltransferases (HMTs)	
Enhancer of zeste homolog 2 (EZH2)	Various cancers
Co-activator associated methyltransferase 1 (CARM1)	Colorectal cancer
G9a	Lung cancer
Histone demethylases (HDMs)	
Lysine-specific demethylase 1 (LSD1)	Prostate cancer
Ubiquitously transcribed tetratricopeptide repeat, X chromosome (UTX)	Multiple cancers
Histone kinases (HKs)	
Janus Kinase 2 (JAK2)	Myeloproliferative neoplasias
Aurora kinase	Multiple cancers
Ataxia telangiectasia mutated (ATM)	Ataxia telangiectasia, multiple cancers

Adapted from Ma & Zhang, 2016 *and* Awasthi, Foiani & Kumar, 2016

effects. They are believed to act mostly by restoring expression of tumor suppressor genes that are silenced due to abnormal heterochromatin formation, a feature of many known cancers. Several of these drugs have already been approved for clinical use in T-cell lymphomas (e.g. vorinostat, belinostat and romidepsin), although reported response rates do not exceed 35% indicating that HDAC inhibitors by themselves might only be effective on a subset of patients (Kelly & Issa, 2017). Other studies have focused on inhibiting proteins that "read" the acetyl modification on histones. These proteins recognize acetyl group through their active bromodomains and have been shown to be mutated in some tumors, leading to increased oncogene expression (Stathis et al., 2016).

Histone methylation is catalysed by histone methyltransferases (HMTs) and removed by histone demethylases (HDMs). HMTs transfer a methyl group to histone tails from a high energy donor, S-adenosyl methionine, but contrary to acetyl groups this does not neutralize a positive charge on histones therefore not causing direct conformational changes in nucleosomes. However, specific histone methylations can serve as binding platforms for chromatin remodelling effectors. For example, trimethylation of lysine 9 of histone 3 (H3K9me3) by the HMT SUV39 creates a binding site for heterochromatin protein-1 (HP1). HP1 is a mediator of heterochromatin formation and expansion, thereby promoting transcription silencing (Cann & Dellaire, 2011). An example seen in yeast is methylation of histone H3 at lysine 4 (H3K4me) which recruits a component of the NURF (nucleosome remodelling factor) complex to activate expression of developmental genes, while at the same time disrupting the binding of the repressive NuRD (nucleosome remodelling deacetylase) complex (Kouzarides, 2007). Finally, trimethylation of histone H3 at lysine 27 (H3K27me3) is associated with transcriptional silencing of genes involved in fundamental cell processes such as cell cycle regulation, cell differentiation and senescence, including many genes involved in tumor suppression. This mark is placed by the methyltransferase EZH2 (enhancer of zeste homolog 2), the catalytic core protein in the polycomb repressor complex 2 (PRC2). H3K27me3 subsequently recruits the polycomb repressor complex 1 (PRC1) to ubiquitinate lysine 119 of histone H2A (H2AK119ub1) to prevent transcriptional elongation. EZH2 is overexpressed in many forms of cancer including breast, prostate, colon, lung, sarcoma and lymphomas, which makes it an appealing target for inhibition. In fact, drugs that target EZH2 have shown

promise in clinical trials, with several EZH2 inhibitors currently being developed (C.-J. Chang & Hung, 2012; Kelly & Issa, 2017).

As mentioned before, histone phosphorylation is a transcription activating modification catalysed by kinases and removed by phosphatases that adds a negatively charged phosphate, usually from ATP or GDP donors, to amino acid residues in histone tails. Similarly to acetylation, the negatively charged phosphate contributes to disrupting DNA-histone electrostatic interactions thereby allowing better accessibility of transcription factors to DNA. Alterations in histone phosphorylation patterns are found in many cancers. An example is Janus Kinase 2 (JAK2), responsible for the phosphorylation of histone 3 on tyrosine 41 (H3Y41ph) that inhibits binding of the HP1α isoform to chromatin (Dawson et al., 2009). JAK2 is mutated in the majority of myeoloproliferative neoplasias and inhibitors for this kinase are being used clinically (Ma & Zhang, 2016). Additionally, the kinase Aurora B responsible for phosphorylation of histone H3 at Serine 10 (H3S10ph), an important activator mark associated with mitosis and repression of heterochromatin propagation, is overexpressed in several carcinomas and is targeted for inhibition (Johansen & Johansen, 2006; Ma & Zhang, 2016). Because of its role in DNA damage repair, it is also worth mentioning phosphorylation of histone H2AX (a variant of H2A) at serine 139 by Ataxia Telangiectasia Mutated (ATM), Ataxia Telangiectasia and Rad3-related (ATR) and DNA-dependent Protein Kinase (DNAPK) which generates gamma-H2AX (γH2AX), a key signalling modification that accumulates at sites of major DNA lesions and initiates recruitment of repair factors. Since patients that suffer from mutations in these enzymes display decreased efficiency in repairing DNA breaks resulting from errors in transcription or replication, they have a high predisposition for tumors (Zeman & Cimprich, 2014; Awasthi, Foiani & Kumar, 2016).

Histone modifications are thus promising targets for cancer therapy since they can affect chromatin condensation to not only reverse the silencing of tumor suppressor genes, but also to potentially allow easier access by DNA damaging agents to chromatin, which could result in more efficient strategies for inducing tumor cell death.

1.3. The DNA damage response to double strand breaks

Cellular DNA is subject to constant damage from reactive oxygen species (ROS), free radicals that are a by-product of endogenous metabolic processes, and from naturally occurring errors during DNA replication, as well as from external sources, predominantly UV and ionizing radiation. Of the different types of DNA lesions that can occur in cells (e.g. modified bases, abasic sites, intra- and interstrand crosslinks, protein-DNA adducts, various strand breaks), DNA double strand breaks (DSBs) pose the greatest threat to genomic integrity since their inefficient repair may lead to mutational defects or culminate in cell death. Indeed, defective DSB repair is associated with several developmental, immunological and neurological disorders, and is a major driving force in cancer (Jakob et al., 2011; Iyama & Wilson, 2013). In the present work, DSBs are the type of DNA lesion chosen for study, for the above reasons, and any allusion to DNA damage and repair will predominantly refer to DSBs.

Maintaining and ensuring a faithful inheritance of genetic information is imperative to all eukaryotic life. To that end, cells have evolved a complex range of mechanisms to sense DNA damage and initiate a stress response to restore genomic integrity, collectively known as the DNA damage response (DDR). In the case of DSBs, DDR can trigger two major repair pathways conserved in most eukaryotes in order to prevent propagation of genomic defects: Non-Homologous End Joining (NHEJ) and Homologous Recombination (HR) (Soria, Polo, & Almouzni, 2012; Raschellà, Melino, & Malewicz, 2017).

Homologous Recombination represents the most elegant solution to DSB repair since it is bases itself on an undamaged template to restore any lost information on the damaged sequence. A downside of this system is, consequently, that it can only function after DNA replication has taken place and a sister chromatid is available to be used as template, which only occurs in S or G2 phases of the cell cycle. Non-Homologous End Joining, on the other hand, is active throughout the entire cell cycle and is the only DSB repair pathway available in G1 when there are no templates for HR. However, because it directly connects broken DNA ends without referring to the former sequence, there is a risk of introducing sequence errors during repair, such as deletions, substitutions or even translocations if DSBs from different regions are ligated. Nevertheless, in certain contexts where there is no modification to terminal nucleotides on DNA ends (“clean” breaks),

NHEJ is known to be error free, and there are as well exceptions where HR can be mutagenic (Chapman, Taylor, & Boulton, 2012; Scully & Xie, 2013).

For the DDR to initiate, DSBs first need to be recognized and signalled to the repair machinery. The phosphorylation of histone variant H2AX, which constitutes approximately 10% of total histone H2A, at serine 139 (resulting in γH2AX) serves as the initiating signal for the DDR. This modification is rapidly catalysed by members of the phosphatidylinositide 3-kinases (PI3K) family of protein kinases (ATM, ATR and DNAPK), in response to DNA damage and can spread over a vast (up to 2Mb) area surrounding the DSB acting as a beacon that can be recognized by a multitude of proteins and be visualized microscopically in the form of nuclear aggregates known as "foci" (van Attikum & Gasser, 2009). Impairment of this phosphorylation results in loss of DDR factor recruitment to DNA breaks and increased radiation sensitivity, as evidenced in H2AX mutant mice (Celeste et al., 2003). The generation of γH2AX depends mainly on the MRN complex formed by the Mre11, Rad50 and NBS1 (Nijmegen breakage syndrome 1) proteins. MRN is the most important DDR sensor due to its ability to recognize free DNA ends and subsequently recruit ATM kinase (ATR and DNAPK can also be recruited but are not the primary kinases) through NBS1 to phosphorylate H2AX in the immediate vicinity of the break. γH2AX is then recognized immediately by MDC1 (Mediator of DNA Damage Checkpoint Protein 1), which needs to be phosphorylated by Casein Kinase 2 (CK2) to be active, subsequently binding to the modified histone and establishing a platform for DDR factor accumulation and retention at the DSB, most notably for the MRN-ATM complex. This complex is then able to expand H2AX phosphorylation to an increasing number of nucleosomes flanking the DSB, thus creating a positive feedback loop that greatly amplifies the signal for recruitment of repair factors (van Attikum & Gasser, 2009; Lukas, Lukas, & Bartek, 2011).

After these initial signalling steps, which are common to both HR and NHEJ, each pathway follows separate routes and relies on distinct sets of factors for DSB repair. During the first step of HR, the ends of the DSB are bound by the MRN complex which then, through means of the endonuclease activity of Mre11, removes nucleotides in a 5'-3' orientation converting both DSB ends into single strand DNA (ssDNA) 3' overhangs, a process that is called "end resection". These ssDNA overhangs are bound in turn by the Replication Protein A (RPA) complex, an heterodimer composed of the subunits RPA1,

RPA2 and RPA3. RPA in concert with Rad52 recruits Rad51 to form ssDNA-Rad51 nucleoprotein filaments that will search for an homologous sequence in the vicinity. A successful search will result in strand invasion and synthesis of a complementary DNA strand. A ligation step then completes this predominantly error-free repair event. NHEJ, on the other hand, initiates by the binding of the Ku heterodimer, consisting of the Ku70 and Ku80 proteins, to the DSB ends locking them in close proximity. DNA bound Ku recruits the catalytic subunit of DNAPK (DNAPKcs) to form the DNAPK holoenzyme complex thereby activating its kinase activity. This complex then undergoes autophosphorylation in serine 2056 and undertakes the recruitment and activation of several DNA end-modifying proteins, including DNA Ligase IV, Artemis, XRCC4, XLF, and the recently discovered PAXX, that together carry out the rejoining of the DNA ends (de Campos-Nebel, Larripa, & González-Cid, 2010; Goodarzi, Jeggo, & Lobrich, 2010; Raschellà et al., 2017) (**Fig.2**).

Initial studies have suggested a relatively simple mechanism controlling the decision to employ either of the two major DSB repair systems, which consists of cyclin-depent-kinase (Cdk) phosphorylation of CtIP, an interaction partner of the MRN complex, at the G1/S transition that allows it to activate DNA end resection by recruiting BRCA1, shifting the balance from NHEJ repair to HR (Yun & Hiom, 2009). However, in more recent years it has become apparent that this decision is quite complex, being subject to heavy regulation in order to restrict the activity of either system to specific cellular circumstances and involving ubiquitination and SUMOylation cascades along with several histone modifications (Daley & Sung, 2014). While extensive investigation into this particular area is still ongoing, two factors have emerged as the key regulators of DSB repair pathway choice: p53-binding protein 1 (53BP1) for NHEJ and breast cancer type 1 susceptibility protein (BRCA1), along with its heterodimer partner BARD1 (BRCA1-associated RING domain protein), for HR (Chapman et al., 2012). Both of these regulators act downstream of the initial γH2AX/MDC1 signal amplification response and compete for binding to mutually exclusive sites within the γH2AX/MDC1 chromatin domain. Knock-out of 53BP1 was proven to be sufficient to restore HR repair capability to cells in which it had been abrogated due to low BRCA1 expression (Cao et al., 2009). In fact, 53BP1 has been shown to inhibit end resection, and thus HR, in G1 phase with RIF1 and PTIP being identified as its effectors though the exact mechanism of inhibition is still unknown. In

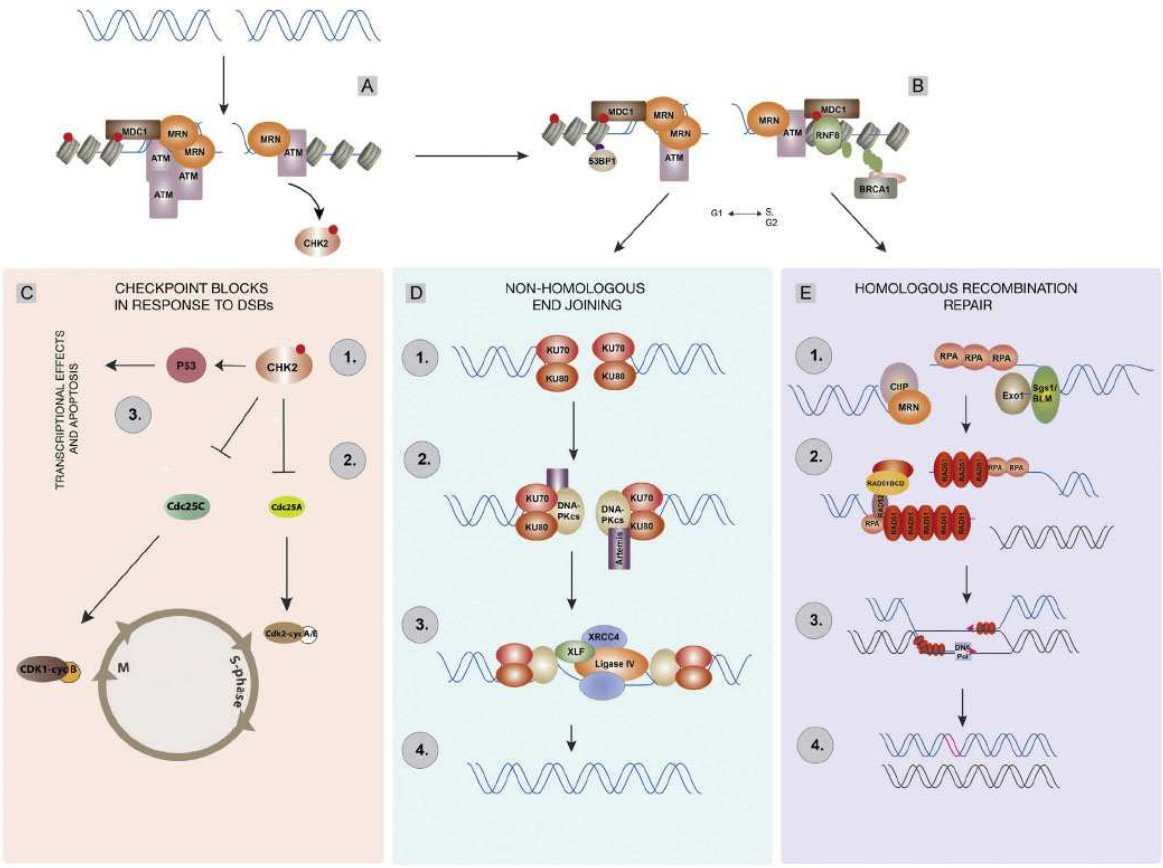

Figure 2. A simplified scheme of the DNA damage response. (A) Following break induction the MRN complex binds the DSB. Recruitment and activation of ATM by the DSBs lead to H2AX phosphorylation, binding of MDC1 and amplification of the damage signal. **(B)** Following additional histone modifications facilitated by MDC1, recruitment of 53BP1 and BRCA1 and depending on the cell cycle stage and other factors, DSB ends are either extensively resected or not, which determine repair pathway choice. **(C)** To provide time for repair the cell cycle is blocked, as Chk2 is phosphorylated by ATM (**C.1.)** and phosphorylates and inactivates Cdc25 phosphatases **(C.2.)**, thus blocking cyclin-dependent kinases and cell cycle transitions. Additionally, Chk2 phosphorylation of p53 elicits transcriptional events and may induce apoptosis **(C.3.)**. **(D)** Non-homologous end joining is the major DSB repair mode in mammals. It is initiated by the binding of Ku proteins **(D.1.)**, which in turn, bind DNA-PKcs **(D.2.)** and activate DNA-PKcs kinase activity. DNA-PK regulates limited processing of DNA ends by the Artemis nuclease **(D.3.)** and brings about the recruitment of the factors that carry out rejoining of the DNA ends **(D.4.)**. **(E)** Homologous recombination repair requires extensive processing of the DSB ends into 3'-ssDNA overhangs **(E.1.)**. Single-strand DNA overhangs are first covered by RPA, later displaced by Rad51 in an exchange reaction dependent on Rad51 paralogues and Rad52 **(E.2.)**. Rad51-covered nucleoprotein filament searches for and invades the homologous duplex and following extension **(E.3.)** of the invading strands and Holliday junction resolution the broken double helix is restored **(E.4.)**. From Gospodinov & Herceg, 2013.

contrast, BRCA1 activity is able to remove 53BP1 from DSBs in S and G2 thereby

unblocking resection (Lowndes, 2010). Importantly, loss of BRCA1 leads to 53BP1 recruitment in G2 while depletion of 53BP1 causes accumulation of BRCA1 at damage foci in G1, suggesting that the potential for the engagement of HR in G1 or NHEJ in G2 exists but is blocked by 53BP1 and BRCA1, respectively (Daley & Sung, 2014).

These factors are thought to respond to different sets of ubiquitination marks on histones H2A and H2AX generated by the E3 ubiquitin ligases RNF8 and RNF168, which are recruited via MDC1. The exact code is not known though it involves H2A ubiquitination on lysines 13 and 15 and formation of long ubiquitin chains at lysine 63 (Stewart, 2009; Panier et al., 2012). RNF8 and RNF168 activities are believed to create a platform for recruitment of the RAP80 complex which in turn is required for efficient BRCA1 enlistment to damage foci (B. Wang et al., 2007). 53BP1, however, interacts directly with the histone modification introduced by RNF168, H2A ubiquitinated on lysine 15, not requiring RAP80 activity to be recruited, as opposed to BRCA1. 53BP1 also requires a constitutive epigenetic mark in chromatin, histone 4 dimethylated on lysine 20 instead ensuring its retention in chromatin surrounding the break. In addition, the acetylation mark H4K16 introduced by the TIP60 acetyltransferase was shown to negatively regulate 53BP1 persistence in damaged chromatin by reducing its affinity to H4K20me2, which means that at least three types of histone modifications, methylation, ubiquitination and acetylation, are involved in regulating 53BP1 recruitment and retention (Daley & Sung, 2014). Further layers of regulation are in place for each of the previously mentioned factors involved in regulating BRCA1 and 53BP1. Together, they create a very complex network of protein interactions controlling the switch from NHEJ to HR surrounding the Cdk-dependent formation of the CtIP-MRN-BRCA1 complex that removes 53BP1 and initiates resection.

1.4. DNA repair in the context of chromatin structure

DNA in eukaryotic cells exists in association with histone proteins and physically wrapped around nucleosomes. As a consequence, repair of DNA damage has to be considered in the greater context of chromatin and its structure. Efficient DNA repair

requires changes at the level of the chromatin structure in the vicinity of lesions to facilitate access of various signaling and repair complexes. These structural changes can take the form of remodeling of nucleosome positions, exchange of histone variants, removal of non-histone chromatin-associated proteins or post-translational modifications to histone tails (Raschellà et al., 2017).

Nucleosome remodeling was found to involve the activity of ATP-dependent chromatin remodelers that operate by weakening DNA-histone interactions at the expense of ATP hydrolysis to slide or evict individual nucleosomes (Kruhlak et al., 2006). Many ATP-dependent chromatin remodelers have been involved in DNA repair including PARP (poly-ADP-ribose polymerase), the SWI/SNF complex, INO80 and SMARCAD1 (Gospodinov & Herceg, 2013).

As mentioned before, histone post-translational modifications, most prominently acetylation, can also weaken the bonds between histones and DNA and can affect chromatin condensation after damage to DNA. The TIP60 acetyltransferase complex, for instance, was shown to be deeply involved in DNA repair. Depletion of core subunits of this complex led to defects in HR repair that were overcome by forced chromatin relaxation, indicating its role in granting repair factors access to DNA (Murr et al., 2006). TIP60 activation was found to be dependent on binding to histone mark H3K9me3 on chromatin, after which it initiates not only chromatin relaxation but also activation of ATM through acetylation (Sun et al., 2009). A considerable number of additional acetyltransferases have been implicated in promoting recruitment and activity of NHEJ and HR factors (Gospodinov & Herceg, 2013).

Over the last decades it has become apparent that heterochromatin (HC) and euchromatin (EC) represent separate entities with respect to both damage sensitivity and repair. The high degree of compaction present in heterochromatin is thought to protect DNA from damage although, when lesions do occur, this compaction further restricts the capability of DNA damage response proteins to access the site to properly signal and mediate repair, as evidenced by the ability of HC to block the expansion of H2AX phosphorylation to neighbouring nucleosomes (Kim, Kruhlak, Dotiwala, Nussenzweig, & Haber, 2007). Indeed, DNA damage in HC has been shown to be refractory to repair considering that DSBs introduced by ionizing radiation are resolved with slower kinetics than in EC (Cann & Dellaire, 2011). HC harbours an abundance of the repressive mark

H3K9me3, introduced by the methyltransferases SETDB1 (SET domain bifurcated 1) and SUV39 (suppressor of variegation 3-9), that acts as a binding site for non-histone proteins to associate with chromatin and promote its compaction. The most central of these proteins are the heterochromatin protein 1 variants (HP1α, β and γ, in mammals) that help to maintain the structure and stability of HC. Surprisingly though, these proteins have been shown to also contribute to DSB repair in HC. After initial dispersion following DNA damage, all HP1 variants are recruited to and accumulate at damage foci in HC regions (Luijsterburg et al., 2009). Loss of HP1 was shown to induce high sensitivity to ionizing radiation, defects in recruiting DDR factors such as 53BP1 and RAD51, and impaired DNA end resection (Baldeyron, Soria, Roche, Cook, & Almouzni, 2011). Another protein that affects chromatin structure is KAP1 (KRAB domain associated protein 1). KAP1 is recruited to HC by sequence-specific-recognizing repressor proteins, subsequently interacting with HP1, SETDB1, HDAC1 and HDAC2, together maintaining a compacted chromatin state (Watts, 2016). Following damage in HC, ATM phosphorylates KAP1 which causes it to disperse throughout chromatin promoting global relaxation. This requirement of ATM phosphorylation seems to be specific for repair in HC as knockdown of KAP-1, HP1 or HDAC1/2 alleviates the need for ATM in DSB repair (Goodarzi et al., 2008). In sum, HC components are dynamic and can contribute to DSB repair in opposing ways, suggesting that repair does not require a DNA region empty of proteins but instead a region with varying levels of compaction but permissive to DDR factors.

Furthermore, studies in *Drosophila* have indicated that localized HC relaxation occurs in the vicinity a DSB followed by rapid relocalization of the break to the periphery of chromatin dense regions before γH2AX foci formation and lesion repair by HR in an ATM-dependent fashion, indicating that there exists an additional level of modulation in HC in response to DSBs involving higher-order chromatin reorganization (Chiolo et al., 2011; Goodarzi & Jeggo, 2012; Jakob et al., 2011). This movement may serve to not only facilitate access of repair proteins to the lesion site, but also to reduce the risk of illegitimate joining during HR caused by the abundance of sequence repeats found in HC. In yeast, it was found that this rearrangement is directed by the yeast homologue of histone variant H2AZ with assistance from the chromatin remodeler complex INO80 and Rad9 (the yeast homologue of 53BP1) along with several components of the homologous recombination machinery (Dion, Kalck, Horigome, Towbin, & Gasser, 2012).

Taken together, these findings point to DSBs located in chromatin dense regions as being particularly reliant on the HR pathway for repair. As such, the state of chromatin condensation and the presence of HC-associated factors at DSB sites have come to light as additional relevant elements capable of determining usage and efficiency of repair systems.

1.5. Cell cycle checkpoint activation and reversal

In a proper functioning cell, DSBs are quickly recognized by DDR proteins which prompt the cell to transiently halt cell cycle progression, initiating what is called a "cell cycle checkpoint". Checkpoint activation allows cells time to repair DNA damage before it can compromise genomic integrity and cell viability. Furthermore, if damage is too extensive to be repaired, it prevents cells harbouring potential oncogenic mutations from proliferating by permanently halting their proliferation (a phenomenon known as cellular senescence) or initiating programmed cell death (apoptosis). Depending on several circumstances, including the complexity of DNA lesions and the cycle phase the cell finds itself in, different repair and checkpoint pathways can be activated which together function as a highly complex and interacting defence mechanism against genotoxic insults. Although our knowledge of how DDR and checkpoint proteins are regulated by post-translational modifications has greatly improved in recent decades, it is still not completely understood how the interaction between repair systems and checkpoint effectors coordinates the decision to maintain cell cycle arrest, or else to terminate checkpoint signaling to allow cycle progression to resume. However, it is becoming increasingly clear that checkpoint activation and reversal mechanisms are precisely tuned to each cell cycle phase (Shaltiel, Krenning, Bruinsma & Medema, 2015).

DNA damage can be particularly harmful in certain cell cycle phases. In S phase, for example, DNA lesions that would be relatively mild in G1 or G2 can interfere with the progression of replication forks and may even lead to fork collapse, causing further DSBs and potential chromosome breakage (Scully & Xie, 2013). The existence of checkpoints at the G1/S and G/M boundaries of the cell cycle is thus thought to prevent cells from

undergoing replication or mitosis, respectively, in the presence of DNA damage. An intra-S phase checkpoint for damaged or incorrectly replicated DNA, and a mitotic spindle assembly checkpoint that senses incorrect alignment of chromosomes at the equatorial plane or impaired attachment of spindle fibers at kinetochores are also in place (Deckbar et al, 2011).

The essential step for checkpoint activation is the recruitment of ATM kinase by the MRN complex once it recognizes DSBs, a requirement that is common to all cycle stages. Afterwards, the downstream effectors of checkpoint activation vary according to each phase. Cycle progression in G1 is mediated by the cyclinD/Cdk4/6 complex, whose rising levels in G1 are responsible for phosphorylation (and inactivation) of the retinoblastoma protein pRb, an inhibitor of transcription factors of the E2F family which are required for cell cycle progression. E2F promotes expression of cyclin E that, together with Cdk2, will coordinate entry into S phase (Deckbar et al., 2011). Detection of DSBs leads to ATM activating Checkpoint Kinase 2 (Chk2), and together they stabilize the key transcription activator p53, which in turn results in expression of a large variety of transcriptional targets including the major Cdk-inhibitor protein p21 that binds to cyclin-Cdk complexes blocking cell cycle progression. ATM and Chk2 activities also promote the degradation of cyclin D and Cdc25A, a phosphatase responsible for reversing the inhibitory phosphorylation on Cdk2, reinforcing the barrier to S phase entry (Deckbar et al., 2010).

In the case of damage in S phase, the removal of 53BP1 from DSBs allows the block on end resection to be lifted and commitment to repair by HR to ensue. Generation of 3’ ssDNA overhangs activates ATR kinase and its effector Chk1, shifting DNA damage signalling away from ATM and Chk2 exclusively. During DNA replication p21 is marked for degradation by the PCNA-associated CRL4-Cdt2 (from the family of cullin ring E3 ubiquitin ligases) that is present at replication forks (Havens & Walter, 2011), which means that the intra-S checkpoint has to rely on a different Cdk inhibitor to arrest cycle progression into G2. Chk1 an d Chk2 activate the kinase Wee1 which in turn phosphorylates Cdk2 inhibiting its activity, while also marking the counteracting phosphatase, Cdc25A, for degradation thus initiating the checkpoint (Beck et al., 2010).

G2 checkpoint activation, on the other hand, requires both p21 and Wee1 activities. Since DNA replication has been concluded, accumulation of p21 levels is

reinstated in G2 and this pathway, involving ATM and Chk2, is necessary for initiation of cell cycle arrest after DNA damage. However, maintenance of a stable checkpoint depends on ATR and Chk1 signalling, suggesting that engagement of HR is critical for G2 checkpoint maintenance (Shibata et al., 2010). In regards to the mitotic spindle assembly checkpoint, it is not of particular relevance for this work since it does not respond to DNA damage due to almost complete inhibition of the DDR response during mitosis (Giunta, Belotserkovskaya, & Jackson, 2010) and thus will not be detailed here.

DNA checkpoints are indeed useful for allowing additional time for DNA repair but only if they can be reversed when appropriate. Just as the DDR is able to trigger a wide range of protein posttranslational modifications that culminate in the activation of checkpoints, removal of these modifications or degradation of modified proteins by dedicated enzymes is necessary to release cells from damage-induced checkpoints and allow them to re-enter their cycle . After G2 checkpoint activation, for instance, polo-like kinase 1 (Plk1) acts as the key regulator of checkpoint reversal by contributing to the activation of the pro-mitotic cyclin B1/Cdk1 complex while also disabling Chk1 by targeting its activator for degradation, as well as negatively regulating Wee1, 53BP1 and Chk2 (Mamely et al., 2006; Van Vugt, Brás, & Medema, 2004). Plk1 thus pushes cells away from arrest in G2 to cycle re-entry into mitosis. The mechanics of G1 checkpoint reversal, on the other hand, are not yet fully understood but have been shown not to depend on Plk1, which is absent in G1, and to require silencing of Chk2 and p38 MAPK (mitogen-activated protein kinase) signalling to prevent the stabilization of p53 and p21, respectively, thus denying enforcement of the checkpoint (Lafarga et al., 2009; Shaltiel et al., 2014).

It is still a general belief that recovery from checkpoints induced by DSBs only occurs following completion of DNA repair. However, this notion has begun to change in recent decades. Although checkpoints do contribute to preventing genomic instability they were found to carry inherent limitations and are no longer considered flawless. For instance, the G1/S checkpoint was shown not to initiate until 4 to 5 hours post-damage, allowing a large fraction of cells to enter S phase with unrepaired DSBs (Deckbar et al., 2010), and the G2/M checkpoint to carry limitations of a different nature, only being activated above a certain threshold level of DNA damage and DDR signalling (Deckbar et al., 2011). Furthermore, despite the presence of DNA damage cells can terminate G2

checkpoint and enter mitosis, a phenomenon that has been termed “checkpoint adaptation”. It has been observed that G2 checkpoint activation is followed by a gradual increase in Plk1 levels and it was hypothesized that once a certain threshold is reached it triggers reversal of the arrest independently of any subsisting DNA damage. Although it was proved that increased Plk1 levels alone could not override an established DNA damage checkpoint, they may be a component of the mechanism behind this event (Shaltiel et al., 2015). More research is still necessary to fully understand what factors determine whether a cell remains blocked from progressing in its cycle while harboring severe DNA damage, or chooses to continue though at the risk of its genomic integrity.

1.6. Topoisomerase-mediated DNA lesions

Under particular non-physiological conditions, certain nuclear enzymes may also generate persistent protein-mediated DSBs. One such example is Topoisomerase II (Topo2), an enzyme consistently present in cells since it solves topological problems of DNA, such as knots and entanglements, which may arise during replication, transcription and chromosome condensation (Wang, 2002). Topo2 acts by generating a transient DSB on DNA while remaining covalently linked to the 5’ end of the break, through which it subsequently promotes the passage of another double-strand of DNA, concluding by catalyzing DSB relegation (**Fig.3**). In mammalian cells there are two Topo2 isoforms, α and β, with similar structures and catalytic activities although Topo2α is mainly implicated in DNA replication, decatenation and segregation and Topo2β is mostly associated with transcription. Their expression is also differently regulated, with Topo2α levels rising from S to M phase while Topo2β remains constant throughout the entire cell cycle (Agostinho et al., 2008; Agostinho, Ferreira, & Steffensen, 2004; de Campos-Nebel et al., 2010) .

Topo2 is the target of several anti-cancer drugs commonly used in chemotherapy, such as Etoposide and Doxorubicin, which poison the enzyme by stabilizing the Topo2-DNA complex, called cleavage complex, preventing religation of the broken DNA ends. While the stabilized cleavage complexes are reversible by drug removal, they can give rise to persistent breaks if they remain for enough time to ultimately collide with either the

transcription or replication machinery as these processes progress through the DNA. The collapse of the cleavage complex that results from this collision leaves behind a permanent DSB that are able to trigger the DDR and checkpoint pathways (Hisang, Lihou, & Liu, 1989; Wu & Liu, 1997). Repair of Topo2-mediated DSBs has been shown to utilize NHEJ and HR in G1 and S/G2, respectively (de Campos-Nebel et al., 2010). Topo2 poisons thus indirectly induce persistent DSBs by converting this enzyme into a potent genotoxin that is particularly harmful to rapidly dividing cells due to its essential role in transcription and replication.

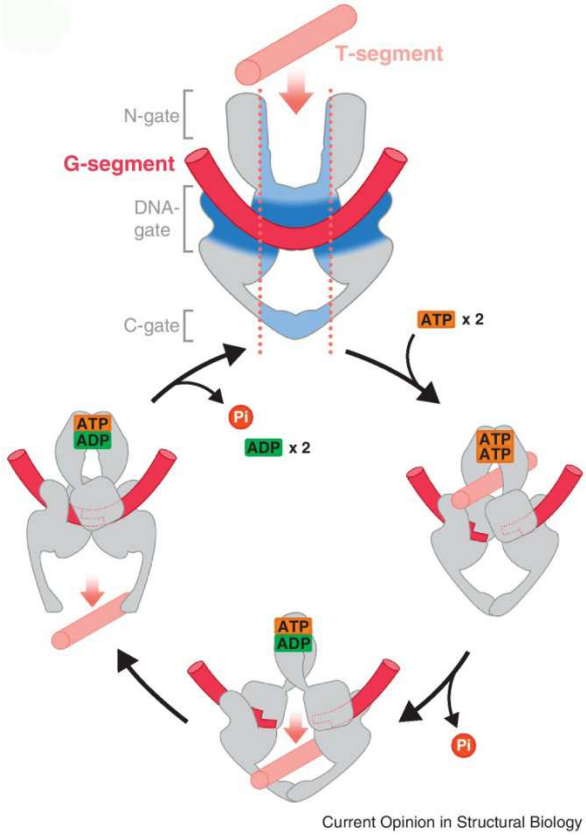

Figure 3. Schematic diagram for the proposed two-gate mechanism of Topoisomerase type IIA enzyme. The catalytic cycle starts from the association of G-segment (red) with its binding pocket (dark blue), followed by the capture and passage of T-segment (pink) through the N-gate, DNA-gate, and C-gate. Regions expected to interact transiently with T-segment during its passage are colored in light blue. From C. C. Chang, Wang, Chen, Wu, & Chan, 2013.

Although Topo2 poisons are currently widely used to induce tumor cell death, they have been associated with development of secondary malignancies in treated patients, most frequently myeloid leukemia (Felix, Kolaris, & Osheroff, 2006). This has generated a significant interest in how cells handle the repair of Topo2-mediated DNA lesions in order to better predict and prevent undesired mutagenic effects of anti-cancer chemotherapy. As an example, the discovery that inhibition of HDAC activity results in increased sensitivity to Topo2-mediated DNA damage has already been translated into practice in

clinical oncology with the development of new chemotherapy schemes combining drugs that target Topo2 and small molecule inhibitors of HDACs (Namdar, Perez, Ngo, & Marks, 2010).

Thesis aims

Many current cancer therapy strategies rely on the use of drugs capable of inducing levels of DNA damage too extreme for cells to repair, reliably causing cellular death or permanent proliferation arrest. Although these agents have preferential targets in cells with rapid cycle turnover or inadequate DNA repair, two characteristics frequent in many tumors, they often also affect non-cancer cells resulting in severe side effects for the patients, thus limiting their therapeutical potential (Hühn, Bolck, & Sartori, 2013).

As previously mentioned in the introduction, the regulation of cell cycle checkpoints, of DNA repair pathways and of chromatin structure have all emerged as key elements that determine how both normal and cancer cells will respond to DSBs introduced by chemotherapy treatments. These three critical components of cellular activity interact and coordinate with each other through vast networks of regulatory proteins that enact post-translational modifications at the protein and chromatin levels, many of which already described as participating in more than one of these processes (**Fig.4**). The precise articulation between these three different mechanisms remains the focus of intense research, directed in particular to the uncovering of exploitable vulnerabilities in tumor cells that may enhance the specificity and efficacy of future cancer therapies.

Correspondingly, the present work is aimed at investigating the interplay between the three systems in response to Topo2-mediated DSBs. The Topo2 poison Etoposide was the preferred agent to induce DNA damage in cultured cancer cell lines. Etoposide-bound Topo2 is able to reliably introduce DSBs at all stages of the cell cycle and, during S phase, it is mainly recruited to assist in DNA replication, which means Etoposide specifically targets replicating DNA when used during that stage of the cell cycle. Since replication of euchromatin and heterochromatin occur separated in time, with EC replicating early in S phase while HC replication takes place in the later S stages (O'Keefe, Henderson, & Spector, 1992), it is possible to selectively introduce DSBs in either replicating EC or HC with proper cell cycle synchronization in early or late S phase, respectively (**Fig.5**). This characteristic of Topo2 conveniently allows for the development of experimental

methodologies to study the interplay between all the three mechanisms: cell cycle, DSB repair and chromatin structure regulation.

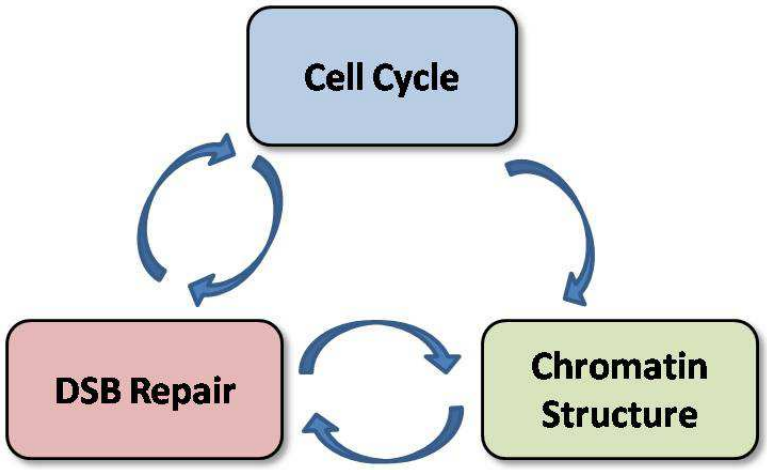

Figure 4. Cell cycle progression, the damage response to DSBs and the regulation of chromatin structure exhibit extensive coordination and overlap of factors. Cell cycle position influences repair system choice and chromatin condensation state (e.g. during replication and chromosome formation), while the DDR can trigger cell cycle checkpoints and chromatin remodeling to facilitate repair. Finally, chromatin structure can also impact efficiency and usage of repair factors.

Therefore, the two main goals of this thesis are as follow:

A) To establish the dependence of distinct cell cycle stages (G1, early S, late S and G2) on each of the two main DSB repair pathways (non-homologous end joining and homologous recombination) for repair of Topo2-mediated DSBs.

B) To determine how different chromatin structural conformations (euchromatin *vs*. heterochromatin) influence repair of Topo2-mediated DSBs and long term cellular outcome.

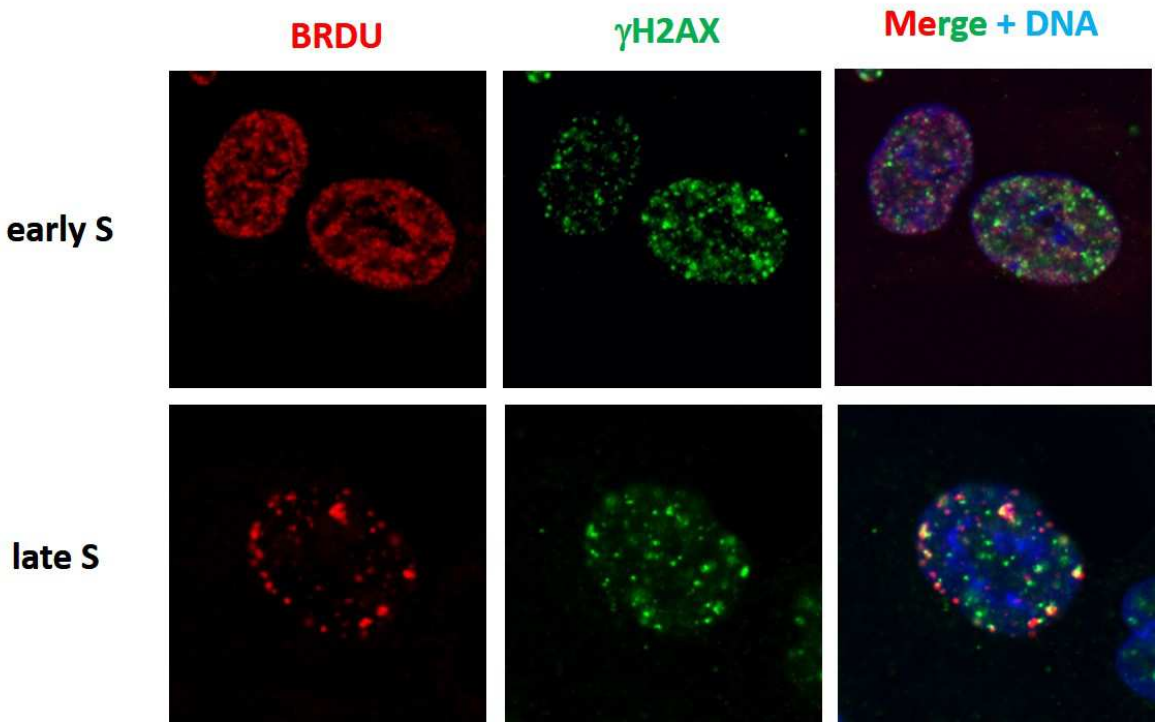

Figure 5. Topoisomerase II specifically targets heterochromatin in late S phase. Cells were exposed to Etoposide (50 µM, 15 mins) prior to immunostaining for BrdU (replicated DNA) and γH2AX (DSBs). Notice signal overlap (yellow) in late S. Red: BRDU; Green: γH2AX; Blue: DAPI.

Chapter 2

Methods

2. Methods

Cell culture, chemicals and antibodies

Human colorectal carcinoma HCT-116 (ATCC CCL-247) and HCT-116 deficient for DNA-PK were obtained from the laboratory of Dr. Bert Vogelstein (Johns Hopkins School of Medicine, Baltimore, MD, USA). HCC1937 (ATCC CRL-2336) breast carcinoma with a homozygous loss of function mutation in the BRCA1 gene (BRCA1(-)), along with HCC1937 cells with retroviral-induced expression of wild type BRCA1 (BRCA1(+)) (Scully et al., 1999) were provided by Dr. Ralph Scully (Harvard Medical School, Boston, MA, USA). These cells also carry a homozygous loss of function mutation in p53. THP1 leukaemia cell line was obtained from ATCC (TIB-202).

HCT-116 cells were cultured in McCoy's 5A Modified medium supplemented with 10% heat inactivated foetal bovine serum (FBS), 2 mM L-glutamine, 10mM MEM non-essential amino acids, and 100 U/ml penicillin/streptomycin (all from Gibco, Thermo-Fisher Scientific, Waltham, MA, USA). HCC1937 cells were cultured in RPMI-1640 medium (Gibco) supplemented as above. THP1 cells were cultured in RPMI-1640 medium (Gibco) supplemented with 10% heat inactivated foetal bovine serum (FBS), 2 mM L-glutamine, 10 mM MEM non-essential amino acids, 100 U/ml penicillin/streptomycin, and 0,05 mM 2-mercaptoethanol. Cells were maintained at 37°C in a humidified incubator at 5% CO2. Cells were passaged on alternate days at a constant plating density of ≈3 x 10^4 cells/cm^2 or ≈2 x 10^5 cells/ml.

Etoposide, RO-3306, thymidine, propidium iodide (PI), 4',6-diamidino-2-phenylindole (DAPI), 3-deazaneplanocin A (DZNep) and RNase A were purchased from Sigma-Aldrich (St. Louis, MO, USA). Suberoylanilide hydroxamic acid (SAHA) was purchased from Cayman Chemical (Ann Harbor, MI, USA).

The following antibodies were used in this research: rabbit polyclonal to histone H2A.X (ab11175, Abcam, UK (Dawson et al., 2009)), mouse monoclonal IgG1 to phospho-histone H2A.X (Ser139; clone JBW 301; Merck-Millipore, Darmstadt, Germany (Smith-Roe et al., 2015)), mouse monoclonal IgG1 to RPA32/RPA2 (clone 9H8; ab2175 Abcam, UK (Ciccia et al., 2009)), affinity-purified rabbit polyclonal to phospho-RPA32/RPA2 (Ser4/Ser8; Cat. A300-245A; Bethyl Laboratories, Montgomery, TX, USA (King et al., 2015)), rabbit

polyclonal to phospho-KAP1 (S824; Cat.A300-767A; Bethyl Laboratories), mouse monoclonal to RAD51 (ab213; Abcam), rabbit polyclonal to p21 (C-19; sc-397, Santa Cruz Biotechnology, Dallas, TX, USA), mouse monoclonal to phospho-ATM (S1981; Rockland Immunochemicals, Limerick, PA, USA), rabbit polyclonal to phospho-DNAPKcs (T2609; Rockland Immunochemicals), rabbit polyclonal to phospho-p53 (S15; ab1431; Abcam), mouse monoclonal to cyclin E (HE12; sc247; Santa Cruz Biotechnologies), rabbit polyclonal to cyclin A (H-432; sc751, Santa Cruz Biotechnologies), mouse monoclonal to α tubulin (B-7; sc5286; Santa Cruz Biotechnologies), rabbit polyclonal to EZH2 (cat.07-689, Merck-Millipore), mouse monoclonal to H3K27me3 (ab6002, Abcam), affinity-purified Alexa 488-conjugated and Cy3-conjugated anti-mouse secondary antibodies (Jackson ImmunoResearch Laboratories, Sacramento, CA, USA), and peroxidase-conjugated affinity-purified goat anti-mouse IgG and goat anti-rabbit IgG (BioRad Laboratories, Hercules, CA, USA).

Flow cytometry instrumentation and data analysis

Samples stained for PI, DAPI and γH2AX were analyzed using a three laser (blue-488nm; red-640nm; violet-605nm) BD LSR Fortessa flow cytometer (BD Biosciences, San Jose, CA). γH2AX and PI signals were measured upon excitation by the blue laser using 530/30 and 695/40 bandpass filters, respectively. DAPI signals were measured upon excitation by the violet laser with the 525/50 bandpass filter. A minimum of 30000 events were acquired per experiment in slow rate mode to avoid doublets. Sample measurements were performed with FACSDiva Software (Version 6.2, BD Biosciences, San Jose, CA, USA). Data analysis for cell cycle parameters and mean fluorescence intensities was performed with FlowJo Software (Ashland, OR, USA). Cell debris and aggregates were excluded from the analysis using pulse processing FSC-A *vs* FSC-H, FSC-H *vs* FSC-W, SSC-H *vs* SSC-W, and FL2-A *vs* Fl2-W when appropriate.

Immunofluorescence staining

For immunofluorescence analysis, HCT-116 cells growing on coverslips were routinely fixed in freshly prepared 3.7% paraformaldehyde in HPEM buffer (30 mM HEPES, 65 mM Pipes, 10 mM EGTA, 2 mM $MgCl_2$ (pH 6.9)) plus 0.5% Triton X-100 for 10 mins at room temperature before incubation with antibodies. All washes were performed

with PBS containing 0.05% Triton X-100. Antibodies used for immunofluorescence were diluted in PBS containing fish skin gelatin (0.1%) and Triton X-100 (0.05%) as follows: anti-phospho-RPA2 at 1/200, anti-RAD51 at 1/200, anti-phospho-histone H2AX (Ser139) at 1/300 and Cy3-conjugated anti-mouse secondary antibodies at 1/100. After immunolabeling, total DNA was stained with DAPI (0.5 μg/mL) and coverslips were mounted in Vectashield (Vector Laboratories Inc., Burlingame, CA, USA) before analysis by fluorescence microscopy.

Confocal microscopy

Samples were examined using a Zeiss 510 confocal microscope (Carl Zeiss, Jena, Germany) equipped with lasers giving excitation lines at 405, 488 and 543 nm. Data from the channels were collected separately using narrow-band-pass filter settings. In multiple staining experiments, the laser intensities were adjusted to avoid bleedthrough between channels. Data were collected with two- to fourfold averaging at resolution of 1024 X 1024 pixels using pinhole settings between 1.05 and 1.10 airy units. Data sets were processed using Zeiss 510 version 2.8 software package and were subsequently exported for preparation for printing using Adobe Photoshop, version CS5.1. Quantification of cell number, foci number, nuclei area and signal amount per image was performed using the UBCr Foci software developed in MATLAB (MathWorks, Natick, MA, USA) by the Bioimmaging unit from Instituto de Medicina Molecular da Faculdade de Medicina de Lisboa (Dr. José Rino).

Cell cycle synchronization and Etoposide exposure

In order to synchronize exponentially growing HCT116 cells at G1/S phase transition, we used the double-thymidine block approach. Briefly, cells were incubated in culture medium containing thymidine at a final concentration of 2 mM for 12 h (1st thymidine block), allowing time for cells to arrest in S phase. Thymidine was removed through repeated washes with fresh medium and cells were incubated with fresh thymidine-free medium for 7.5 h, to allow full exit from S phase. Cells were subsequently incubated with 2 mM thymidine for another 12 h (2nd thymidine block) to obtain a population precisely arrested at the G1/S phase transition that will progress into S phase upon release from thymidine. To induce DSBs in cells synchronized at different cycle

phases, 50 μM Etoposide was added to separate groups of cells at specific times after thymidine release. Cells were exposed to drug 15 mins, after which drug was removed through washing and cells incubated with fresh medium until collection at different time points after Etoposide pulse. Times for cycle phase specific Etoposide pulse: early S at 30 mins post thymidine release; late S at 3.5h, G2 at 5.5h and G1 at 10.5h.

Western blotting

For immunoblotting, cell lysates were prepared in boiling 1X Laemmli´s sample buffer were supplemented with PMSF (1 mM) and a commercially available mixture of protease inhibitors (Complete Mini EDTA-free; Roche Diagnostics, Mannheim, Germany; 1 tablet/mL). DNA was first fragmented mechanically by passing the sample into a syringe (≈10 times) through a 25-gauge needle and, subsequently, after supplementation with $MgCl_2$ (5 mM), by digestion with benzonase (0.4 Units/ml; Sigma-Aldrich) for 30 mins at room temperature. Lysates were then separated on 12 or 14% SDS-PAGE under reducing conditions and transferred to nitrocellulose membranes (Schleicher & Schuel, Keene, NH). Membranes were blocked for 1h with 5% non-fat dry milk powder in PBS and incubated for a minimum of 2h with the specific primary and secondary antibodies. Antibodies used for immunoblotting were diluted in PBS supplemented with nonfat dry milk (2.5%) and Triton X-100 (0.05%) and used at the following dilutions: anti-phospho-RPA2 (Ser4/Ser8; 1/2000), anti-phospho-histone H2AX (Ser139; 1/1000), anti-histone H2AX (total H2AX; 1/1000), anti-phospho-KAP1 (S824; 1/1000), anti-p21 (1/1000), anti-phospho-ATM (S1981; 1/1000), anti-phospho-DNAPKcs (T2609; 1/2000), anti-cyclin E (1/500), anti-phospho-p53 (S15; 1/500), anti-tubulin α (1/5000) and peroxidase-conjugated affinity-purified goat anti-mouse and goat anti-rabbit were diluted at 1/3000. Total H2AX, tubulin-α and Ponceau staining provided loading controls. The detection reaction was developed by enhanced chemoluminescent (ECL) staining according to the specifications of the manufacturer (ECL Amersham, Western Blotting Detection Reagents, UK).

shEZH2 lentiviral transfection

Plasmids clones for expression of shEZH2 were selected from a library of shRNA enriched for human kinases and phosphatases from Prof. Luís Moita (Rato et al., 2010).

Functional clones were selected by their ability to confer resistance to puromycin (resistance gene is co-expressed with shEZH2) to HCT116 cell cultures.

For transfections, HCT116 cells were seeded at the appropriate density according to the type of plate one day prior to infection. Medium was removed and virus added to cells. Fresh medium with polybrene (Sigma-Aldrich) at a final concentration of 8 µg/ml was added and cells centrifuged for 90 mins at 37ºC. Medium was replaced and cells were incubated for 24h at 37ºC, 5% CO_2. Medium containing puromycin (Sigma-Aldrich) was added and cells were incubated for 3 days, replacing growth medium with puromycin each day. Surviving cells were incubated in the presence of puromycin until reaching proper density for experiments.

Drug combinations assays

For sequential incubations of DZNep and Etoposide, THP1 cells were diluted to 1 x 10^5 cells/ml and seeded in 6-well plates, at 1 ml per well. 1 ml of medium containing different concentrations of DZNep was added to wells followed by 24h incubation. Cells were washed and 2ml drug-free fresh medium was added, followed by 48h incubation. 100 µl from each well were resuspended and transferred several times to fill the wells of a 96-well plate. 50 µl of respective Etoposide dilution was added to each well and plates were incubated for 72h. Cells were washed and fresh medium and drugs added every 24h. 50 µl (final concentration 1/200) of alamarBlue reagent (Invitrogen, Carlsbad, CA, USA) was added to each well and incubated for 2h. Plates were read for luminescence resulting from metabolic activity in the presence of alamarBlue using a Tecan Infinite 200 microplate reader (Tecan Group, Mannedorf, Switzerland).

For simultaneous combinations of SAHA and Etoposide, THP1 cells were diluted to 1 x 10^5 cells/ml and seeded in 96 well plates, 100 µl per well. 50 µl of different SAHA-Etop combinations was added to each well. Cells were incubated for 72h. Drug medium was refreshed every 24h. 50 µl (final concentration 1/200) of alamarBlue reagent was added to each well and incubated for 2h. Plates were read for luminescence as previously.

Clonogenic assay

For clonogenic survival assays, cells lines were first subjected to Etoposide pulses of varying concentrations for 15 mins then washed, trypsinized and seeded at ≈2000

cells/plate. After 8 days of unperturbed incubation, cells were washed and fixed for 5 mins in methanol, followed by staining of nuclei with nuclear fast red dye solution (Sigma-Aldrich) for 5 mins, followed by several washes with ethanol. Proliferating and senescent-like colonies were counted using a 20x magnifying lens.

Statistical analysis

Data are reported as the mean ± SD or mean ± SE, as specified. Results were compared by 2-tailed Student's t test for two groups and one-way ANOVA followed by Dunnett's multiple comparison test for multiple groups. GraphPad Prism version 5.03 for Windows (GraphPad Software, La Jolla, CA, USA) was used for statistical analysis. Differences were considered statistically significant at $P < 0.05$

Chapter 3

Results

3. Results

3.1. Damage checkpoint activation in separate cell cycle phases

Herein we aim to address the first proposed objective which consists of determining whether Topo2-induced DNA lesions are differently handled when introduced in separate cell cycle phases, and to what extent they rely on HR and NHEJ for repair. To this end, we first established a protocol to reliably synchronize populations of cells at each of the intended cell cycle phases. Briefly, by means of a double thymidine block followed by carefully planned periods of unblocked cell cycle progression (see Methods), entire populations of HCT116 cells were synchronized in either G1, early S, late S or G2 phases prior to induction of DNA damage. Afterwards, DSBs were induced by a short pulse of Topo2 poison Etoposide (50 μM, 15 mins). Cell cycle progression was monitored at predetermined time points after DNA damage by DNA content (PI staining) analysis using flow cytometry. Since the normal duration of each cell cycle phase in proliferating HCT116 cells is well established (≈ 5.5h for G1, 6.5h for S and 4h for G2; see article in this thesis: Pereira et al., 2017), we thus have a base of comparison for cell cycle profiles of synchronized cells after Etoposide exposure. This allows us to detect potential deviations from expected cycling times, which serve as indications of checkpoint activation.

As shown by the cell cycle profiles in **Figure 6**, the starting populations collected prior to Etoposide treatment were all properly synchronized at the different cell cycle stages. Subsequently, Etoposide-Topo2 mediated DSBs triggered the respective cycle checkpoints in G1- and G2-damaged cells. This is indicated by the considerable loss of population synchronization these cells have suffered 8 hours after DNA damage. 24 hours after DNA damage, the G1-damaged population was clearly divided into two main fractions determined by DNA content, a 2n fraction corresponding to cells still in G1 phase, and 4n fraction corresponding to cells that had reached G2. The G2-damaged population at 24h was also composed of two prominent subpopulations, one still halted in G2 and another

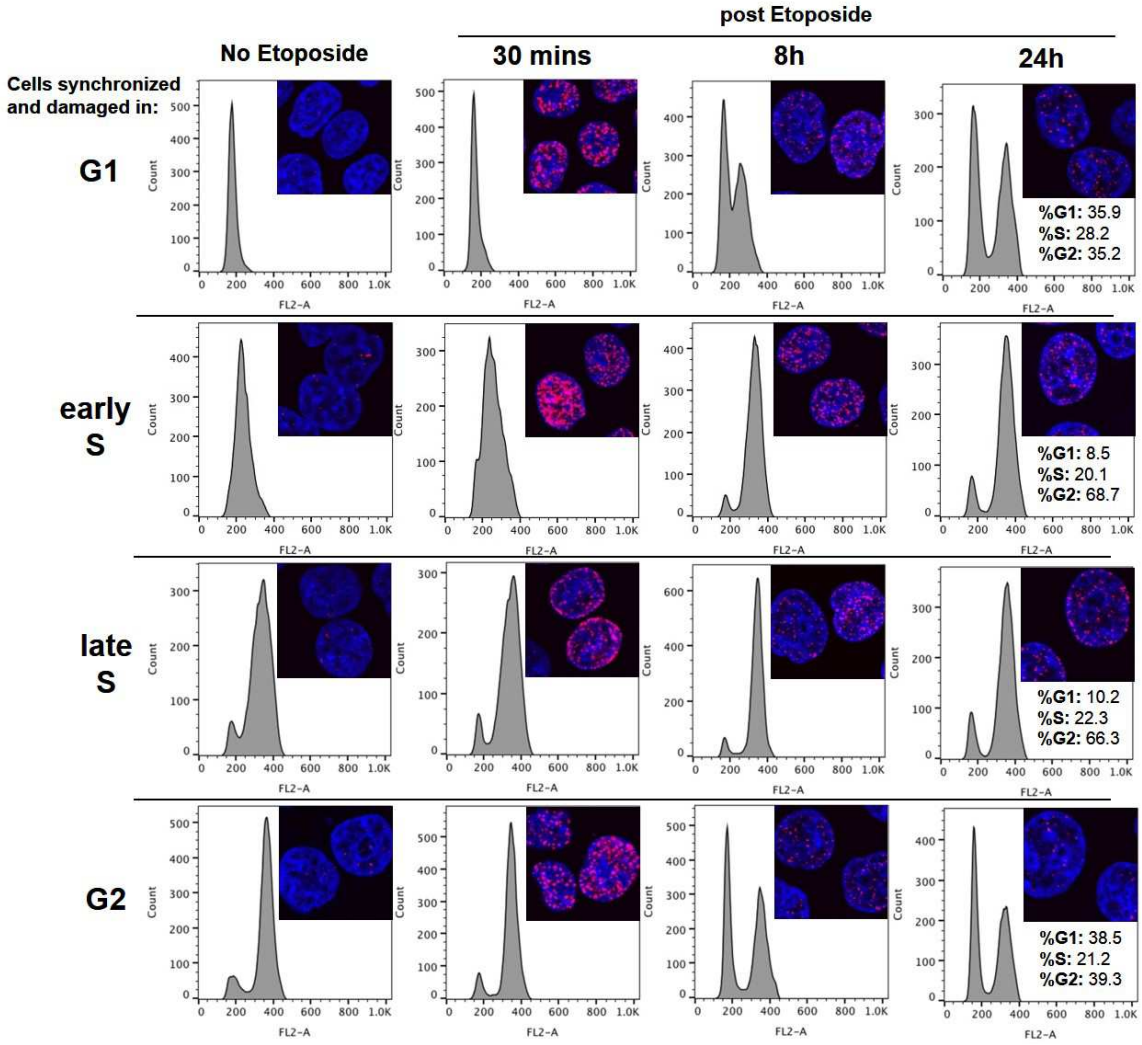

Figure 6. At 8h post Etoposide the G1- and G2-damaged populations have lost synchronization, an indication of that only a portion of these populations was delayed by checkpoint arrest. Shown are differences in cell cycle progression and γH2AX foci in synchronized HCT116 cells after Etoposide pulse at separate cell cycle stages. Separate populations of cells were synchronized in G1, early S, late S or G2 using the double-thymidine block methodology, subjected to an Etoposide pulse (50 μM, 15 mins), and collected at the specified time points post Etoposide. DNA was stained using Propidium Iodide and cell cycle profiles were obtained by flow cytometry. Also, notice that a substancial number of γH2AX foci still remain 24h after Etoposide. Population percentages in each phase were estimated using the Dean/Jett/Fox algorythm within FlowJo software. Shown are results representative of 3 independent experiments. Red: γH2AX; Blue: DAPI.

already in G1. Cells damaged in either early or late S phase remained well synchronized and reached the S/G2 transition by the 8h time point, indicating they were not substantially delayed by the intra-S checkpoint (based on S-phase lasting ≈ 6.5h). However, these cells did not advance into G1 even after an additional 16 hours (24h time

point), which taking into account that S + G2 phase duration is expectedly 10.5h, highlights the occurrence of a robust G2 checkpoint arrest. These results show that while Topo2-mediated DSBs do trigger checkpoint activation in the same cycle phase in which they are introduced, a substantial fraction of the cell population is able to escape prolonged cell cycle arrest.

Next, we wanted to investigate whether cells were exiting from their checkpoints due to genuine repair of DSBs to basal levels. Thus, to evaluate DSB repair dynamics immunofluorescent staining of cells against histone H2AX phosphorylated in serine 139 (γH2AX), an histone mark known to signal DSBs (Rogakou, Pilch, Orr, Ivanova, & Bonner, 1998), was performed in cells collected in parallel with the ones for flow cytometry. Cells were then documented by confocal microscopy. For quantification of γH2AX foci numbers to be performed in large numbers of cells in a time-efficient manner, analysis software was developed by the Bioimaging Unit of Lisbon's Instituto de Medicina Molecular (IMM). Using this software we were capable of extracting these data from cell images in an automated fashion (see Methods). This showed that γH2AX foci numbers were at their highest 30 minutes after exposure to Etoposide in all cell cycle phases (mean number of foci per cell 42 ± 0.8 for G1; 52 ± 0.9 for early S; 50 ± 0.8 for late S and 39 ± 0.7 for G2;) and significantly decrease in subsequent time points as cells repair their DNA (**Fig.6** and **7A**). Interestingly, this analysis revealed that the great majority of cells in all phases tested still contained substantial amounts of γH2Ax foci 8h after Etoposide exposure compared to non-damaged controls. Cells damaged in early S (37 ± 1 foci per cell) presented the highest average number of foci at 8h followed by late-S-damaged cells (24 ± 0.8 foci per cell). Cells damaged in G1 or G2 displayed lower γH2Ax foci numbers (17 ± 0.7 and 14 ± 0.5 foci per cell, respectively) than replicating cells, but nonetheless much superior to non-damaged controls (2 ± 3 foci per cell).

By comparing these results with the cell cycle data previously obtained using flow cytometry, we conclude that, at 8h, approximately half of G1- and G2-damaged cells escapes checkpoint arrest and advances into the subsequent cell cycle stage, while still harbouring non-basal levels (though much less than at 30 minutes) of potentially harmful DSBs. This becomes even more evident at 24h. Also, almost all cells damaged in early or late S phase were able to reach G2 by 24h with high levels of DSBs (31 ± 1.2 and 19 ± 0.8 foci per cell, respectively). An estimate of DSB levels was also obtained by

immunostaining cells with fluorescent anti-γH2AX antibodies and measuring total cell intensity by flow cytometry. This type analysis revealed a similar trend to immunofluorescence results except for the presence of elevated γH2AX levels in controls (**Fig.7B**). This was not totally unexpected since signal quantification by flow cytometry detects all background signals from dispersed histone γH2AX, while in microscopy images signals are concentrated in foci, which are easy to separate from the background, resulting in the very low damage levels seen in controls.

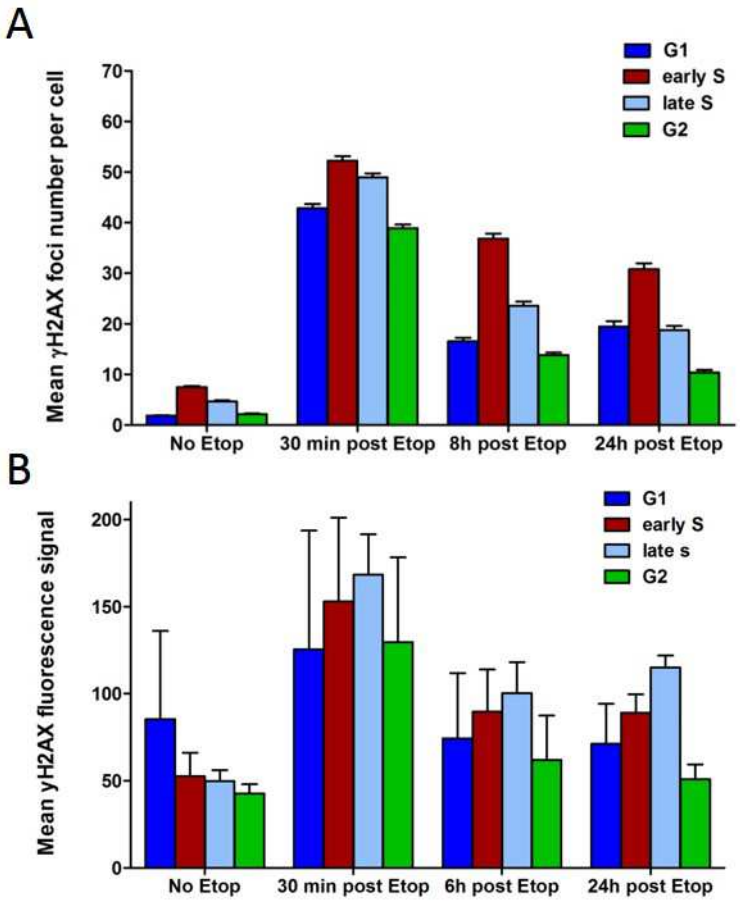

Figure 7. Two different methodologies confirm that DSBs still remain 24h after Etoposide exposure. Quantification of γH2AX at different time points in synchronized HCT116 cells damaged with Etoposide at separate cell cycle phases. **(A)** Mean γH2AX foci number per cell. Cells grown on glass slides were immunostained against γH2AX and visualized using confocal microscopy. Foci numbers were quantified by software analysis. Results are shown as mean + SEM of three independent experiments**. (B)** Mean γH2AX fluorescence signal. Cells in suspension were immunostained against γH2AX and mean fluorescence intensity for each population was measured by flow cytometry. Results are shown as mean + SD of three independent experiments.

To confirm if checkpoint activation was in fact being triggered after DNA damage induction in all the targeted cycle phases, we decided to detect the presence of key

checkpoint and cell cycle regulation factors by protein immunobloting (western blot), using extracts collected from cells at the same time points as the previous experiments. The targeted proteins included the major regulators and effectors of checkpoint arrest phosphorylated ATM, phosphorylated p53, p21, phosphorylated KAP1, and also cyclins A and E to certify positioning of cells along the cell cycle. We also detected γH2AX for comparison with previously used methods. The response patterns obtained were indeed reflective of checkpoint activation in all cell cycle stages after Etoposide treatment (**Fig.8**). Levels of γH2AX followed a pattern that seen with previous techniques, with detection of signal peaking at 30 minutes and gradually decreasing for ensuing time points. Phosphorylated ATM kinase displayed a rapid increase at 30 mins in response to Etoposide exposure, though this increase was not as prominent in early-S-damaged cells given the role of ATR as the predominant DDR master kinase in that phase (Awasthi et al., 2016). Phospho-ATM remained detectable up to 24h in cells damaged at all cell cycle stages, except for those damaged in early S phase. Two direct phosphorylation targets of ATM that lead to checkpoint activation, p53 and KAP1, also exhibited a clear increase in their active (phosphorylated) forms following DNA damage and ATM activation. In the case of KAP1, this increase was most noticeable at 30 mins post Etoposide in all synchronized populations, particularly in G1, and remained detectable up to 24h, though at decreased levels compared to the 30 mins time point. p53, on the other hand, presented a slow but sustained increment peaking at 24h in all synchronized populations, with G1-damaged cells showing the highest detected signal. This is consistent with the known higher dependence of G1 checkpoint on p53 activation compared to other checkpoints (Shaltiel et al., 2015). p21, a major repressor of cyclin/Cdk complexes whose expression is activated by p53, began to be noticed at 8h in G1 and early-S-damaged populations, becoming very prominent by 24h. In late-S- and G2-damaged cells, p21 was not noticeable up until 8h but revealed a strong presence by 24h. Taken together, the temporal patterns of these proteins serve as evidence of initiation of checkpoint activation in all targeted cell cycle stages. However, the late manifestation of phospho-p53 and p21 indicates that a robust arrest of progression through the cell cycle only occurs 8 to 24 hours after DNA damage.

Detection of cyclins A and E throughout the course of these experiments served as an additional control to monitor at which phase of the cell cycle cells were positioned at

each time point. The pattern of oscillation of these cyclins fully complied with cell cycle

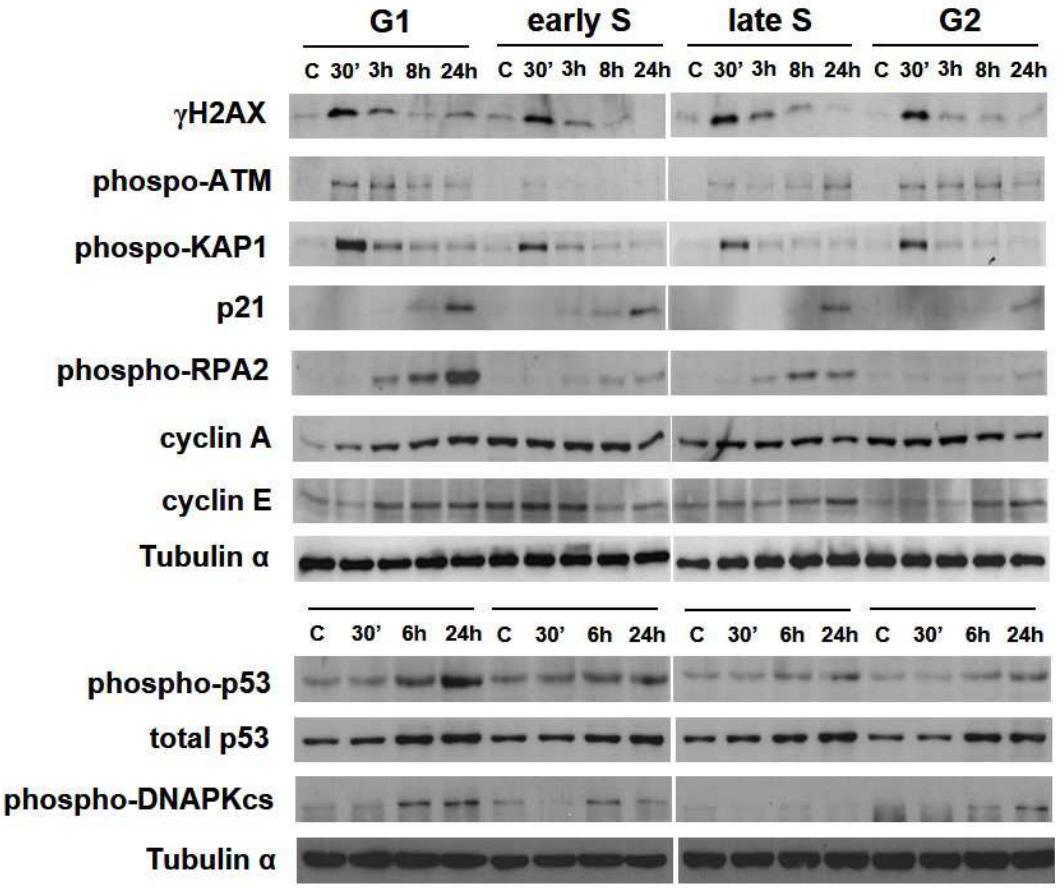

Figure 8. G1-damaged cells display high levels of phospho-RPA2, contrary to G2-damaged cells. Western blot assays performed with cellular extracts from HCT116 cells synchronized at different phases and damaged using Etoposide (50 μM, 15 mins). Presence of phospho-ATM and phospho-KAP1 is indicative of checkpoint activation, p21 and phospho-p53 are indicative of persistence of cell cycle arrest. Notice also that Topo2-induced lesions in late S trigger phosphorylation of RPA2, but not in early S. Shown are results representative of several experiments.

data obtained through flow cytometry analyses (**Fig.6**). For example, cells damaged in G1 had low starting levels of cyclin A but a gradual increase up to 24h indicative of advancement into G2, whereas cells synchronized in G2 showed a reversed pattern.

In sum, these results point to the occurrence of "checkpoint leakage", i.e. substantial transition of cells from one cycle phase to the next while full repair of DSBs has not yet taken place, in the hours following Topo2-mediated DNA damage, independently of the phase at which DNA lesions have been introduced.

3.2. Topo2-mediated DNA damage in separate cycle phases and repair system usage

If cells were indeed slipping through their checkpoints while still carrying considerable levels of DSBs, it is conceivable that these lesions would still be able to activate a response from the DNA repair pathways operating in subsequent cycle phases. To test this hypothesis, western blotting was also performed for major components of the HR and NHEJ pathways. Tested proteins included the end-resection protein RPA2 in its active (phosphorylated) form, and the activated catalytic subunit of the DNAPK complex, phospho-DNAPKcs (**Fig.8**). DSBs introduced in G1 elicited the strongest reaction from RPA2 compared to other groups, which started increasing at 3h and strongly intensified up until the 24h time point. Curiously, the later time points for G1-synchronized (8h and 24h) cells were previously shown to already contain a substantial fraction of cells in phases subsequent to G1 (**Fig.6**). At those later time points, phospho-DNAPKcs detection was also high in these cells. Cells damaged in G2, on the other hand, exhibited the lowest phospho-RPA2 signal detection of all groups with little variation across all time points. Phospho-DNAPKcs, by contrast, displayed a steady increase in these cells 6h after DNA damage that was even more prominent at 24h. The 24h time point coincides with the occurrence of a large fraction of cells that have exited G2 and entered G1, as shown by flow cytometry results (**Fig.6**). Finally, lesions introduced in either early or late S phase seemed to elicit a different use of repair systems. DSBs in late S clearly induced a higher phospho-RPA2 signal than those in early S, although its detection followed a similar pattern for both, starting to increase at 3h but only peaking at 8 and 24h. However, while phospho-DNAPKcs levels displayed an increase at 6 and 24h after DNA damage in the early-S-damaged group, this increase was barely noticeable in late S cells.

To complement western blot results, fluorescent immunostaining for RAD51, an HR partner of RPA2 that acts later in end-resection, and for phospho-DNAPKcs was also performed in cells subjected to identical synchronization procedures and Etoposide-Topo2 damage induction. Quantification of the fluorescent signal emitted by the nuclei of

these cells after DNA damage was performed using the same software as before for images obtained by confocal microscopy. Unfortunately, the anti-phospho-DNAPKcs antibody proved unreliable for immunofluorescence staining. There were, however, clear similarities between the patterns of phospho-RPA2 levels obtained by western blot (**Fig.8**) and by microscopic quantification of RAD51 signal per nuclear area (**Fig.9**). For instance, G1-damaged cells showed the highest RAD51 signal of all synchronized populations, particularly at 6h after Etoposide. A rapid increase in RAD51 signal intensity was already noticeable at 30 minutes in late-S-damaged cells, and this level was sustained in subsequent time points, which also coincides with the high level of HR observed in these cells in western blots. Cells damaged earlier in S phase also aligned very well with blot results, showing reduced signal emission at all time points compared to other stages, though presenting a small, gradual increase over time. Only cells damaged in G2 displayed a pattern different to that of western blots with an increase in signal at 6h, but less pronounced than in G1 cells. Overall, these results support to the observations obtained using protein blotting which suggest, on one hand, existence of variations in repair factor activity dependent on the initial cell cycle phase at which DSBs are introduced. And on the other hand, that these changes in repair factor activity coincide with times at which significant transitions of cells harbouring DSBs occur between different cycle phases, even though checkpoint activation was initiated.

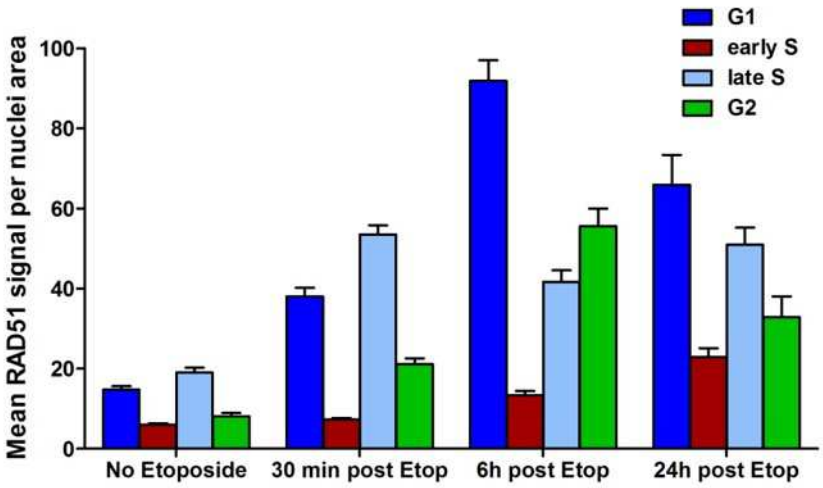

Figure 9. RAD51 fluorescence signal supports RPA2 results obtained by western blot. HCT116 cells synchronized at different cycle phases and damaged with Etoposide (50 µM, 15 mins). Cells immunostained against RAD51 were documented by confocal microscopy and amount of signal per nuclei area was measured by software analysis. Results are shown as mean + SEM of three independent experiements.

3.3. Effects of targeted repair system impairment on repair dynamics and checkpoint arrest

Based on the previous results, we thus decided to test if we could induce changes in repair system usage and if these changes could contribute to the reversal or maintenance of damage-induced checkpoint arrest. To this end, different cell lines were employed to investigate whether, by decreasing the efficacy of one of the two repair pathways, cells can shift their reliance towards the alternative pathway and whether this affects checkpoint behaviour. These included two HCT116 cell lines, one with a targeted loss-of-function mutation in one of the DNAPKcs alleles (designated as HCT DNAPK(+/-)) and another with loss of both alleles (HCT DNAPK(-/-)). Additionally, a breast carcinoma cell line with a germline inactivating mutation in the BRCA1 gene (HCC1937 BRCA1(-)) was also used, along with a congenic line in which expression of wild type BRCA1 was restored by means of retroviral insertion (HCC1937 BRCA1(+)) (Scully et al., 1999). Non-synchronized populations of these different cell lines were exposed to a short term Etoposide pulse (50 μM, 15 mins) and collected at subsequent time points. We next stained cells for DNA content flow cytometry analysis and performed protein immnunobloting against key participants in HR and NHEJ repair systems.

Analysis of HCC1937 BRCA1(+) and BRCA1(-) cell cycle profiles after drug exposure revealed that both populations tended to accumulate in G2 phase at the 12h time point after damage induction (≈55% of both populations in G2). However, a substantial fraction of BRCA1(-) cells was able to progress into G1 by 24h (≈ 48% in G1, 42% in G2) as opposed to BRCA1(+) cells that retained a robust G2 arrest (≈ 16% in G1, 70% in G2) (**Fig.10A**). Western blot assays showed that HCC BRCA(-) cells appear to suffer from impairment in DSB repair since these cells had higher γH2AX levels at 6 and 24 h after being exposed to Etoposide when compared to BRCA1(+) cells. Additionally, loss of BRCA1 clearly promoted a switch towards DNAPK activation for DNA repair, while drastically reducing the levels of active RPA2 across the entire time course, in agreement with impaired repair of DSBs by

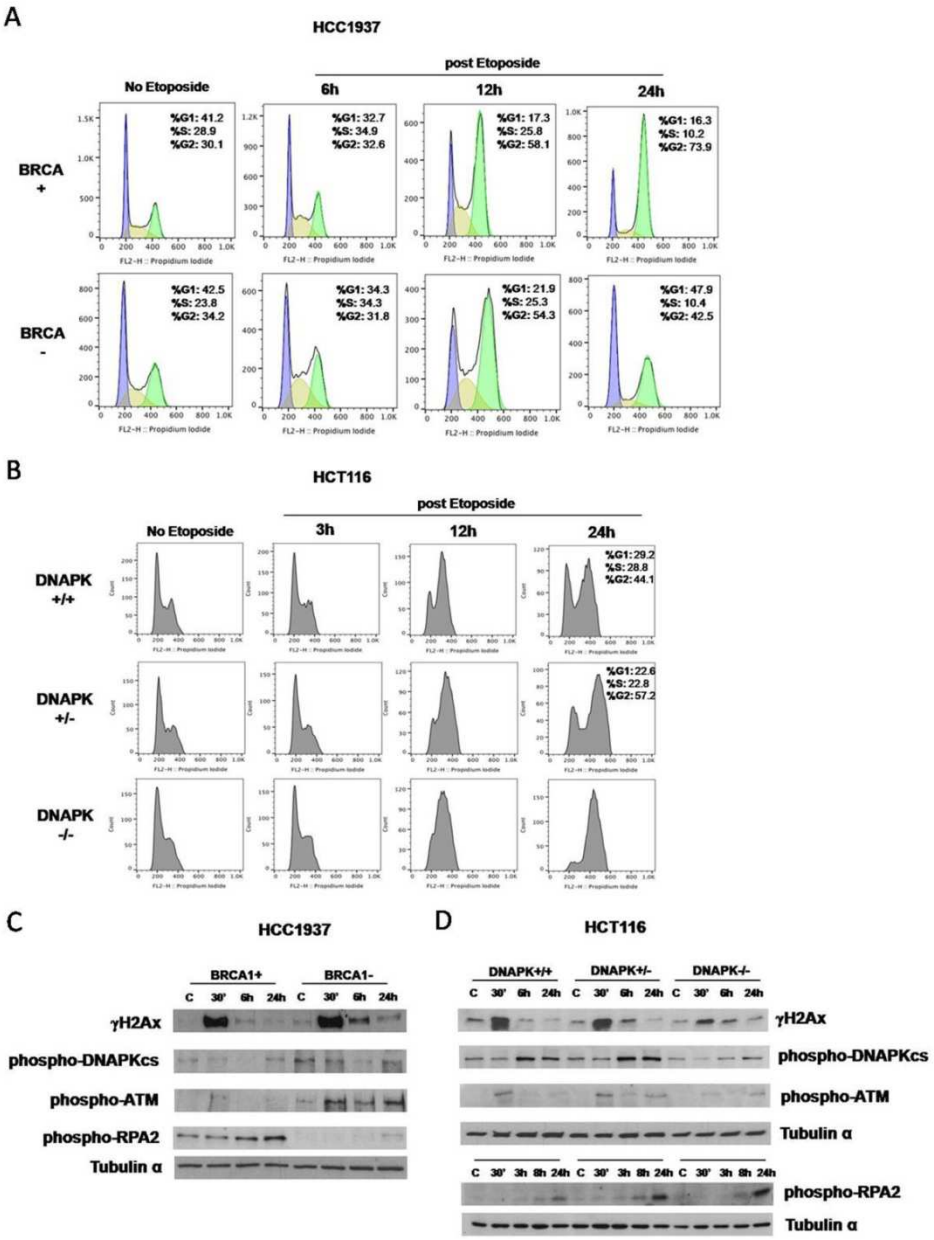

Figure 10. Deficiency in BRCA1 causes an increase in phospho-DNAPKcs levels along with G2/M checkpoint slippage, whereas deficiency in DNAPKcs leads to increased levels of phospho-RPA2 and a more robust G2/M arrest. Asynchronous HCC1937 and HCT116 populations with different BRCA1 and DNAPKcs genetic backgrounds after Etoposide pulse (50 μM, 15 mins). **(A)** Cell cycle profiles of HCC1937 BRCA1(+) and (-) cells. Cells were stained with Propidium Iodide and analysed by flow cytometry. **(B)** Cell cycle profiles of HCT116 DNAPKcs (+/+), (+/-) and (-/-) cells. Cells were stained with Propidium Iodide and analysed by flow cytometry. Cell cycle percentages were estimated using Dean/Jett/Fox algorythm. **(C)** Western blot for detection of repair factor activation in HCC1937 BRCA1(+) and (-) cells. **(D)** Western blot for repair factors in HCT116 DNAPKcs (+/+), (+/-) and (-/-) cells. Shown are results representative of three independent experiments.

HR. Phospho-ATM levels were also markedly increased in BRCA1(-) cells at all time points after DNA damage when compared to BRCA1(+) cells (**Fig.10C**).

By comparison, cell cycle profiles in wild type HCT116 DNAPK(+/+) and DNAPK knockout lines revealed that, while almost the entire population of DNAPK(-/-) cells was arrested in G2 phase 24 hours after Etoposide insult, a large fraction of DNAPK(+/+) and, to a lesser extent, DNAPK(+/-) cells had escaped into G1 (**Fig.10B**). Additionally, depletion of DNAPK also seemed to affect the progression of cells through S phase, as can be noticed at the 12h time point. This is likely due to an intensification of the intra-S checkpoint. Regarding the behaviour of repair factors in DNAPK-deficient lines, DNAPK(-/-) cells displayed, as was expected, a marked decline in detectable phospho-DNAPKcs compared to the other cell lines. This was consistent with higher γH2AX signalling in these cells at 24h, suggesting impaired repair of DSBs (**Fig.10D**). RPA2 activation, however, showed a pronounced increase at the 24h time point compared to DNAPK(+/+) cells. DNAPK(+/-) exhibited intermediate levels of γH2AX and phospho-RPA2 compared to DNAPK(+/+) and DNAPK(-/-), but maintained levels of activated DNAPK similar to the DNAPK(+/+) group. These observations therefore support the hypothesis that cells are able to compensate loss of function in one system with increased activation of the remaining functional one, if available. Also, this change in system usage influences checkpoint arrest duration.

We wanted to further explore how loss of function in one repair system affects checkpoint arrest and DNA repair, but this time at the level of different cell cycle phases. As such, the cell lines HCT116 DNAPK(+/+) and DNAPK(+/-) were synchronized at G1, early S, late S and G2 phases and exposed to a short term Etoposide pulse to induce DSBs; synchronization of DNAPK(-/-) cells was not possible due to high levels of cell death. Cell cycle analysis by flow cytometry was performed for all groups as previously. We observed a clear divergence between DNAPK(+/+) and (+/-) cell cycle profiles at the later time point (22h after Etoposide pulse) (**Fig.11A**). DNAPK(+/-) cells damaged in G2, late S and early S phases displayed a higher tendency to accumulate in G2 at 22h, at the expense of a noticeable decrease in G1 transition when compared with DNAPK(+/+) populations. Interestingly, there were no observable differences in cell cycle progression between G1-damaged DNAPK(+/+) and (+/-) groups, suggesting that loss of DNAPK function affects the G2/M transition but not necessarily G1/S.

We also performed immunoblotting to detect differences in repair factor dynamics between G1- and G2-damaged populations with impairment in NHEJ (**Fig.11B**). DNAPK(+/-) cells damaged in G1 showed an overall similar but stronger pattern of RPA2 activation to DNAPK(+/+). A stronger RPA2 phosphorylation was also observed for DNAPK (+/-) cells relative to their DNAPK(+/+) counterparts when Etoposide-Topo2 mediated DNA damage was introduced in G2. Also, in DNAPK-deficient cells, the levels of γH2AX remained higher until 12h after exposure to Etoposide. This once more supports our hypothesis that loss of NHEJ factor DNAPK elicits a stronger end resection response,

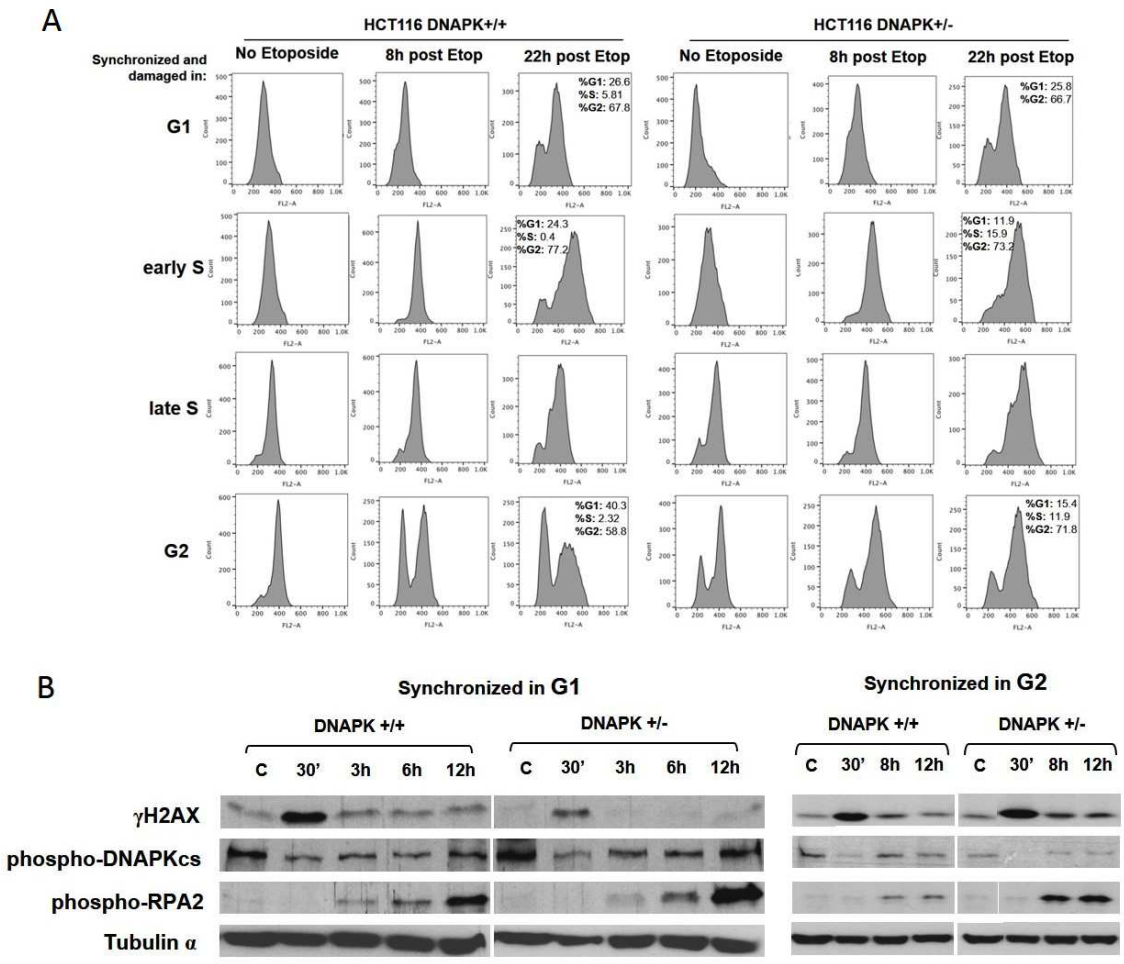

Figure 11. DNAPKcs deficiency induces an increase of end-ressection by phospho-RPA2 and a robust G2/M arrest at 22h after Etoposide. HCT116 DNAPK(+/+) and (+/-) cells synchronized at separate cell cycle phases and exposed to Etoposide pulse (50μM, 15 mins). **(A)** Cell cycle profiles obtained by flow cytometry. Cellular DNA was stained with Propidium Iodide. Cell cycle phase frequencies were estimated using Dean/Jett/Fox algorythm. **(B)** Western blot for detection of repair factor usage. Shown are representative results from several independent experiments.

particularly noticeable in G2-damaged cells. Once again, the switch in repair system leading to activation of HR is accompanied by a prolonged G2 arrest.

3.4. DNA repair under forced cell cycle arrest at the G2/M transition

In order to understand if the switch from NHEJ to HR that occurs in G2, when DNAPK function is decreased, affects the level of lesion repair, we used a competitive inhibitor of Cdk1, RO-3306, at a final concentration of 10 μM in HCT116 cells synchronized in G2 and subjected to a short Etoposide pulse. Cdk1 is necessary for initiation of mitosis as it acts as an essential mediator of chromosome segregation (Enserink & Kolodner, 2010). Its inhibition thus prevents cells from advancing past the G2/M transition point, effectively inducing a forced cell cycle arrest. Staining of DNA content and flow cytometry analysis confirmed that cells treated with Cdk1 inhibitor were unable to exit from G2/M even after 18 hours, in clear contrast to non-Cdk1i treated cells, which were already mostly in G1 after 10h (**Fig.12A**). Immunoblotting for γH2AX, along with quantification of immunofluorescent foci by confocal microscopy imaging and software analysis, revealed that Cdk1 inhibition resulted in cells accumulating higher γH2AX levels than non-treated controls (**Fig.12B** and **12C**). Interestingly, Cdk1-inhibited cells also displayed an evident intensification of phospho-RPA2 levels after DNA damage, whereas phospho-DNAPKcs and phospho-53BP1 levels appeared to be reduced compared to the control group (**Fig.12B**). A prolonged G2/M arrest seems therefore to allow for an intensification of end-resection-based repair, though it curiously appears to not promote conclusion of DSB repair.

3.5. Loss of function in DSB repair factors and resulting cellular outcomes after Topo2-mediated DNA damage

Since predominance of one DSB repair system over the other seems to influence the maintenance or reversal of checkpoint arrest, particularly in the case of the G2/M checkpoint, we decided to investigate the long term consequences of loss of function in either NHEJ or HR repair pathways in terms of cell survival and cellular fate. As previously shown, DNAPK knockout (-/-) and BRCA1(-) cell lines have very different G2/M checkpoint behaviours after Topo2-mediated DNA damage. DNAPK(-/-) exhibited a robust checkpoint arrest, with almost the entire population in G2 24 hours after exposure to Etoposide,

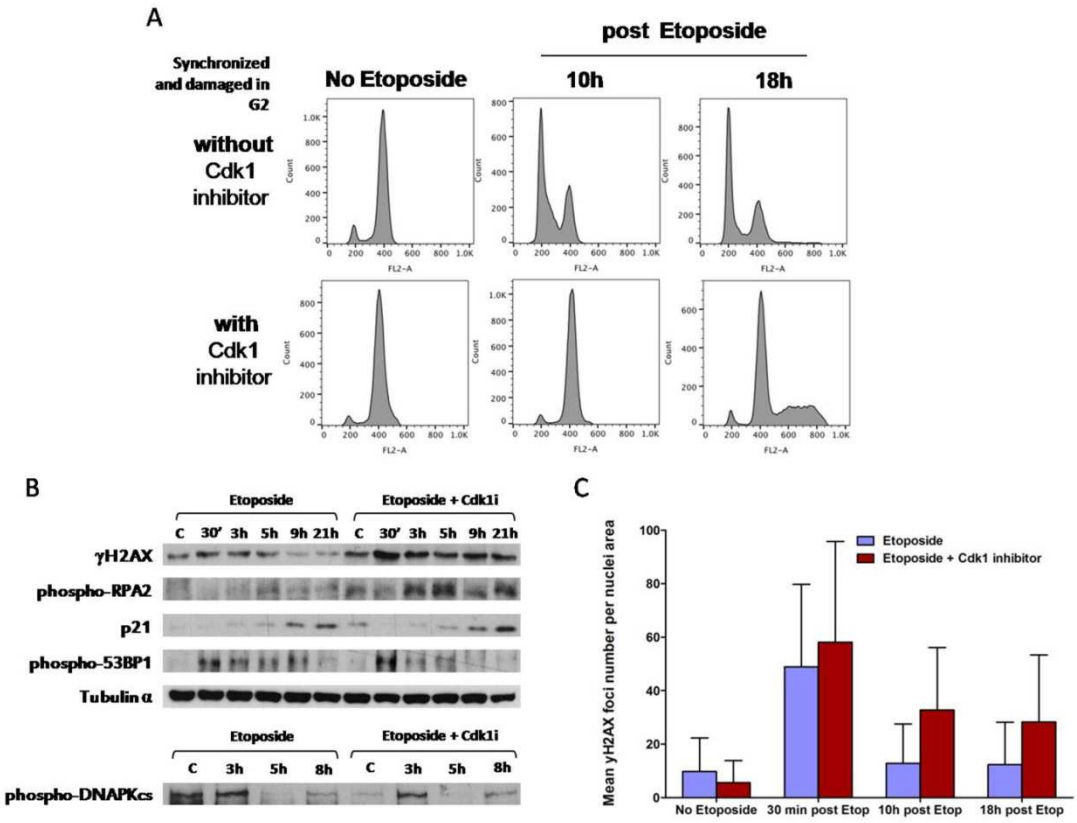

Figure 12. Forced arrest at G2/M transition by use of Cdk1 inhibitor RO-3306 leads to increased RPA2 phosphorylation but decrease of lesion repair efficiency. HCT116 cells were synchronized in G2, pulsed with Etoposide (50 µM, 15 mins) and incubated in the presence of RO-3306 (10 µM) until collection. **(A)** Cell cycle profiles with and without Ro-3306. Propidium Iodide was used to stain celular DNA. Notice that after prolonged arrest with RO-3306 a supra-4n population begins to appear as a result of mitotic aberrations. **(B)** Western blot for the detection of repair factor usage. **(C)** Mean γH2AX foci number per nuclei area. Cells were immunostained against γH2AX and documented by confocal microscopy. Foci number and nuclear areas were measured by software analysis. Notice the number of γH2AXfoci remaining at 18h in Cdk1-inhibitided cells compared to no Cdk1 inhibitor. Results are shown as mean + SD.

while half of the population of BRCA1(-) cells was already in G1 at the same time point after passing through mitosis. Since NHEJ repair is known to be error prone and undergoing mitosis in the presence of unrepaired DSBs further adds to the risk of genomic instability, these divergent responses to DSBs could also have divergent long term effects on cellular fate. So in order to determine if these cell lines would differ in terms of cellular outcomes, we seeded HCT116 DNAPK(+/+), (+/-) and (-/-), and HCC1937 BRCA1(+) and (-) at clonogenic dilutions (≈2000 cells/plate) and subjected them to short pulses of varying concentrations of Etoposide. Clonogenic survival assays were preferred because they allow us to monitor cell fate at an almost individual level. Also, under mass-growth conditions non-proliferating cells are quickly overcome by proliferating ones, causing underestimation of cell fates such as senescence. After 8 days in culture, cell plates were fixed and stained and percentages of proliferating and senescent colonies were quantified after examining colony size and morphology (see Methods).

Results show, interestingly, that loss of function in either BRCA1 or DNAPK indeed yielded contrasting cell fates. HCC1937 BRCA1(-) populations displayed a very high percentage of colonies with the senescent phenotype, becoming very large, flat and filled with lysosomes. However, this effect was not dependent on Etoposide since, even with no drug exposure, ≈54% of these colonies already showed signs of spontaneous senescence compared to ≈26% in BRCA1 (+) cells (**Fig.13A**). Although Etoposide did increase senescent outcome in concentrations up to 5 μM, this increase was similar in both BRCA1(-) (≈65%, increased 11%) and (+) groups (≈45%, increased 19%). Also, higher drug doses did not increase senescence numbers further. Such a high initial propensity for the senescent outcome was unexpected since the HCC1937 cell line carries an inactivating mutation in the p53 gene, a key promoter of senescence. The high percentage of non-proliferating colonies (including senescent-like colonies and colonies with very few cells, an indication of cell death or proliferation arrest) exhibited by these cell lines after Etoposide insult (≈78% in BRCA1(-) and ≈65% in BRCA1(+), 30 μM Etop) is thus mostly a result of cellular senescence. Since BRCA(-) cells have a high percentage of checkpoint leakage into G1 while carrying unrepaired DSBs, they incur the risk of chromosome segregation defects, which might be associated with the high propensity for senescence seen in these cells.

In HCT cells, the senescent phenotype was not as prevalent as in HCC cells, though there was a small dose-dependent increase in senescent colonies after Etoposide pulse that was consistent for all DNAPK backgrounds (**Fig.13B**). DNAPK (-/-) cells displayed ≈28% of senescent colonies after a 50 μM dose of Etoposide, followed by DNAPK (+/-) (≈16%) and (+/+) cells (≈11%), from initial basal levels of ≈14%, ≈5% and ≈2%, respectively. The viability of DNAPK knockout lines was nonetheless still seriously compromised by exposure to Etoposide in a clear dose-dependent manner. DNAPK (-/-) cells suffered an

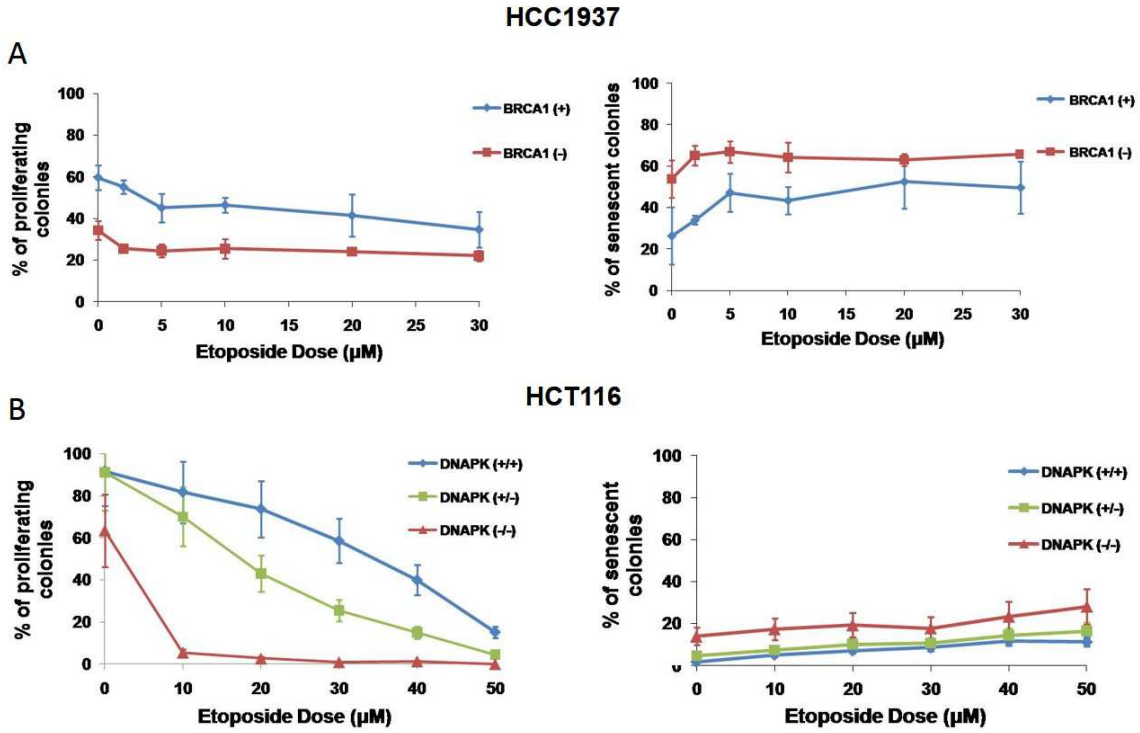

Figure 13. HCC1937 cells deficient in BRCA1 have increased spontaneous senescence, whereas HCT116 cells deficient in DNAPKcs display na Etoposide-dose-dependent loss of viability by causes other than senescence. Clonogenic assays for assessing long term (after 8 days) effects of loss of repair factor combined with Etoposide pulses (15 mins) of increasing concentrations. **(A**) Percentage of proliferating colonies and senescent colonies in HCC1937 BRCA1(+) and (-) cells**. (B)** Percentage of proliferating colonies and senescent colonies in HCT116 DNAPKcs(+/+), (+/-) and (-/-). Results are shown as mean + SD of three independent experiments per cell line.

almost complete loss of proliferating capability with a 10 μM Etoposide dose (only ≈6% of proliferating colonies compared to ≈63% initially) and, at high concentrations of 50 μM, DNAPK (+/-) cells also evidenced a similar response (down to ≈15% compared to 91% initially). Curiously, this loss of viability did not present the morphological hallmarks of

senescence. Cells maintained normal size and appearance, but did not divide, appearing to be in an arrested, quiescent state.

These observations support our proposition that limiting the availability of either NHEJ or HR repair factors can result in different cellular outcomes, with loss of function in BRCA1 eliciting a predominance of cellular senescence that is not dependent on Topo2-mediated DNA damage, while decreased DNAPK activity seems to favor quiescence or cell death, but in a Etoposide-dose dependent manner.

3.6. Disruption of heterochromatin structure and resulting cellular outcomes after Topo2-mediated DNA damage

We next decided to address our second main objective, to determine if different chromatin states, relaxed (EC) or condensed (HC), can influence the response to Topo2-mediated DNA lesions and long term cell fate. To that end, we first performed the knockdown of the catalytic subunit of the polycomb repressor complex (PRC2), EZH2, in HCT116 cells. PRC2 is a major effector of gene silencing responsible for catalyzing the trimethylation of histone 3 on lysine 27 (H3K27me3), a repressive mark associated with heterochromatin formation (Kadoch, Copeland, & Keilhack, 2016). EZH2 knockdown was performed by lentiviral transfection of a plasmid vector encoding a shRNA (small hairpin RNA) that specifically interferes with EZH2 mRNA (shEZH2) (see Methods). A separate group of cells was transfected with plasmids expressing a scrambled shRNA with no cellular target to serve as control for any effects caused by the transfection process itself. Knockdown effectiveness was then tested by protein immunoblotting directed against EZH2 and against the product of EZH2 activity, the H3K27me3 mark on chromatin. Results confirmed that the knockdown had the desired effect, as EZH2 was not detectable in cells transfected with shEZH2 compared to scrambled controls, and the presence of the H3K27me3 mark was greatly reduced in the shEZH2 group as well (**Fig.14A**).

Following knockdown confirmation, we performed clonogenic survival assays for HCT116 cells transfected with shEZH2 and Scrambled shRNA to investigate whether this

change in an epigenetic heterochromatin mark could affect cellular outcomes after Topo2-mediated DNA damage. Results revealed a clear dose-dependent response to Etoposide in terms of loss of proliferating capability in these cells (**Fig.14B**). shEZH2-transfected cells displayed a basal percentage of non-proliferating colonies of ≈50% in the absence of the Topo2 poison, which gradually increased to ≈76% when Etoposide concentrations reached 40 µM, while Scrambled cells had a basal frequency of non-proliferating colonies of ≈25%, but it also rose to ≈75% at 40 µM of Etoposide. In terms of how much of this loss of viability is attributable to the senescence fate, EZH2-knockdown

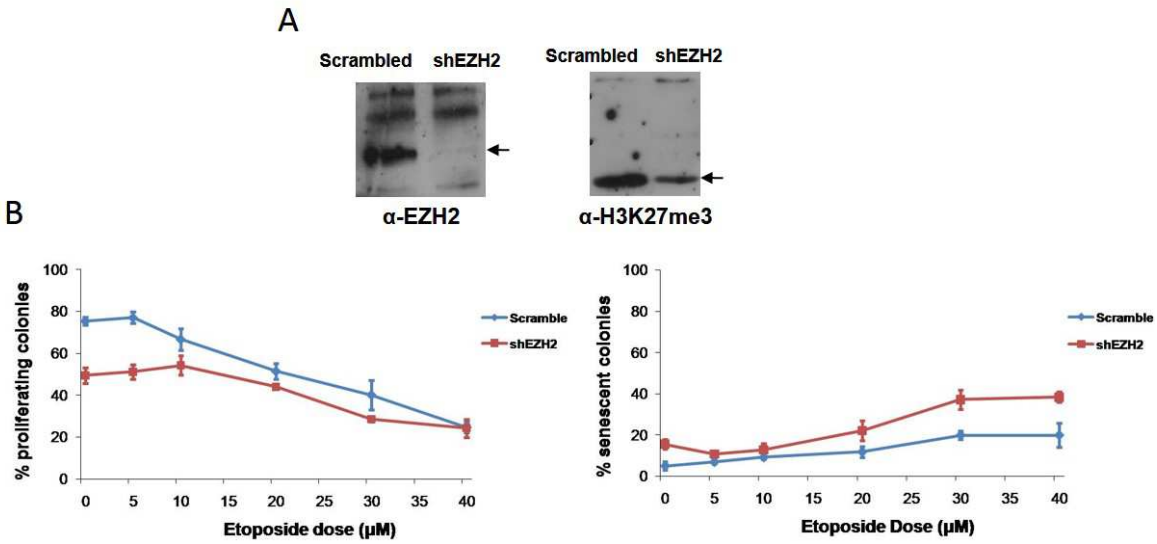

Figure 14. Cells with EZH2 knockdown showed a dose-dependent response to Etoposide similar to controls. HCT116 cells were knockdown for EZH2 by lentiviral infection with shRNA targeting EZH2 mRNA. (A) Western blot assays testing EZH2 knockdown efficiency and its effect on the heterochromatin mark catalyzed by EZH2 H3K27me3. (B) Clonogenic assays to assess long-term effects of shEZH2 knockdown, combined with Etoposide pulses (15 mins) of increasing of concentrations, on percentage of proliferating colonies and senescent colonies after 8 days of incubation. Results are shown as mean + SD of three independent experiments.

cells showed a basal senescence rate of ≈15% compared to ≈5% in Scrambled cells, gradually rising to ≈38% and ≈20% with Etoposide doses up to 40 µM, respectively. These results indicate that knockdown of EZH2 by itself is enough to substantially promote cellular senescence at the basal level (a three-fold increase compared to controls). While the number of senescent colonies increased with Etoposide dose, even at high drug concentrations the increase in senescence fate with loss of EZH2 was only two-fold that of controls. There appears to be only an added effect of the two factors, Etoposide and

depletion of EZH2, instead of an increase in cell sensitivity to Etoposide by means of EZH2 knockdown.

We therefore hypothesized that a reduction in a specific heterochromatin mark might not be sufficient to compromise heterochromatin structure in a manner that noticeably sensitizes cells to the action of a poisoned Topo2 enzyme, or affects cellular fates. In order to induce depletion in the levels of other repressive histone marks, such as H4K20me3 and H3K9me2, a potent global histone methylation inhibitor, 3-deazaneplanocin A (DZNep), capable of inhibiting EZH2 as well as most histone methyltransferases (Miranda et al., 2009), was used in combination with Etoposide. Western blotting against EZH2 in HCT116 cells exposed to 5 or 10 μM DZNep for one or two days confirmed that this drug is indeed effective at depleting EZH2, drastically reducing the levels of this protein after a 2 days incubation period with DZNep (**Fig.15A**). We next decided to test what combination scheme would be more effective at inducing sensitivity to Topo2-mediated lesions in terms of the sequence in which the two drugs were used. We tested incubation of HCT116 cells with 10 μM DZNep alone for 24h; DZNep incubation prior to Etoposide pulse (15 mins, 50 μM) followed by a 24h period of incubation free of both drugs; Etoposide pulse prior to 24h incubation with DZNep; both periods of incubation with DZNep between Etop pulse; and Etoposide alone followed by 24h without any drug. Immunofluorescent detection of γH2AX was performed and average of number foci per cell was quantified by software analysis (**Fig.15C**). Post-incubation with DZNep following Etoposide pulse did not display any potentiating effect of the methyltransferase inhibitor over Topo2-mediated lesions (7 ± 1 foci per cell) compared to the combined sum of DZNep (2.6 ± 0.3 foci per cell) or Etoposide (5.1 ± 0.7 foci per cell) alone. However, interestingly, pre-incubation with DZNep followed by Etoposide pulse presented an unexpected increase in the average number of damage foci observed in cells (12.1 ± 1.2 foci per cell). DZNep pre-incubation combined with post-incubation did not substantially increased foci number (13.6 ± 1.4) compared to pre-incubation alone, indeed pointing to the 24h pre-incubation period as being the crucial step in sensitizing cells to Etoposide. This possibly occurs by exposing heterochromatic regions to Topo2-mediated DNA damage.

We subsequently performed flow cytometry analysis to measure DNA content in cells subjected to the previous combination schemes to verify if there existed any

significant alterations to cell cycle progression between them. Results revealed that when incubation for 24h with DZNep was performed prior to Etoposide pulse, there was an increase in the frequency of cells in G2/M phases (50%) compared to either drug alone (DZNep: 32%; Etoposide: 37%) or no drug (27%) (**Fig.15B**). The increased level of Topo2-mediated DSBs remaining 24h after the "DZNep then Etop" drug combination scheme is thus likely inducing a prolonged G2/M checkpoint arrest, contrasting with a faster return to normal cycle progression by 24h when either drug is used alone. These results show that the potentiating effect of DZNep on the DNA-damaging capability of Etoposide-bound Topo2 is only seen when DZNep is allowed to act before Topo2 cleaves the DNA, indicating the existence of a potential synergistic interaction between global histone demethylation and the introduction of Topo2-mediated DSBs.

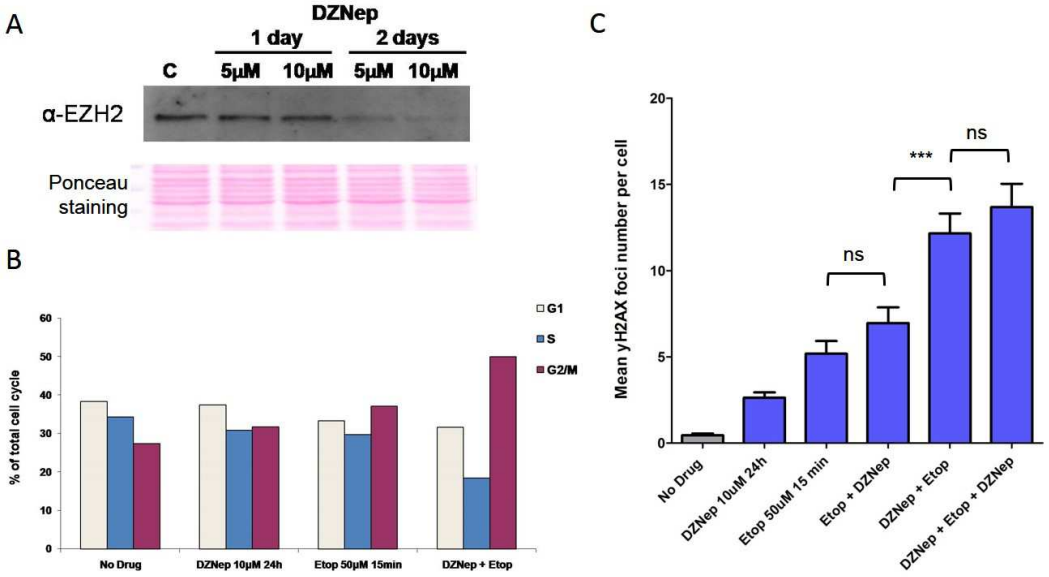

Figure 15. DZNep pre-treatment sensitizes cells to Etoposide-induced DSBs. DZNep (10 μM) effects were tested in HCT116 cells in combination with Etoposide (50 μM, 15 mins). **(A)** Western blot against EZH2 to confirm the inhibitory effects of DZNep on histone methyltransferases. Ponceau staining served as loading control. **(B)** Effects of DZNep (10 μM for 24h) and Etoposide (50 μM, 15 mins) alone and in combination (DZNep prior to Etop) on cell cycle frequencies after 24h. Cellular DNA was stained with PI and analysed by flow cytometry. **(C)** Mean γH2AX foci numbers per cell. Different sequences of DZNep (10 μM, 24h) and Etoposide (50 μM, 15 mins) were tested: DZNep alone; Etop alone followed by a 24h incubation period; Etop followed by DZNep; DZNep followed by Etop and a 24h incubation period; DZNep prior to Etop, followed by DZNep again. Cells were immunostained for γH2AX and documented by confocal microscopy. Foci numbers were measured by software analysis. Results are shown as mean + SD of three independent experiments. ***: $p<0.001$; ns: non-significant.

3.7. Detection of synergism between Etoposide and DZNep

Drug synergism requires that the combined potency of two or more drugs be more than the sum of the individual potencies of each drug used alone. This is a deviation from additivity, when each drug constituent contributes to the end effect with only its own potency. These deviations, which may also occur in the direction of a loss of combined potency known as antagonism, can be useful for illuminating the mechanisms behind the action of each drug and their interaction (Tallarida, 2001).

With possible clinical applications in mind, we decided to investigate if the detected synergistic effect of DZNep pre-treatment could also be found at low concentrations, which we anticipated would be more similar to a chemotherapy setting. To this end, we used an acute monocytic leukemia cell line, THP1, incubated for two days with different concentrations of DZNep in 6-well plates, after which cells were divided into 96-well plates and incubated with the respective DZNep-Etoposide combinations for three days. The different combinations resulted from the following concentrations of DZNep (0.1, 0.5, 1, 2.5, 5 and 10 μM) and Etoposide (0.05, 0.1, 0.2 and 0.4 μM), with each dose in one group combining with all doses from the other group. We then used the alamarBlue survivability assay to measure cell viability after exposure to drug combinations. Results were read using a luminescence microplate reader (see Methods) (**Fig.16A**). Using the results obtained for cell viability we then calculated the interaction index for each drug combination based on the Loewe additivity model (Lee, Kong, Ayers, & Lotan, 2007). An interaction index =1 means additivity, <1 synergy and >1 antagonism. Analysis of this data showed that we were indeed able to detect synergism with simultaneous low doses of DZNep and Etoposide. Two combinations, 0,5 μM DZNep with 0,05 μM Etoposide, and 1 μM DZNep with 0,05 μM Etoposide, showed a particularly low interaction index (≈0,2), suggesting a very strong synergistic potential for inducing death in leukemia cells at low, clinically relevant, drug concentrations (**Fig.16B**).

3.8. Detection of synergism between Etoposide and SAHA

Finally, as a proof of concept that our previous approach for the DZNep- Etoposide combination study was technically valid, we decided to also characterize the interaction between Etoposide and the HDAC inhibitor Vorinostat, also known as suberoylanilide hydroxamic acid (SAHA). SAHA was the first HDAC inhibitor approved for clinical use in

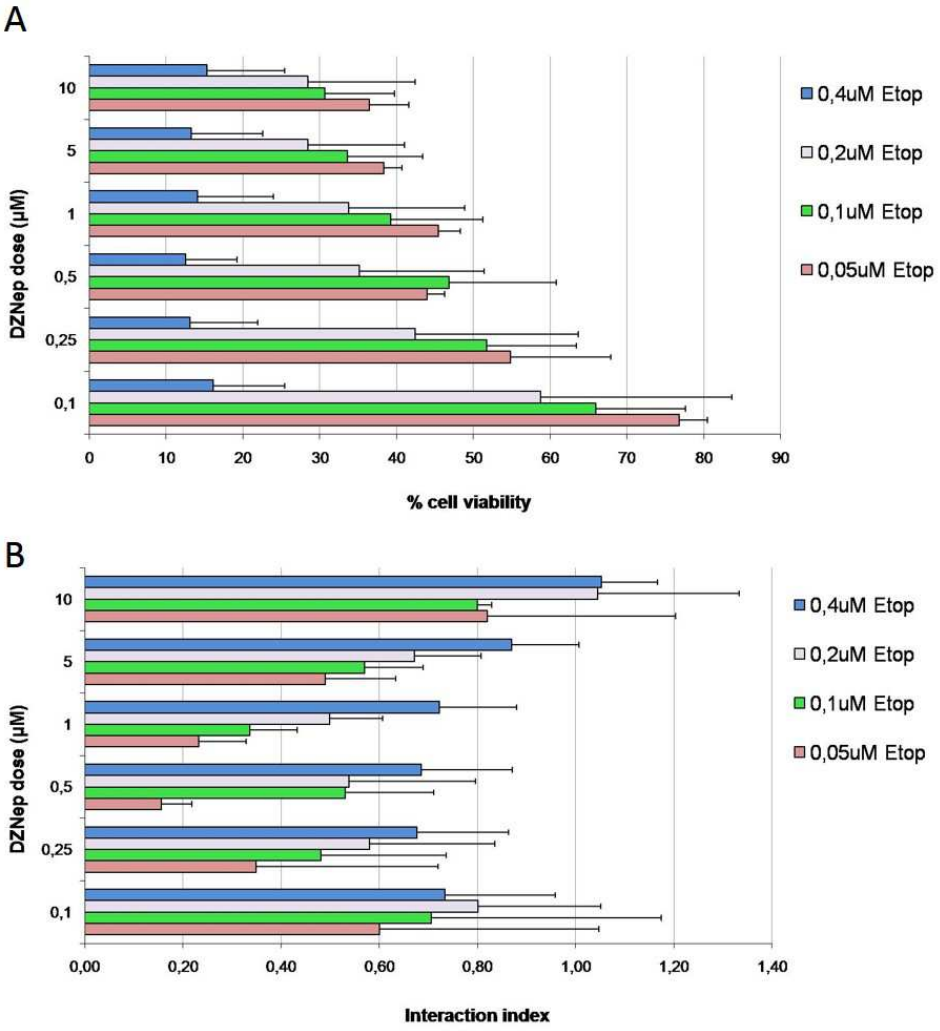

Figure 16. Pre-treatment with low concentations of DZNep synergizes with low concentrations of Etoposide to induce increased cell death in a leukemia cell line.THP1 cells were incubated for two days with different concentrations of DZNep, followed by a pulse of different Etoposide concentrations and incubation for three days. (A) Percentages of cell viability were obtained using alamarBlue assay to measure metabolic activity of cells. (B) Interaction índex values were calculated using the Loewe additivity model (see Methods). Interaction index =1 means additivity; >1 means antagonism and <1 means synergism. Results are shown as mean + SD of several independent experiments.

cancer therapy and has been shown to induce growth arrest, differentiation and cell death in tumor cells. It can also have synergistic effects when used in combination with

other anti-tumor strategies, including Topo2 poisons such as Etoposide (Marchion et al., 2004). We determined dose-response curves for THP1 cells incubated for three days with increasing concentrations of Etoposide and SAHA individually by alamarBlue assay (**Fig.17A**). A program package for R software, SynStat (University of Maryland, USA), was then utilized to, based on the on the individual dose-response curves, generate a matrix of drug combinations to be tested (see Methods). THP1 cells were incubated in 96-well plates for three days with simultaneous addition of Etoposide-SAHA dose combinations and cell viability was quantified by alamarBlue assay, as previously. The resulting matrix of toxicity effects of drug combinations was inputted into the SynStat software, which then generated a contour plot of interaction index values for a range of Etoposide-SAHA concentrations (**Fig.17B**). We then used this plot to select combinations representative of synergy (0,1 µM SAHA + 0,6 µM Etop; 1 µM SAHA + 1 µM Etop) , additivity (0,5 µM SAHA + 1 µM Etop) and antagonism (1 µM SAHA + 0,2 µM Etop; 1,5 µM SAHA + 0,2 µM Etop), that had not been used before when building the plot, in order to test the validity of the projection. THP1 cells were incubated for three days with the selected drug combinations, after which cell viability was measured and used to calculate interaction index values. Comparing the experimentally obtained index values with the predicted values given by the contour plot for those combinations, we observe that most predicted interactions were confirmed correct, except for 1 µM SAHA + 1 µM Etop where only additivity was detected instead of synergy (**Fig.17C**). This suggests a consistent model fit, although it would be desirable to test more combinations. In sum, our technical approach appears to be a valid methodology to study drug combination interactions, which could prove useful in developing new combination strategies to increase tumor cell death with lower drug concentrations.

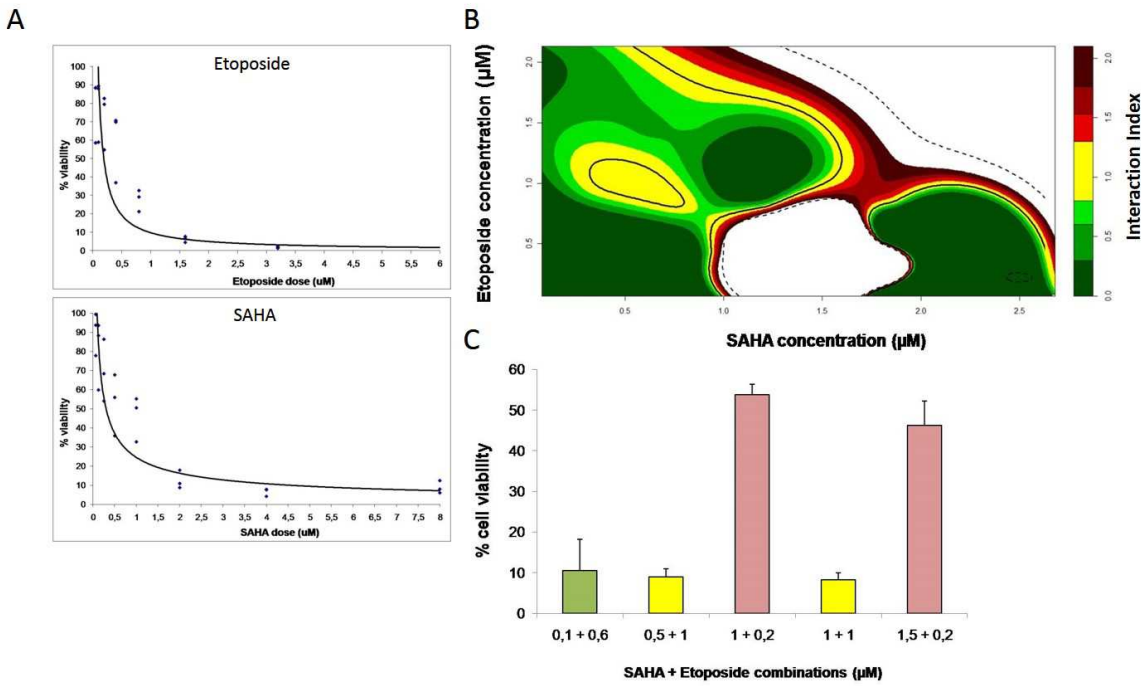

Figure 17. Predicted synergism between SAHA and Etoposide was confirmed. THP1 cells were incubated with different combinations of the HDAC inhibitor SAHA and Etoposide simultaneously for three days. **(A)** Dose-response curves for SAHA and Etoposide alone. Cell viability was measured by alamarBlue assay. **(B)** Contour plot of SAHA and Etoposide combinations (isobologram). The boundaries of regions with different colors indicate the levels of the interaction index (τ) at the exact value of 0, 0.3, 0.6, 0.8, 1.3, 1.53, 1.76 and 2.1, respectively. The solid curve indicates the additive combinations (τ=1) and the dotted black lines indicate the 95% confidence interval contour for additivity. Green: Synergism (Interaction index <1); Yellow: Additivity (Interaction index =1); Red: Antagonism (Interaction index >1). **(C)** Confirmation of predicted effects on THP1 cell viability of SAHA and Etoposide combinations. Colors represent the interaction index obtained after experimental testing. All combinations yielded the predicted interaction index values except 1 µM SAHa + 1µM Etop that was predicted to be synergistic but only displayed additivity. Results are shown as mean + SD of several independent experiments.

Author Contribution

All experiments were planned by Pedro Pereira and João Ferreira. All experiments were performed by Pedro Pereira with occasional support from João Ferreira, particularly for cell synchronization. Valuable input for microscopy data analysis was provided by José Rino. Joana Cardoso provided assistance with the use of R software and selection of shEZH2 clones.

References

Agostinho, M., Ferreira, F., & Steffensen, S. (2004). Human Topoisomerase II ␣ : Targeting to Subchromosomal Sites of Activity during Interphase and Mitosis. *Molecular Biology of the Cell*, *15*(May), 2388–2400. doi:10.1091/mbc.E03

Agostinho, M., Santos, V., Ferreira, F., Costa, R., Cardoso, J., Pinheiro, I., … Ferreira, J. (2008). Conjugation of human topoisomerase 2 alpha with small ubiquitin-like modifiers 2/3 in response to topoisomerase inhibitors: cell cycle stage and chromosome domain specificity. *Cancer Research*, *68*(7), 2409–18. doi:10.1158/0008-5472.CAN-07-2092

Awasthi, P., Foiani, M., & Kumar, A. (2016). ATM and ATR signaling at a glance. *Journal of Cell Science*, *129*(6), 1285–1285. doi:10.1242/jcs.188631

Bach, S. V., & Hegde, A. N. (2016). The proteasome and epigenetics: Zooming in on histone modifications. *Biomolecular Concepts*, *7*(4), 215–227. doi:10.1515/bmc-2016-0016

Baldeyron, C., Soria, G., Roche, D., Cook, A. J. L., & Almouzni, G. (2011). HP1α recruitment to DNA damage by p150CAF-1 promotes homologous recombination repair. *Journal of Cell Biology*, *193*(1), 81–95. doi:10.1083/jcb.201101030

Barski, A., Cuddapah, S., Cui, K., Roh, T.-Y., Schones, D. E., Wang, Z., … Zhao, K. (2007). High-resolution profiling of histone methylations in the human genome. *Cell*, *129*(4), 823–37. doi:10.1016/j.cell.2007.05.009

Beck, H., Nähse, V., Larsen, M. S. Y., Groth, P., Clancy, T., Lees, M., … Sørensen, C. S. (2010). Regulators of cyclin-dependent kinases are crucial for maintaining genome integrity in S phase. *Journal of Cell Biology*, *188*(5), 629–638. doi:10.1083/jcb.200905059

Cann, K. L., & Dellaire, G. (2011). Heterochromatin and the DNA damage response: the need to relax. *Biochemistry and Cell Biology = Biochimie et Biologie Cellulaire*, *89*(1), 45–60. doi:10.1139/O10-113

Cao, L., Xu, X., Bunting, S. F., Liu, J., Wang, R. H., Cao, L. L., … Finkel, T. (2009). A Selective Requirement for 53BP1 in the Biological Response to Genomic Instability Induced by Brca1 Deficiency. *Molecular Cell*, *35*(4), 534–541.

doi:10.1016/j.molcel.2009.06.037

Celeste, A., Difilippantonio, S., Difilippantonio, M. J., Fernandez-Capetillo, O., Pilch, D. R., Sedelnikova, O. A., … Nussenzweig, A. (2003). H2AX haploinsufficiency modifies genomic stability and tumor susceptibility. *Cell*, *114*(3), 371–383. doi:10.1016/S0092-8674(03)00567-1

Chang, C. C., Wang, Y. R., Chen, S. F., Wu, C. C., & Chan, N. L. (2013). New insights into DNA-binding by type IIA topoisomerases. *Current Opinion in Structural Biology*, *23*(1), 125–133. doi:10.1016/j.sbi.2012.11.011

Chang, C.-J., & Hung, M.-C. (2012). The role of EZH2 in tumour progression. *British Journal of Cancer*, *106*(2), 243–7. doi:10.1038/bjc.2011.551

Chapman, J. R., Taylor, M. R. G., & Boulton, S. J. (2012). Playing the end game: DNA double-strand break repair pathway choice. *Molecular Cell*, *47*(4), 497–510. doi:10.1016/j.molcel.2012.07.029

Chiolo, I., Minoda, A., Colmenares, S. U., Polyzos, A., Costes, S. V, & Karpen, G. H. (2011). Double-strand breaks in heterochromatin move outside of a dynamic HP1a domain to complete recombinational repair. *Cell*, *144*(5), 732–44. doi:10.1016/j.cell.2011.02.012

Choudhuri, S. (2011). From Waddington's epigenetic landscape to small noncoding RNA: some important milestones in the history of epigenetics research. *Toxicology Mechanisms and Methods*, *21*(4), 252–74. doi:10.3109/15376516.2011.559695

Ciccia, A., Bredemeyer, A. L., Sowa, M. E., Terret, M. E., Jallepalli, P. V., Harper, J. W., & Elledge, S. J. (2009). The SIOD disorder protein SMARCAL1 is an RPA-interacting protein involved in replication fork restart. *Genes and Development*, *23*(20), 2415–2425. doi:10.1101/gad.1832309

Daley, J. M., & Sung, P. (2014). 53BP1, BRCA1, and the choice between recombination and end joining at DNA double-strand breaks. *Molecular and Cellular Biology*, *34*(8), 1380–8. doi:10.1128/MCB.01639-13

Dawson, M. a, Bannister, A. J., Göttgens, B., Foster, S. D., Bartke, T., Green, A. R., & Kouzarides, T. (2009). JAK2 phosphorylates histone H3Y41 and excludes HP1alpha from chromatin. *Nature*, *461*(7265), 819–822. doi:10.1038/nature08448

de Campos-Nebel, M., Larripa, I., & González-Cid, M. (2010). Topoisomerase II-mediated

DNA damage is differently repaired during the cell cycle by non-homologous end joining and homologous recombination. *PloS One*, *5*(9). doi:10.1371/journal.pone.0012541

Deckbar, D., Jeggo, P. a, & Löbrich, M. (2011). Understanding the limitations of radiation-induced cell cycle checkpoints. *Critical Reviews in Biochemistry and Molecular Biology*, *46*(4), 271–83. doi:10.3109/10409238.2011.575764

Deckbar, D., Stiff, T., Koch, B., Reis, C., Löbrich, M., & Jeggo, P. A. (2010). The limitations of the G1-S checkpoint. *Cancer Research*, *70*(11), 4412–4421. doi:10.1158/0008-5472.CAN-09-3198

Dion, V., Kalck, V., Horigome, C., Towbin, B. D., & Gasser, S. M. (2012). Increased mobility of double-strand breaks requires Mec1, Rad9 and the homologous recombination machinery. *Nature Cell Biology*, *14*(5), 502–509. doi:10.1038/ncb2465

Enserink, J. M., & Kolodner, R. D. (2010). An overview of Cdk1-controlled targets and processes. *Cell Division*, *5*(1), 11. doi:10.1186/1747-1028-5-11

Felix, C. A., Kolaris, C. P., & Osheroff, N. (2006). Topoisomerase II and the etiology of chromosomal translocations. *DNA Repair*, *5*(9-10), 1093–1108. doi:10.1016/j.dnarep.2006.05.031

Giunta, S., Belotserkovskaya, R., & Jackson, S. P. (2010). DNA damage signaling in response to double-strand breaks during mitosis. *The Journal of Cell Biology*, *190*(2), 197–207. doi:10.1083/jcb.200911156

Goodarzi, A. a, & Jeggo, P. a. (2012). The heterochromatic barrier to DNA double strand break repair: how to get the entry visa. *International Journal of Molecular Sciences*, *13*(9), 11844–60. doi:10.3390/ijms130911844

Goodarzi, A. a, Jeggo, P., & Lobrich, M. (2010). The influence of heterochromatin on DNA double strand break repair: Getting the strong, silent type to relax. *DNA Repair*, *9*(12), 1273–82. doi:10.1016/j.dnarep.2010.09.013

Goodarzi, A. a, Noon, A. T., Deckbar, D., Ziv, Y., Shiloh, Y., Löbrich, M., & Jeggo, P. a. (2008). ATM signaling facilitates repair of DNA double-strand breaks associated with heterochromatin. *Molecular Cell*, *31*(2), 167–77. doi:10.1016/j.molcel.2008.05.017

Gospodinov, A., & Herceg, Z. (2013). Chromatin structure in double strand break repair. *DNA Repair*, *12*(10), 800–10. doi:10.1016/j.dnarep.2013.07.006

Havens, C. G., & Walter, J. C. (2011). Mechanism of CRL4(Cdt2), a PCNA-dependent E3 ubiquitin ligase. *Genes & Development*, *25*(15), 1568–82. doi:10.1101/gad.2068611

Hisang, Y. H., Lihou, M. ., & Liu, L. . (1989). Arrest of replication fork by drug-stabilized topoisomerase I - DNA cleavable complexes as a mechanism of cell killing by camptothecin. *Cancer Res*, *47*, 5077–5082.

Hühn, D., Bolck, H. a, & Sartori, A. a. (2013). Targeting DNA double-strand break signalling and repair: recent advances in cancer therapy. *Swiss Medical Weekly*, *143*(July), w13837. doi:10.4414/smw.2013.13837

Iyama, T., & Wilson, D. M. (2013). DNA repair mechanisms in dividing and non-dividing cells. *DNA Repair*, *12*(8), 620–636. doi:10.1016/j.dnarep.2013.04.015

Jakob, B., Splinter, J., Conrad, S., Voss, K.-O., Zink, D., Durante, M., … Taucher-Scholz, G. (2011). DNA double-strand breaks in heterochromatin elicit fast repair protein recruitment, histone H2AX phosphorylation and relocation to euchromatin. *Nucleic Acids Research*, *39*(15), 6489–99. doi:10.1093/nar/gkr230

Johansen, K. M., & Johansen, J. (2006). Regulation of chromatin structure by histone H3S10 phosphorylation. *Chromosome Research*, *14*(4), 393–404. doi:10.1007/s10577-006-1063-4

Kadoch, C., Copeland, R. A., & Keilhack, H. (2016). PRC2 and SWI/SNF Chromatin Remodeling Complexes in Health and Disease. *Biochemistry*, *55*(11), 1600–1614. doi:10.1021/acs.biochem.5b01191

Kelly, A. D., & Issa, J.-P. J. (2017). The promise of epigenetic therapy: reprogramming the cancer epigenome. *Current Opinion in Genetics & Development*, *42*, 68–77. doi:10.1016/j.gde.2017.03.015

Kim, J. A., Kruhlak, M., Dotiwala, F., Nussenzweig, A., & Haber, J. E. (2007). Heterochromatin is refractory to γ-H2AX modification in yeast and mammals. *Journal of Cell Biology*, *178*(2), 209–218. doi:10.1083/jcb.200612031

King, C., Diaz, H. B., McNeely, S., Barnard, D., Dempsey, J., Blosser, W., … Marshall, M. S. (2015). LY2606368 causes replication catastrophe and anti-tumor effects through CHK1-dependent mechanisms. *Molecular Cancer Therapeutics*, *14*(September), 2004–2014. doi:10.1158/1535-7163.MCT-14-1037

Kornberg, R. (1974). Chromatin Structure : A Repeating Unit of Histones and DNA

Chromatin structure is based on a repeating unit of eight. *Science*, *184*, 868–871.

Kouzarides, T. (2007). Chromatin modifications and their function. *Cell*, *128*(4), 693–705. doi:10.1016/j.cell.2007.02.005

Kruhlak, M. J., Celeste, A., Dellaire, G., Fernandez-Capetillo, O., Müller, W. G., McNally, J. G., … Nussenzweig, A. (2006). Changes in chromatin structure and mobility in living cells at sites of DNA double-strand breaks. *The Journal of Cell Biology*, *172*(6), 823–834. doi:10.1083/jcb.200510015

Lafarga, V., Cuadrado, A., Lopez de Silanes, I., Bengoechea, R., Fernandez-Capetillo, O., & Nebreda, A. R. (2009). p38 Mitogen-Activated Protein Kinase- and HuR-Dependent Stabilization of p21Cip1 mRNA Mediates the G1/S Checkpoint. *Molecular and Cellular Biology*, *29*(16), 4341–4351. doi:10.1128/MCB.00210-09

Lee, J. J., Kong, M., Ayers, G. D., & Lotan, R. (2007). Interaction Index and Different Methods for Determining Drug Interaction in Combination Therapy. *Journal of Biopharmaceutical Statistics*, *17*(3), 461–480. doi:10.1080/10543400701199593

Lowndes, N. F. (2010). The interplay between BRCA1 and 53BP1 influences death, aging, senescence and cancer. *DNA Repair*, *9*(10), 1112–6. doi:10.1016/j.dnarep.2010.07.012

Luijsterburg, M. S., Dinant, C., Lans, H., Stap, J., Wiernasz, E., Lagerwerf, S., … van Driel, R. (2009). Heterochromatin protein 1 is recruited to various types of DNA damage. *The Journal of Cell Biology*, *185*(4), 577–86. doi:10.1083/jcb.200810035

Lukas, J., Lukas, C., & Bartek, J. (2011). More than just a focus: The chromatin response to DNA damage and its role in genome integrity maintenance. *Nature Cell Biology*, *13*(10), 1161–9. doi:10.1038/ncb2344

Ma, F., & Zhang, C. (2016). Histone modifying enzymes: novel disease biomarkers and assay development. *Expert Review of Molecular Diagnostics*, *16*(3), 297–306. doi:10.1586/14737159.2016.1135057

Mamely, I., van Vugt, M. A., Smits, V. A., Semple, J. I., Lemmens, B., Perrakis, A., … Freire, R. (2006). Polo-like Kinase-1 Controls Proteasome-Dependent Degradation of Claspin during Checkpoint Recovery. *Current Biology*, *16*(19), 1950–1955. doi:10.1016/j.cub.2006.08.026

Marchion, D. C., Bicaku, E., Daud, A. I., Richon, V., Sullivan, D. M., & Munster, P. N.

(2004). Sequence-specific potentiation of topoisomerase II inhibitors by the histone deacetylase inhibitor suberoylanilide hydroxamic acid. *Journal of Cellular Biochemistry*, *92*(2), 223–237. doi:10.1002/jcb.20045

Miranda, T. B., Cortez, C. C., Yoo, C. B., Liang, G., Abe, M., Kelly, T. K., … Jones, P. A. (2009). DZNep is a Global Histone Methylation Inhinbitor that Reactivates Developmental Genes Not silenced by DNA Methylation. *Molecular Cancer Therapeutics*, *8*(6), 1579–1588. doi:10.1158/1535-7163.MCT-09-0013.DZNep

Murr, R., Loizou, J. I., Yang, Y.-G., Cuenin, C., Li, H., Wang, Z.-Q., & Herceg, Z. (2006). Histone acetylation by Trrap–Tip60 modulates loading of repair proteins and repair of DNA double-strand breaks. *Nature Cell Biology*, *8*(1), 91–99. doi:10.1038/ncb1343

Namdar, M., Perez, G., Ngo, L., & Marks, P. A. (2010). Selective inhibition of histone deacetylase 6 (HDAC6) induces DNA damage and sensitizes transformed cells to anticancer agents. *Proceedings of the National Academy of Sciences*, *107*(46), 20003–20008. doi:10.1073/pnas.1013754107

O'Keefe, R. T., Henderson, S. C., & Spector, D. L. (1992). Dynamic organization of DNA replication in mammalian cell nuclei: Spatially and temporally defined replication of chromosome-specific ??-satellite DNA sequences. *Journal of Cell Biology*, *116*(5), 1095–1110. doi:10.1083/jcb.116.5.1095

Panier, S., Ichijima, Y., Fradet-Turcotte, A., Leung, C. C. Y., Kaustov, L., Arrowsmith, C. H., & Durocher, D. (2012). Tandem Protein Interaction Modules Organize the Ubiquitin-Dependent Response to DNA Double-Strand Breaks. *Molecular Cell*, *47*(3), 383–395. doi:10.1016/j.molcel.2012.05.045

Pereira, P. D., Serra-caetano, A., Cabrita, M., Bekman, E., Braga, J., Rino, J., … Ferreira, J. (2017). Quantification of cell cycle kinetics by EdU (5-ethynyl-2 ′ - deoxyuridine) -coupled-fluorescence-intensity analysis. *Oncotarget*.

Raschellà, G., Melino, G., & Malewicz, M. (2017). New factors in mammalian DNA repair—the chromatin connection. *Oncogene*, (February), 1–9. doi:10.1038/onc.2017.60

Rato, S., Maia, S., Brito, P. M., Resende, L., Pereira, C. F., Moita, C., … Goncalves, J. (2010). Novel HIV-1 knockdown targets identified by an enriched kinases/phosphatases shRNA library using a long-term iterative screen in jurkat T-cells. *PLoS ONE*, *5*(2). doi:10.1371/journal.pone.0009276

Reddy, M. A., Park, J. T., & Natarajan, R. (2012). Kidney Research and Clinical Practice Epigenetic modifications and diabetic nephropathy. *Kidney Research and Clinical Practice*, *31*(3), 139–150. doi:10.1016/j.krcp.2012.07.004

Rogakou, E. P., Pilch, D. R., Orr, a H., Ivanova, V. S., & Bonner, W. M. (1998). DNA double-stranded breaks induce histone H2AX phosphorylation on serine 139. *The Journal of Biological Chemistry*, *273*(10), 5858–68.

Santos-Rosa, H., & Caldas, C. (2005). Chromatin modifier enzymes, the histone code and cancer. *European Journal of Cancer (Oxford, England : 1990)*, *41*(16), 2381–402. doi:10.1016/j.ejca.2005.08.010

Scully, R., Ganesan, S., Vlasakova, K., Chen, J., Socolovsky, M., & Livingston, D. M. (1999). Genetic Analysis of BRCA1 Function in a Defined Tumor Cell Line. *Molecular Cell*, *4*(6), 1093–1099. doi:10.1016/S1097-2765(00)80238-5

Scully, R., & Xie, A. (2013). Double strand break repair functions of histone H2AX. *Mutation Research*, *750*(1-2), 5–14. doi:10.1016/j.mrfmmm.2013.07.007

Shaltiel, I. A., Aprelia, M., Saurin, A. T., Chowdhury, D., Kops, G. J. P. L., Voest, E. E., & Medema, R. H. (2014). Distinct phosphatases antagonize the p53 response in different phases of the cell cycle. *Proceedings of the National Academy of Sciences*, *111*(20), 7313–7318. doi:10.1073/pnas.1322021111

Shaltiel, I. A., Krenning, L., Bruinsma, W., & Medema, R. H. (2015). The same, only different - DNA damage checkpoints and their reversal throughout the cell cycle. *Journal of Cell Science*, *128*(4), 607–620. doi:10.1242/jcs.163766

Shibata, A., Barton, O., Noon, A. T., Dahm, K., Deckbar, D., Goodarzi, A. A., … Jeggo, P. A. (2010). Role of ATM and the Damage Response Mediator Proteins 53BP1 and MDC1 in the Maintenance of G2/M Checkpoint Arrest. *Molecular and Cellular Biology*, *30*(13), 3371–3383. doi:10.1128/MCB.01644-09

Smith-Roe, S. L., Nakamura, J., Holley, D., Chastain, P. D. 2nd, Rosson, G. B., Simpson, D. A., … Bultman, S. J. (2015). SWI/SNF complexes are required for full activation of the DNA-damage response. *Oncotarget*, *6*(2), 732–745.

Soria, G., Polo, S. E., & Almouzni, G. (2012). Prime, repair, restore: the active role of chromatin in the DNA damage response. *Molecular Cell*, *46*(6), 722–34. doi:10.1016/j.molcel.2012.06.002

Stathis, A., Zucca, E., Bekradda, M., Gomez-Roca, C., Delord, J. P., Rouge, T. de L. M., … French, C. A. (2016). Clinical response of carcinomas harboring the BRD4-NUT oncoprotein to the targeted bromodomain inhibitor OTX015/MK-8628. *Cancer Discovery*, *6*(5), 492–500. doi:10.1158/2159-8290.CD-15-1335

Stewart, G. S. (2009). Solving the RIDDLE of 53BP1 recruitment to sites of damage. *Cell Cycle (Georgetown, Tex.)*, *8*(10), 1532–8.

Strahl, B. D., & Allis, C. D. (2000). The language of covalent histone modifications. *Nature*, *403*(6765), 41–45. doi:10.1038/47412

Sun, Y., Jiang, X., Xu, Y., Ayrapetov, M. K., Moreau, L. A., Whetstine, J. R., & Price, B. D. (2009). Histone H3 methylation links DNA damage detection to activation of the tumour suppressor Tip60. *Nature Cell Biology*, *11*(11), 1376–1382. doi:10.1038/ncb1982

Tallarida, R. J. (2001). Drug synergism: its detection and applications. *The Journal of Pharmacology and Experimental Therapeutics*, *298*(3), 865–872. doi:10.1074/jbc.M503833200

van Attikum, H., & Gasser, S. M. (2009). Crosstalk between histone modifications during the DNA damage response. *Trends in Cell Biology*, *19*(5), 207–17. doi:10.1016/j.tcb.2009.03.001

Van Vugt, M. A. T. M., Brás, A., & Medema, R. H. (2004). Polo-like kinase-1 controls recovery from a G2 DNA damage-induced arrest in mammalian cells. *Molecular Cell*, *15*(5), 799–811. doi:10.1016/j.molcel.2004.07.015

Wang, B., Matsuoka, S., Ballif, B. a, Zhang, D., Smogorzewska, A., Gygi, S. P., & Elledge, S. J. (2007). Abraxas and RAP80 form a BRCA1 protein complex required for the DNA damage response, *316*(May), 1194–1198.

Wang, J. (2002). CELLULAR ROLES OF DNA TOPOISOMERASES: A MOLECULAR PERSPECTIVE. *Nature Reviews. Molecular Cell Biology*, *3*, 430–440. doi:10.1038/nrm831

Watts, F. Z. (2016). Repair of DNA double-strand breaks in heterochromatin. *Biomolecules*, *6*(4), 1–11. doi:10.3390/biom6040047

Wu, J., & Liu, L. F. (1997). Processing of topoisomerase I cleavable complexes into DNA damage by transcription. *Nucleic Acids Research*, *25*(21), 4181–4186.

doi:10.1093/nar/25.21.4181

Yun, M. H., & Hiom, K. (2009). CtIP-BRCA1 modulates the choice of DNA double-strand-break repair pathway throughout the cell cycle. *Nature*, *459*(7245), 460–3. doi:10.1038/nature07955

Zeman, M. K., & Cimprich, K. A. (2014). Causes and consequences of replication stress. *Nature Cell Biology*, *16*(1), 2–9. doi:10.1038/ncb2897

Chapter 4

Quantification of cell cycle kinetics by EdU (5-ethynyl-2'-deoxyuridine) - Coupled-Fluorescence-Intensity analysis

Pedro Pereira[1*], Ana Serra- Caetano[1*], Marisa Cabrita[2], José Braga[1], José Rino[1], Renè Santus[3], Paulo L. Filipe[1], Ana E. Sousa[1], João A. Ferreira[1]

[1] Instituto de Medicina Molecular, Faculdade Medicina da Universidade de Lisboa, Av. Prof. Egas Moniz, 1649-028 Lisboa, Portugal

[2] Kennedy Institute of Rheumatology, University of Oxford, Oxford OX3 7FY, United Kingdom

[3] Muséum National d´Histoire Naturelle, Département RDDM, 43 Rue Cuvier, 75231 Paris, France

*These authors contributed equally to this work

Keywords: **cell cycle, EdU, S phase, DNA replication**

In this chapter we describe the implementation of a new methodology to reliably quantify duration of cell cycle phases. This effort was undertaken alongside the work described in the previous chapter as a result of mainly two factors: 1) constantly requiring more accurate measurements of cell cycle percentages than those provided by standard DNA content mono-parametric analysis. This was especially true for cell lines with atypical cell cycles namely with very long G1 phase, or very short G1 and G2 phases; 2) the shift from using BrdU (5-bromo-2'-deoxyuridine) to using EDU (5-ethynyl-2'-deoxyuridine) in flow cytometry procedures and realizing the potential of its stoichiometric properties.

Although this new methodology was not applied directly in the key experimental procedures of the previous chapter of this thesis since it was not yet fully validated, the characterization of the cells lines used, namely HCT116 wild type and DNAPK knockouts, proved very useful as a proof of concept, providing a comparison standard for all previously shown results obtained using these lines.

This work was published in April 2017 in the online journal Oncotarget.

ABSTRACT

We propose a novel single-deoxynucleoside-based assay that is easy to perform and provides accurate values for the absolute length (in units of time) of each of the cell cycle stages (G1, S and G2/M). This flow-cytometric assay takes advantage of the excellent stoichiometric properties of azide-fluorochrome detection of DNA substituted with 5-ethynyl-2'-deoxyuridine (EdU). We show that by pulsing cells with EdU for incremental periods of time maximal EdU-coupled fluorescence is reached when pulsing times match the length of S phase. These pulsing times, allowing labelling for a full S phase of a fraction of cells in asynchronous populations, provide accurate values for the absolute length of S phase. We characterized additional, lower intensity signals that allowed quantification of the absolute durations of G1 and G2 phases.

Importantly, using this novel assay data on the lengths of G1, S and G2/M phases are obtained in parallel. Therefore, these parameters can be estimated within a time frame that is shorter than a full cell cycle. This method, which we designate as EdU-Coupled Fluorescence Intensity (E-CFI) analysis, was successfully applied to cell types with distinctive cell cycle features and shows excellent agreement with established methodologies for analysis of cell cycle kinetics.

INTRODUCTION

The rate at which mammalian cells entry and progress through the different stages of their cell cycle is subject to strict regulatory mechanisms to avoid abnormal cell growth and division that may pose a threat to structure and function at the tissue level [1]. Intensive efforts have been done to accurately monitor cell cycle progression in order to better understand and predict tumor development [2]. By identifying changes in proliferation rates in response to treatment important contributes can be made to the development of anti-cancer therapeutic agents targeting specific steps of the cell cycle and the tailoring of treatment strategies for oncologic patients. In addition, determining cell cycle kinetics for distinct cell cycle stages is an important step for characterization of cancer cell lines [3].

Kinetics of S phase, in particular, can provide important information on control mechanisms and shifts in DNA replication. For instance, during early embryogenesis changes in S phase duration are frequent and reflect a progressive slowing down of firing rates of replication origins [4], while neuronal progenitor cells seem to shorten their S phase as they switch transcription factors on the path to neuron differentiation [5].

Currently, various techniques are available to estimate the duration of specific cycle phases, each with particular advantages and short-comings. Possibly the quickest, easiest and most widely used approach is to stain cellular DNA with a fluorescent dye to measure the DNA content of a cell population using flow cytometry analysis. With the aid of statistical algorithms implemented within the analysis software this results in the distribution of cells along the G1/G0 (2n), G2/M (4n) and S (2n to 4n) phases of the cycle [6,7]. This method, however, only provides cell cycle distributions – i.e. relative lengths - at a fixed time point and suffers from variability associated with technical artifacts introduced by sample preparation, and density and condition of cells that can interfere with a uniform staining of cellular DNA [8]. Furthermore, the use of different statistical algorithms potentially introduces additional variability in the interpretation of DNA measurements between laboratories [9,10].

Higher sensitivity strategies providing data on absolute durations of each stage of the cell cycle usually involve incorporation of detectable nucleoside analogues, the most

widely used being the thymidine analogue BrdU (5-bromo-2'-deoxyuridine). BrdU is incorporated into cellular DNA during replication to tag cells in S phase, allowing their identification by immunofluorescence microscopy or flow cytometry [11]. BrdU has become standard use in proliferation studies for the past two decades as it significantly reduced the cost and time associated with previously used radioactive analogues (e.g. tritium-labelled thymidine). A drawback, however, is that antibody-based detection of BrdU has poor stoichiometry and requires a DNA denaturation step. This step, essential to expose incorporated BrdU to antibodies, can induce degradation of DNA structure and cause variability in the detected fluorescent signals [12].

In one immunofluorescence microscopy-based approach cell populations are briefly pulsed with BrdU to mark cells traversing S phase, and subsequently checked in mitosis over incremental chasing periods. Parameters on cell cycle phases can then be estimated from the time required for BrdU-labelled cells to reach M phase, yielding absolute G2 duration, and from the time BrdU-positive cells persist showing up in mitosis, corresponding to absolute S phase duration [13,14]. This method boasts high resolution and reproducibility, although the technical steps involved in sample preparation and microscopic analysis can be very time consuming. Instead of screening for tagged mitotic fractions to identify cells that have left S phase other options involve pulsing replicating cells with two distinct nucleoside analogues at different times; or else, synchronizing the entire cell population to ensure an homogeneous entry in S phase and removal of the noise associated with double-pulsing methods [15]. Dual labelling requires the simultaneous use and detection of two antibodies specific for different analogues, hence special care needs to be taken to avoid cross hybridization signals [16]. Cell synchronization, on the other hand, carries the risk of disturbing normal cycle progression and inducing cell death, even when performed avoiding the use of drugs that target the cell cycle [17].

In recent years another thymidine analogue, EdU (5-ethynyl-2'-deoxyuridine), has become established as a viable alternative to BrdU for labeling replicating DNA. EdU harbours a terminal alkyne group that can be detected by its highly specific covalent reaction with a fluorochrome-conjugated azide. This property confers several advantages over BrdU, namely extremely high sensitivity and ease of use, along with the small size

and high intracellular penetration capability of EdU reagents (1/500th the size of an antibody molecule). This eliminates the need for the harsh cell permeabilization and DNA denaturation steps typical of antibody-based detection techniques [12,18]. The characteristics of the EdU-azide reaction further suggest the potential for optimum stoichiometry detection of EdU incorporated into DNA by a quantitative methodology such as flow cytometry.

We therefore reasoned that, instead of just scoring fractions of EdU-positive cells, it would be possible to extract accurate information on the kinetics of S phase by measuring the fluorescent intensities stemming from EdU-substituted DNA (EdU-DNA). The basic assumption was that, by pulsing asynchronous cell populations with EdU for incremental periods of time, when pulsing times match the length of S phase at least a cohort of cells would be labelled for a full S phase. These cells should thus show maximum labelling intensity, and the corresponding pulsing time should equal the absolute length of S phase. Further increments in pulsing times should only increase the percentage of cells featuring such intensities.

Herein, we provide compelling evidence that this principle can be applied to measure the length of S phase with high temporal resolution even under conditions where cell cycle progression is perturbed. Furthermore, analysis of the fluorescence intensity plots obtained by flow cytometry also yields additional useful information on the lengths of G1 and G2 phases of the cell cycle. This novel method, designated here as EdU-Coupled Fluorescence Intensity (E-CFI) analysis, can be used to characterize cell types featuring highly distinct cell cycle characteristics.

RESULTS

Effects of EdU on DNA damage response, genomic instability and cell cycle progression

Replacement of natural thymidine by halogenated or alkylated analogues, including EdU, has been shown to introduce conformational changes in the DNA helix and nucleotide pool imbalance; also, alterations in DNA synthesis and cell cycle progression, DNA damage and genomic instability, and increased cell death [19]. We have, therefore, tested the potentially noxious effects of EdU on HCT-116 cells to establish temporal and dosage constraints to the use of EdU in estimating cell cycle parameters.

To this end, HCT-116 cells were synchronized at the G1/S transition by a double thymidine block and exposed to a range of EdU concentrations (5, 10, 20 and 30 μM) for a full S phase (see materials and methods). Cells were then analyzed 5 days later for the presence of EdU-labeled individual chromosome territories (CTs), only present in cells that underwent several rounds of mitotic division [20,21], and of micronuclei and giant nuclei, hallmarks of genomic instability [22]. Of note, nuclei displaying EdU-labeled CTs, giant nuclei and micronuclei may concur within the same cell. At low EdU concentrations (5 and 10 μM), a significant fraction (>80%) of labeled nuclei shows individual CTs consistent with continued cell division (Figure 1A). However, the presence of cells harboring micronuclei (19.4 ± 1.6% and 36.5 ± 5.9% for 5 and 10 μM EdU, respectively) and giant nuclei (8.8 ± 2.7% and 16.2 ± 3.5% for 5 and 10 μM EdU, respectively) were noticeably higher than in EdU-negative controls (5.9 ± 1.9% for micronuclei and 1.6 ± 0.7% for giant nuclei) (Figure 1A). At 30 μM, EdU induced a drastic reduction of CTs (only 11.3 ± 4.3% of positive cells) and a sharp increase in cells with signs of genomic instability (micronuclei: 31.9 ± 4.3%; giant nuclei: 64.3 ± 9.7%). These data indicate that in the long-term EdU induces overt signs of genomic instability.

Since the novel approach proposed here does not require long exposures to EdU, we next tested whether pulsing HCT-116 cells with EdU (2.5, 5, 10 and 20 μM) for a short period (11 h) induced DNA damage in the form of DNA breaks and replication stress; negative controls were provided by cells exposed to solvent alone. Testing the presence of DNA breaks (single- and double-stranded) by alkaline single-cell gel electrophoresis

(comet assay) revealed that EdU induced statistically significant, though modest (tail moments less than twice background), levels of DNA breaks (Figure 1B, also cf. Figure S1 in Supplementary Data for percentage of DNA in comet tails). By contrast, camptothecin (CPT; 5 μM), a known inducer of DNA breaks, and CPT plus EdU (20 μM) induced more significant amounts of DNA breakage, as expected. To specifically check for the presence of EdU-induced DNA double-stranded breaks (DSBs), HCT-116 cells were immunostained for histone γH2AX (variant histone H2AX phosphorylated on serine 139), known to accumulate as nuclear foci at genomic sites harboring DSBs [23]. Enumeration of γH2AX foci showed that EdU at 20 μM induced a significant increase in damage foci (average of 12 foci per cell; Figure 1C). Although γH2AX DNA damage foci still increased significantly after a 11 h exposure to 5 and 10 μM EdU (3 foci per cell on average), this increase was only twice background levels, becoming non-significantly different from control levels at 2.5 μM (Figure 1C). Moreover, nuclear foci concentrating phospho-RPA (Replication protein A), indicative of replicative stress, were not increased in HCT-116 cells exposed to EdU 2.5, 5, 10 or 20 μM for 11 h (Figure 1D). In accordance, western blotting analysis for the presence of increased levels of phospho-RPA and γH2AX after short term exposures to EdU (11 h; 10 and 20 μM) did not show any noticeable difference relative to EdU-less controls; however, as anticipated, cells treated with CPT (plus/minus 20 μM EdU) displayed high levels of both phospho-RPA and γH2AX (Figure 1E). Importantly, exposure of different cell types namely HCT-116, mouse embryonic fibroblasts (MEFs), and mouse embryonic stem cells (mESCs) to EdU (10, 5 and 2.5 μM, respectively; 11 h) did not change cell cycle profiles obtained by flow cytometry (propidium iodide/PI and 4',6-diamidino-2-phenylindole/ DAPI staining; Figure 1F). These data are consistent with DNA damage and replication stress sensitive checkpoints not being activated within this timeframe.

Altogether, these results show that in the long-term (5 days) even low doses of EdU induce prominent signs of genomic instability and alterations in cell division, in line with previously reported genotoxic effects of EdU [19,24]. However, short term exposures (11 to 12 h) to low concentrations of EdU (2.5 to 10 μM) can conciliate with unperturbed cell cycle progression and thus be used in subsequent analyses.

Stoichiometry of detection of EdU-labeled DNA

Herein, we aimed at developing a novel methodology for extracting absolute values (i.e. in units of time) on the duration of S phase through the analysis of fluorescence intensities of EdU incorporated into replicating DNA (EdU-DNA). To do so, we first assessed whether detection of EdU-DNA followed strict stoichiometry. Incorporation of different concentrations of EdU (0, 5, 10, 15, 20 and 30 μM) into cultured HCT-116 cells for a defined period of time (9 h) showed that, as expected, emitted fluorescence intensities were not proportional to EdU concentrations (Figure 2A). However, for a defined concentration of EdU (10 μM), incorporation for incremental periods of time (1 h increments) from 0 h to 11 h revealed robust stoichiometry. Indeed, increasing periods of incorporation correlated linearly with increased amounts of total fluorescence, expressed as an integral, within the cell populations (Figure 2B).

Finally, HCT-116 cells synchronized at G1/S transition by a double-thymidine block were released into S phase and allowed to incorporate EdU (10 μM) continuously for 7 h to achieve full-S labeling before harvesting. Cells were then collected first in G2/M phase (8 h after release from thymidine) and later when emerging in G1 phase of the next cell cycle (11 h after release). As quality controls for synchronization, analysis by flow cytometry (PI staining) revealed that after release from G1/S most cells progressed with remarkable synchrony (Figure 2C). Also, more than 80% of the metaphase spreads obtained from cells incorporating EdU for 7 h after release from the G1/S block displayed fluorescent labeling of EdU-DNA across the entire length of chromosome arms; this is consistent with full S labeling. In contrast, a partial (banded) EdU staining pattern was seen when cells were only briefly pulsed with EdU (10 min, 15 μM) at 2.5 h or 4 h post release from thymidine (Figure S2 in Supplemental data). We then compared the intensities of EdU-coupled fluorescence between cells labeled for a full S phase and collected at G2/M stages (DNA = 4n) with those allowed to progress into G1 stage (DNA = 2n). This revealed that appearance of G1 cells harboring half the amount of EdU-DNA coincided with the emergence of a half-intensity peak (mean fluorescence intensity (MFI) of the G2/M peak and the G1 peak are, respectively, 443 and 212; Figure 2C).

In all, these data showed a strict correspondence between amounts of EdU-substituted DNA and intensities of EdU-coupled fluorescence and predicated our subsequent use of EdU in experiments aimed at estimating accurate cell cycle parameters.

Analysis of EdU-coupled fluorescence intensities

In the approach proposed here it is assumed that exposing asynchronously growing cell populations to EdU for incremental periods of time the maximum labeling intensity of EdU-DNA should be reached when the pulsing times approach, or equal, the duration of S phase. For such pulsing times, the cohort of cells in which the beginning of the pulse coincides with initiation of S phase shall become labeled for a full S phase and shall thus feature maximal labeling intensity. Absolute length of S phase shall then be equivalent to the minimum pulsing period with EdU that is required to achieve maximal EdU-coupled fluorescence intensity. Thereafter, increments in pulsing periods are expected to just increase the fraction of cells showing maximal labeling (Figure 3).

To test this idea, parallel cultures of colon cancer cells (HCT-116) were pulsed with EdU for incremental periods from 1 h to 11 h (1 h increments). Fluorescent detection of EdU-DNA was performed utilizing an azide-coupled fluorophore (Alexa 488) as part of Click-iT chemistry (cf. Materials and Methods) and bulk DNA was stained with either PI or DAPI. These experiments showed that fluorescence intensities associated with EdU-DNA increase steadily with increasing pulsing times (Figure 4; x axis represents fluorescence intensities). Maximal fluorescence intensities were first reached between 6 h and 7 h of continuous incorporation of EdU (Figure 4, 7 h time point, peak 3; MFI: 2677). According to our hypothesis this should be consistent with S phase duration of 6-7 h, indeed in good agreement with data obtained for HCT-116 cells using established methods of cell cycle analysis (cf. Table 1). To estimate the duration of S phase by E-CFI with higher temporal resolution (n=10) HCT-116 cells were exposed for 6 to 8 h to EdU (10 µM) using pulsing increments of 30 min (i.e., 6, 6.5, 7, 7.5 and 8 h). This provided a more refined appraisal for S phase length (6.80 ± 0.35 h; Table 1). As expected, longer pulses with 10 µM EdU (8 h to 11 h) resulted in no discernible increment in maximal fluorescence intensities (Figure

4). However, these longer pulsing times led to an increase in the height, i.e. number of events/EdU-labeled cells (y axis), of the peak corresponding to the maximally labeled cell population (peak 3 in Figure 4). This is also anticipated given the higher chance for maximal (full S) labeling by increasing pulsing periods with EdU (Figure 3).

We then assessed whether the minimum pulsing time with EdU required for achieving maximal fluorescence intensity of EdU-DNA, assumed here to correspond to S phase length, indeed corresponds to incorporation of EdU for a single, full S phase. To do so, exposure to EdU was restricted to a single S phase by blocking cell cycle progression in G2 stage with the Cdk1 inhibitor RO-3306. Asynchronous HCT-116 cultures were thus exposed simultaneously to EdU (10 μM) and to RO-3306 (10 μM) for 5, 7, 9 and 16 h. Controls were provided by parallel cultures exposed to EdU alone for identical periods of time and by cells not exposed to EdU (solvent alone). This experimental design ensures that a substantial fraction of cells (≈24%), i.e. those that were traversing G1 stage upon addition of EdU, will incorporate EdU for a full (and single) S phase and will not progress into the next cell cycle.

As seen in the cell cycle histograms for bulk DNA staining (PI), after addition of the Cdk1 inhibitor the cell population initially in G1 stage progressively disappears before cells finally arrest in G2 stage, as expected (Figure 5). Analysis of EdU-coupled fluorescence further showed that maximal fluorescence intensities of EdU-DNA overlapped irrespectively of the presence of RO-3306 (Figure 5).

These data strongly support the notion that the intensity maxima seen in our initial founder experiments indeed correspond to labeling for a full, single S phase (Figure 4). Importantly, the length of S phase estimated here by flow cytometric analyses of intensity maxima of EdU-coupled fluorescence is in excellent agreement with data obtained for HCT-116 cells utilizing other, previously validated methodologies (cf. Table 1 and text further below in this section).

Exploiting other EdU-coupled fluorescence intensity peaks

We initially focused on a sub-maximum intensity peak that in HCT-116 cells is evident after 9 h of EdU incorporation and becomes increasingly prominent thereafter

(Figure 4, peak 4). Use of the Cdk1 inhibitor RO-3306 allowed elucidation of the nature of this intensity peak. When cells are blocked in their progression into the subsequent G1 phase by RO-3306 this peak is absent (Figure 5, 9 h and 16 h, peak 4). Importantly, the mean fluorescence intensity of this accessory peak is half the intensity of the maximally (full S) labeled cell population (MFI of peak 4 and peak 3 are, correspondingly, 345 and 671). Moreover, in control cells (RO-3306-minus) that progressed unperturbed for 16 h to G1 stage of the next cell cycle, this peak became the most prominent (Figure 5, peak 4). Together, these data implicate this half-maximum intensity peak as originating from G1 cells that resulted from the mitotic division of full-S-labeled cells. Since these G1 cells harbor half the amount of EdU-DNA as their progenitors and, correspondingly, emitted half the mean fluorescence intensity, this further confirms the good stoichiometric properties of the EdU detection system.

Careful analysis of the EdU incorporation histograms depicted in Figure 4 reveals the consistent presence of additional, lower intensity peaks of fluorescence that change over time; of note, these peaks are already present in cells not exposed to EdU (No-EdU control; cf. Figure 4). Interestingly, the lower intensity background peaks seen in this EdU-negative population, likely due to the non-specific binding of the azide-Alexa 488 to bulk DNA, decomposed in two peaks after exposure to EdU even for short periods (Figure 4, peaks 1 and 2). Indeed, dual parameter analyses (EdU-coupled fluorescence *vs* total DNA/PI) showed that these two remaining peaks corresponded, respectively, to cells with G1 DNA content (2n; lower intensity peak) and G2 DNA content (4n; higher intensity peak) (Figure 6A). Cells with intermediate DNA contents (2n to 4n; S population), contributing to intermediate background intensities, have shifted to higher intensity regions upon incorporation of EdU leaving behind the double-peak (G1+G2) configuration of the background staining (Figure 6A, peaks 1 and 2). We note that background peaks do not always present the double-peak configuration. However, these peaks were consistently present in the many experiments performed here, acting as robust markers for the EdU-negative G1 and G2 populations. As expected, under continuous exposure to EdU these G1/G2 background peaks progressively disappear as cells initially at G1 and G2 stages move steadily into S phase and acquire strongly fluorescent EdU-coupled signals (Figure 4). We reasoned that the dynamics of these G1/G2 background peaks during time-

course experiments may reflect the absolute lengths of G1 and G2 stages. The duration of G2 stage shall therefore correspond to the period of time during which cells with G2 DNA content (4n) persist featuring background staining. Since this cohort of G2 cells feeds into the next G1 phase, the duration of G1 shall be estimated after subtracting the length of G2 phase from the total duration of the G1 (2n) background peak.

We then utilized dual parameter analysis (EdU-coupled fluorescence *vs* total DNA/PI) to monitor over time the dynamics of G1 and G2 cell populations that are EdU-unlabeled, i.e. just featuring non-specific background staining. As shown in Figure 6B (n=5) the percentage of G2 cells in the whole population steeply declined over time, reaching baseline levels after ≈4 h of exposure to EdU (G2 length: 3.8 ± 0.45 h; Table 1). After an initial plateau, the percentage of G1 cells decreased until 8-9 h of EdU incorporation followed by a smoother decline afterwards (Figure 6B). The initial plateau highlights the exit of G1 cells into S phase being compensated by entry into G1 stage of cells from the preceding G2 phase; the slower decline after the 8 h time point underscores the further existence of a minor population in the G1 compartment (< 5%) comprised of slow-(or non-)cycling cells . The length for G1 phase (5.40 ± 0.95 h) was estimated as the duration of G2 subtracted from the time for decline of the whole G1 population to baseline levels; this provided a good match to data gathered using validated methods (Table 1).

To further test the sensitivity of this approach we introduced in our analyses HCT-116 cells that are deficient (knock-out/KO) for the DNA repair enzyme DNA-dependent Protein Kinase (DNA-PK; HCT-116 DNA-PK KO). Using the EdU-pulsing method described herein (E-CFI) HCT-116 DNA-PK KO cells reached maximum EdU-coupled fluorescence intensity after ≈7 h of EdU incorporation (Figure S3 in Supplementary data). As previously performed for HCT-116 (DNA-PK wt) cells, short (30 min) increments in EdU pulsing between 6 and 8 h allowed a more accurate estimate for S phase length in HCT-116 DNA-PK KO cells (6.75 ± 0.42 h; n=6; Table 1). This value is similar to that obtained for the DNA-PK proficient (wt) HCT-116 cells used throughout this research, and was confirmed by previously validated methodologies (Table 1).

We subsequently tested in HCT-116 DNA-PK KO cells, as described above for HCT-116 cells, whether quantitative analysis of G1/G2 background peaks again provided

accurate values for the lengths of G1 and G2 phases. Analysis of five independent experiments showed that the percentage of G2 cells sharply decreased over 4 h of EdU incorporation before reaching baseline levels (Figure 6C). This is consistent with a G2 phase length (3.60 ± 0.55 h; n=5) in HCT-116 DNA-PK KO cells that is similar to HCT-116 cells that are proficient for DNA-PK (Table 1). However, the decline in G1 cells lasted longer in DNA-PK KO cells than in their DNA-PK-wt counterparts. Near-baseline levels were reached at 9 h, with a slower decline thereafter (Figure 6C). After subtracting the duration of G2 this yields a length for G1 phase that is slightly higher (6.0 ± 1.45 h; n=5) for DNA-PK KO than for DNA-PK wt HCT-116 cells (Table 1). Note that the fraction of slow/non-cycling cells (between 5 and 10%) is clearly more prominent than in HCT-116 cells harboring wt DNA-PK (< 5%) (Figures 6B and 6C). Indeed, the fraction of slow/non-cycling cells which do not incorporate modified deoxy-nucleosides even after prolonged exposure times was also shown to be higher in HCT-116 DNA-PK KO cells using other methods of cell cycle analysis (Figures 8C and 8D).

In sum, these data highlight the relevance of analyzing other peaks present in EdU-coupled fluorescence intensity histograms. Specifically, it was shown that quantitation of background intensity peaks provides accurate measurements for the lengths of G1 and G2 phases. These low intensity peaks also allow quantitative estimates of slow/non-cycling cells within a population.

EdU-coupled fluorescence intensity analysis in non-transformed mouse cells

We next tested whether the analysis of fluorescence intensities associated with EdU-DNA could be applied to accurately judge cell cycle parameters in other cell types, namely in non-transformed cells. To this end, we utilized pre-quiescent (passage 26-28) mouse embryonic fibroblasts (MEFs) and mouse embryonic stem cells (mESCs). These cell types were chosen for their remarkably different duplication times. Pre-quiescent MEFs duplicate over a period of days, with a large proportion of cells in G1 and G2 stages (Figure 1F). By contrast, when under logarithmic growth mESCs feature a short cell cycle length with fast gap and S phases [25]. Given the exquisite sensitivity of ESCs to EdU [26], in this set of experiments we have consistently used lower doses of EdU (2.5 and 5 μM).

MEFs and mESCs were therefore exposed for increasing periods of time (0 to 11 h; 1 h increments) to EdU (MEFs/5 μM; mESCs/2.5 μM) before analysis of EdU-DNA fluorescence intensities by flow cytometry, as previously described. This showed that MEFs reached maximal intensity after 8 h of continuous incorporation of EdU (Figure 7A). As expected for pre-quiescent cell populations with a long G1 phase, the G1/G2 background peaks remained remarkably stable over the incremental pulsing periods used here (Figure 7A plus data not shown). By contrast, mESCs displayed maximal intensity of EdU-coupled fluorescence after just ≈5 h of exposure to EdU (Figure 7B; MFI: 60636). Also, in mESCs the G1/G2 background peak decreased to residual levels after incorporation of EdU for 4 to 5 h (Figure 7B plus data not shown). Quantitative analysis of background peaks as performed above for HCT-116 cells showed that G1 and G2 phases lasted ≈2 h each (data not shown). These data are consistent with a total length of ≈9 h for the full cell cycle in mESCs, in excellent agreement with previously published data [25]. These experiments further extend the applicability of the novel E-CFI method to other cell types, even under the constraint of utilizing very low concentrations of EdU.

Comparison with other methods of cell cycle analysis

We subsequently tested how the method developed here compared to previously implemented assays aimed at estimating cell cycle parameters.

In a robust pulse-chase method – termed “Fraction of Labeled Mitoses” - that allows absolute estimates of the duration of S and G2 phases, cells are first briefly pulsed with a radioactive or a modified deoxy-nucleoside (e.g. BrdU), chased in mitosis for incremental periods of time and scored for the presence of labeled chromosomes [13,14,27]. In this assay, the time between pulsing and the emergence of the first labeled mitotic cells (≈50% of labeled cells) equals the absolute duration of G2. The time period during which the cohort of cells previously labeled in S phase with BrdU continues showing up in mitosis with BrdU-labeled chromosomes corresponds to the absolute duration of S phase [14].

Parallel cultures of HCT-116 cells (DNA-PK wt and DNA-PK KO) were therefore pulsed with BrdU (20 μM; 15 min), collected at hourly intervals up until 12 h after pulsing,

immuno-stained for BrdU, and the percentage of BrdU positive mitotic cells (prometaphase plus metaphase stages) was assessed for each time point. These experiments showed values for S and G2 phases very close to those obtained using E-CFI, for both DNA-PK deficient and proficient HCT-116 cells (Figure 8A and Table 1).

We also used the "Leaving Fraction" method in which cells are first pulsed with a modified deoxy-nucleoside, chased for a defined time period in medium free of modified nucleosides, and subjected to a second pulse with a differently modified nucleoside before collection (cf. Materials and Methods). The fraction of cells labeled by the first modified nucleoside but not by the second corresponds to the so-called leaving fraction, i.e. the fraction of cells that although initially in S phase have reached G2 during the chase period. Through extrapolation, the time required for all cells to leave S phase, which equals S phase duration, can be estimated as an absolute value (see also Materials and Methods) [28–30]. Notably, this microscopy-based method also yielded an S phase duration (6.3 ± 0.4 h) similar to that we have obtained throughout this research for HCT-116 cells using E-CFI (Table 1).

In a third approach we used a "Cumulative Labeling" method, also known as "Saturation Labeling" [31], to assess the absolute duration of G1 plus G2 stages. The underlying principle is that upon a brief exposure to a modified deoxy-nucleoside this is exclusively incorporated into the replicating DNA of cells traversing S phase. However, if pulsing times are progressively extended to encompass the duration of G1 plus G2 all cells initially at these stages will ultimately be allowed to reach S phase and thus to incorporate the analogue. Therefore, the minimal pulsing times with the analogue that allow labeling of the whole cell population will match the combined duration of G1 plus G2 stages for that population [32,33]. HCT-116 cells (DNA-PK wt and DNA-PK KO) were thus pulsed with BrdU (10 µM) for incremental periods of time up until 10.5 h before scoring by fluorescence microscopy. Again, the estimates for the combined duration of G1 plus G2 (HCT-116 DNA-PK wt: 7.5 to 9 h ; HCT-116 DNA-PK KO: ≈9 h) closely agree for both cell lines with those obtained using E-CFI (Figure 8C, 8D and Table 1). Interestingly, for both cell lines a sub-population of slow-/non-cycling cells was identified that was slightly more prominent in DNA-PK KO cells, as previously seen in experiments using E-CFI (Figure 8C and 8D).

Additionally, we used a pulse-chase methodology for estimation of the lengths of S and G2 phases [19]. To this end, HCT-116 (DNA-PK wt and DNA-PK KO) and mESCs were pulsed with EdU (10 μM and 5 μM, respectively) for 30 min and collected either immediately (no chase), or else chased in EdU-free medium before collection at hourly intervals. The length of G2 phase was estimated as the period of time between the end of the EdU pulse and the time point at which the population harboring G2 DNA content (4n) showed the highest percentage of EdU-positive cells. This expectedly occurs when the cohort of EdU-labeled cells (i.e. in S phase during EdU pulsing) reaches the G2/M transition after traversal of G2 phase. The interval between this latter time point and the time point where the population with 4n DNA content reaches its lowest percentage of EdU-positive cells was considered as the duration of S phase. This corresponds to the period during which the cohort of EdU-labeled cells fully passes through the G2/M transition into the next G1 phase.

Analysis by dual-parameter flow cytometry (EdU *vs* total DNA/PI) showed that the cohorts of EdU-labeled *vs* unlabeled cells progress evenly over time between cellular compartments harboring 2n and 4n DNA amounts (HCT-116 cells; Figure S4 in Supplementary data, plus data not shown). However, as depicted in Figures S4 and S5 (Supplementary data; HCT-116 cells), for each of four independent experiments it proved difficult to judge for cells with 4n DNA the time points at which the percentage of EdU-positive cells reached a maximum. Indeed, in these bowl-shaped curves these maximal values - typically reached at 4 to 6 h after the EdU pulse - are almost identical between neighbor time points (cf. Figure S5). When these data were combined (n=4) in a single line chart this showed that the maximal percentages of EdU-positive cells (4n DNA) seen at the 4, 5 and 6 h time points were not significantly different (81.2 ± 12.3%, 86.6 ± 9.7%, 86.4 ± 3.5%; 4, 5 and 6 h , respectively; Figure S6A in Supplementary data). Within the constraints of this method, we estimated the length of S and G2 phases for HCT-116 cells (DNA-PK wt, n=5; DNA-PK KO, n=4; Table 1). These values, despite their lower temporal resolution in particular for S phase, are in broad agreement with those obtained by E-CFI (Table 1). Assessment of mESCs by EdU pulse-chasing yielded better homogeneity between different experiments as shown in the graph depicting pooled data (n=4; Figure S6B in Supplemental data). The durations of S (5.75 ± 0.5 h) and G2 (4.25 ± 0.5 h) phases

were estimated taking the 4 h time point as that corresponding to the highest percentage of EdU-positive cells within the 4n DNA population (cf. Figure S6B in Supplementary data). Finally, we combined the commonly used analysis of the cell cycle by flow cytometry after PI staining of DNA with estimates of the absolute duration of the cell cycle in HCT-116 cells. This latter parameter is essential to convert the percentage of cells at a given cell cycle phase, which directly correlates with the relative length of that same phase in reference to the full cell cycle, into absolute lengths (i.e., in units of time).

Taking the duration of the cell cycle as the absolute parameter (14-15 h for HCT-116 cells), the percentage of cells seen at each cell cycle stage in flow cytometry histograms of PI-stained DNA was then converted into absolute lengths (hours). We note that the two available mathematical models within FlowJo, Watson Pragmatic (WP) and Dean/Jett/Fox (D/J/F), yielded discrepant percentages for each of the cell cycle stages in HCT-116 cells. The values obtained through the WP algorithm provided a better fit to the data gathered throughout this research using different methodologies, including E-CFI (cf. Table 1, and Table 2 in Supplemental data). However, using either of these algorithms (WP or D/J/F) we could not generate any reliable estimates for the much less canonical cell cycle histograms from exponentially growing mESCs (depicted in Figure 1F).

In sum, the E-CFI method described herein shows excellent concordance with data obtained through various well established methods of cell cycle analysis.

DISCUSSION

We have herein described an assay which we termed E-CFI that allows easy and accurate measurements of the absolute length of all stages of the cell cycle (G1, S and G2/M) by flow cytometry.

The approach of reference to analyze the duration of the different stages of the cell cycle is based on flow cytometric analysis of cellular DNA stained with a fluorescent dye that binds stoichiometrically, and thus allows measurement of DNA content [34]. This provides values on the proportion of cells found at each phase (G1, S and G2/M) which directly correspond to relative durations in reference to the length of a full cell cycle. Despite the use of algorithms that attempt at fitting Gaussian curves to each phase, a clear distinction between cells traversing very early or late S phase from cells in G1 and G2 phase, respectively, remains difficult by single parameter DNA analysis [10,34]. This difficulty becomes more obvious for cell types with atypical cell cycles namely with very long G1 phases, as is the case of pre-quiescent MEFs, or very short G1 and G2 phases, such as mESCs (Figure 1F; also Table 1). In such cases, under or overestimation of the length of S phase is the typical result [35]. Indeed, applying two different mathematical models, Dean/Jett/Fox and Watson Pragmatic, discrepant data was obtained for HCT-116 cells with D/J/F yielding unusually short durations for S phase (≈5 h; Table 1, and Table 2 in Supplemental data). Unfortunately, clear criteria for choice between different algorithms do not exist. In mESCs, in which S phase typically lasts more than 50% of the total cell cycle, both the D/J/F and the WP algorithms proved unreliable. Moreover, the conversion of these data on relative durations into absolute lengths for each phase requires an additional, accurate estimate of the absolute length of the cell cycle under the conditions being tested [7].

Pulse-chase methods utilizing EdU (or BrdU) also provide data on absolute durations of cell cycle phases and stand as possible contenders to the E-CFI assay described herein [19]. These methods, however, rely critically on selecting the fraction of EdU-positive cells within sub-populations of defined DNA content. They therefore share the known constraints of quantitative analyses of single parameter DNA histograms [7,36]. As a result, estimates for the duration of S and G2 stages have lower temporal

resolution (higher dispersion) than those obtained with either E-CFI or other classical, validated methods (Table 1).

Herein, we have utilized pulse-chasing with EdU on HCT-116 cells (DNA-PK wt and DNA-PK KO) and mESCs, and found that the critical time points to judge the duration of G2 and S phase proved difficult to determine unambiguously. Setting up these time points allows tracking of the cohort of EdU-positive cells over time. These correspond, specifically, to the time point(s) at which the G2 (4n DNA) population features the highest percentage of EdU-positive cells and, later, the lowest percentage of EdU-positive cells. The time interval between the end of the EdU pulse and the point(s) of maximal labeling corresponds to the length of G2; the interval between maximal and minimal labeling time point(s) corresponds to the length of S phase.

The exemplary case is provided by mESCs (Figure S6B in Supplemental data). In these cells, the time points corresponding to maxima of EdU-positive cells (≈92% to ≈96%) distribute broadly between 2 and 5 h after pulsing with EdU, with the minimal fraction of EdU-positive cells seen at 10 h after pulsing (cf. Figure S6B in Supplemental data). Taking the 2 h time point as the most significant maximum would be consistent with a ≈2 h duration of G2 phase in mESCs, in agreement with previously published data and the results obtained herein using E-CFI [25]. However, the interval between this and the 10 h time point (minimal percentage of EdU-positive cells) would lead to an excessively long estimate for S phase (≈8 h). This dilemma stems, at least in part, from the duration of G2 being much shorter than that of S phase, and also from the poor discrimination between cells at later stages of S phase (close-to-4n DNA) and genuine G2 cells. This latter issue can be appreciated at the end of the EdU pulse when most cells (>60%) harboring 4n DNA content have indeed incorporated EdU (cf. Figure S6B in Supplemental data; 0 h after EdU pulse).

The assay we describe here, E-CFI, is easy to perform and allows accurate estimates of absolute lengths (in units of time) of all the different stages of the cell cycle (G1, S, and G2/M). The duration of S phase is assessed without selection of cell populations based on DNA content. Although this is required for analysis of G1 and G2 phases, these two phases can be accurately separated given the absence of cells in the intervening S phase in background peaks. The classical problem of discriminating cells at

the G1/S and S/G2 borders is thus avoided [7,36]. Furthermore, E-CFI allowed the identification and quantification of sub-populations with decreased proliferative potential (slow-/non-cycling cells) within the G1 compartment in HCT-116 cells. We note that, in contrast to E-CFI, the duration of G1 is difficult to quantify in dual-parameter histograms from EdU pulse-chase experiments (Figure S4 in Supplemental data).

Herein, we have used the Cdk1 inhibitor (RO-3306) to demonstrate that the intensity maxima reached after continuous incorporation of EdU correspond indeed to labeling for a single, full S phase (Figure 5). These experiments further showed that E-CFI allows accurate estimation of S phase length even when cell cycle progression is blocked. Of note, this blockage would preclude the use of other methods of cell cycle analysis namely pulse-chase, cumulative labeling and methods in which labeled mitosis are scored.

E-CFI showed excellent correlation with the highly reproducible and precise methods of “Cumulative Labeling” and “Fraction-of-labeled mitosis/FLM”[15,31–33] (Table 1). These microscopy-based classical methods are, however, highly time consuming and thus not amenable to routine use. By contrast, E-CFI yields fast results by acting in a time-compressing fashion whereby G1, S and G2/M phases are assessed in parallel. This allows absolute estimates on the lengths of each cell cycle stage to be collected over a time period that is shorter than the duration of a full cell cycle. For example, for HCT-116 cells whose full cell cycle lasts for 15-16 h, the length of all cell cycle phases can be determined in 8-9 h.

We anticipate that E-CFI may provide a very valuable tool in the analysis of drugs targeting the cell cycle in the context of cancer chemotherapy, especially if coupled to powerful multiparametric analyses using flow cytometry or high-content imaging [7,37,36,38]. Also, the basic principle that predicated the development of E-CFI may be applied in the future to quantitative fluorescence microscopy-based approaches aimed at estimating absolute, accurate cell cycle parameters.

MATERIALS AND METHODS

Cell culture, chemicals and antibodies

Human colorectal carcinoma HCT-116 (ATCC CCL-247) and HCT-116 knock-out for DNA-PK were obtained from the laboratory of Dr. Bert Vogelstein, Johns Hopkins School of Medicine, Baltimore, MD. HCT-116 cells were cultured in McCoy's 5A Modified medium supplemented with 10% heat inactivated foetal bovine serum (FBS), 2 mM L-glutamine, 10mM MEM non-essential amino acids, and 100 U/ml penicillin/streptomycin (all from Gibco, Thermo-Fisher Scientific, Waltham, MA, USA) and maintained at 37°C in a humidified incubator at 5% CO2. Mouse embryonic fibroblasts (MEFs) were cultured in Dulbecco's Modified Eagle's Medium (DMEM) supplemented with 10% ES Cell-qualified FBS (Invitrogen, Thermo-Fisher Scientific, Waltham, MA, USA), 10 mM MEM non-essential amino acids, and 0.1 mM 2-mercaptoethanol (Gibco). Mouse embryonic stem cells (mESCs) were grown at 37°C in 5% CO2, in Glasgow Modified Eagle´s Medium (GMEM, Invitrogen) supplemented with 10% FBS (ES-Cell qualified), 10 mM MEM non-essential amino acids, 1% GlutaMAX, 1 mM 2-mercaptoethanol and 2 ng/mL Recombinant Human Leukemia Inhibitory Factor (LIF; serum/LIF conditions), on gelatin-coated (0.1% v/v) dishes (Nunc, Roskilde, Denmark). Cells were passaged on alternate days at a constant plating density of ≈3 x 10^4 cells/cm^2.

Camptothecin, RO-3306, 5-bromo-2´-deoxyuridine (BrdU), thymidine, propidium iodide (PI), 4',6-diamidino-2-phenylindole (DAPI) and RNase A were purchased from Sigma-Aldrich (St. Louis, MO, USA).

The following antibodies were used in this research: rabbit polyclonal to histone H2A.X (ab11175, Abcam, UK [39]), mouse monoclonal IgG1 to phospho-histone H2A.X (Ser139; clone JBW 301; Merck-Millipore, Darmstadt, Germany [40]), mouse monoclonal IgG1 to RPA32/RPA2 (clone 9H8; ab2175 Abcam, UK [41]), affinity-purified rabbit polyclonal to phospho-RPA32/RPA2 (Ser4/Ser8; Cat. A300-245A; Bethyl Laboratories, Montgomery, TX, USA [42]), mouse monoclonal antibodies to BrdU (clones BU-33 and BMC 9318; Sigma-Aldrich), affinity-purified Alexa 488-conjugated and Cy3-conjugated anti-mouse secondary antibodies (Jackson ImmunoResearch Laboratories, Sacramento,

CA, USA), and peroxidase-conjugated affinity-purified goat anti-mouse IgG and goat anti-rabbit IgG (BioRad Laboratories, Hercules, CA, USA).

EdU incorporation and detection for flow cytometry

EdU (5-ethynyl-2'-deoxyuridine), supplied with Click-iT EdU Alexa Fluor 488 Imaging Kit (#C10337, Thermo-Fisher Scientific, Waltham, MA, USA), was diluted in DMSO to a final concentration of 10 mM and kept at -20^{o}C. Typically, EdU was added to parallel cultures growing exponentially in 30 cm^2 petri dishes to final concentrations ranging from 2.5 to 30 μM for varying lengths of time until collection. Cells exposed to DMSO (solvent) alone served as controls. Cell pellets (approx. 5 x 10^5 cells) were vigorously resuspended in 200 μL of ice cold 2% formaldehyde in PBS and fixed for 2 min, permeabilized by subsequent addition of 1 mL of 70% ice-cold ethanol (without removal of formaldehyde), and kept on ice for a minimum of 10 min. Cells were then washed three times in 1 mL PBS containing 0.05% Triton X-100 (PBS-Tx) before detection of EdU-substituted DNA (EdU-DNA). Detection of EdU-DNA was performed according to the Click-iT EdU Alexa Fluor 488 Imaging Kit as per manufacturer's instructions. Cell pellets were incubated in 100 μl of reaction buffer for 35 min at 37°C protected from light. Cells were subsequently washed 4 X 10 min in 1 mL PBS-Tx 0.05% under constant shaking before staining of bulk DNA with PI or DAPI.

For PI staining, cell pellets were resuspended in 300 μL of a solution comprised of 10 μg/mL PI, 192 μg/mL RNase A and 0.1% Triton X-100 in PBS and incubated for 30 min on ice, followed by a further incubation for 30 min at 37°C, protected from light. For DAPI staining, cell pellets were resuspended in a solution of 1 μg/mL of DAPI in PBS containing 0.1% TritonX-100 and incubated protected from light for 1h at 37°C. Cells were washed three times in PBS-Tx before measuring their fluorescence by flow cytometry.

Flow cytometry instrumentation and data analysis

Samples stained for EdU, PI and DAPI were analyzed using a three laser (blue-488nm; red-640nm; violet-605nm) BD LSR Fortessa flow cytometer (BD Biosciences, San Jose, CA). EdU–Alexa 488 and PI signals were measured upon excitation by the blue laser using 530/30 and 695/40 bandpass filters, respectively. DAPI signals were measured upon

excitation by the violet laser with the 525/50 bandpass filter. A minimum of 30000 events were acquired per experiment in slow rate mode to avoid doublets. Sample measurements were performed with FACSDiva Software (Version 6.2, BD Biosciences, San Jose, CA, USA). Data analysis, such as mean fluorescence intensity (MFI) measurements, was performed with FlowJo Software (Ashland, OR, USA). Cell debris and aggregates were excluded from the analysis using pulse processing FSC-A *vs* FSC-H, FSC-H *vs* FSC-W, SSC-H *vs* SSC-W, and FL2-A *vs* Fl2-W when appropriate.

Immunofluorescence staining

For immunofluorescence analysis, HCT-116 cells growing on coverslips were routinely fixed in freshly prepared 3.7% paraformaldehyde in HPEM buffer (30 mM HEPES, 65 mM Pipes, 10 mM EGTA, 2 mM $MgCl_2$ (pH 6.9)) plus 0.5% Triton X-100 for 10 min at room temperature before incubation with antibodies. All washes were performed with PBS containing 0.05% Triton X-100. For detection of BrdU incorporated into replicating DNA, fixed cells were further incubated with 4N HCl for 10 min to depurinate DNA and washed four times for 10 min in Tris 50 mM (pH 8) preceding incubation with anti-BrdU antibodies. For the double labeling of BrdU and EdU immunostaining of BrdU preceded detection of EdU by the Click-iT method. Antibodies used for immunofluorescence were diluted in PBS containing fish skin gelatin (0.1%) and Triton X-100 (0.05%) as follows: anti-RPA32/RPA2 at 1/200, anti-phospho-histone H2A.X (Ser139) at 1/300, anti-BrdU at 1/100 and Cy3-conjugated anti-mouse secondary antibodies at 1/100. After immunolabeling, total DNA was stained with DAPI (0.5 μg/mL) and coverslips were mounted in Vectashield (Vector Laboratories Inc., Burlingame, CA, USA) before analysis by fluorescence microscopy.

Confocal microscopy

Samples were examined using a Zeiss 510 confocal microscope (Carl Zeiss, Jena, Germany) equipped with lasers giving excitation lines at 405, 488 and 543 nm. Data from the channels were collected separately using narrow-band-pass filter settings. In multiple staining experiments, the laser intensities were adjusted to avoid bleedthrough between channels. Data were collected with two- to fourfold averaging at resolution of 1024 X

1024 pixels using pinhole settings between 1.05 and 1.10 airy units. Data sets were processed using Zeiss 510 version 2.8 software package and were subsequently exported for preparation for printing using Adobe Photoshop, version CS5.1.

Other methods for estimation of cell cycle parameters

In the methods described below BrdU was administered either as a single pulse or in association with a second, distinct pulse with EdU (double-pulsing). Asynchronous cultures of HCT-116 cells were grown on glass coverslips before fixation and microscopic analysis.

To estimate the absolute durations of G2 and S phases HCT-116 cells were briefly pulsed with BrdU (10 μM, 15 min) and chased in BrdU-free medium for incremental periods of time from 3 to 11 h (1 h increments) before collection. Cells were then fixed in paraformaldehyde and immunostained for BrdU as described herein. After staining of DNA with DAPI (0.5 μg/mL) cell populations were scored for the presence of BrdU-positive mitotic cells under the fluorescence microscope (Olympus BX50). G2 length was estimated as the shorter chasing time that resulted in ≈50% of BrdU-labeled mitotic cells, and the duration of S phase as the interval of time during which ≥50% of mitotic cells displayed staining for BrdU [13,27].

Duration of the G1 plus G2 phases of the cell cycle was assessed using a cumulative (or saturation) labeling method [32]. Briefly, exponentially growing HCT-116 cells were continuously pulsed with BrdU (10 μM) for incremental periods from 1.5 h to 9 h (1.5 h increments) before collection. Cells were fixed in paraformaldehyde and immunostained for BrdU, and the percentage of BrdU-positive cells was scored for each time point. The duration of G1 + G2 stages was estimated as the minimum pulsing time required for ≈100% of the cells to become positive for BrdU [33].

To judge the absolute length of S phase we also used the so-called “leaving fraction” method [28,29]. To this end, HCT-116 cells were first pulsed with BrdU (10 μM, 15 min) and chased in BrdU-free medium for 75 min before exposure to a second pulse with EdU (15 μM, 15 min). Cells were then processed for the simultaneous detection of BrdU and EdU, as described here. The leaving fraction, corresponding to the fraction of cells that although initially in S phase – and thus BrdU-positive - have left S phase during the

chasing period (thus EdU-negative) was used for extrapolation of the length of S phase according to the formula: $BrdU^{positive}/BrdU^{positive}+ EdU^{negative}$ *X chase time (h) = Length of S (h)*.

Cell cycle synchronization

In order to synchronize exponentially growing HCT116 cells at G1/S phase transition, we used the double-thymidine block approach. Briefly, cells were incubated in culture medium containing thymidine at a final concentration of 2 mM for 12 h (1^{st} thymidine block), allowing time for cells to arrest in S phase. Thymidine was removed through repeated washes with fresh medium and cells were incubated with fresh thymidine-free medium for 7.5 h, to allow full exit from S phase. Cells were subsequently incubated with 2 mM thymidine for another 12 h (2^{nd} thymidine block) to obtain a population precisely arrested at the G1/S phase transition that will progress into S phase upon release from thymidine.

Metaphase spreads

Metaphase spreads were prepared as described [43]. EdU-substituted DNA was detected using the Click-iT assay exactly as described herein for flow cytometry except that the 100 µL of reaction buffer were applied per coverslip (4 cm^2). Total DNA was stained with DAPI (0.5 µg/mL) immediately before mounting in Vectashield and imaging by confocal microscopy.

Western blotting

For immunoblotting, cell lysates prepared in boiling 1X Laemmli´s sample buffer were supplemented with PMSF (1 mM) and a commercially available mixture of protease inhibitors (Complete Mini EDTA-free; Roche Diagnostics, Mannheim, Germany; 1 tablet/mL). DNA was first fragmented mechanically by passing the sample into a syringe (≈10 times) through a 25-gauge needle and, subsequently, after supplementation with $MgCl_2$ (5 mM), by digestion with benzonase (0.4 Units/ml; Sigma-Aldrich) for 30 min at room temperature. Lysates were then separated on 12 or 14% SDS-PAGE under reducing

conditions and transferred to nitrocellulose membranes (Schleicher & Schuel, Keene, NH). Membranes were blocked for 1 h with 5% nonfat dry milk powder in PBS and incubated for a minimum of 2 h with the specific primary and secondary antibodies. Antibodies used for immunoblotting were diluted in PBS supplemented with nonfat dry milk (2.5%) and Triton X-100 (0.05%) and used at the following dilutions: anti-phospho-RPA32/RPA2 (Ser4/Ser8; 1/2000), anti-RPA32/RPA2 (total RPA32; 1/1000), anti-phospho-histone H2A.X (Ser139; 1/1000), anti-histone H2A.X (total H2A.X; 1/1000), and peroxidase-conjugated affinity-purified goat anti-mouse and goat anti-rabbit were diluted at 1/3000. Total H2A.X provided loading controls. The detection reaction was developed by enhanced chemoluminescent (ECL) staining according to the specifications of the manufacturer (ECL Amersham, Western Blotting Detection Reagents, UK).

Alkaline comet assay

DNA strand breaks were measured using Trevigen Comet Assay kit (Trevigen Inc., Gaithersburg, MD, USA). Cells were resuspended in ice cold PBS (Ca^{2+} and Mg^{2+} free) to a concentration of 1×10^5 cells/ml. A 5 µl aliquot of cells was added to 50 µl of molten 1% low-melting agarose warmed to 37 °C. 50 µl were immediately pipetted and evenly spread onto the comet slides. Slides were incubated at 4°C in the dark for 10 min to accelerate gelling of the agarose disc and then transferred to prechilled lysis solution (2.5 M NaCl, 100 mM EDTA, 10 mM Tris-base, 1% sodium lauryl sarcosinate, 1% Triton X-100, pH 10) for 30 min at 4 °C. A denaturation step was performed in alkali solution (300 mM NaOH, 1 mM EDTA, pH > 13) at room temperature for 30 min in the dark. Slides were then transferred to prechilled alkaline electrophoresis solution pH > 13 (300 mM NaOH, 1 mM EDTA) and subjected to electrophoresis at 1 V/cm, 300 mA for 30 min in the dark at 4°C. Subsequently, the slides were washed with deionized water and immersed in 70% ethanol at room temperature for 5 min and air dried. DNA was stained with 100 µl of SYBR Green I dye (supplied with the kit) for 10 min at 4ºC in the dark and immediately analyzed using a CCD camera (Roper Scientific Coolsnap HQ CCD, Roper Technologies Inc., Sarasota, FA, USA) attached to a Zeiss Axiovert 200M wide field fluorescence microscope. For each slide, 100 randomly chosen comets were analyzed with an excitation filter of 450–490 nm and an emission filter of 515 nm. Images were scored for tail length and

percentage of DNA in tail using the Tritek CometScore Freeware v1.5 image analysis software (TriTek Corp., Sumerduck, VA, USA).

Statistical analysis

Data are reported as the mean ± SD. Results were compared by 2-tailed Student's t test for two groups and one-way ANOVA followed by Dunnett's multiple comparison test for multiple groups. GraphPad Prism version 5.03 for Windows (GraphPad Software, La Jolla, CA, USA) was used for statistical analysis. Differences were considered statistically significant at $P < 0.05$

When using incremental pulsing times with EdU in the context of EdU -Coupled-Fluorescence-Intensity analysis (E-CFI), the duration of S phase was estimated as the first time point after which maximal EdU-coupled fluorescence intensities clustered within 2 SDs from each other. Also in the context of E-CFI, total length of cell cycle was estimated from the lengths of G1, G2 and S phases by standard error propagation.

Author Contribution

Pedro Pereira and João Ferreira planned all experiments with additional input from other authors. Pedro Pereira and João Ferreira performed all laboratory experiments. Ana Serra-Caetano performed flow cytometry analysis. José Rino provided support with statistical analysis. Pedro Pereira and João Ferreira wrote the paper with input from other authors.

REFERENCES

[1] Hanahan D, Weinberg RA. Hallmarks of cancer: the next generation. Cell. 2011; 144:646–74.

[2] Krabbe LM, Margulis V, Lotan Y. Prognostic Role of Cell Cycle and Proliferative Markers in Clear Cell Renal Cell Carcinoma. Urol Clin North Am. 2016; 43:105–18.

[3] Beresford MJ, Wilson GD, Makris A. Measuring proliferation in breast cancer : practicalities and applications. Breast Cancer Res. 2006; 11:1–11.

[4] Duronio RJ. Developing S-phase control. Genes Dev. 2012; 26:746–50.

[5] Turrero García M, Chang Y, Arai Y, Huttner WB. S-phase duration is the main target of cell cycle regulation in neural progenitors of developing ferret neocortex. J Comp Neurol. 2016; 524:456–70.

[6] Rabinovitch P. Introduction to cell cycle analysis. Basics of DNA Cell Cycle Analysis. Phoenix Flow Systems, Inc; 1994.

[7] Pozarowski P, Darzynkiewicz Z. Analysis of cell cycle by flow cytometry. Methods Mol Biol. 2004; 281:301–11.

[8] Darzynkiewicz Z, Huang X. Analysis of Cellular DNA Content by Flow Citometry. Current Protocols in Immunology. 2004:5.7.1–5.7.18.

[9] Dressler LG. DNA Flow Cytometry Measurements as Surrogate Endpoints in Chemoprevention Trials : Clinical , Biological , and Quality Control Considerations. J Cell Biochem. 1993; 218:212–8.

[10] Baldetorp B, Bendahl PO, Ferno M, Alanen K, Delle U, Falkmer U, Hansson-Aggesjo B, Hockenstrom T, Lindgren A, Mossberg L, Nordling S, Sigurdsson H, et al. Reproducibility in DNA flow cytometric analysis of breast cancer: Comparison of 12 laboratories' results for 67 sample homogenates. Cytometry. 1995; 22:115–27.

[11] Mcfadden ML, Humphreys RE, Woda BA. Detection of 5-Bromo-2-Deoxyuridine (BrdUrd) Incorporation With Monoclonal Anti-BrdUrd Antibody After Deoxyribonuclease Treatment. Cytometry. 1993; 648:640–8.

[12] Cavanagh BL, Walker T, Norazit A, Meedeniya ACB. Thymidine analogues for

tracking DNA synthesis. Molecules. 2011; 16:7980–93.

[13] Quastler H, Sherman FG. Cell population kinetics in the intestinal epithelium of the mouse. Exp Cell Res. 1959; 17:420–38.

[14] Zou Y, Gryaznov SM, Shay JW, Wright WE, Cornforth MN. Asynchronous replication timing of telomeres at opposite arms of mammalian chromosomes. Proc Natl Acad Sci U S A. 2004; 101:12928–33.

[15] Schorl C, Sedivy JM. Analysis of Cell Cycle Phases and Progression in Cultured Mammalian Cells. Methods. 2007; 41:143–50.

[16] Hilchenbach M. The use of fluorescent probes in immunochemistry. Photochem Photobiol. 1990; 52:431–8.

[17] Banfalvi G. Cell Cycle Synchronization. In: Banfalvi G (ed.), Cell Cycle Synchronization, vol. 761. Totowa, NJ: Humana Press; 2011.

[18] Salic A, Mitchison TJ. A chemical method for fast and sensitive detection of DNA synthesis in vivo. Proc Natl Acad Sci U S A. 2008; 105:2415–20.

[19] Diermeier-Daucher S, Clarke ST, Hill D, Vollmann-Zwerenz A, Bradford J a, Brockhoff G. Cell type specific applicability of 5-ethynyl-2'-deoxyuridine (EdU) for dynamic proliferation assessment in flow cytometry. Cytometry A. 2009; 75:535–46.

[20] Ferreira J, Paolella G, Ramos C, Lamond AI. Spatial organization of large-scale chromatin domains in the nucleus: A magnified view of single chromosome territories. J Cell Biol. 1997; 139:1597–610.

[21] Camps J, Wangsa D, Falke M, Brown M, Case CM, Erdos MR, Ried T. Loss of lamin B1 results in prolongation of S phase and decondensation of chromosome territories. FASEB J. 2014; 28:3423–34.

[22] Bhatia A, Kumar Y. Cancer cell micronucleus: an update on clinical and diagnostic applications. APMIS. 2013; 121:569–81.

[23] Rogakou EP, Pilch DR, Orr a H, Ivanova VS, Bonner WM. DNA double-stranded breaks induce histone H2AX phosphorylation on serine 139. J Biol Chem. 1998; 273:5858–68.

[24] Ross HH, Rahman M, Levkoff LH, Millette S, Martin-Carreras T, Dunbar EM,

Reynolds B a., Laywell ED. Ethynyldeoxyuridine (EdU) suppresses in vitro population expansion and in vivo tumor progression of human glioblastoma cells. J Neurooncol. 2011; 105:485–98.

[25] White J, Dalton S. Cell cycle control of embryonic stem cells. Stem Cell Rev. 2005; 1:131–8.

[26] Kohlmeier F, Maya-Mendoza A, Jackson D a. EdU induces DNA damage response and cell death in mESC in culture. Chromosome Res. 2013; 21:87–100.

[27] Rajewsky MF. Proliferative parameters of mammalian cell systems and their role in tumor growth and carcinogenesis. Zeitschrift Fur Krebsforsch Und Klin Onkol. 1972; 78:12–30.

[28] Takahashi T, Nowakowski RS, Caviness VS. Mode of cell proliferation in the developing mouse neocortex. Proc Natl Acad Sci U S A. 1994; 91:375–9.

[29] Martynoga B, Morrison H, Price D, Mason J. Foxg1 is required for specification of ventral telencephalon and region-specific regulation of dorsal telencephalic precursor proliferation and apoptosis. Dev Biol. 2005:113–27.

[30] Yamada K. Discrimination of Cell Nuclei in Early S-phase, Mid-to-late S-phase, and G2/M-phase by Sequential Administration of 5-Bromo-2'-Deoxyuridine and 5-Chloro-2'-Deoxyuridine. J Histochem Cytochem. 2005; 53:1365–70.

[31] Nowakowski RS, Lewin SB, Miller MW. Bromodeoxyuridine immunohistochemical determination of the lengths of the cell cycle and the DNA-synthetic phase for an anatomically defined population. J Neurocytol. 1989; 18:311–8.

[32] Takahashi T. Cell cycle parameters and patterns of nuclear movement in the neocortical proliferative zone of the fetal mouse. J Neurosci. 1993:820–33.

[33] Yuasa S, Nakajima M, Aizawa H, Sahara N, Koizumi KI, Sakai T, Usami M, Kobayashi SI, Kuroyanagi H, Mori H, Koseki H, Shirasawa T. Impaired cell cycle control of neuronal precursor cells in the neocortical primordium of presenilin-1-deficient mice. J Neurosci Res. 2002; 70:501–13.

[34] Nunez R. DNA measurement and cell cycle analysis by flow cytometry. Curr Issues Mol Biol. 2001; 3:67–70.

[35] Raventos-Suarez C, Long B. A multiparameter approach to cell cycle analysis as a

standard tool in oncology drug discovery. Flow Cytometry in Drug Discovery and Development. 2011:99–122.

[36] Vignon C, Debeissat C, Georget MT, Bouscary D, Gyan E, Rosset P, Herault O. Flow Cytometric Quantification of All Phases of the Cell Cycle and Apoptosis in a Two-Color Fluorescence Plot. PLoS One. 2013; 8:1–8.

[37] Hang H, Fox MH. Analysis of the mammalian cell cycle by flow cytometry. Methods Mol Biol. 2004; 241:23–35.

[38] Massey AJ. Multiparametric cell cycle analysis using the operetta high-content imager and harmony software with PhenoLOGIC. PLoS One. 2015; 10:1–16.

[39] Dawson M a, Bannister AJ, Göttgens B, Foster SD, Bartke T, Green AR, Kouzarides T. JAK2 phosphorylates histone H3Y41 and excludes HP1alpha from chromatin. Nature. 2009; 461:819–22.

[40] Smith-Roe SL, Nakamura J, Holley D, Chastain PD 2nd, Rosson GB, Simpson DA, Ridpath JR, Kaufman DG, Kaufmann WK, Bultman SJ. SWI/SNF complexes are required for full activation of the DNA-damage response. Oncotarget. 2015; 6:732–45.

[41] Ciccia A, Bredemeyer AL, Sowa ME, Terret ME, Jallepalli P V., Harper JW, Elledge SJ. The SIOD disorder protein SMARCAL1 is an RPA-interacting protein involved in replication fork restart. Genes Dev. 2009; 23:2415–25.

[42] King C, Diaz HB, McNeely S, Barnard D, Dempsey J, Blosser W, Beckmann R, Barda D, Marshall MS. LY2606368 causes replication catastrophe and anti-tumor effects through CHK1-dependent mechanisms. Mol Cancer Ther. 2015; 14:2004–14.

[43] Earnshaw WC, Ratrie H, Stetten G. Visualization of centromere proteins CENP-B and CENP-C on a stable dicentric chromosome in cytological spreads. Chromosoma. 1989; 98:1–12.

FIGURES

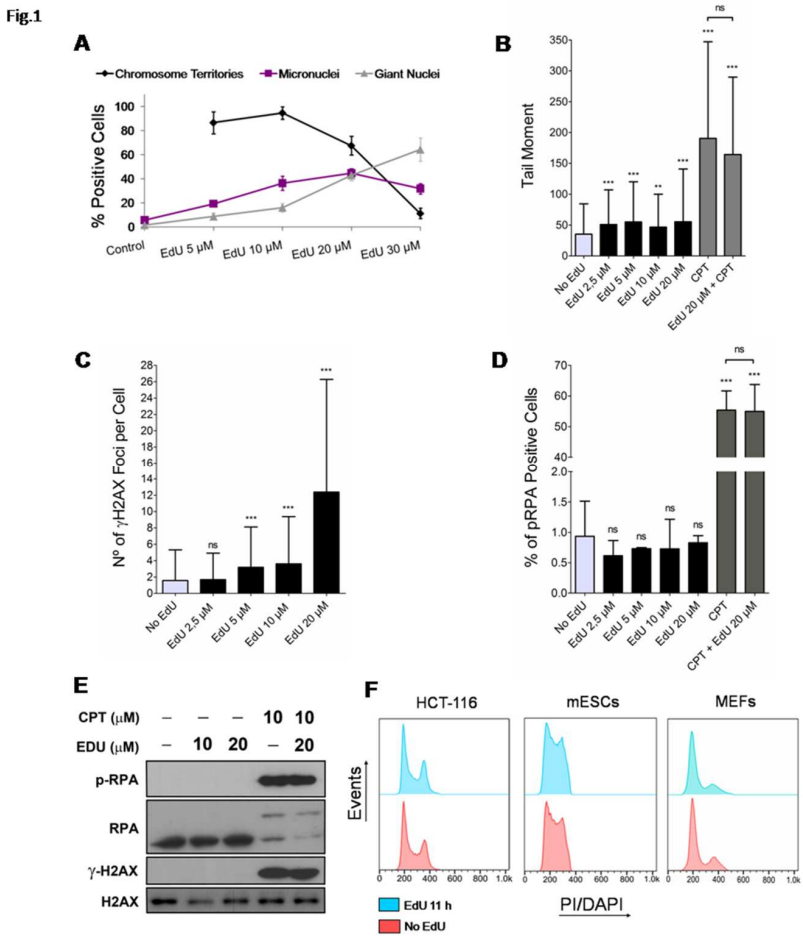

FIGURE 1 Effects of EdU on genomic instability, DNA damage and cell cycle progression. (**A**) Synchronized HCT-116 cells exposed for a single full S phase (7 h) to different concentrations of EdU (5, 10, 20 and 30 µM; controls exposed to solvent/DMSO alone) and analyzed 5 days later for the presence of chromosome territories, micronuclei and giant nuclei. Note that chromosome territories cannot be formally assessed in controls not exposed to EdU. (**B**) HCT-116 cells exposed for 11 h to EdU (2.5, 5, 10 and 20 µM; negative controls exposed to DMSO) or CPT (positive control; +/- EdU 20 µM) and analyzed by alkaline single-cell gel electrophoresis (comet assay; parameter: tail moment). (**C**) HCT-116 exposed to EdU (11 h) as above and analyzed for the presence of γH2AX nuclear foci by immunofluorescence. (**D**) HCT-116 exposed to EdU (11 h) or CPT (+/- EdU 20 µM) as above and analyzed by immunofluorescence for the presence of nuclear foci concentrating RPA. (**E**) Western blots of cells exposed to EdU (11 h; +/- CPT; negative controls exposed to DMSO) and probed for phospho-RPA, RPA, γH2AX and H2AX. H2AX provides loading controls. (**F**) Flow cytometry histograms of HCT-116 cells and mESCs (PI staining), and MEFs (DAPI staining) either exposed to EdU for 11 h (HCT-116: 10 µM; mESCs: 2.5 µM; MEFs: 5 µM; blue) or not (controls; red). Results for all figures are presented as mean + SD; ***: $p<0.001$; **: $p<0.01$; ns: $p>0.05$.

Fig.2

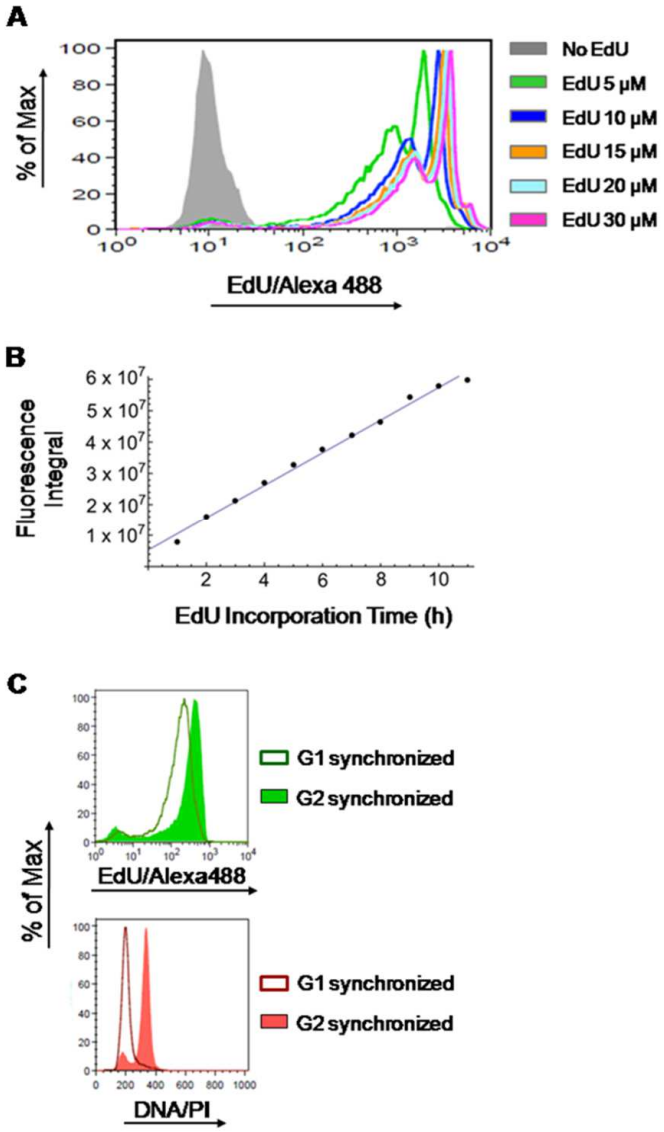

FIGURE 2 Stoichiometry of detection of EdU-labeled DNA. (**A**) HCT-116 cells were exposed to different concentrations of EdU (5, 10, 15, 20 and 30 µM) or DMSO (controls) for 9 h followed by detection of EdU-DNA by Click-iT chemistry (Alexa Fluor 488). (**B**) HCT-116 cells exposed to a fixed concentration of EdU (10 µM) for incremental periods of time (1 to 11 h; 1 h increments) before detection of EdU-DNA by Click-iT chemistry. Results are expressed as an integral (sum of fluorescence intensities above background levels) for each time point. (**C**) Synchronized HCT-116 cells were allowed to incorporate EdU for a single full S phase and collected while traversing G2 stage, and later after passage into G1 stage of the next cell cycle. Histograms from cells stained for EdU-DNA (Click-iT; Alexa 488; green) and bulk DNA (PI staining; red) are depicted. Note that the EdU-coupled fluorescence peak of G1-synchronized cells (MFI: 212) has ≈48% of the intensity of the peak resulting from G2-synchronized cells (MFI: 443).

Fig.3

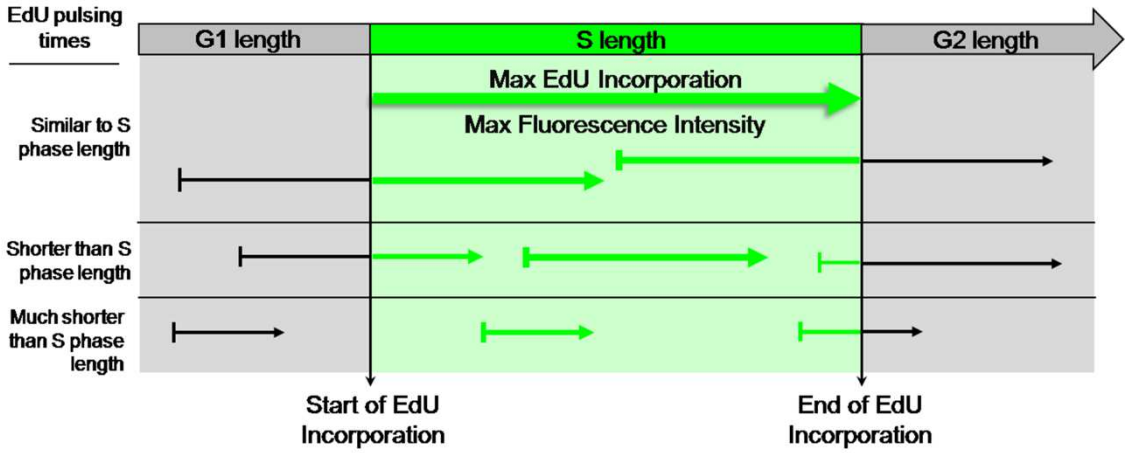

FIGURE 3 EdU-coupled Fluorescence Intensity analysis – the principle. Arrows represent pulsing times of different lengths with EdU. Fluorescence intensities are denoted by thickness of arrows. Note that cells in asynchronous populations are placed at any of many possible positions of the cell cycle upon exposure to the EdU pulse. Duration of S phase is probed by pulsing cells with EdU for defined, incremental periods of time. When pulsing times match the duration of S phase the cohort of cells that, by chance, at the beginning of the pulse are initiating S phase will incorporate EdU for a full S phase. This cell population shall thus feature maximal EdU-coupled fluorescence intensity. Increasing pulsing times beyond the duration of S phase shall not increase maximal fluorescence intensities but just the percentage of cells displaying intensity maxima. Duration of S phase is thus estimated from the minimal pulsing time with EdU that elicits emergence of a population featuring maximal fluorescence intensity. Clearly, pulsing times shorter than S phase length shall not allow reaching maximal intensities. In this assay the time variable is introduced by pulsing times of defined duration and the key parameter is fluorescence intensity, not the fraction of labeled cells.

Fig.4

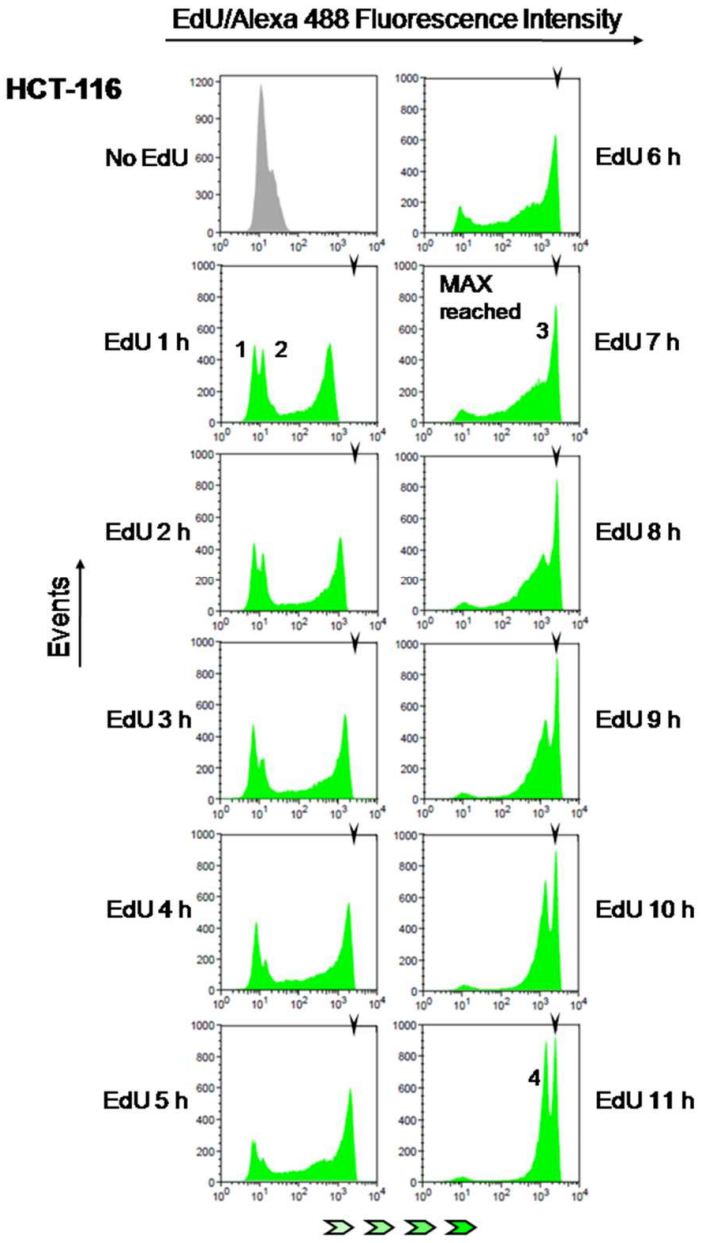

FIGURE 4 Estimation of S phase duration. HCT-116 cells were exposed to EdU (10 µM) for 1 to 11 h (1 h increments) followed by detection of EdU-DNA by Click-iT chemistry (Alexa 488) and analysis by flow cytometry. EdU-coupled fluorescence intensities are displayed along the x axis in logarithmic scale. Arrowheads denote the mean fluorescence intensity (MFI) reached by maximally labeled cell populations that incorporated EdU for a full S phase (peak **3**; MFI: 2677). Background peaks **1** and **2** correspond to, respectively, G1 and G2 cells that have not yet incorporated EdU. Note that peak **4** stemming from maximally labeled cells that reached G1 stage of the subsequent cell cycle features ≈1/2 the mean intensity of peak 3 (MFI: 1430, ≈53% of peak 3). Histograms are representative of one out of twelve independent experiments. Minimum number of analyzed events was 30000 per time point.

Fig.5

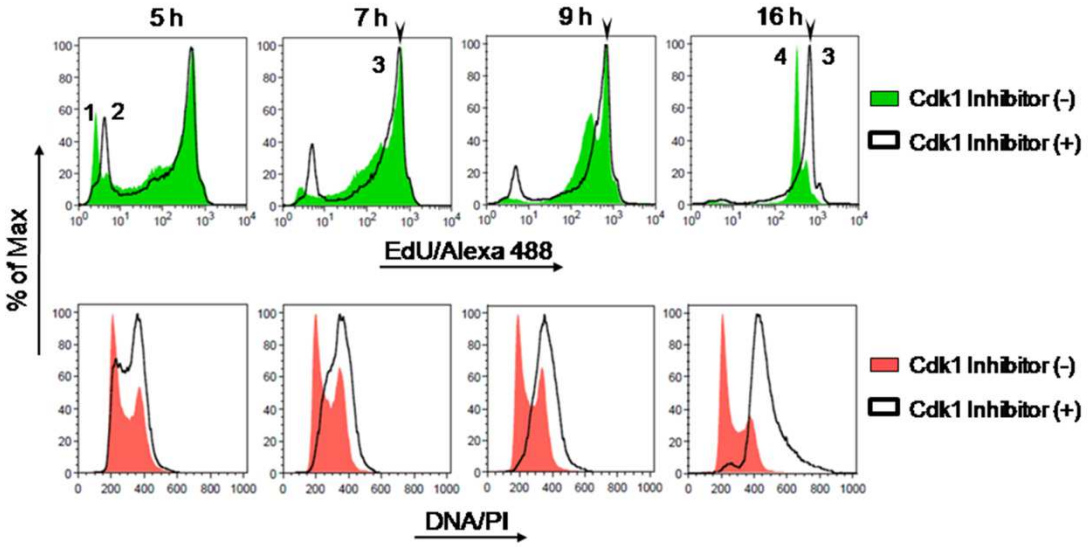

FIGURE 5 Intensity maxima of EdU-coupled fluorescence correspond to labeling for a single full S phase. Asynchronous HCT-116 cells pulsed with EdU (10 µM) +/- Cdk inhibitor (RO-3306; 10 µM) and collected at defined time points (5, 7, 9 and 16 h) were analyzed by flow cytometry. Detection of EdU-DNA was done with Click-iT chemistry (Alexa 488; green) and total DNA was stained with PI (red). Fluorescence peak **1** corresponds to G1 background; peak **2** to G2 background; peak **3** to maximal intensity coupled to cells maximally labeled for EdU-DNA (MFI: 671); and peak **4** to half-maximal intensity associated to cells that reached G1 stage of the next cell cycle (RO-3306-minus group, MFI: 345). Note that maximal fluorescence intensities are similar irrespectively of the presence of RO-3306, and that peak 4 is absent from cells arrested in G2 by RO-3306.

Fig.6

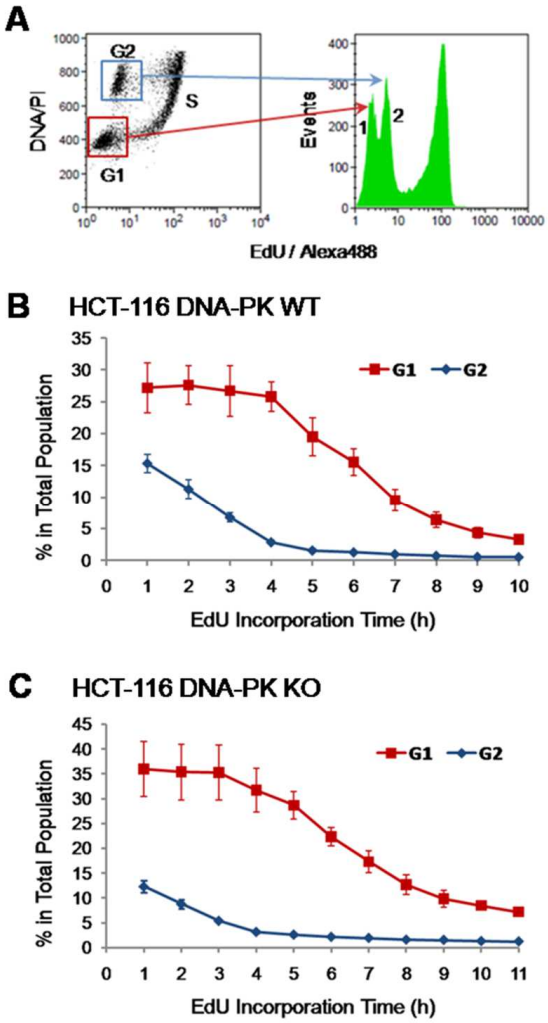

FIGURE 6 Identity of background intensity peaks. (**A**) HCT-116 cells exposed for 1 h to EdU (10 µM) were stained for EdU-DNA (Click-iT; Alexa 488; green) and total DNA (PI) and subjected to dual-parameter processing (EdU *vs* total DNA). Gating for G1 and G2 populations and superimposing their fluorescence profiles with those of the entire cell population reveals the identity of the two background peaks. Note that the G1 peak (red frame) overlaps with background peak **1** and that the G2 peak (blue frame) overlaps with background peak **2**. (**B**) HCT-116 cells were exposed to EdU (10 µM) for incremental pulsing times (1-10 h) according to the E-CFI protocol. The corresponding background peaks were decomposed in their constituent G1 (red line) and G2 (blue line) populations which were quantified over time. Data shown are from 5 independent experiments. (**C**) HCT-116 cells (DNA-PK KO) and the corresponding background peaks were processed as above for DNA-PK wt HCT-116 cells. Data shown are from 4 independent experiments. Results in B and C are presented as mean + SD.

Fig.7

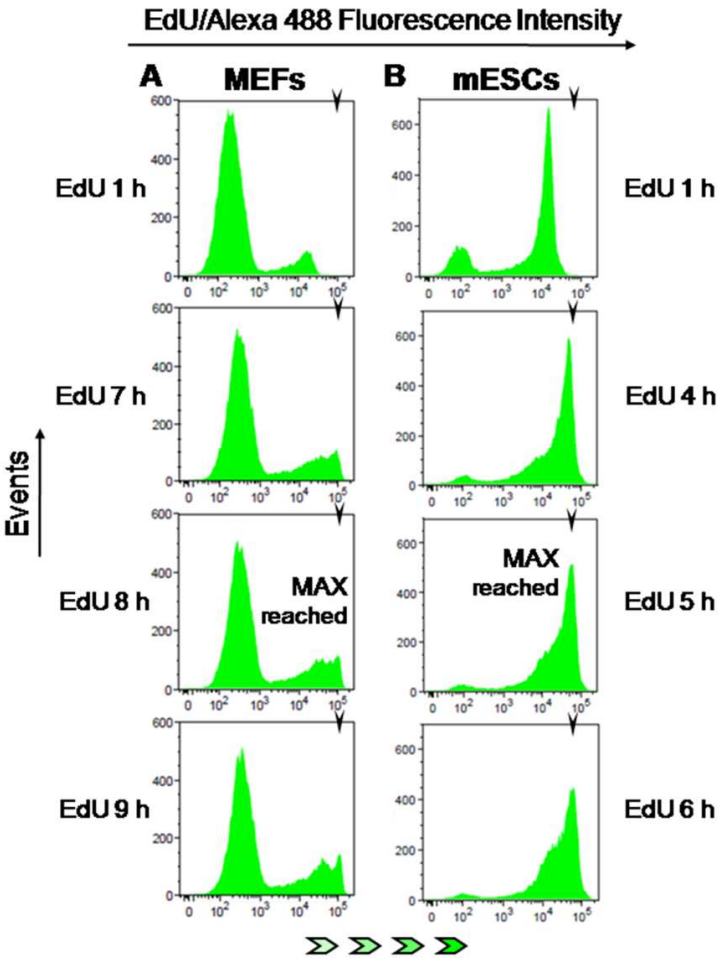

FIGURE 7 EdU-coupled fluorescence intensity analysis in non-transformed mouse cells. Arrowheads denote the mean fluorescence intensity (MFI) reached by maximally labeled cell populations that incorporated EdU for a full S phase. EdU-coupled fluorescence intensities are displayed along the x axis in logarithmic scale. (**A**) MEFs were pulsed with EdU (5 µM) for 1 to 11 h (1 h increments) followed by detection of EdU-DNA by Click-iT chemistry (Alexa 488) and analysis by flow cytometry. Only select pulsing times are shown. Note that maximal fluorescence intensity is reached at 7-8 h. (**B**) Mouse ESCs were pulsed with EdU (2.5 µM) and processed as above. Maximal fluorescence intensity is reached at 5 h.

Fig.8

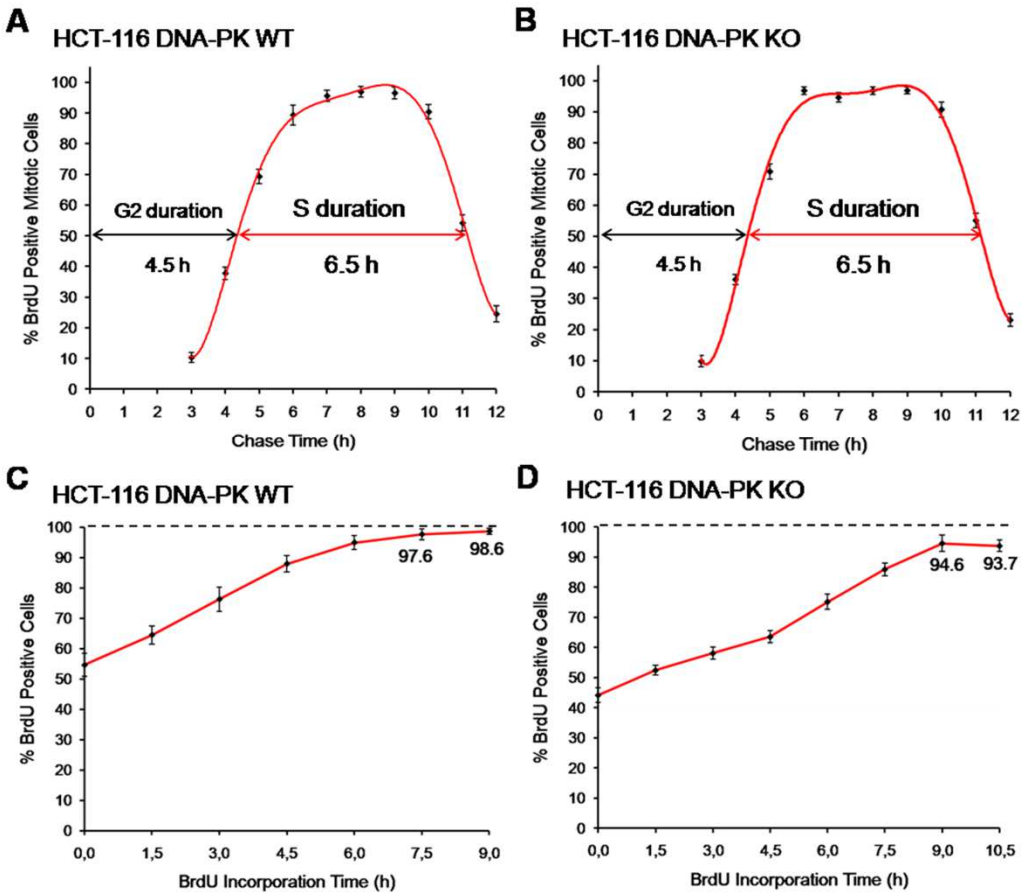

FIGURE 8 Comparison with other methods of cell cycle analysis. (**A**) Fraction of labelled mitoses, HCT-116 cells. Cells were briefly pulsed with BrdU (20 µM; 15 min) and collected hourly up until 12 h after pulsing. The fraction of BrdU-positive mitotic cells was assessed per time point. Three independent experiments were performed per time point, each scored in technical triplicates; a minimum of 300 mitotic cells were counted per technical triplicate. (**B**) Fraction of labelled mitoses, HCT-116 DNA-PK KO cells. Cells were processed and scored as above for HCT-116 DNA-PK wt cells. Shown are results from three independent experiments. (**C**) Cumulative labeling, HCT-116 cells. Asynchronous HCT-116 cells were pulsed with BrdU (10 µM) for incremental periods (1.5 to 9 h; 1.5 h increments). Three independent experiments were performed per time point, each scored in technical triplicates; a minimum of 600 cells were counted per technical triplicate. (**D**) Cumulative labeling, HCT-116 DNA-PK KO cells. Cells were processed and scored exactly as in C, except that continuous pulsing with BrdU was extended to 10.5 h. Shown are results from three independent. All results are presented as mean + SD.

TABLE

Table 1. Comparison of estimates for cell cycle phase length obtained for HCT-116 DNA-PK WT and HCT-116 DNA-PK KO through different methodologies.

HCT-116 DNA-PK WT					
Method	**G1**	**G2**	**G1+G2**	**S**	**Tc**
EdU-coupled Fluorescence Intensity (E-CFI)	3-4 h	4-5 h	≈8 h	≈7 h	14-15 h
Fraction of Labeled Mitotic cells (FLM)		≈4.5 h		≈6.5 h	
Cumulative Labeling			≈7.5 h (EdU^+ cells: 97.6 ± 1.8%)		
Leaving Fraction				6.3 ± 0.4 h	
EdU pulse-chase		4-6 h		6-8 h	
DNA Content (Dean Jett Fox cell cycle algorithm)*	4.8 ± 0.7 h	3.9 ± 0.6 h		5 ± 1.2 h	
DNA Content (Watson Pragmatic cell cycle algorithm)*	4.3 ± 0.6 h	4.1 ± 2.5 h		6.7 ± 2 h	
HCT-116 DNA-PK KO					
Method	**G1**	**G2**	**G1+G2**	**S**	**Tc**
EdU-coupled Fluorescence Intensity (E-CFI)	4-5 h	4-5 h	≈9 h	≈7 h	15-16 h
Fraction of Labeled Mitotic cells (FLM)		4-5 h		≈6.5 h	
Cumulative Labeling			≈9 h (EdU^+ cells: 94.6 ± 2.8%)		
EdU pulse-chase		4-6 h		6-8 h	

***** Estimated cell phase durations are derived from the percentage of cells in each cell cycle stage calculated using cell cycle analysis algorithms within FlowJo software, assuming a total cell cycle length of 15 h. **Tc:** Total length of cell cycle.

SUPPLEMENTAL DATA

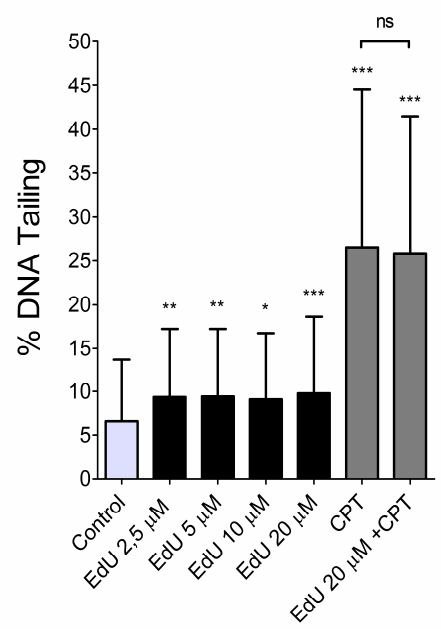

FIGURE S1 DNA damage induced by EdU – comet assay. HCT-116 cells exposed for 11 h to EdU (2.5, 5, 10 and 20 µM; negative controls exposed to DMSO) or CPT (positive control; +/- EdU 20 µM) and analyzed by alkaline single-cell gel electrophoresis (comet assay; parameter: percentage of DNA in tail). Results are presented as mean + SD; ***: $p<0.001$; **: $p<0.01$; *: $p<0.05$; ns: $p>0.05$.

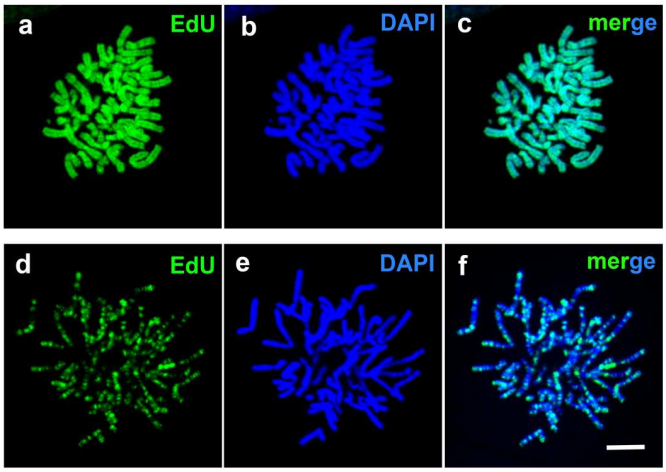

FIGURE S2 Metaphase spreads after full and partial S phase labeling. (**a**, **b** and **c**) Synchronized HCT-116 cells (double-thymidine block) were pulsed with EdU (10 µM; 7 h) for a full S phase before harvesting in M phase. Metaphase spreads were stained for (**a**) EdU (Click-iT; Alexa 488; green) and (**b**) DNA (DAPI; blue); (**c**) merge of EdU and DAPI staining. Note labeling for EdU across the entire length of chromosome arms. (**d**, **e** and **f**) HCT-116 cells synchronized as above were allowed to progress 4 h into S phase and briefly pulsed with EdU (15min, 10 µM) before harvesting in M phase. Metaphase spreads were stained for (**d**) EdU and (**e**) DNA, as above; (**f**) merge of both channels. Note discontinuous (banded) labeling for EdU. Bar: 10 µm.

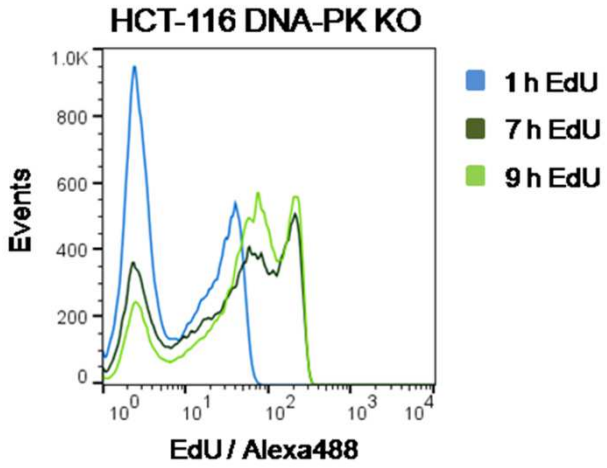

FIGURE S3 Estimation of S phase length in HCT-116 DNA-PK KO cells using E-CFI. Asynchronous HCT-116 DNA-PK KO cells cells were exposed to EdU (10 µM) for 1 to 11 h (1 h increments) followed by detection of EdU-DNA using Click-iT chemistry (Alexa 488) and analysis by flow cytometry. Fluorescence intensities after 1 h (blue), 7 h (dark green) and 9 h (light green) of EdU incorporation are depicted along the x axis in logarithmic scale (other pulsing times not shown). Note that the 7 h and 9 h time points share identical maxima of EdU-coupled fluorescence intensity.

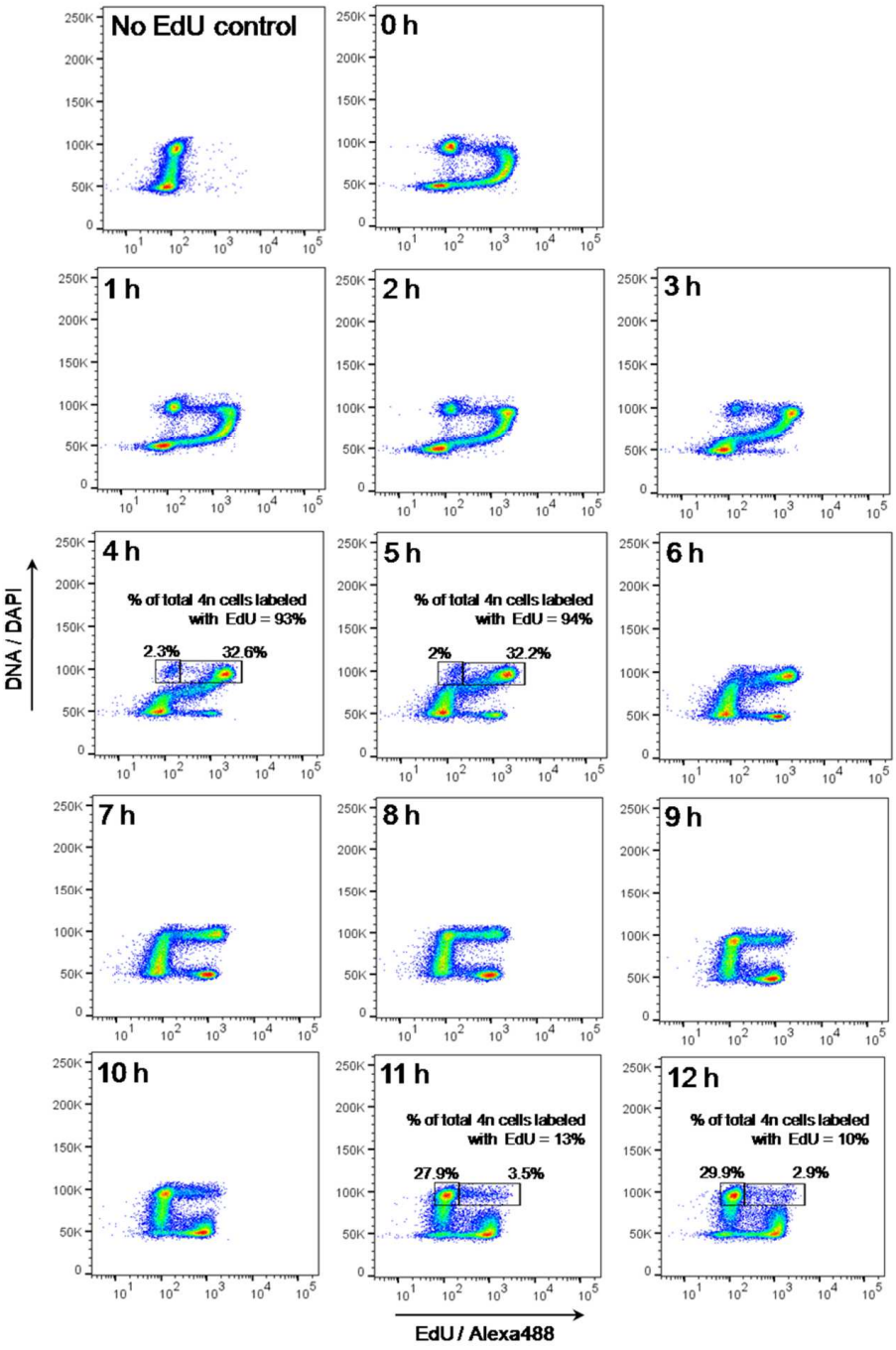

FIGURE S4 Dual parameter histograms (EdU *vs* total DNA) after EdU pulse-chase. Asynchronous HCT-116 cells pulsed with EdU (10 μM; 30 min) were either collected immediately after pulsing (0 h) or else chased for the indicated times (1-12 h) before collection. EdU-DNA was detected using Click-iT chemistry (azide-Alexa 488); total DNA was stained with DAPI before dual-parameter processing (EdU *vs* total DNA). Controls comprise EdU-minus cells that were exposed to azide-Alexa 488 (EdU detection system) before staining with DAPI (No EdU control). Selected events (within boxes) in chase times 4 and 5 h, and 11 and 12 h denote populations with 4n DNA that are either EdU-negative (left) or EdU-positive (right). The corresponding percentages within the whole cell population are denoted. Also denoted are the percentages of 4n DNA cells that are EdU-positive within the whole 4n DNA population. Data from a single experiment are shown.

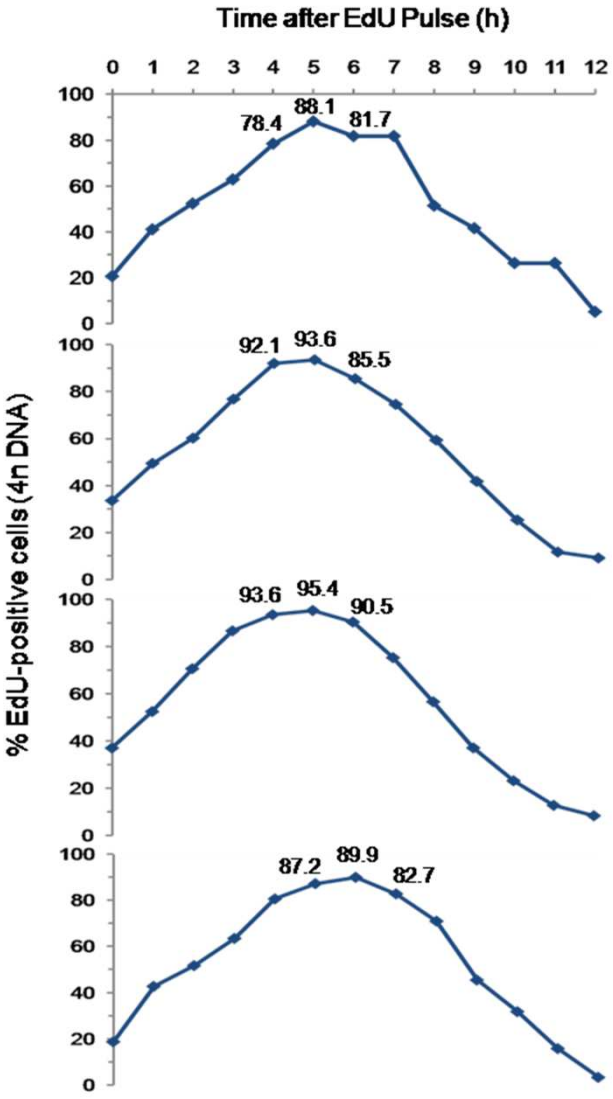

FIGURE S5 Fraction of EdU-labeled cells harboring 4n DNA over time – single experiments. Asynchronous HCT-116 cells pulsed with EdU (10 µM; 30 min) were collected immediately after pulsing (0 h) and for the indicated times (1-12 h) thereafter. Shown at defined times after EdU pulsing are the percentages of cells with 4n DNA content that are labeled for EdU; numbers above the curves denote the highest percentages of EdU-positive cells. Data were extracted from dual-parameter histograms after detection of EdU-DNA using Click-iT chemistry (azide-Alexa 488) and staining total DNA with PI. Data shown are from four independent experiments.

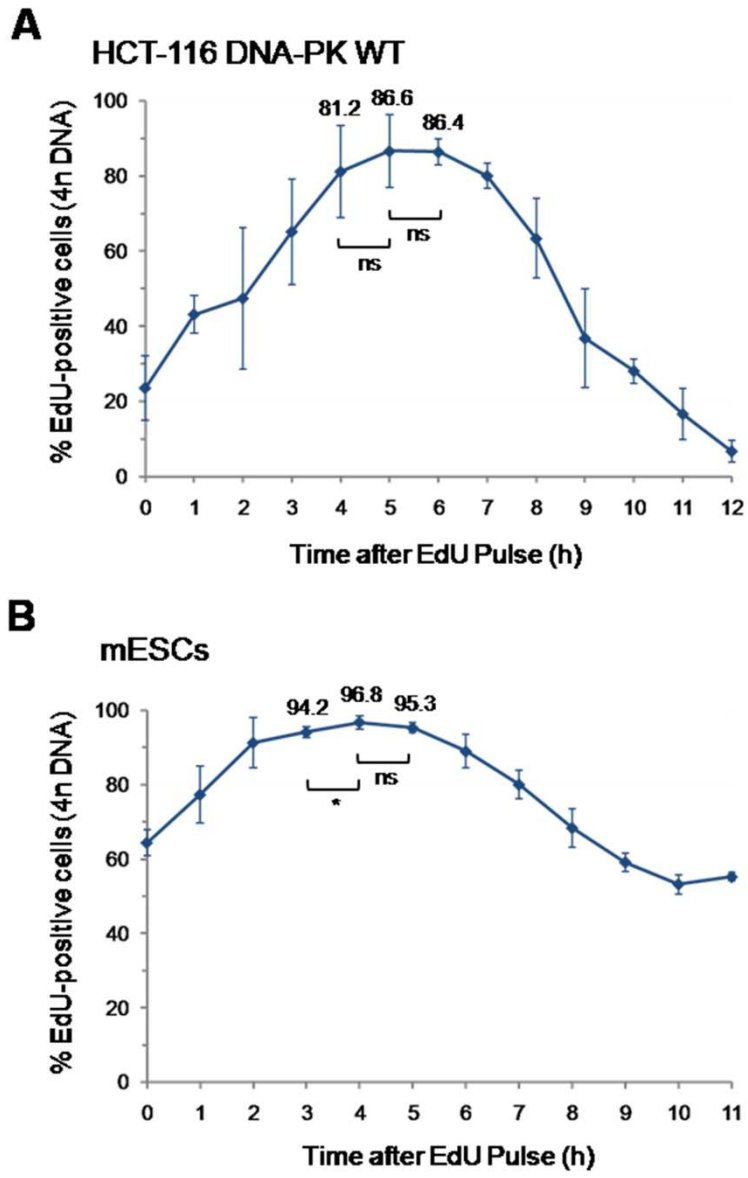

FIGURE S6 Fraction of EdU-labeled cells harboring 4n DNA over time – pooled data. (**A**) Asynchronous HCT-116 cells were pulsed with EdU (10 µM; 30 min) and collected at the indicated times (0-12 h). Dual-parameter histograms (EdU/DNA *vs* total DNA/PI) were used to distinguish cells with 4n DNA content that incorporated EdU. Represented over time are the percentages of cells with 4n DNA content that are EdU-positive. (**B**) mESCs were pulsed with EdU (5 µM; 30 min) and processed as above. Results are presented as mean + SD from four independent experiments per cell line. Values for maximal percentages are presented above time points. 2-tailed Student's t test was used to compare neighboring time points; *: $p<0.05$; ns: $p>0.05$.

Supplemental Table 2. Comparison of estimates for cell cycle phase length calculated for HCT-116 DNA-PK WT (DAPI stained, 3 independent experiments, mean + SD) using two different cell cycle analysis algorithms.

Cell Cycle Algorithm	G1	G2	S
Dean Jett Fox			
Population percentage	32.3 ± 5 %	25.9 ± 4.2 %	33.5 ± 8.3 %
Estimated length*	4.8 ± 0.7 h	3.9 ± 0.6 h	5 ± 1.2 h
Watson Pragmatic			
Population percentage	28.9 ± 4.3 %	27.5 ± 16.5 %	44.9 ± 7.9 %
Estimated length*	4.3 ± 0.6 h	4.1 ± 2.5 h	6.7 ± 1. 2 h

***** Estimated cell phase durations are derived from the percentage of cells in each cell cycle stage calculated using cell cycle algorithms within FlowJo software, assuming a total cell cycle length of 15 h.

Chapter 5

General Discussion

5. General discussion

Topoisomerase II (Topo2) poisons are already extensively used in cancer therapy strategies, although most studies on cellular response to DNA damage, along with long-term consequences, have relied on ionizing radiation (IR) to generate DNA damage (Deckbar, Jeggo, & Löbrich, 2011; Ikura et al., 2007; Kakarougkas et al., 2013; Suzuki, Suzuki, Kodama, & Watanabe, 2006). IR can induce several types of DNA lesions in an indiscriminate manner across the whole genome including cross-links, modified bases and abasic sites, as well as single- and double-strand breaks. DSBs generated by IR often display "messy" DNA ends with deletions and loss of sequence homology (Nikitaki et al., 2016; Sankaranarayanan & Wassom, 2005). Topo2 poisons, on the other hand, generate protein-DNA complexes that require the enzyme securing the break to first be removed, leaving behind "clean" DSBs with high DNA end homology (McClendon & Osheroff, 2007). Another important difference between IR- and Topo2-induced lesions is that Topo2 function requires unobstructed access to DNA, suggesting that chromatin condensation could potentially influence the sensitivity of certain chromatin regions to this type of DNA damage. As such, the cellular response to the particular type of DSBs introduced by Topo2 is necessarily different from IR-induced lesions but more studies are needed to detail how this may translate into different outcomes post cancer therapy.

One of the aims of the present work was to clarify how each of the two main DSB repair pathways, non-homologous end joining (NHEJ) and homologous recombination (HR), contributes to repair of Topo2-mediated DSBs introduced in separate cell cycle phases. The results obtained in synchronized HCT116 cells damaged using the Topo2 poison Etoposide in G1, early S, late S or G2 cycle stages revealed that, while the respective damage checkpoints of each phase are activated in response to the drug insult, there is substantial passage of cells with above-basal levels of DSBs to subsequent cell cycle phases. While this goes against the generalized idea that full repair of DNA lesions needs to occur after cell cycle arrest for the cell cycle to resume, this phenomenon is well characterized in yeast and is known as checkpoint adaptation (Paulovich, Toczyski, & Hartwell, 1997). It has been proposed that checkpoints have in wired mechanisms for

their overcoming after a certain time independently of DNA repair. The G2/M checkpoint is the best understood in this regard, as it has been shown that Cdk2 levels during arrest are finely regulated to be low enough to suppress Cdk-driven transcriptional activation of genes promoting mitotic entry, but retain sufficient expression to be able to drive an eventual recovery from arrest (Shaltiel, Krenning, Bruinsma, & Medema, 2015). Indeed, checkpoint adaptation might be an evolutionarily conserved process necessary for cells to maintain the ability to exit from permanent arrest caused by high levels of DNA damage to potentially undergo genetic changes that may give them a selective advantage. The fact that this phenomenon has also been observed in non-transformed cell lines - since there is a clear advantage for cancer cells to lose checkpoint regulation (Alvarez-Fernández & Medema, 2010) - supports this proposition.

By comparing cell cycle and protein immunoblotting results, a diverging pattern of DSB repair system usage was found between lesions introduced in different cell cycle stages. The G1/S checkpoint has been described as taking 4 to 6 hours to initiate in response to irradiation damage (Deckbar et al., 2011) and this also appears to be true for Topo2-mediated DSBs. Cells damaged in G1 showed a strong activation of RPA2 starting at 3 hours after introduction of DSBs. Phosphorylation of RPA2 correlates with DNA end-resection, a step that occurs early during HR, which requires cells to be in S or G2 phase (Scully & Xie, 2013). Afterwards, at 8h, an arrest in G1 was observable by the separation of cells into G1 and S subpopulations. This suggests that the large fraction of G1-damaged cells that progress into S phase are predominantly repaired by HR, since the G1/S checkpoint did not activate in time to allow NHEJ to work. On the other hand, in G2-damaged cells that could potentially take more advantage of HR than G1 cells, a substantial increase in levels of phosphorylated RPA2, which highlights ongoing HR, was not observed. In fact, these cells relied instead on NHEJ for DSB repair, as indicated by phosphorylation of DNAPKcs, a central factor in NHEJ. This is in accordance with previous studies using ionizing radiation that point to NHEJ as the major DSB repair system in G2 (Beucher et al., 2009).

We also show that cells damaged in the beginning of S phase do not elicit a significant RPA2 activation compared to late-S-damaged cells. This provides evidence that DSBs in euchromatin (EC) are preferentially repaired by NHEJ, but DSBs within

heterochromatin (HC) require HR. Replication of EC takes place in early S phase while HC regions only replicate towards the end of the phase (Folle, 2008). This means that Etoposide-poisoned Topo2, which is particularly active during replication since Topo2 is required to unwind the DNA to allow for replication fork progression, will predominantly cleave replicating EC in early S and replicating HC in late S. The behaviour of RPA2 in respect to lesions introduced in late S instead of G2 was also surprisingly different. Late-S-damaged cells triggered RPA2 activation at 24h during their subsequent arrest in G2, whereas for G2-damaged cells, as mentioned before, the requirement for HR was less obvious. This indicates that HR in G2 is devoted specifically towards the repair of DNA damage in HC.

The interplay between the two key regulators of DSB repair system choice, BRCA1 and 53BP1, has been well detailed in recent years (Daley & Sung, 2014; Kakarougkas et al., 2013). Loss of BRCA1 is described as leading to 53BP1 recruitment to DSBs in G2, increasing repair by NHEJ by blocking of HR (Daley & Sung, 2014). This was verified by us in HCC1937 cells, which carry a homozygous loss of function mutation in the BRCA1 gene. Accordingly, BRCA1(-) cells displayed an almost complete absence of phospho-RPA2 after exposure to Etoposide, showing instead an increase in activated DNAPKcs, a key component of the DNAPK complex recruited by 53BP1 during NHEJ. We showed that these cells lose the ability to activate a robust G2/M checkpoint, and, conversely, that HCT116 cells harbouring a knockout of the gene codifying DNAPKcs feature increased levels of phospho-RPA2 at 8h and 24h after Etoposide insult, along with a very robust and sustained G2/M arrest in their cycle. We thus propose that the decrease in NHEJ repair efficiency caused by DNAPKcs loss results in a heavy lesion burden that causes cells to activate and maintain a very strong checkpoint arrest when they reach G2. Checkpoint signalling, in parallel with accumulation of unrepaired DSBs, is then able to presumably bypass the 53BP1 block on end-resection. Also, deficiency in NHEJ was shown not to increase γH2AX levels for cells damaged in G1, supporting the low requirement of damage introduced in G1 for NHEJ repair.

A consequence of the defect in G2/M checkpoint arrest seen in the absence of BRCA1 could be manifested in the increased frequency of spontaneous senescent cells (≈54% compared to ≈26% in BRCA1(+) cells) observed in this cell line after 8 days of

incubation under clonogenic conditions. Not being able to properly delay mitotic entry to allow sufficient time for repair means that cells undergo mitosis in the presence of severe DNA damage, which can result in cell death through mitotic catastrophe (Bunz et al., 1998). Moreover, surviving cells have a high risk of carrying abnormal chromosome ploidy, such as aneuploidy and tetraploidy. Tetraploid cells are known to trigger cell death and cell cycle arrest pathways, such as senescence, as a defence against the tumorigenic effects of these aberrations (Hayashi & Karlseder, 2013). Curiously, high levels of senescence in a cell line carrying a homozygous loss of function mutation in the p53 gene were unexpected since p53 activation is considered a requirement for initiation of the senescence pathway (Itahana, Dimri, & Campisi, 2001). However, low levels of p53 have been found to be sufficient to permit, and to potentially even promote, cellular senescence over either quiescence or cell death (Leontieva, Gudkov, & Blagosklonny, 2010). By comparison, DNAPKcs knockout lines, which have functional p53, displayed a G2/M checkpoint behaviour opposite to that of BRCA1(-) cells along with a lower propensity for senescence (≈ 14%, 5% and 2% in non-damaged DNAPK(-/-), (+/-) and (+/+), respectively). Furthermore, loss of DNAPKcs elicited a pronounced increase in cellular sensitivity to Etoposide, in a dose-dependent manner, drastically reducing colony viability (by almost 100% at 50μM Etoposide). This indicates that prolongation of G2/M arrest might promote other cell death or arrest pathways besides senescence, such as quiescence or apoptosis.

Our results also showed that a forced G2/M arrest induced by cdk1 inhibition, although leading to an intensification of end-resection by phospho-RPA2, does not benefit cells in terms of repair efficiency. It is possible that this forced cell cycle arrest, by means of a feedback mechanism, also forces the switch from NHEJ to HR, driving lesions that could otherwise be repaired by NHEJ to accumulate while waiting for HR. This point remains to be clarified. It should be mentioned that prolonged Cdk1 inhibition can result in the occurrence of mitotic defects due to impaired mitotic spindle formation, such as generation of cells with wrong numbers of segregated chromosomes (Enserink & Kolodner, 2010), a likely cause for the supra-4n population seen at 18h.

We also provide evidence that, when G2/M checkpoint is maintained for longer periods, these consistently correspond to increases in the levels of phosphorylation of

RPA2, which reflect an increment in end resection and HR repair. Shibata et.al. demonstrated utilizing ionizing radiation that ATM-dependent DNA end resection, even at a low level, is required to initiate ATR-dependent recruitment of Chk1 in G2, contributing to checkpoint maintenance (Shibata et al., 2010). We thus hypothesize that when HR has to take on the task of major repair system left by impaired NHEJ, in the presence of a severe lesion burden a persistent G2/M arrest occurs as cells continuously activate Chk1 through end-resection-dependent ATR activation. On the other hand, our clonogenic experiments suggest that when BRCA1 is depleted, NHEJ is able to ensure that increasing doses of Etoposide do not affect long term viability, which raises interesting questions: are DSBs in HC able to be repaired efficiently also by NHEJ when necessary? Or is this specific to Topo2-mediated DSBs that are by nature more “clean” and easier to repair? More studies will be necessary to enlighten these issues.

Overall, these results lead us to propose a model where slippage through checkpoint arrest is also a major determinant of repair system usage, particularly for DSBs arising in G1 and G2 phase since escaping arrest and passing to the following cell cycle phase will change the availability of repair pathways. Because of intrinsic limitations of the checkpoints operating at these stages, we conclude that a significant number of DSBs introduced in G1 are repaired by HR in S and G2 phases, whereas DSBs induced in G2 are mostly repaired by NHEJ in both G2 and G1.

In regards to chromatin structure sensitivity to Etoposide-mediated lesions, the differences observed between early S (when DSBs are introduced mostly in replicating EC) and late S (when HC becomes the preferential target) were not significant or consistent enough across different techniques to allow for a conclusive distinction between the two. Although late S lesions do rely on HR contrary to EC lesions, the overall level of repair was similar. We will need to test more restrictive time points to allow for differences in the early steps of repair to be noticed.

Knockdown of EZH2 and consequent decrease in H3K27 methylation showed that the loss of this heterochromatin mark is not sufficient to disrupt heterochromatin structure in a way that facilitates the DNA damaging effect of Etoposide-bound Topo2. This was evidenced by the fact that increasing Etoposide concentrations did not result in a decrease in HCT116 cell viability beyond the level induced by EZH2 knockdown alone. The

decreased level of proliferative ability, as well as the increase in spontaneous senescence outcome, caused by EZH2 knockdown is thus likely associated to expression of genes formerly repressed by the H3K27me3 mark. This is in accordance with previous studies that showed that EZH2 represses expression of genes up-regulated by the E2F transcription factor family, which include mainly proliferation, differentiation and apoptosis regulators (Wu et al., 2010). EZH2 function therefore suppresses a large number of tumor suppressor genes, which understandably results in its over-expression in several tumors (Chang & Hung, 2012).

In an effort to disturb heterochromatin stability in a more effective manner, we also tested the global histone methylation inhibitor DZNep. Interestingly, we found that a one to two hours exposure period to DZNep prior to an Etoposide pulse greatly potentiated the number of Topo2-mediated DSBs observable in HCT116 cells 24h after insult. This effect was seen only in pre-treatment and not by adding DZNep after Etoposide, which points to DZNep sensitizing cells to the introduction of DSBs by Topo2. We believe that this effect could result from global destabilization of heterochromatin regions, which would allow easier access to Topo2. We even wonder if Topo2 might actively be recruited to these regions as a result of topological problems that may arise with such chromatin decompaction. Again, this remains to be confirmed in future experiments. As a note, the synergistic effect of DZNep prior to Etoposide treatment was subsequently confirmed by another study (Unland et al., 2015). We confirmed that this effect also induced severe viability loss in a leukaemia cell line and used a drug combination study approach to identify low concentrations of each drug that are most effective at killing tumor cells. Although these were just exploratory experiments, there is potential for the use of DZNep in new clinical strategies.

In light of our interest in monitoring cycle progression of unconventional cell populations, we found a new use for the thymidine analogue EdU (5-ethynyl-2'-deoxyuridine), detailed in chapter 4 of this thesis, in allowing to accurately measure cell cycle kinetics in absolute values (hours) in asynchronous populations and without prior knowledge of population doubling times. We hope that this new methodology will prove useful for characterization of new cell types and for the analysis of drugs targeting the cell cycle, as is frequent in the context of cancer chemotherapy.

References

Alvarez-Fernández, M., & Medema, R. (2010). A new role for Cdks in the DNA damage response. *Cell Cycle*, *9*(15), 2915–2916.

Beucher, A., Birraux, J., Tchouandong, L., Barton, O., Shibata, A., Conrad, S., … Löbrich, M. (2009). ATM and Artemis promote homologous recombination of radiation-induced DNA double-strand breaks in G2. *The EMBO Journal*, *28*(21), 3413–27.

Bunz, F., Dutriaux, A., Lengauer, C., Waldman, T., Zhou, S., Brown, J. P., … Vogelstein, B. (1998). Requirement for p53 and p21 to Sustain G, Arrest After DNA Damage. *Science*, *282*(5393), 1497–1501.

Chang, C.-J., & Hung, M.-C. (2012). The role of EZH2 in tumour progression. *British Journal of Cancer*, *106*(2), 243–7.

Daley, J. M., & Sung, P. (2014). 53BP1, BRCA1, and the choice between recombination and end joining at DNA double-strand breaks. *Molecular and Cellular Biology*, *34*(8), 1380–8.

Deckbar, D., Jeggo, P. a, & Löbrich, M. (2011). Understanding the limitations of radiation-induced cell cycle checkpoints. *Critical Reviews in Biochemistry and Molecular Biology*, *46*(4), 271–83.

Enserink, J. M., & Kolodner, R. D. (2010). An overview of Cdk1-controlled targets and processes. *Cell Division*, *5*(1), 11.

Folle, G. a. (2008). Nuclear architecture, chromosome domains and genetic damage. *Mutation Research*, *658*(3), 172–83.

Hayashi, M., & Karlseder, J. (2013). DNA damage associated with mitosis and cytokinesis failure. *Oncogene*, (32), 4593–4601.

Ikura, T., Tashiro, S., Kakino, A., Shima, H., Jacob, N., Amunugama, R., … Kamiya, K. (2007). DNA damage-dependent acetylation and ubiquitination of H2AX enhances chromatin dynamics. *Molecular and Cellular Biology*, *27*(20), 7028–40.

Itahana, K., Dimri, G. P., & Campisi, J. (2001). Regulation of cellular senescence by p53.pdf. *European Journal of Biochemestry*, (268), 2784–2791.

Kakarougkas, A., Ismail, A., Klement, K., Goodarzi, A. A., Conrad, S., Freire, R., … Jeggo, P. A. (2013). Opposing roles for 53BP1 during homologous recombination. *Nucleic Acids Research*, *41*(21), 9719–9731.

Leontieva, O. V., Gudkov, A. V., & Blagosklonny, M. V. (2010). Weak p53 permits senescence during cell cycle arrest. *Cell Cycle*, *9*(21), 4323–4327.

McClendon, A., & Osheroff, N. (2007). DNA Topoisomerase II, Genotoxicity, and Cancer. *Mutation Research*, *23*(623), 83–97.

Nikitaki, Z., Mavragani, I. V., Laskaratou, D. A., Gika, V., Moskvin, V. P., Theofilatos, K., … Georgakilas, A. G. (2016). Systemic mechanisms and effects of ionizing radiation: A new "old" paradigm of how the bystanders and distant can become the players. *Seminars in Cancer Biology*, *37-38*, 77–95.

Paulovich, A. G., Toczyski, D. P., & Hartwell, L. H. (1997). When checkpoints fail. *Cell*, *88*(3), 315–321.

Sankaranarayanan, K., & Wassom, J. S. (2005). Ionizing radiation and genetic risks: XIV. Potential research directions in the post-genome era based on knowledge of repair of radiation-induced DNA double-strand breaks in mammalian somatic cells and the origin of deletions associated with human genomic. *Mutation Research - Fundamental and Molecular Mechanisms of Mutagenesis*, *578*(1-2), 333–370.

Scully, R., & Xie, A. (2013). Double strand break repair functions of histone H2AX. *Mutation Research*, *750*(1-2), 5–14.

Shaltiel, I. A., Krenning, L., Bruinsma, W., & Medema, R. H. (2015). The same, only different - DNA damage checkpoints and their reversal throughout the cell cycle. *Journal of Cell Science*, *128*(4), 607–620.

Shibata, A., Barton, O., Noon, A. T., Dahm, K., Deckbar, D., Goodarzi, A. A., … Jeggo, P. A. (2010). Role of ATM and the Damage Response Mediator Proteins 53BP1 and MDC1 in the Maintenance of G2/M Checkpoint Arrest. *Molecular and Cellular Biology*, *30*(13), 3371–3383.

Suzuki, M., Suzuki, K., Kodama, S., & Watanabe, M. (2006). Phosphorylated histone H2AX foci persist on rejoined mitotic chromosomes in normal human diploid cells exposed to ionizing radiation. *Radiation Research*, *165*(3), 269–76.

Unland, R., Borchardt, C., Clemens, D., Kool, M., Dirksen, U., & Frühwald, M. C. (2015). Analysis of the antiproliferative effects of 3-deazaneoplanocin A in combination with standard anticancer agents in rhabdoid tumor cell lines. *Anti-Cancer Drugs*, *26*(3), 301–311.

Wu, Z. L., Zheng, S. S., Li, Z. M., Qiao, Y. Y., Aau, M. Y., & Yu, Q. (2010). Polycomb protein EZH2 regulates E2F1-dependent apoptosis through epigenetically modulating Bim expression. *Cell Death and Differentiation*, *17*(5), 801–10.

Publications

Toxicology Reports 1 (2014) 1096–1105

Contents lists available at ScienceDirect

Toxicology Reports

journal homepage: www.elsevier.com/locate/toxrep

DNA damage induced by hydroquinone can be prevented by fungal detoxification

Pedro Pereira[b], Francisco J. Enguita[b], João Ferreira[b], Ana Lúcia Leitão[a,*]

[a] Departamento de Ciências e Tecnologia da Biomassa, Faculdade de Ciências e Tecnologia, Universidade Nova de Lisboa, Campus de Caparica, 2829-516 Caparica, Portugal

[b] Instituto de Medicina Molecular, Faculdade de Medicina da Universidade de Lisboa, Av. Prof. Egas Moniz, 1649-028 Lisboa, Portugal

ARTICLE INFO

Article history:
Received 31 August 2014
Received in revised form 25 October 2014
Accepted 28 October 2014
Available online 4 November 2014

Keywords:
Hydroquinone
Genotoxicity
Cytotoxicity
Penicillium chrysogenum var. *halophenolicum*
Detoxification

ABSTRACT

Hydroquinone is a benzene metabolite with a wide range of industrial applications, which has potential for widespread human exposure; however, the toxicity of hydroquinone on human cells remains unclear. The aims of this study are to investigate the cytotoxicity and genotoxicity of hydroquinone in human primary fibroblasts and human colon cancer cells (HCT116). Low doses of hydroquinone (227-454 μM) reduce the viability of fibroblasts and HCT116 cells, determined by resazurin conversion, and induce genotoxic damage (DNA strand breaks), as assessed by alkaline comet assays. Bioremediation may provide an excellent alternative to promote the degradation of hydroquinone, however few microorganisms are known that efficiently degrade it. Here we also investigate the capacity of a halotolerant fungus, *Penicillium chrysogenum* var. *halophenolicum*, to remove hydroquinone toxicity under hypersaline condition. The fungus is able to tolerate high concentrations of hydroquinone and can reverse these noxious effects via degradation of hydroquinone to completion, even when the initial concentration of this compound is as high as 7265 μM. Our findings reveal that *P. chrysogenum* var. *halophenolicum* efficiently degrade hydroquinone under hypersaline conditions, placing this fungus among the best candidates for the detoxification of habitats contaminated with this aromatic compound.

1. Introduction

Human exposure to hydroquinone, a phenolic compound also known as the major benzene metabolite, can occur by dietary, smoke, occupational and environmental sources. Due to the rapid industrialization and urbanization, the number of hydroquinone sources has increased and consequently its discharge into the environment, leading to serious toxic effects on fauna and flora. Hydroquinone is commonly used as a photographic developer, dye intermediate, stabilizer in paints, varnishes oils and motor fuels as well as in the rubber, antioxidant and food industry. Moreover, hydroquinone can be the product of several phenolic biotransformations, such as benzaldehyde, benzoic acid, 4-ethylphenol, 4-hydroxyacetophenone, phenol and substituted phenols, including 4-chloro, 4-fluoro, 4-bromo, 4-iodo and 4-nitrophenol [3,11,18,20,22,31]. It is known that phenolic compounds can negatively influence the organoleptic properties of fish and shellfish when present at concentrations of part-per-billion [14]. In fact, phenolic compounds are one of the priority pollutants of the United States Environmental Protection Agency (USEPA) list.

Although there are already some studies on the hydroquinone potential hazard to aquatic organisms, its genotoxic capacity and mechanism remain largely

* Corresponding author. Tel.: +351 21 2948543; fax: +351 21 2948543.
E-mail address: aldl@fct.unl.pt (A.L. Leitão).

http://dx.doi.org/10.1016/j.toxrep.2014.10.024

unknown. Most of the attention has been focused on acute toxicity. Bahrs and coworkers [4] determined 48-h EC_{50} values of 1.5 mg/l, 0.68 mg/l, 0.21 mg/l and 0.054 mg/l for *Desmodesmus armatus, Synechocystis* sp., *Nostoc* sp. and *Microcystis aeruginosa*, respectively, showing that hydroquinone can be highly toxic to aquatic organisms at concentrations of parts-per-million. Green algal species were found to be relatively less sensitive to hydroquinone than cyanobacterial species [4]. Meanwhile, 48-h EC_{50} value of 0.15 mg/l for *Daphnia magna* and 24-h LC_{50} values ranging from 0.22 to 0.28 mg/l for *Brachionus plicatilis* have been reported [14]. Hydroquinone was also toxic to marine bacteria as well as to fishes like rainbow trout and fathead minnows [9]. Indeed, hydroquinone can be a thousand times more toxic to *Vibrio fischeri* NRRL B-11177 than its isomers [19]. In epidemiological studies, correlations between the genotoxic concern of aquatic ecosystems and carcinogenic effects in human have been detected [7,12,15].

Despite the fact that hydroquinone seems to be one of the benzene metabolites implicated as causative agent of benzene-associated disease, there is no consensus among researchers regarding the relevance of the severity of hydroquinone on human cell viability and DNA damage. Some researchers proposed that hydroquinone could induce DNA damage by a combination of damage to the mitotic spindle, inhibition of topoisomerase II and the formation of DNA strand breaks via generation of reactive oxygen species [1,32,34], however others considered hydroquinone to be inactive by analyzing the frequency of DNA breaks using comet assay [21]. For the above reason, in the present study, we evaluated the cytotoxic effects of hydroquinone on the viability of human primary fibroblasts and human colon cancer cells (HCT116) using a commercial cell health indicator assay, and for assessment of the genotoxicity, alkaline comet assay was performed. In addition, the potential of a *Penicillium chrysogenum* strain for reducing hydroquinone concentrations and reversing its noxious effects via degradation of hydroquinone was evaluated. Cyto/genotoxic studies were conducted to determine the effect of exposure to medium conditioned by the metabolic activity of this fungal strain.

2. Materials and methods

2.1. Design of fungal experiments

P. chrysogenum var. *halophenolicum* was used throughout this study; this strain was isolated from a salt mine in Algarve, Portugal, and previously characterized [22,23]. The fungal strain was maintained at 4 °C on nutrient agar plates with 5.9% (w/v) NaCl. Precultures of cells were routinely aerobically cultivated in MC medium as described by [13].

To study the utilization of hydroquinone, the strain was cultivated in 500-ml flasks containing 100 ml of MC medium for 68 h at 160 rpm in an orbital shaker (Certomat® BS-T Incubator, Sartorius Stedim Biotech, Goettingen, Germany). Cells were centrifuged for 10 min at 10,000 × *g* and washed three times in 0.85% (w/v) of NaCl. Then, a 10% aliquot was inoculated in MMFe medium (50 ml in 250-ml flasks) [13] with different concentrations of hydroquinone (Sigma–Aldrich, ReagentPlus™, ≥99%, Batch#: 114K2623) (see Section 3). Three replicates were used per test for each hydroquinone concentration. Uninoculated control flasks (duplicates) were incubated and aerated in parallel as negative controls of the experiment. Hydroquinone concentration was monitored up to an incubation time of 96 h.

Biosorption by dead biomass was determined by batch adsorption equilibrium experiments as follows. The strain *P. chrysogenum* var. *halophenolicum* was grown in the MC liquid medium at 25 °C in a shaker incubator at 160 rpm for 68 h. Mycelium pellets were separated from the growth medium by centrifugation and washed twice with NaCl solution (0.85% (w/v)). The biomass was sterilized for 15 min at 121 °C and 124 kPa to kill the fungus, preventing biodegradation and bioaccumulation of hydroquinone in the subsequent adsorption experiments. The biomass was then rewashed with NaCl solution (0.85% (w/v)), centrifuged and approximately 50 ml of MMFe with 300 mg/l of hydroquinone were mixed with 0.10 g biomass (dry weight). The suspension was shaken at 25 °C in a rotary shaker at 160 rpm for 56 h, before the residual aqueous concentration of hydroquinone was measured by HPLC.

2.2. Analytical methods

Hydroquinone concentrations were quantified by High Performance Liquid Chromatography apparatus L-7100 (LaChrom HPLC System, Merck), equipped with a quaternary pump system, and L-7400 UV detector according to a previously published method [22]. Hydroquinone could be separated and concentrations estimated within 10 min, using standard (Sigma–Aldrich, ReagentPlus™, ≥99%).

The OxiTop® respirometric system (WTW, Germany) was used for assessing the biodegradability of hydroquinone over 5 days. The principle of the operation was based on the measurement of the pressure difference in the closed system. During hydroquinone biodegradation the respiration increases, the produced CO_2 was captured by an alkaline solution, and microbial oxygen consumption resulted in the subsequent pressure drop. All experiments were performed in reactors consisting of headspace and glass bottles (510 ml nominal volume) with a carbon dioxide trap (approximately 0.5 g of NaOH was added in each trap) with 97 ml of sample volume (MMFe with 5% of inoculum supplemented with 4541 and 7265 μM of hydroquinone). Fungal blanks were analyzed in parallel to correct for endogenous respiration. Respirometric analyses were conducted for 120 h in a temperature controlled chamber at 20 ± 1 °C and in the darkness. Decrease in headspace pressure inside the reactor was continuously and automatically recorded. Three experiments were performed, samples were done in triplicate and controls in duplicate. The quantity of oxygen consumption was calculated according to the manufacturer instructions.

2.3. Culture of human cells and cell viability assay

Colon cancer HCT116 cells (ATCC number CCL-247) and human primary fibroblasts (Coriell Institute, Candem,

NJ, Ref. GM05565) were cultured in McCoy's 5a Modified medium supplemented with 10% heat inactivated fetal bovine serum, 2 mM L-glutamine, 1% MEM non-essential amino acids and 100 U/ml penicillin/streptomycin (Gibco, Life Technologies), and maintained at 37 °C in a humidified incubator under 6% CO_2. Cells were cultured in 24-well plates for 24 h before initiation of experiments using McCoy's supplemented with either (1) MMFe medium originating from cultures of *P. chrysogenum* var. *halophenolicum* (conditioned composite medium), (2) freshly prepared MMFe medium (plain composite medium), or (3) either hydroquinone, etoposide or drug solvent (controls).

Cell viability was assessed using Alamar Blue® (Molecular Probes, Life Technologies), a commercial assay which is based on the reduction of the cell permeable redox indicator resazurin (deep blue) into resorufin (pink and fluorescent) by viable, metabolically active cells. At the end of specified incubation times, 50 μl of Alamar Blue® solution was added per 1 ml of culture medium and incubated for an additional 2 h. Plates were then analysed for fluorescence emission in a Tecan Infinite M200 plate reader, using an excitation wavelength of 530 nm and an emission wavelength of 590 nm. Results were read using Tecan i-Control v. 1.4.5.0 plate reader software. Each experiment was performed as a triplicate.

2.4. Alkaline single cell gel electrophoresis

DNA strand breaks were evaluated using Trevigen Comet Assay® kit (Trevigen Inc., Gaithersburg, MD, USA). Briefly, cells were resuspended in ice cold PBS (Ca^{2+} and Mg^{2+} free) to a concentration of 1×10^5 cells/ml. An aliquot of 5 μl of cells was added to 50 μl of molten LM Agarose (1% low-melting agarose) kept at 37 °C. 50 μl were pipetted immediately and evenly spread onto the comet slides. Slides were incubated at 4 °C in the dark for 10 min to accelerate gelling of the agarose disc and then transferred to prechilled lysis solution (2.5 M NaCl, 100 mM EDTA, 10 mM Tris-base, 1% sodium lauryl sarcosinate, 1% Triton X-100, pH 10) for 30 min at 4 °C. A denaturation step was performed in alkali solution (300 mM NaOH, 1 mM EDTA, pH > 13) at room temperature for 30 min, in the dark. Slides were then transferred to prechilled alkaline electrophoresis solution pH > 13 (300 mM NaOH, 1 mM EDTA) and subjected to electrophoresis at 1 V/cm, 300 mA for 30 min in the dark at 4 °C. The slides were then washed with deionized water and immersed in 70% ethanol at room temperature for 5 min and air dried. DNA was stained with 100 μl of SYBR Green I dye (Trevigen, 1:10,000 in Tris–EDTA buffer, pH 7.5) for 10 min at 4 °C in the dark and immediately analyzed using a CCD camera (Roper Scientific Coolsnap HQ CCD) attached to a Zeiss Axiovert 200M widefield fluorescence microscope. Comets were visualized with an excitation filter of 450–490 nm and an emission filter of 515 nm and fluorescent images of single cells were captured at 200× magnification. A minimum of 100 randomly chosen cells per experimental group were scored for comet parameters such as tail length and percentage of DNA in tail [28] using the Tritek CometScore Freeware v1.5 image analysis software.

3. Results

3.1. Cytotoxicity effects of hydroquinone

Results from the Alamar Blue® assay showed that hydroquinone treatment reduced the viability of human primary fibroblasts and colon cancer HCT116 cells in a dose-dependent manner. As shown in Fig. 1, high concentrations of hydroquinone (227 μM, 454 μM, 908 μM, 2270 μM and 4541 μM) greatly decreased cell viability. Compared to control, metabolic activity drastically dropped after exposure to any concentration equal or above 227 μM of hydroquinone. This negative effect on metabolic activity is more effective in HCT116 cells (11.25%) than fibroblasts cells (43.22%). EC_{50} for cytotoxicity in fibroblasts and HCT116 cells was 329.2 ± 4.8 μM and 132.3 ± 10.7 μM, respectively. There is a good fit between the dose response curve and the data points for cytotoxic effects on HCT116 cells and fibroblasts cells after 24 h ($r^2 = 0.9175$ and $r^2 = 0.9773$, respectively).

3.2. Genotoxicity of hydroquinone in cancer cells

One of the possible ways by which hydroquinone reduces cell survival could be through induction of DNA damage. We then addressed whether hydroquinone induced DNA damage in primary human skin fibroblasts and HCT116 cells, using the same range of concentrations previously demonstrated to reduce survival of both cells. To this end, we exposed HCT116 cells to increasing concentrations of hydroquinone (9.08, 45.4, 90.8, 227.0 and 454.1 μM; Table 1) for 24 h using as controls cells exposed to either no drug (solvent alone; negative control), or to etoposide for 15 min (50 μM; positive control), a well-known potent inducer of DNA breaks [10]. Since fibroblasts cells were less sensitive to hydroquinone as shown by the Alamar Blue® assay, we exposed fibroblasts cells to concentrations of 454.1 and 908.2 μM of hydroquinone (Table 1). DNA breaks were detected using the highly sensitive alkaline comet assay, an electrophoresis-based assay that allows detection of both single and double-stranded DNA breaks at the single cell level. As expected, etoposide induced significant DNA damage on fibroblasts and HCT116 cells with ~50% and 80%, respectively, of the DNA leaving the nucleus and migrating as the comet tail (Table 1). Importantly, treatment of HCT116 cells with 227 or 454 μM hydroquinone induced DNA damage similar to that caused by sub-apoptotic levels of etoposide in the same cell line. In fibroblasts, however, exposure to 454.1 μM of hydroquinone induced a much higher % of tail DNA in comets compared to etoposide (Table 1).

3.3. Genotoxicity of hydroquinone in cancer cells can be abolished by fungal treatment

To investigate if the presence of a fungal strain capable of degrading phenols, *P. chrysogenum* var. *halophenolicum*, reduces the toxicity of hydroquinone in fibroblasts and human colon cancer cells (HCT116), new experiments were done. Fungal cultures in minimal medium containing hydroquinone were incubated at several times to ensure

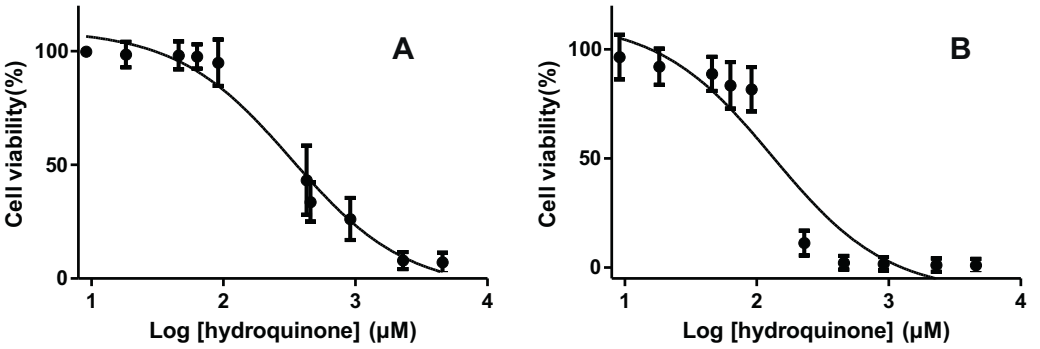

Fig. 1. Dose response curves of hydroquinone in fibroblasts cells (A) and HCT 116 cells (B).

Table 1
Evaluation of primary DNA damage measured in HCT 116 and fibroblasts cells following exposure to hydroquinone.

Cell treatment	Conc. (μM)	Tail intensity (%DNA)	Tail length (pixels)	Tail moment
HCT116				
Etop 15 min	50.0[a]	85.58 ± 5.30	161.23 ± 7.13	91.29 ± 9.75
NegC 24 h		18.09 ± 3.52	47.61 ± 7.09	7.30 ± 1.89
HQ 24 h	0	12.90 ± 1.88	60.97 ± 5.97	4.73 ± 1.25
	9.08	22.05 ± 3.42	75.76 ± 8.63	10.79 ± 2.70
	45.4	17.74 ± 3.16	87.37 ± 6.55	8.16 ± 1.97
	90.8	17.13 ± 4.28	95.93 ± 11.11	12.25 ± 5.44
	227.0	85.45 ± 4.60	298.40 ± 31.50	150.22 ± 16.42
	454.1	89.15 ± 1.44	320.78 ± 26.82	163.35 ± 10.95
Fibroblasts				
Etop 15 min	50.0*	46.12 ± 3.24	55.97 ± 2.23	19.78 ± 1.76
NegC 24 h		10.22 ± 1.05	35.09 ± 1.82	9.99 ± 2.46
HQ 24 h	454.1	82.82 ± 6.31	244.30 ± 34.40	123.50 ± 21.90
	908.0	87.42 ± 2.31	215.00 ± 14.05	107.20 ± 6.60

HQ, hydroquinone; Etop, etoposide; NegC, no drug.
[a] mg/l.

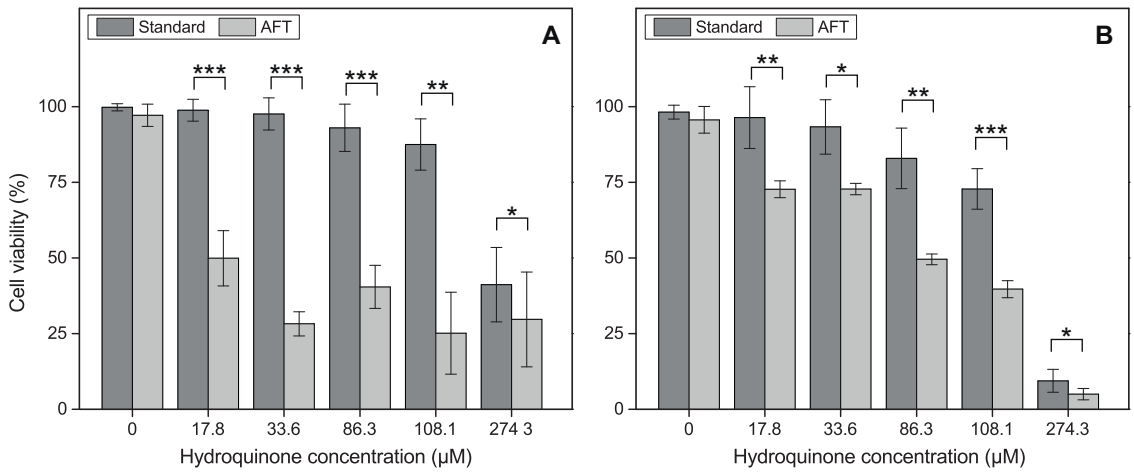

Fig. 2. Effects of the remaining hydroquinone concentrations after fungal treatment (AFT) on cell viability of fibroblasts (A) and HCT116 (B) cells after 24 h of exposure. Data are expressed as the mean with SD of three independent experiments. The probability in the ANOVA one-way test for the difference between controls and each treatment is given in parentheses: ***, $P < 0.001$; **, $P < 0.01$; *, $P < 0.05$.

different degradation yields. Fungal mycelium was then separated by centrifugation and the supernatants buffered to pH 7.4 and isotonic conditions. Those samples obtained after fungal treatment (AFT) were then added to the fibroblast and HCT116 cells growing in McCoy's medium (Fig. 2). Cell survival was evaluated by a well-established method based on the fluorescent conversion of a redox indicator (Alamar Blue®) after 24 h of culture on AFT samples. Controls were provided by fibroblasts and HCT116 cells cultivated exactly for the same periods of time in plain MMFe medium i.e. in which the fraction of saline medium was freshly prepared without hydroquinone. The data show a

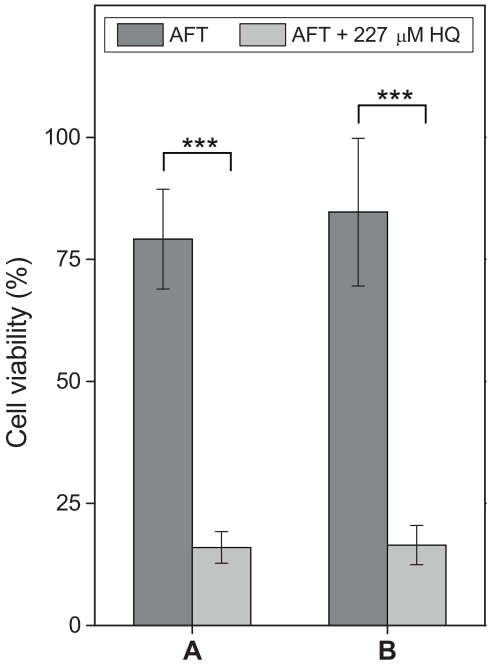

Fig. 3. Cytotoxicity effects of fungal treated samples (AFT) in HCT 116 cells observed in the presence or absence of hydroquinone addition (227 μM). (A) Sample from a batch with an initial concentration of hydroquinone of 4541 μM; (B) sample from a batch with an initial concentration of hydroquinone of 7265 μM. Data are expressed as the mean with SD of three independent experiments. The probability in the ANOVA one-way test for the difference between controls and each treatment is given in parentheses: ***, $P < 0.001$.

strong correlation between higher remaining concentrations of hydroquinone and reduced survival of HCT116 cells (Fig. 2). A different survival pattern was observed on fibroblasts; data depicted in Fig. 2 shows that concentrations of 33.6 μM of hydroquinone obtained after fungal treatment can reduce approximately 70% of the survival of fibroblasts cells. These data suggests that *P. chrysogenum* var. *halophenolicum* produces one or more metabolites during hydroquinone degradation that increase its toxicity, in particularly to fibroblasts cells. On the other hand, the salt medium composition (controls) did not affect cell viability.

To further address whether hydroquinone itself did play the key role in reduced survival of human cells, we cultivated HCT116 cells in medium in which hydroquinone had been reduced to undetectable levels by *P. chrysogenum* from initial concentrations of 4541 or 7265 μM (Fig. 3). The results show that, irrespectively of the initial concentration of hydroquinone, survival of HCT116 cells is only minimally affected when compared to controls cultured in freshly prepared salt medium (Figs. 2 and 3). Importantly, when purified hydroquinone was added back to a final concentration of 227 μM, survival of HCT116 cells were reduced to levels comparable to those observed when hydroquinone reached similar concentrations via *P. chrysogenum*-dependent degradation (Figs. 2 and 3). Together, these data demonstrate that *P. chrysogenum var. halophenolicum* is able to reduce the toxicity exerted by hydroquinone on cultured human cells.

3.4. *P. chrysogenum var. halophenolicum eliminate toxicity via degradation of hydroquinone*

We subsequently tested whether the capacity *P. chrysogenum* to eliminate the negative effect of hydroquinone on fibroblasts and HCT116 cells observed previously, was due to the hydroquinone degradation to undetectable levels in culture. To do so, batch cultures with *P. chrysogenum* var. *halophenolicum* and hydroquinone at different initial concentrations of 4541 and 7265 μM in saline liquid media (MMFe) were performed. The results are shown in Fig. 4. Since no abiotic loss of hydroquinone was detected in controls and less than 3% of hydroquinone becomes adsorbed to fungal cell surface, the decrease of hydroquinone concentration in the presence of fungus can be mostly attributed to cell metabolism. Hydroquinone at initial concentration of 4541 μM was completely removed within 56 h of treatment; while 75% of hydroquinone was removed in fungal cultures when the initial concentration was 7265 μM after the same time of treatment. These results demonstrate that *Penicillium* var. *halophenolicum* can remove hydroquinone to undetectable concentrations by HPLC method.

Additional studies were done to assess the complete biological conversion of hydroquinone to CO_2 and H_2O by the *P. chrysogenum* strain, using the OxiTop® respirometric system. The OxiTop® respirometric system is a simple, batch device, which is appropriate and sensitive for determination and analysis of wastewater biological oxygen demand (BOD). Fig. 5 shows hydroquinone BOD data from the respirometric study. Each BOD value was corrected for endogenous respiration (i.e., BOD obtained from the fungal blank). Since the biodegradation test was carried out within a brown dark bottle container and in the absence of light, the possible existence of photodegradation was withdrawn. The 5-day BOD for the initial concentrations of 4541 and 7265 μM of hydroquinone was 440 mg/l and 720 mg/l, respectively. The initial mineralization of the biodegraded hydroquinone is slightly lower at the initial concentration of 7265 μM than that at 4541 μM up to the first day. This fact suggests that hydroquinone at high concentrations induces smaller rates of respiration than low initial concentrations and agrees with the observation that hydroquinone can reduce enzyme activity of microbial biomass [8].

3.5. *Effect of P. chrysogenum var. halophenolicum on hydroquinone genotoxic activity*

Finally, we tested whether *P. chrysogenum* could degrade hydroquinone to levels that were non-genotoxic to cultured human cells. HCT116 and fibroblasts cells were thus exposed for 24 h to fungal treated samples containing different concentrations of hydroquinone as the result of progressive degradation of this compound by *P. chrysogenum* and then subjected to the alkaline comet assay protocol; controls were provided by cells exposed to plain medium without hydroquinone for the same duration (Table 2 and Fig. 6). As expected for a genotoxic agent, metabolites coming from an incomplete degradation of hydroquinone still might led to significant DNA damage in

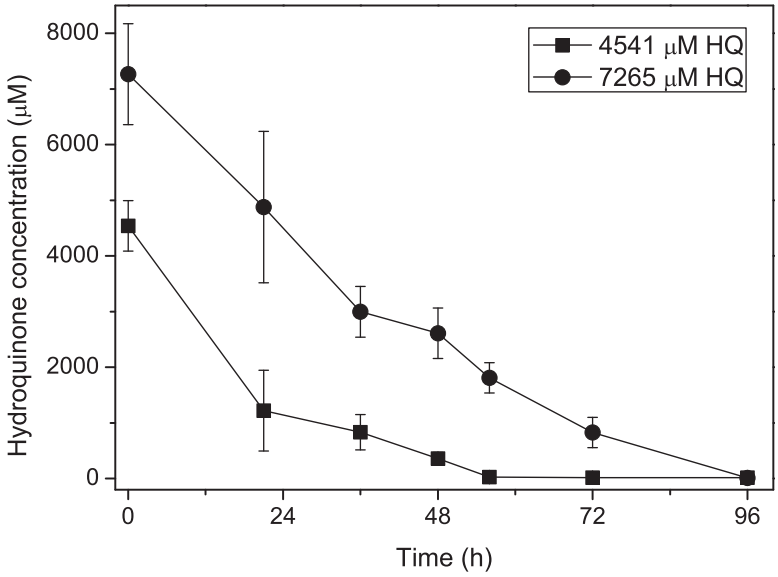

Fig. 4. Hydroquinone removal by *P. chrysogenum* var. *halophenolicum* at different initial concentrations as indicated in the legend. Data shown represents average of triplicates ± standard deviations.

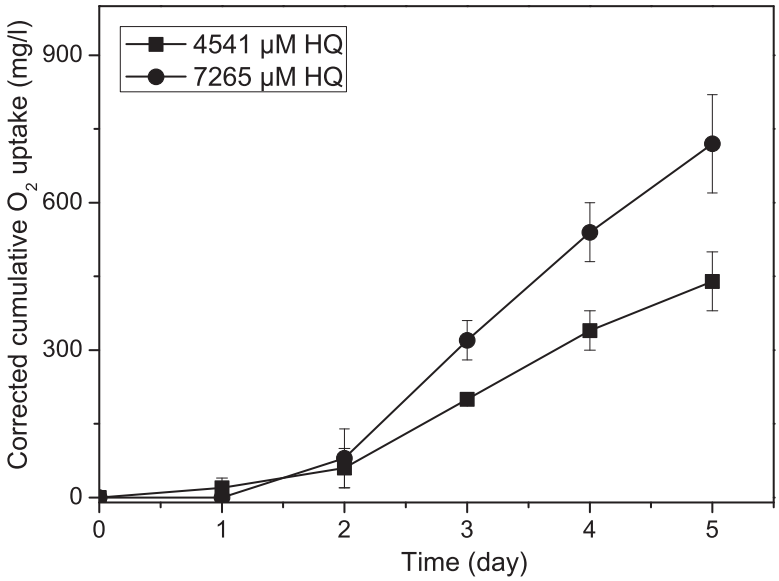

Fig. 5. Biochemical oxygen demand of hydroquinone. Data are corrected against the fungal blank BOD from respirometric analysis. Error bars are based on samples from duplicate reactors.

HCT116 or fibroblasts cells. HCT116 cells exposed to 86.3, 108.1 and 274.3 μM of remaining hydroquinone after fungal treatment showed in the range between 40% and 80% of total DNA fractured enough to leave the cell nucleus and form the comet tail (Fig. 6 and Table 2). In the case of fibroblasts, a remaining hydroquinone concentration of 86.3 μM did not induce a noticeable increase in DNA damage, while with 274.3 μM more than 80% of DNA in the comet tail was observed (Table 2). However, when hydroquinone was either fully degraded (0 μM) or degraded almost to completion (33.6 μM final concentration) by *P. chrysogenum*, the amount of DNA damage induced in HCT116 and fibroblasts cells was similar to that observed in the control cells (NegC) (Table 2).

Overall, these data show that *P. chrysogenum* var. *halophenolicum* is capable of degrading hydroquinone from highly cytotoxic initial concentrations to levels that are non-genotoxic and are well tolerated by fibroblasts and HCT116 cell (Fig. 7).

4. Discussion

The toxicity of hydroquinone may have been underestimated, given the small number of studies performed

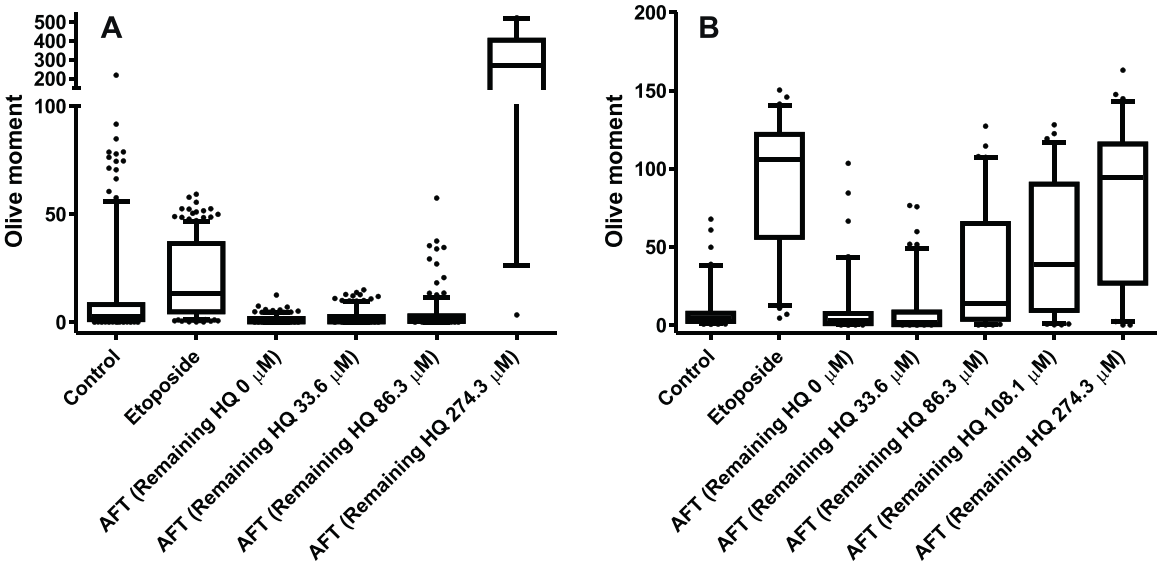

Fig. 6. Depicted are the results of alkaline comet assays performed using fibroblasts (a) and HCT116 cells (b) cultured for 24 h in medium containing either drug solvent alone (controls), etoposide (50 μM for 15 min), AFT medium containing varying final concentrations of hydroquinone. The different concentrations of hydroquinone were obtained by progressive treatment of hydroquinone by *P. chrysogenum* var. *halophenolicum* (initial concentration 4541 and 7265 μM). The 0 μM concentration corresponds to full (maximal) degradation. Controls correspond to HCT116 cells and fibroblasts grown in the absence of hydroquinone. In the graphs, boxes correspond to the 75th percentile, whiskers to the 95th percentile and lines identify the median obtained from triplicates.

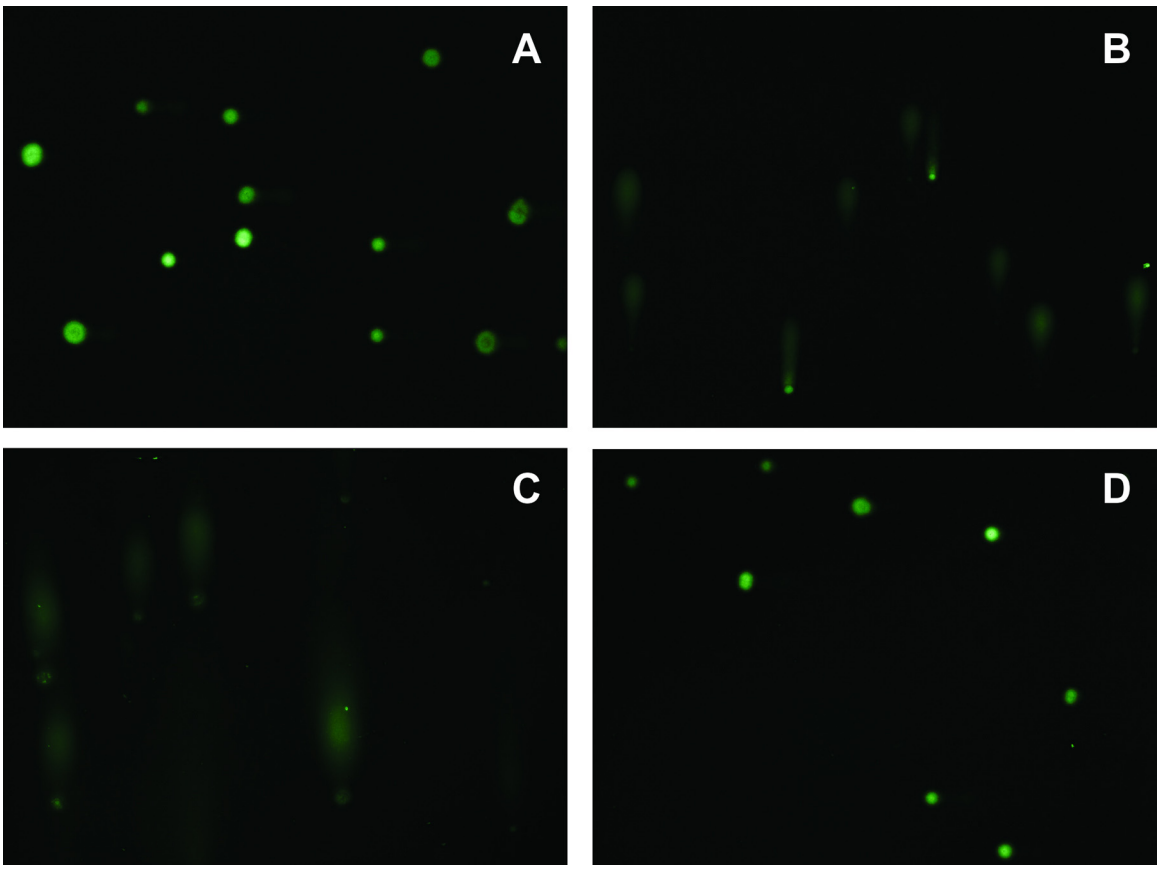

Fig. 7. Hydroquinone induces DNA double-strand breaks in HCT116 cancer cells. Representative photos are shown for (A) negative control (medium), (B) positive control (etoposide), (C) standard hydroquinone (454 μM) and (D) AFT sample where the remaining concentration of hydroquinone is zero.

Table 2
Measurement of DNA damage-related parameters obtained by alkaline comet assay in HCT 116 and fibroblast cells following exposure to AFT medium. Data are expressed as the mean with SD of three independent experiments. The probability in the ANOVA one-way test for the difference between controls and each treatment is given in parentheses: ***, $P < 0.001$; **, $P < 0.01$; *, $P < 0.05$; ns, $P > 0.05$.

Cell treatment	Concentration (μM)	% DNA in tail	Tail length (pixels)
HCT116			
Control		18.09 ± 3.52	47.61 ± 3.56
HQ 24 h	0	17.77 ± 4.50 (ns)	38.01 ± 3.88 (ns)
	33.6	16.06 ± 4.30 (ns)	40.10 ± 3.24 (ns)
	86.3	43.61 ± 7.86 (***)	93.26 ± 5.81 (***)
	108.1	57.77 ± 7.43 (***)	110.00 ± 5.51 (***)
	274.3	73.97 ± 7.63 (***)	153.70 ± 8.64 (***)
Fibroblasts			
Control		10.22 ± 1.05	35.09 ± 0.93
HQ 24 h	0	5.58 ± 0.84 (***)	21.89 ± 0.94 (**)
	33.6	6.47 ± 1.06 (***)	29.10 ± 1.30 (ns)
	86.3	11.03 ± 1.90 (ns)	27.40 ± 1.11 (ns)
	274.3	87.26 ± 5.50 (***)	506.00 ± 39.28 (***)

HQ, hydroquinone.

in animal models, the difficulty to extrapolate to humans most of the data obtained in models, and the limited statistical power of cohort studies already performed in human subjects [30]. There is growing evidence that hydroquinone and some of its metabolites have genotoxic activity to mammalian cells, namely human cells, either primary or transformed [11].

In initial work on the cytotoxicity of hydroquinone on mammalian cells a requirement for copper was described [25]. Indeed, Cu(II) through a copper-redox cycling mechanism promotes the oxidation of hydroquinone with generation of benzoquinone and reactive oxygen species (ROS) [26], and several reports have subsequently implicated oxidative damage to DNA as a major mechanism for the cytotoxic effects of hydroquinone (reviewed in [11]). Later, Luo and coworkers showed that hydroquinone induced genotoxicity and oxidative DNA damage in human hepatoma HepG2 cells independently of the presence of transition metals, and afterwards several articles were published supporting these researchers [16,29,33]. In this study, *P. chrysogenum* var. *halophenolicum* ability to degrade hydroquinone was investigated using saline medium (MMFe) with iron in its composition. The presence of iron did not affect the toxicity of hydroquinone over fibroblasts and HCT116 cells. These findings in fibroblasts and HCT116 cells, are in agreement with previously published data obtained using other cell types [24], not excluding a role for endogenous copper in mediating the cellular effects of hydroquinone. The median effective concentration (EC_{50}) of hydroquinone in several cancer lines was reported to be 8.5 μM, 10.0 μM, 88 μM for HL-60, HL-60/MX2 and Huh7, respectively, and >100 μM for Hep3B and HepG2 [16]. Our data showed that hydroquinone decreased cell viability of HCT116 cells (EC_{50} = 132.3 μM) and, to a lesser extent, primary human fibroblasts (EC_{50} = 329.2 μM). These data are in agreement with the data published by other researcher who has found that primary human fibroblasts were relatively more resistant to hydroquinone compared to lymphocytes [24]. As it was previously reported, differences between a cancer cell line and primary fibroblasts can be attributed to differences in cell sensitivity to the compound that was assayed and would be mainly related with the cell division rate [36].

Reactive species generated by hydroquinone have been implicated in the formation of modified bases (e.g., 8-oxo-deoxyguanine) in the DNA molecule, which appear to be removed with fast kinetics [33], but also single and double-stranded DNA strand breaks [17,29,33]. Moreover, both hydroquinone and its degradation product benzoquinone are topoisomerase II poisons which inhibit the final ligation step of the catalytic cycle of the enzyme, thus stabilizing topoisomerase-mediated DNA scissions [27]. Although the relative contributions of reactive oxygen species and topoisomerases in hydroquinone-mediated genotoxicity remain to be elucidated, it is clear that that DNA breaks generated by hydroquinone pose a serious challenge to genome integrity [5,11]. Herein, we have analyzed the capacity of hydroquinone to generate both single and double-strand DNA breaks using the well characterized comet assay under alkaline conditions (cf. Table 1). We showed that the hydroquinone-induced increment in DNA strand breaks in HCT116 cells was dose-related. In HCT116 cells, hydroquinone at concentrations of 227.0 and 454.1 μM caused a marked increase of the olive tail moment (the product of % tail DNA and tail length) compared to lower concentrations. Hydroquinone concentrations up to 90.8 μM induced a gradual but slow increment of the olive tail moments and this was due more to the increase in the tail length of comets than to the amount of DNA in the tail. The relative amount of DNA in the comet tail (the % tail DNA or tail intensity) has been related to DNA break frequency over a wide genome range, while tail length has been related to the frequency of the smallest detectable DNA fragments and, since it quickly reaches a maximum, its useful only for low levels of damage [2]. Taking this into account, we can say that hydroquinone concentrations higher than 90.8 μM are required in order to induce a high frequency of DNA breaks throughout the whole genome of HCT116 cells, resulting in overall cell death, as evidenced by the survivability assay (Fig. 2). Hydroquinone alone induced greater loss of viability in HTC116 cells than in fibroblasts cells (cf. Fig. 1) but surprisingly, when cells were exposed to medium

previously incubated with *P. chrysogenum* var. *halophenolicum*, fibroblast survivability seemed to be dependent on more than just the remaining hydroquinone concentration in the medium. This suggests that fibroblasts are more sensitive than HCT116 cells to the metabolites resulting from hydroquinone degradation. Interestingly, the comet assay data also indicates that, except for very high remaining hydroquinone concentrations, DNA strand breaks are not the major cause of the viability loss in fibroblasts after fungal treatment (compare Figs. 2 and 6). This data suggest that the toxic effect of the hydroquinone metabolites originated by fungal treatment on primary fibroblasts may be due to a mechanism which does not involve DNA damage.

This increase of DNA damage on fibroblasts and HCT116 cells may be due to fungal metabolites originated during hydroquinone degradation. Nevertheless, this fungal strain showed the capacity to reduce hydroquinone to concentrations at which DNA strand breaks become basal level in human fibroblasts and HCT116 cells (Table 2).

Given that hydroquinone is a relevant environment pollutant, and that bioremediation has obvious advantages over chemical degradation, efforts have been made to identify microorganisms capable of hydroquinone degradation under harsh conditions [6,11,23,35]. However, studies monitoring the efficiency of hydroquinone removal have remained scarce. The present study shows that *P. chrysogenum* var. *halophenolicum* exhibits high tolerance and degradation capacity to hydroquinone, as it was able to remove up to 7265 μM of the aromatic compound under 1 M NaCl. Furthermore, a cumulative O_2 uptake of 440 and 720 mg/l was obtained in respirometric assays for initial hydroquinone concentrations of 4541 μM and 7265 μM, respectively. Since the theoretical carbonaceous oxygen demand (ThOD) for 4541 and 7265 μM of hydroquinone was calculated to be 872 mg/l and 1395 mg/l, respectively, our results indicate that at least 50% of carbon from hydroquinone is converted to CO_2, supporting the hypothesis that hydroquinone is a substrate readily and efficiently used by fungus.

In conclusion, *in vitro* tests showed that hydroquinone is cytotoxic for human fibroblasts and HCT116 cells. Moreover, hydroquinone induces DNA damage to fibroblast and HCT116 cells in the form of DNA single and double strand breaks as it was demonstrated by alkaline comet assay. Our data provides also the first evidence that, without prior acclimation, *P. chrysogenum* var. *halophenolicum* has the capacity to degrade hydroquinone present at high initial concentrations in hypersaline media to levels that are non-genotoxic to human cells. Overall, the present study supports the potential of *P. chrysogenum* var. *halophenolicum* for the treatment of salty phenolic-contaminated wastewaters.

Conflict of interest

None declared.

Transparency document

The Transparency document associated with this article can be found in the online version.

Acknowledgments

This work was partially supported by a Gulbenkian Foundation research grant (#96526/2009) awarded to JF, and PD received support from Fundação para a Ciência e Tecnologia/FCT-Portugal (SFRH/BD/45502/2008).

References

[1] T.J. Atkinson, A review of the role of benzene metabolites and mechanisms in malignant transformation: summative evidence for a lack of research in nonmyelogenous cancer types, Int. J. Hyg. Environ. Health 212 (2009) 1–10.
[2] A. Azqueta, A.R. Collins, The essential comet assay: a comprehensive guide to measuring DNA damage and repair, Arch. Toxicol. 87 (2013) 949–968.
[3] H.S. Bae, J.M. Lee, S.T. Lee, Biodegradation of 4-chlorophenol via a hydroquinone pathway by *Arthrobacter ureafaciens* CPR706, FEMS Microbiol. Lett. 145 (1996) 125–129.
[4] H. Bahrs, A. Putschew, C.E. Steinberg, Toxicity of hydroquinone to different freshwater phototrophs is influenced by time of exposure and pH, Environ. Sci. Pollut. Res. Int. 20 (2013) 146–154.
[5] G. Barreto, D. Madureira, F. Capani, L. Aon-Bertolino, E. Saraceno, L.D. Alvarez-Giraldez, The role of catechols and free radicals in benzene toxicity: an oxidative DNA damage pathway, Environ. Mol. Mutagen. 50 (2009) 771–780.
[6] P. Bergauer, P.A. Fonteyne, N. Nolard, F. Schinner, R. Margesin, Biodegradation of phenol and phenol-related compounds by psychrophilic and cold-tolerant alpine yeasts, Chemosphere 59 (2005) 909–918.
[7] J.J. Black, P.C. Baumann, Carcinogens and cancers in freshwater fishes, Environ. Health Perspect. 90 (1991) 27–33.
[8] H. Chen, J. Yao, F. Wang, M.M. Choi, E. Bramanti, G. Zaray, Study on the toxic effects of diphenol compounds on soil microbial activity by a combination of methods, J. Hazard. Mater. 167 (2009) 846–851.
[9] G.M. DeGraeve, D.L. Greiger, J.S. Meyer, H.L. Bergman, Acute and embryo-larval toxicity of phenolic compounds to aquatic biota, Arch. Environ. Contam. Toxicol. 9 (2008) 557–568.
[10] J.E. Deweese, N. Osheroff, The DNA cleavage reaction of topoisomerase II: wolf in sheep's clothing, Nucleic Acids Res. 37 (2009) 738–748.
[11] F.J. Enguita, A.L. Leitão, Hydroquinone: environmental pollution, toxicity, and microbial answers, BioMed Res. Int. (2013), http://dx.doi.org/10.1155/2013/542168.
[12] J. Griffith, R.C. Duncan, W.B. Riggan, A.C. Pellom, Cancer mortality in US. counties with hazardous waste sites and ground water pollution, Arch. Environ. Health 44 (1989) 69–74.
[13] S.F. Guedes, B. Mendes, A.L. Leitão, Resorcinol degradation by a *Penicillium chrysogenum* strain under osmotic stress: mono and binary substrate matrices with phenol, Biodegradation 22 (2011) 409–419.
[14] R. Guerra, Ecotoxicological and chemical evaluation of phenolic compounds in industrial effluents, Chemosphere 44 (2001) 1737–1747.
[15] M. Hendryx, J. Conley, E. Fedorko, J. Luo, M. Armistead, Permitted water pollution discharges and population cancer and non-cancer mortality: toxicity weights and upstream discharge effects in US rural–urban areas, Int. J. Health Geogr. 11 (2012) 9.
[16] C.P. Huang, W.H. Fang, L.I. Lin, R.Y. Chiou, L.S. Kan, N.H. Chi, Y.R. Chen, T.Y. Lin, S.B. Lin, Anticancer activity of botanical alkyl hydroquinones attributed to topoisomerase II poisoning, Toxicol. Appl. Pharmacol. 227 (2008) 331–338.
[17] M. Ishihama, T. Toyooka, Y. Ibuki, Generation of phosphorylated histone H2AX by benzene metabolites, Toxicol. In Vitro 22 (2008) 1861–1868.
[18] K.H. Jones, P.W. Trudgill, D.J. Hopper, 4-Ethylphenol metabolism by *Aspergillus fumigatus*, Appl. Environ. Microbiol. 60 (1994) 1978–1983.
[19] K.L.E. Kaiser, V.S. Palabrica, *Photobacterium phosphoreum* toxicity data index, Water Poll. Res. J. Can. 26 (1991) 361–431.
[20] F. Kamada, S. Abe, N. Hiratsuka, H. Wariishi, H. Tanaka, Mineralization of aromatic compounds by brown-rot basidiomycetes – mechanisms involved in initial attack on the aromatic ring, Microbiology 148 (2002) 1939–1946.
[21] M. Kiffe, P. Christen, P. Arni, Characterization of cytotoxic and genotoxic effects of different compounds in CHO K5 cells with the comet assay (single-cell gel electrophoresis assay), Mutat. Res. 537 (2003) 151–168.

[22] A.L. Leitão, M.P. Duarte, J. Santos Oliveira, Degradation of phenol by a halotolerant strain of *Penicillium chrysogenum*, Int. Biodeterior. Biodegrad. 59 (2007) 220–225.
[23] A.L. Leitão, C. Garcia-Estrada, R.V. Ullan, S.F. Guedes, P. Martin-Jimenez, B. Mendes, J.F. Martin, *Penicillium chrysogenum* var. *halophenolicum* a new halotolerant strain with potential in the remediation of aromatic compounds in high salt environments, Microbiol. Res. 167 (2012) 79–89.
[24] Q. Li, M.T. Aubrey, T. Christian, B.M. Freed, Differential inhibition of DNA synthesis in human T cells by the cigarette tar components hydroquinone and catechol, Fundam. Appl. Toxicol. 38 (1997) 158–165.
[25] Y. Li, M.A. Trush, DNA damage resulting from the oxidation of hydroquinone by copper: role for a Cu(II)/Cu(I) redox cycle and reactive oxygen generation, Carcinogenesis 14 (1993) 1303–1311.
[26] Y. Li, M.A. Trush, Oxidation of hydroquinone by copper: chemical mechanism and biological effects, Arch. Biochem. Biophys. 300 (1993) 346–355.
[27] R.H. Lindsey Jr., R.P. Bender, N. Osheroff, Effects of benzene metabolites on DNA cleavage mediated by human topoisomerase II alpha: 1,4-hydroquinone is a topoisomerase II poison, Chem. Res. Toxicol. 18 (2005) 761–770.
[28] P.D. Lovell, T. Omori, Statistical issues in the use of the comet assay, Mutagenesis 23 (2008) 171–182.
[29] L. Luo, L. Jiang, C. Geng, J. Cao, L. Zhong, Hydroquinone-induced genotoxicity and oxidative DNA damage in HepG2 cells, Chem. Biol. Interact. 173 (2008) 1–8.
[30] D. McGregor, Hydroquinone: an evaluation of the human risks from its carcinogenic and mutagenic properties, Crit. Rev. Toxicol. 37 (2007) 887–914.
[31] M.J. Moonen, S.A. Synowsky, W.A. van den Berg, A.H. Westphal, A.J. Heck, R.H. van den Heuvel, M.W. Fraaije, W.J. van Berkel, Hydroquinone dioxygenase from *Pseudomonas fluorescens* ACB: a novel member of the family of nonheme-iron(II)-dependent dioxygenases, J. Bacteriol. 190 (2008) 5199–5209.
[32] M. North, V.J. Tandon, R. Thomas, A. Loguinov, I. Gerlovina, A.E. Hubbard, L. Zhang, M.T. Smith, C.D. Vulpe, Genome-wide functional profiling reveals genes required for tolerance to benzene metabolites in yeast, PLoS ONE 6 (2011) e24205.
[33] C. Peng, D. Arthur, F. Liu, J. Lee, Q. Xia, M.F. Lavin, J.C. Ng, Genotoxicity of hydroquinone in A549 cells, Cell Biol. Toxicol. 29 (2013) 213–227.
[34] M.T. Smith, Advances in understanding benzene health effects and susceptibility, Annu. Rev. Public Health 31 (2010) 133–148.
[35] U. Szewzyk, B. Schink, Degradation of hydroquinone, gentisate, and benzoate by a fermenting bacterium in pure or defined mixed culture, Arch. Microbiol. 151 (1989) 541–545.
[36] V. Ugartondo, M. Mitjans, M.P. Vinardell, Comparative antioxidant and cytotoxic effects of lignins from different sources, Biores. Technol. 99 (2008) 6683–6687.

Published in final edited form as:
Immunity. 2013 November 14; 39(5): 874–884. doi:10.1016/j.immuni.2013.08.039.

Anthracyclines Induce DNA Damage Response-Mediated Protection against Severe Sepsis

Nuno Figueiredo[1,2,3,4,*], **Angelo Chora**[1,*], **Helena Raquel**[1,*], **Nadja Pejanovic**[1], **Pedro Pereira**[1], **Björn Hartleben**[5], **Ana Neves-Costa**[1], **Catarina Moita**[1], **Dora Pedroso**[1], **Andreia Pinto**[1], **Sofia Marques**[1], **Hafeez Faridi**[6], **Paulo Costa**[2], **Raffaella Gozzelino**[7], **Jimmy L. Zhao**[8], **Miguel P. Soares**[7], **Margarida Gama-Carvalho**[9], **Jennifer Martinez**[10], **Qingshuo Zhang**[11], **Gerd Döring**[12], **Markus Grompe**[11], **J. Pedro Simas**[1], **Tobias B. Huber**[5], **David Baltimore**[8], **Vineet Gupta**[6], **Douglas R. Green**[10], **João A. Ferreira**[1], and **Luis F. Moita**[1,13]

[1]Instituto de Medicina Molecular, Faculdade de Medicina, Universidade de Lisboa, 1649-028 Lisboa, Portugal

[2]Clínica Universitária de Cirurgia I, Centro Hospitalar Lisboa Norte, EPE, 1649-028 Lisboa, Portugal

[3]Gulbenkian Programme for Advanced Medical Education, 2780-156 Oeiras, Portugal

[4]Champalimaud Foundation, 1400-038 Lisboa, Portugal

[5]Renal Division, University Hospital Freiburg, 79106 Freiburg, Germany

[6]Department of Internal Medicine, Rush University Medical Center, Chicago, IL 60612

[7]Instituto Gulbenkian de Ciência, Rua da Quinta Grande 6, 2780-156 Oeiras, Portugal

[8]Division of Biology, California Institute of Technology, Pasadena, CA 91125, U.S.A

[9]Centro de Biodiversidade, Genómica Funcional e Integrativa (BioFIG), Faculdade de Ciências, Universidade de Lisboa, 1749-016 Lisboa, Portugal

[10]Department of Immunology, St Jude Children's Research Hospital, Memphis, TN 38105, USA

[11]Oregon Stem Cell Center, Department of Pediatrics, Oregon Health & Science University, Portland, OR 97239, USA

[12]Institut für Medizinische Mikrobiologie und Hygiene, University of Tübingen, 72076 Tübingen, Germany

[13]Clinical Research Center of The Lisbon Academic Medical Center, 1649-028 Lisboa, Portugal

Summary

Severe sepsis remains a poorly understood systemic inflammatory condition with high mortality rates and limited therapeutic options in addition to organ support measures. Here we show that the clinically approved group of anthracyclines acts therapeutically at a low dose regimen to confer

Correspondence: Luis Ferreira Moita, Innate Immunity and Inflammation Unit, Instituto de Medicina Molecular, Edifício Egas Moniz, Faculdade de Medicina da Universidade de Lisboa, Av. Professor Egas Moniz, 1649-028 Lisboa, Tel: (+351) 217999544, Fax: (+351) 217999459, lmoita@fm.ul.pt.
*Equal contributions.

robust protection against severe sepsis in mice. This salutary effect is strictly dependent on the activation of DNA damage response and autophagy pathways in the lung, as demonstrated by deletion of the ataxia telangiectasia mutated (*Atm*) or the autophagy-related protein 7 (*Atg7*) specifically in this organ. The protective effect of anthracyclines occurs irrespectively of pathogen burden, conferring disease tolerance to severe sepsis. These findings demonstrate that DNA damage responses, including the ATM and Fancony Anemia pathways, are important modulators of immune responses and might be exploited to confer protection to inflammation-driven conditions, including severe sepsis.

Keywords

Sepsis; ATM; Autophagy; Anthracyclines

INTRODUCTION

Sepsis is a life-threatening condition that arises as a systemic inflammatory response to an infection (Bone et al., 1992; Levy et al., 2003). It includes a continuum of clinical severity ranging from systemic inflammatory response syndrome (SIRS), sepsis, severe sepsis to septic shock (Suffredini and Munford, 2011). It is the leading cause of death in intensive care units and the third cause of overall hospital mortality (Angus and Wax, 2001; Ulloa and Tracey, 2005). In spite of substantial improvement in diagnosis and support measures, the global annual mortality rate is ~28% (Hotchkiss and Karl, 2003), ranging from less than 10% in SIRS to up to 70% in septic shock (Angus and Wax, 2001; Annane et al., 2003). The pathophysiology of sepsis remains poorly understood. As a result, the basic elements of treatment – early antibiotics, prompt control of the source of infection and organ support - have not changed substantially in the last fifty years, and attempts to translate basic research results into effective new interventions have been met with limited or no success (Suffredini and Munford, 2011). In the same period, the incidence of sepsis and its economic burden has increased by 1% each year (Martin et al., 2003; Ulloa and Tracey, 2005), indicating the urgent need for novel therapeutic options.

Inflammation is a response to harmful stimuli that limits tissue damage and aims at restoring homeostasis (Medzhitov, 2008). Pathogen-associated molecular patterns (PAMPs) on microorganisms and damage-associated molecular patterns (DAMPs) originating from dying cells are sensed by the host through germline-encoded pattern recognition receptors (PRRs) that recognize conserved signature structures in non-self and self (Janeway and Medzhitov, 2002). These sensors are present in both professional (including neutrophils, macrophages and dendritic cells) and non-professional immune cells and their activation initiates intracellular signaling cascades leading to the transcriptional expression of inflammatory mediators, such as cytokines and chemokines. Inflammation needs to be effectively terminated after removal of the original trigger for repair of damaged tissue to occur. In the susceptible host, overproduction of inflammatory mediators or an exaggerated response to their presence can lead to septic shock, tissue destruction or permanent loss of function (Takeuchi and Akira, 2010).

There are two evolutionarily conserved defense strategies against infection that can limit host disease severity. One relies on reducing pathogen load, i.e. resistance to infection, while the other provides host tissue damage control, limiting disease severity irrespectively of pathogen load, i.e. tolerance to infection (Raberg et al., 2009; Schneider and Ayres, 2008). As demonstrated originally for plants and thereafter in *Drosophila*, tolerance to infection also operates in mammals, as revealed for *Plasmodium* (Raberg et al., 2007; Seixas et al., 2009) and polymicrobial infections in severe sepsis (Larsen et al., 2010).

Here we show in an experimental mouse model that anthracyclines confer strong protection against sepsis by increasing disease tolerance to infection, that is, acting irrespectively of pathogen burden. We further show that ATM (ataxia telangiectasia mutated) kinase and the induction of autophagy are strictly required for the in vivo protection against sepsis. These molecular pathways provide strong damage control in tissues, specifically in the lung.

RESULTS

Anthracyclines confer strong protection against severe sepsis

In an *in vitro* chemical screen using ~2320 compounds, we identified several lead candidates capable of inhibiting inflammatory cytokine production in response to *E. coli* challenge by the THP-1 macrophage line (Figure S1a and Supplemental Table S1). This inhibitory effect was dissociated from cytotoxicity of the compounds tested on THP-1 cells (Figure S1b). Among these, we found 3 representatives of the anthracycline family of chemotherapeutic agents namely epirubicin, doxorubicin and daunorubicin, and validated their inhibitory activity on cytokine production (Figure S1c).

We then used the cecal ligation and puncture (CLP) mouse model of experimental sepsis to investigate the *in vivo* effects of epirubicin (Rittirsch et al., 2009). In CLP, sepsis results from a polymicrobial infection of abdominal origin, leading to bacteremia and a systemic inflammatory response (Rittirsch et al., 2009). We adjusted CLP severity to a high-grade sepsis, where at least 80% of C57BL/6 mice succumbed within 48 h after the initial procedure. Under these conditions, epirubicin administered i.p. at the time of CLP and again 24 h later in a total of 1.2μg/g of body weight reproducibly and significantly ($p<0.001$) increased the survival of C57BL/6 mice subjected to CLP by nearly 80%, without the use of antibiotics (Figure 1a). A similar protective effect was observed in epirubicin-treated animals with the same dose and schedule but administered i.v. (Figure S1d). This appeared to be a general property of the anthracycline family because other representative members of this family of drugs identified in the initial chemical screen conferred a similar degree of protection against CLP (Figure 1b). The protective effect of anthracyclines was not dependent on the mouse strain as outbread NMRI mice were similarly protected by epirubicin (Figure 1c). Epirubicin was equally effective against another clinically relevant pathogen causing sepsis, *K. pneumoniae* administered intranasally (Figure 1d), arguing that epirubicin can be effective in the treatment of sepsis of different origins in addition to peritoneal sepsis. Mice previously subjected to CLP and treated with epirubicin were not immunocompromised as they could clear a secondary intranasal viral infection similarly to control mice (Figure 1e). Taken together, these results indicate that low doses of the anthracycline family of chemotherapeutic agents confer strong protection against severe sepsis, without causing host immunosuppression.

Epirubicin acts therapeutically to promote disease tolerance to severe sepsis

We found that in epirubicin-treated mice subjected to CLP the bacterial load in blood and target organs of sepsis, e.g., lung, liver, kidney and spleen 24 h post-CLP did not differ from that of untreated controls (Figure 2a). While at 48 h post-CLP we noticed a trend towards a lower bacterial load in the target organs of epirubicin-treated animals, the differences were not statistically significant, even if most untreated control animals die between 24 and 48 h after the CLP procedure. These results raised the possibility that the protective effect of epirubicin *in vivo* is related to disease tolerance without directly affecting the pathogen burden(Medzhitov et al., 2012). This idea was supported by the observation that the serum concentrations of several markers of tissue damage such as LDH (lung and general cellular damage), CK (muscle), ALT (liver) and urea (kidney) were substantially reduced to almost basal levels in epirubicin-treated mice, 24 h after CLP, compared to untreated mice (Figure

2b). In addition, we observed a substantial reduction in the levels of inflammatory mediators including TNF, IL-1β, IL-6 and HMGB1 compared to non-treated CLP mice (Figure 2c). We have also observed improvement of histological lesions in the lung, liver and kidney after CLP by treatment with epirubicin (Figure S2). To explore this further in the absence of bacteria, we found that the drug protected C57BL/6 mice from lethal septic shock caused by lipopolysaccharide (LPS, endotoxin) (Figure 2d).

Large spectrum antibiotics such as meropenem are very effective at lowering bacteremia and are standard drugs used in sepsis (Russell, 2006). We tested the efficacy of meropenem in CLP in comparison to epirubicin and found that while meropenem delayed the death rate of CLP-subjected mice, it did not prevent mortality (Figure 2e), in spite of a strong impact on bacterial burden (Figure 2f). This was in sharp contrast to the action of epirubicin, that did not interfere with bacteremia (Figure 2f) but prevented CLP-induced mortality (Figure 2e), again arguing for a role of epirubicin in conferring disease tolerance against severe sepsis (Larsen et al., 2010; Medzhitov et al., 2012).

Both epirubicin and meropenem decreased the amounts of IL-1β, TNF and HMGB1 in the serum of mice subjected to CLP (Figure 2g). This indicates that whereas decreased circulating levels of inflammatory mediators may contribute to confer protection against severe sepsis, inhibition of IL-1β, TNF and HMGB1 is not sufficient *per se* to explain the protective effect of epirubicin, which is in accordance with what is observed for other therapeutic approaches in the clinical setting (Hotchkiss and Karl, 2003). Taken together these data suggest that epirubicin acts through an additional alternative mechanism to cytokine inhibition to confer tolerance to sepsis.

Epirubicin protection against sepsis is mediated by ATM

Next, in order to explore the molecular mechanism behind the protective effects of anthracyclines, we used our *in vitro* assay system to perform a short hairpin RNA (shRNA)-based screen in THP-1 cells, focusing on kinases and phosphatases and using IL-1β and TNF secretion as assay readouts. While our *in vivo* results suggested the possibility that anthracyclines ameliorate the lethal effects of sepsis by a mechanism affecting tissue tolerance, we reasoned that our *in vitro* assay would be useful for the identification of candidate pathways mediating the anthracycline effects. We found several negative regulators of IL-1β productionin response to *E. coli* challenge, including the genes encoding Ataxia Telangiectasia Mutated (ATM), Checkpoint Kinase 1 (CHEK1) and Ataxia Telangiectasia and Rad3 Related (ATR) (Figure S3 and Supplemental Table S2). These findings suggest that DNA damage response (DDR) components are negative regulators of IL-1β secretion. Using a phospho-specific antibody against the activated form of ATM, we found that although *E. coli* alone was a poor, but reproducible ATM activator (Figure S3), epirubicin alone or in combination with *E. coli* triggered a robust ATM activation (Figure S3). This was confirmed using immunoblotting (Figure S3).

ATM is a master regulator of the DDR (Ciccia and Elledge, 2010) and is known to be activated by anthracyclines and other DNA damaging agents (Siu et al., 2004). Therefore we used ATM-deficient mice to test the contribution of the DDR to the protective effect of anthracyclines against severe sepsis. ATM-deficient ($Atm^{-/-}$) mice were not protected by epirubicin against CLP and died with similar kinetics to those of wild-type ($Atm^{+/+}$) animals that were treated with PBS alone (Figure 3a). We conclude that ATM expression is necessary to mediate the protective effect of epirubicin in sepsis. In striking contrast to wild-type mice (Figures 2b and c), in the absence of ATM, epirubicin no longer normalized the serologic markers of organ lesion (Figure 3b) or decreased the levels of inflammatory mediators (Figure 3c). However, in mice subjected to CLP and treated with etoposide (after *in vivo* titration to find the best and most effective dose), an agent known to cause DNA

double strand breaks and to activate ATM-dependent pathways (Montecucco and Biamonti, 2007), mortality induced by CLP was only partially rescued (Figure 3d), suggesting that ATM is necessary but not sufficient for the protection conferred by anthracyclines against sepsis.

In addition to double strand breaks (repaired in an ATM-dependent manner), anthracyclines also cause DNA interstrand cross-links, a DNA lesion known to be repaired by the Fanconi Anemia (FA) pathway (Ciccia and Elledge, 2010). Interestingly, FA patients were reported to spontaneously overproduce TNF (Briot et al., 2008; Vanderwerf et al., 2009), possibly because the FA protein FANCD2can directly inhibit TNF promoter activity (Matsushita et al., 2011). In THP-1 cells, we observed that FANCD2 is activated in an ATM-independent manner upon epirubicin treatment, as shown by its mono-ubiquitination (Figure 3e). These findings support the independence of signaling events initiated by the generation of DNA double strand breaks and DNA interstrand cross-links. We examined the contribution of this pathway for epirubicin protection of CLP and found that *Fancd2*$^{-/-}$ mice were slightly but significantly ($p<0.05$) impaired for the protective effects (Figure 3f).

These results suggest that activation of DDR is protective against sepsis. To further test this hypothesis we have used whole body sub-lethal γ-irradiation. We found a significant increase in the number of cells with γH2AX-positive foci ($p<0.001$), a surrogate marker of ATM activation (Ciccia and Elledge, 2010), in the lungs of whole body sub-lethal γ-irradiated mice as compared to controls (figure 3g). Mice subjected to CLP that were irradiated showed a significant increased survival ($p<0.001$) as compared to non-irradiated mice (Figure 3h). We conclude that the protective phenotype induced by epirubicin is dependent on the activation of multiple pathways downstream of a DDR. The activation of the ATM pathway is the main contributor, but the full protection requires the activation of additional DDR pathways, including the FA pathway.

The protective effect of epirubicin is dependent on the autophagy pathway

Although it is possible that the dominant ATM-mediated protection against sepsis might rely on ROS scavenging (Cosentino et al., 2010), on the induction of apoptosis of inflammatory cells (Garrison et al., 2011), on the preservation of genomic stability (Westbrook and Schiestl, 2010), or on the biogenesis of anti-inflammatory microRNAs such as miR-146a (Zhang et al., 2011), we found no significant contribution for any of these processes (Figure S4). We, therefore, explored a possible role for autophagy in this process, given that ATM is a negative regulator of mTOR, which is itself, an inhibitor of autophagy (Alexander et al., 2010a; Alexander et al., 2010b). Using autophagy-defective (*Lc3b*$^{-/-}$) mice, we found that the autophagy pathway is required for the *in vivo* effect of epirubicin (Figure 4a). Similarly to *Atm*$^{-/-}$ mice (Figure 3b and c), epirubicin was not able to decrease the serologic markers associated with organ lesion (Figure 4b) or to normalize cytokine levels in autophagy-defective mice (Figure 4c).

We then used LC3b-GFP mice to study the contribution of the autophagy pathway in the protection conferred by epirubicin. While FACS analysis shows that CLP alone induces LC3b aggregation in different splenocyte populations, namely monocytes and neutrophils, epirubicin treatment did not increase the autophagy pathway in these critical players in sepsis (Figure 5a). We then tested the impact of epirubicin on the survival of a conditional depletion of *Atg7* specifically in neutrophils and monocytes upon CLP, using *Atg7*$^{\text{loxP/loxP}}$*LysM*$^{\text{Cre}}$ GFP-LC3b animals. Strikingly, these animals were equally protected by epirubicin as compared to control mice (Figure 5b), suggesting that the autophagy pathway is not required in the myeloid compartment for the protective effects of epirubicin against sepsis.

Autophagy can be effectively monitored by the conversion and immobilization of LC3 (Kabeya et al., 2000). Because the autophagy pathway was not required in the myeloid compartment for protection against sepsis by epirubicin, we then looked at target organs of sepsis (lung, liver and kidney) using immunobloting to identify lipidation of LC3b as indicative of activation of the autophagy pathway. We found that epirubicin specifically induced lipidation of LC3b in the lung at 6 h, but not in the liver or kidney (Figure 5c). Although LC3 was transiently lipidated after CLP in the liver at 6 and 24 h as previously reported (Chien et al., 2011), levels of LC3 were not altered by epirubicin treatment (Figure 5c). We have further confirmed that autophagy was induced in the lung as shown by the increase of LC3b positive vesicles in lung sections at 6 h and 24 h comparing epirubicin treated and non-treated mice (Figure 5d).

We then deleted *Atg7* specifically in the lung (Figure S5), using an adenovirus-expressing CRE (Ad^{cre}) to intranasally infect $Atg7^{loxP/loxP}$ mice (Komatsu et al., 2005). When subjected to CLP, these mice were no longer protected from CLP by epirubicin treatment (Figure 5e). In contrast to control mice, in $Atg7^{loxP/loxP}Ad^{cre}$ mice the treatment with epirubicin does not improve the levels of circulating markers of organ lesion (Figure 5f). Accordingly, we observed a significant protective effect in survival after overexpression of ATG7 in the lung using adenovirus (Figure 5g).

By assessing the levels of γH2AX in the lungs of control or epirubicin-treated CLP-subjected mice, we found a significant increase in the number of cells with γH2AX-positive foci in lungs of epirubicin-treated mice (Figure 5h). To test whether ATM activation was also required in the lung, we used $Atm^{loxP/loxP}$ mice and Ad^{cre} to delete ATM specifically in the lung. Upon Ad^{cre}-mediated ATM deletion in the lung, mice were no longer protected against sepsis by treatment with epirubicin (Figure 5i). We therefore conclude that the protective effect of epirubicin in sepsis is, at least in part, dependent on the activation of ATM and of autophagy in target organs, namely the lung. These conclusions are further supported by intranasal delivery of epirubicin or etoposide to the lung (Figure 5j), because the protective effects as measured by survival are similar to the i.p. administration of those drugs (Figure 5j).

Epirubicin has a 24 h therapeutic window to protect against sepsis

Finally, we studied the therapeutic window of epirubicin in mice. When given alone, epirubicin conferred strong protection at the time of the procedure or until 3 h after the initiation of CLP (Figure 6a). When administered only 6 h after CLP, epirubicin quickly lost its protective effect (Figure 6a). However, if given in combination with meropenem, even when this antibiotic is only administered 12 h after CLP, low dose epirubicin conferred complete protection until at least 24 h after the initial procedure (Figure 6b and 6c). These results suggest that anthracyclines can be used not only to prevent sepsis, but also that they can act therapeutically when their administration is combined with a large spectrum antibiotic.

Discussion

Here we report that epirubicin, and more generally the group of anthracyclines, are very effective at conferring protection against severe sepsis in mice, even when used up to 24 h after the onset of infection. This therapeutic window is likely to be sufficient to make these drugs good candidates as useful therapeutic options in the clinic to reduce the mortality of sepsis in most patients that are either in the hospital or seek medical attention within the first few hours of symptoms initiation.

Although we began our investigation of the use of anthracyclines in sepsis by virtue of their effects in inhibiting inflammatory cytokine expression in myeloid cells *in vitro*, our studies have identified a mode of protection that seems to be much stronger and perhaps completely independent of such effects, and rather manifests at the level of DNA damage response and autophagy-induced protection in the lung. Thus, our findings uncover an unexpected role for these pathways in tissue (lung) tolerance to the pathological consequences of infection. These findings are especially relevant given that agents discovered in studies over the last few years targeting various pro-inflammatory cytokines have had limited success in humans. Our studies suggest a critical role for protecting host tissues thereby conferring protection against sepsis. Recent studies have highlighted the role of tissue tolerance to infection as an important aspect of host pathology (Medzhitov et al., 2012).

Interestingly, the protective effect of epirubicin seems to act irrespectively of the host pathogen burden, revealing that it confers disease tolerance to polymicrobial infection (Larsen et al., 2010; Raberg et al., 2009; Schneider and Ayres, 2008). This finding reveals that pharmacologic agents that provide tissue damage control can limit disease severity irrespectively of pathogen load and represent a promising therapeutic strategy against sepsis. Moreover, based on our identification of ATM as a major mediator of epirubicin effects, we propose that this protein and other components of the DNA damage response machinery constitute novel regulators of tolerance, without affecting pathogen resistance mechanisms.

Recent reports make our findings counter-intuitive as doxorubicin and daunorubicin have been shown to induce acute inflammation when injected in the abdomen where they induce cytokine secretion (Krysko et al., 2011; Sauter et al., 2011). However, the concentrations of anthracyclines utilized in these studies were more than 10-fold higher than those used here. By using lower concentrations we may reduce the cytotoxicity of these drugs and the resulting release of pro-inflammatory DAMPs by dying cells and reveal the additional pharmacological effects mediated by the surviving target cells. Interestingly, fluoroquinolones that are bacterial type II topoisomerase inhibitors, as opposed to anthracyclines, which are eukaryotic type II topoisomerase inhibitors, were reported to have immunomodulatory effects (Dalhoff and Shalit, 2003) when used in supra-therapeutic concentrations. Fluoroquinolones have been shown to protect against LPS model of septic shock (Khan et al., 2000). While the molecular mechanisms that explain these effects have not been elucidated, it has been proposed that higher doses of fluoroquinolones can inhibit mammalian topoisomerase type II enzymes in addition to their bacterial targets (Dalhoff and Shalit, 2003), an effect that can be achieved with very low doses of anthracyclines.

The induction of autophagy is a common response to many forms of cellular stress, including DNA damage (Mizushima and Komatsu, 2011). The rationale for testing the role of autophagy was based on the knowledge that ATM is a negative regulator of mTOR and that mTOR is a negative regulator of autophagy(Alexander et al., 2010a; Alexander et al., 2010b). We therefore reasoned that if epirubicin activates ATM (as we have confirmed), then it is possible that it induces autophagy. This line of investigation made sense because several reports(Chien et al., 2011; Nakahira et al., 2010) have suggested a protective role for autophagy in sepsis. To probe the contribution of autophagy for the protective phenotype conferred by epirubicin, we have used two different genetic deletions in the autophagy pathway (LC3b and ATG7) and in both cases the protection normally conferred by epirubicin is lost. This is considered one of the best and most compelling ways to test the contribution of autophagy and the direction of autophagic flow (Klionsky et al., 2012).

Chien et al. have previously found that autophagy is transiently induced in the rat liver after CLP (Chien et al., 2011), and later made similar observations in the rat kidney (Hsiao et al., 2012). Chien et al. have speculated that the transient induction of autophagy in these organs

could be required for protection and its decline at a later stage could contribute to the functional failure in liver during polymicrobial sepsis. After we found autophagy induction by epirubicin, we thought that one reason to explain anthracycline protection against CLP could be the sustained activation of autophagy in the liver and/or kidney preventing its decline as observed by Chien et al. Instead we found that both in the liver and in the kidney, treatment with epirubicin did not change this pattern, but instead transiently induced autophagy in the lung, a response that was not present in mice subjected to CLP in the absence of epirubicin treatment. We also report that epirubicin is highly protective when delivered directly to the lung and that overexpression of ATG7 specifically in the lung improves survival to CLP. Together, these observations strongly suggest that lung protection is critical and likely dominant because it prevents failure of additional organs, which makes our findings all the more relevant as the lung is the organ that often shows the first signs of dysfunction in septic patients and drives the failure of other target organs particularly the kidney and later the liver (Hotchkiss and Karl, 2003).

Nakahira et al. demonstrate that depletion of the autophagic proteins LC3b and beclin 1 enhanced the activation of caspase-1 and secretion of IL-1β and IL-18 (Nakahira et al., 2010). While we also observe inhibition of IL-1β secretion *in vitro* and *in vivo* by treatment with epirubicin, this finding is not dependent on the decreased activation of caspase-1 mediated by autophagy because even low concentrations of epirubicin lead to higher levels of active caspase-1 (Chora et al., data not shown) but this event is overshadowed by a strong inhibition of IL-1β, as well as most of pro-inflammatory mediators that are NF-kB dependent, at the transcriptional level. We have now identified the mechanism: epirubicin targets the N-terminal region of p65, inhibiting transcription by blocking the DNA-binding ability of NF-kB (Chora et al., data not shown). The Nakahira et al. report also suggested to us that severe sepsis could cause DNA lesions capable of activating the inflammasome leading to chronic inflammation and that the induction of autophagy could block the inflammasome and prevent excessive inflammation. To address this possibility, we have used comet assays to look at different types of DNA damage in response to bacterial challenge in the presence and absence of epirubicin. We did find that *E. coli* alone triggers a small but measurable increase of DNA single strand breaks (Neves-Costa et al., unpublished). However the presence of epirubicin does not decrease, rather it increases DNA damage as compared to *E. coli* alone. Therefore, epirubicin does not decrease the generation of DNA damaged species that can activate the inflammasome. We conclude that while the Nakahira et al. work clearly shows that autophagic proteins regulate NALP3-dependent inflammation by preserving mitochondrial integrity, the autophagy protection conferred by epirubicin to CLP does not depend on the mechanisms demonstrated in the Nakahira et al. paper, specifically the negative regulation of IL-1β secretion by autophagy.

Interestingly, the protective phenotype of epirubicin is strikingly similar to that of RIPK3-deficient mice (Duprez et al., 2011), suggesting that epirubicin-mediated, ATM-dependent, autophagy induction can possibly prevent TNF-driven necroptosis in such key organs in sepsis pathology as the lung. In fact, there have been recent works that support the role of autophagy in the inhibition of necroptosis (Bray et al., 2012; Degenhardt et al., 2006; Lu and Walsh, 2012; Shen and Codogno, 2012), which could be achieved by targeting key necroptosis signaling components (such as RIPK1 and RIPK3) for degradation. It is also possible that autophagy protects against severe sepsis because its activation increases the degradation of pro-inflammatory mediators with an important role in sepsis, like HMGB1 (Li et al., 2011). In addition, increased effective autophagy can be beneficial in sepsis due to its critical role in the removal of damaged mitochondria in an ATM-dependent manner(Valentin-Vega and Kastan, 2012). The molecular mechanisms at the basis of epirubicin-induced protection in sepsis by autophagy are certainly an interesting topic for future studies.

Experimental Procedures

Animal Model and Anthracycline Treatment

Animal care and experimental procedures were conducted in accordance with Portuguese and US guidelines and regulations after approval by the respective local committees (Instituto de Medicina Molecular and Instituto Gulbenkian de Ciência). All mice used were 8–12 weeks old. Mice were bred and maintained under specific pathogen-free (SPF) conditions. C57BL/6 and C57BL/6 *Atm*$^{-/-}$ mi ce were obtained from the Instituto Gulbenkian de Ciência (a kind gift from Dr. Vasco Barreto). C57BL/6 *Nrf2*$^{-/-}$ mice were provided originally from the RIKEN BioResource Center (Koyadai, Tsukuba, Ibaraki, Japan) and subsequently by the Instituto Gulbenkian de Ciência. LC3b$^{-/-}$ (B6129PF2/J background) and NMRI mice were purchased from Jackson and Charles River laboratories, respectively. miR-146-deficient mice were generated in the Baltimore's laboratory (Boldin et al., 2011). *Fancd2*$^{-/-}$ mice were generated by the Grompe laboratory (Houghtaling et al., 2003). *Atg7*$^{loxP/loxP}$ were generated by Masaaki Komatsu and obtained from the Green laboratory. *Atm*$^{loxP/loxP}$ mice were generated and obtained from the F.W. Alt's laboratory. CLP was performed as described previously (Rittirsch et al., 2009). The endotoxemia model was performed by injecting intraperitoneally (i.p.) a single dose of 50 μg/g body weight of LPS (from *E. coli* serotype 026:B6; Sigma-Aldrich). Pulmonary monostrain infections were carried out as described previously (Weber et al., 2011), using intranasal injection of *Klebsiella pneumoniae* (ATCC13803) at 8x10^7 colony-forming units (CFU). Epirubicin (Sigma-Aldrich), doxorubicin (Sigma-Aldrich), daunorubicin (Sigma-Aldrich) were dissolved in PBS, etoposide (Sigma-Aldrich) was dissolved in DMSO, aliquoted and stored at −80°C. Meropenem (AstraZeneca, Lisbon, Portugal). Epirubicin and daunorubicin (0.6μg/g body weight), doxorubicin (0.5μg/g body weight), etoposide (2μg/g body weight) were injected intraperitoneally at 0 and 24 h following CLP. Meropenem (20μg/g body weight b.i.d.) was injected i.p. for 5 consecutive days.

Colony-Forming Units Assay

Blood samples from septic or mock CLP mice were collected by cardiac puncture at indicated times after surgery. Mice were subsequentially perfused *in toto* with 10mL ice cold PBS and spleen, liver and kidneys were surgically removed and homogenized in 5mL of sterile PBS. Serial dilutions of blood and tissue homogenates were immediately plated on Trypticase Soy Agar II plates supplemented with 5% Sheep Blood. CFUs were counted after a 12 h incubation at 37 C.

Serology and Cytokine Measurement

Plasma from blood samples obtained 24 h post-CLP was collected after centrifugation. LDH, CK, ALT and urea levels were measured using the BioAssay Systems kits (BioAssay Systems, California) according to company's protocol. Levels of TNF, IL-1β and IL-6 were measured using the murine ELISA kits (R&D Systems, Minneapolis) according to company's protocol. Levels of HMGB1 were assessed using a murine ELISA kit (Shino Test Corporation, Tokyo) according to company's protocol.

Histology

Mice were euthanized, perfused *in toto* with 10mL ice cold PBS and lungs and livers were surgically removed. Livers were placed in 10% phosphate buffered formalin for 24 h after which were embedded in paraffin. Sections were subsequently incubated with a primary antibody reactive to HMGB1 (Abcam, Cambridge, UK) followed by incubation with biotinylated secondary antibody and then with biotinylated horseradish peroxidase. Staining was developed by addition of diaminobenzidine (DAB) substrate (Vector Labs, Burlingame,

CA) and counterstained with hematoxylin. Lungs were embedded in Tissue-Tek OCT (Sakura, Alphen aan den Rijn, Netherlands), and snap-frozen in liquid nitrogen. Lung sections (7 μm) were fixed in 1% paraformaldehyde in PBS for 2 min, followed by methanol at −20°C for 10 min and then in acetone for 2 min. Detection of LC3b and histone γH2AX was performed by incubating sections overnight at 4°C with rabbit polyclonal antibodies specific for, respectively, LC3b (L7543, Sigma Aldrich, USA) and γH2AX (phosphoS139) (ab2893; Abcam, Cambridge, UK); incubation with a secondary DyLight 488-coupled antibody (Jackson ImmunoResearch Laboratories, West Grove, PA, USA) was for 1 h at room temperature. Sections were counterstained with DAPI (0.5 μg/mL) to visualize DNA and mounted in Vectashield (Vector Laboratories Inc., Burlingame, CA) before confocal microscopy. Samples were examined with a Zeiss LSM 510 META laser scanning confocal microscope (Carl Zeiss, Jena, Germany). The acquired images were analyzed using a MATLAB (Mathworks; Natick, MA) routine developed in-house to perform automatic threshold segmentation and enumeration of individual cell nuclei stained with DAPI.

In vivo Viral Infection and Viral Titer Assay

Murid herpesvirus-4 infection and viral particle quantification was performed as previously described (Marques et al., 2008). Briefly, mice were intranasally inoculated with 1000 PFU of MuHV-4 strain 68 in 20 μLof PBS under light isoflurane anaesthesia. At 6 and 12 days post-infection, lungs were removed and homogenized in 5mLof Glasgow's modified Eagle's medium (GMEM). Infectious virus titers in freeze-thawed lung homogenates were determined by serial diluted suspension assay using Baby hamster kidney cells (BHK-21) cultured in GMEM supplemented with 10% fetal bovine serum, 10% tryptose phosphate broth, 2 mM glutamine, 100 U/ml penicillin and 100 μg/ml streptomycin (GMEM). Plates were incubated for four days, fixed with 10% formal saline and counterstained with toluidine blue. Viral plaques were counted with a plate microscope. *Cre*-adenovirus were obtained from the University of Iowa, prepared as a calcium-phosphate coprecipitate and incubated for 20 min at room temperature. $Atg7^{loxP/loxP}$ and $ATM^{loxP/loxP}$ were subjected to light isoflurane anesthesia and allowed to inhale 125μLof virus at a concentration of 2.5×10^7PFU. Additionally, wild -type C57BL/6 mice were included as controls. Mice were allowed to rest for 5 days after inhalation after which were subjected to CLP.

Stainings and Flow Cytometry

Peritoneal infiltrating leukocytes from either wild-type or LC3b-GFP transgenic animals were obtained 24 h post CLP by lavage with 5 mL of sterile ice-cold PBS, washed and blocked with mouse Ab anti-FcγIII/II (clone 93) receptor diluted in PBS containing 2% FCS (v/v) for 20 min at 4°C. Surface markers were detected by incubating for 30 min at 4°C with mouse Ab anti-CD4 (clone GK1.5), -CD8 (clone 53–6.7), -CD19 (clone 6D5), -Ly-6G (clone 1A8) (all Biolegend) and -neutrophil monoclonal antibody (clone 7/4) (Abcam, Cambridge, UK). Dead cells were excluded by co-staining with propidium iodide. Total cell number was determined by flow cytometry using a fixed number of latex beads (Beckman Coulter, CA, USA) co-acquired with a pre-established volume of the cellular suspension. For phospho-ATM intracellular staining, stimulated THP-1 cells were washed and fixed with ice-cold methanol. Mouse Ab anti-phosphoATM pS1981, clone 10H11.E12 (IgG1k) (Rockland, MA, USA) was incubated for 60 min at room temperature followed by an incubation of secondary Ab conjugated with Alexa 488 (Molecular Probes, CA, USA). Fluorescence was measured by flow cytometry, and data analyzed using FlowJo software.

Immunoblotting

Mouse phospho-ATM (4526, Cell Signaling, Danvers, MA, 1:1000 dilution), rabbit total ATM (2873, Cell Signaling, Danvers, MA, 1:1000 dilution), rabbit LC3b (Sigma, 1:1000

dilution) and the rabbit Fancd2 (Novus Biologicals, CO, USA; 1:1000 dilution) Ab were used overnight at 4°C. Primary Ab were detected using peroxidase conjugated secondary Ab (1h; RT) and developed with SuperSignal chemiluminescent detection kit (Pierce, Carcavelos, Portugal).

Supplementary Material

Refer to Web version on PubMed Central for supplementary material.

Acknowledgments

We are grateful to Vasco Barreto for *Atm*$^{-/-}$ and Frederick Alt for *Atm*$^{loxP/loxP}$ mice. We thank Mario Ramirez for bacterial strains to probe epirubicin protection in different models of sepsis. L.F.M. receives support from FLAD and FCT (grants PTDC/SAU-IMU/110303/2009, PTDC/SAU-MII/100780/2008, and PTDC/SAU-IMU/110303/2009), A.C. receives support from FCT (PTDC/SAU-IMU/110303/2009), J.F. receives support from a Gulbenkian grant (96526/2009) and P.P. is an FCT fellow (SFRH/BD/45502/2008).

References

Alexander A, Cai SL, Kim J, Nanez A, Sahin M, MacLean KH, Inoki K, Guan KL, Shen J, Person MD, et al. ATM signals to TSC2 in the cytoplasm to regulate mTORC1 in response to ROS. Proc Natl Acad Sci U S A. 2010a; 107:4153–4158. [PubMed: 20160076]

Alexander A, Kim J, Walker CL. ATM engages the TSC2/mTORC1 signaling node to regulate autophagy. Autophagy. 2010b; 6

Angus DC, Wax RS. Epidemiology of sepsis: an update. Crit Care Med. 2001; 29:S109–116. [PubMed: 11445744]

Annane D, Aegerter P, Jars-Guincestre MC, Guidet B. Current epidemiology of septic shock: the CUB-Rea Network. Am J Respir Crit Care Med. 2003; 168:165–172. [PubMed: 12851245]

Boldin MP, Taganov KD, Rao DS, Yang L, Zhao JL, Kalwani M, Garcia-Flores Y, Luong M, Devrekanli A, Xu J, et al. miR-146a is a significant brake on autoimmunity, myeloproliferation, and cancer in mice. J Exp Med. 2011; 208:1189–1201. [PubMed: 21555486]

Bone RC, Sibbald WJ, Sprung CL. The ACCP-SCCM consensus conference on sepsis and organ failure. Chest. 1992; 101:1481–1483. [PubMed: 1600757]

Bray K, Mathew R, Lau A, Kamphorst JJ, Fan J, Chen J, Chen HY, Ghavami A, Stein M, DiPaola RS, et al. Autophagy suppresses RIP kinase-dependent necrosis enabling survival to mTOR inhibition. PLoS One. 2012; 7:e41831. [PubMed: 22848625]

Briot D, Mace-Aime G, Subra F, Rosselli F. Aberrant activation of stress-response pathways leads to TNF-alpha oversecretion in Fanconi anemia. Blood. 2008; 111:1913–1923. [PubMed: 18055871]

Chien WS, Chen YH, Chiang PC, Hsiao HW, Chuang SM, Lue SI, Hsu C. Suppression of autophagy in rat liver at late stage of polymicrobial sepsis. Shock. 2011; 35:506–511. [PubMed: 21263383]

Ciccia A, Elledge SJ. The DNA damage response: making it safe to play with knives. Mol Cell. 2010; 40:179–204. [PubMed: 20965415]

Cosentino C, Grieco D, Costanzo V. ATM activates the pentose phosphate pathway promoting anti-oxidant defence and DNA repair. EMBO J. 2010; 30:546–555. [PubMed: 21157431]

Dalhoff A, Shalit I. Immunomodulatory effects of quinolones. Lancet Infect Dis. 2003; 3:359–371. [PubMed: 12781508]

Degenhardt K, Mathew R, Beaudoin B, Bray K, Anderson D, Chen G, Mukherjee C, Shi Y, Gelinas C, Fan Y, et al. Autophagy promotes tumor cell survival and restricts necrosis, inflammation, and tumorigenesis. Cancer Cell. 2006; 10:51–64. [PubMed: 16843265]

Duprez L, Takahashi N, Van Hauwermeiren F, Vandendriessche B, Goossens V, Vanden Berghe T, Declercq W, Libert C, Cauwels A, Vandenabeele P. RIP kinase-dependent necrosis drives lethal systemic inflammatory response syndrome. Immunity. 2011; 35:908–918. [PubMed: 22195746]

Garrison SP, Thornton JA, Hacker H, Webby R, Rehg JE, Parganas E, Zambetti GP, Tuomanen EI. The p53-target gene puma drives neutrophil-mediated protection against lethal bacterial sepsis. PLoS Pathog. 2011; 6:e1001240. [PubMed: 21203486]

Hotchkiss RS, Karl IE. The pathophysiology and treatment of sepsis. N Engl J Med. 2003; 348:138–150. [PubMed: 12519925]

Houghtaling S, Timmers C, Noll M, Finegold MJ, Jones SN, Meyn MS, Grompe M. Epithelial cancer in Fanconi anemia complementation group D2 (Fancd2) knockout mice. Genes Dev. 2003; 17:2021–2035. [PubMed: 12893777]

Hsiao HW, Tsai KL, Wang LF, Chen YH, Chiang PC, Chuang SM, Hsu C. The decline of autophagy contributes to proximal tubular dysfunction during sepsis. Shock. 2012; 37:289–296. [PubMed: 22089196]

Janeway CA Jr, Medzhitov R. Innate immune recognition. Annu Rev Immunol. 2002; 20:197–216. [PubMed: 11861602]

Kabeya Y, Mizushima N, Ueno T, Yamamoto A, Kirisako T, Noda T, Kominami E, Ohsumi Y, Yoshimori T. LC3, a mammalian homologue of yeast Apg8p, is localized in autophagosome membranes after processing. EMBO J. 2000; 19:5720–5728. [PubMed: 11060023]

Khan AA, Slifer TR, Araujo FG, Suzuki Y, Remington JS. Protection against lipopolysaccharide-induced death by fluoroquinolones. Antimicrob Agents Chemother. 2000; 44:3169–3173. [PubMed: 11036044]

Klionsky DJ, Abdalla FC, Abeliovich H, Abraham RT, Acevedo-Arozena A, Adeli K, Agholme L, Agnello M, Agostinis P, Aguirre-Ghiso JA, et al. Guidelines for the use and interpretation of assays for monitoring autophagy. Autophagy. 2012; 8:445–544. [PubMed: 22966490]

Komatsu M, Waguri S, Ueno T, Iwata J, Murata S, Tanida I, Ezaki J, Mizushima N, Ohsumi Y, Uchiyama Y, et al. Impairment of starvation-induced and constitutive autophagy in Atg7-deficient mice. J Cell Biol. 2005; 169:425–434. [PubMed: 15866887]

Krysko DV, Kaczmarek A, Krysko O, Heyndrickx L, Woznicki J, Bogaert P, Cauwels A, Takahashi N, Magez S, Bachert C, Vandenabeele P. TLR-2 and TLR-9 are sensors of apoptosis in a mouse model of doxorubicin-induced acute inflammation. Cell Death Differ. 2011; 18:1316–1325. [PubMed: 21311566]

Larsen R, Gozzelino R, Jeney V, Tokaji L, Bozza FA, Japiassu AM, Bonaparte D, Cavalcante MM, Chora A, Ferreira A, et al. A central role for free heme in the pathogenesis of severe sepsis. Sci Transl Med. 2010; 2:51ra71.

Levy MM, Fink MP, Marshall JC, Abraham E, Angus D, Cook D, Cohen J, Opal SM, Vincent JL, Ramsay G. 2001 SCCM/ESICM/ACCP/ATS/SIS International Sepsis Definitions Conference. Crit Care Med. 2003; 31:1250–1256. [PubMed: 12682500]

Li W, Zhu S, Li J, Assa A, Jundoria A, Xu J, Fan S, Eissa NT, Tracey KJ, Sama AE, Wang H. EGCG stimulates autophagy and reduces cytoplasmic HMGB1 levels in endotoxin-stimulated macrophages. Biochem Pharmacol. 2011; 81:1152–1163. [PubMed: 21371444]

Lu JV, Walsh CM. Programmed necrosis and autophagy in immune function. Immunol Rev. 2012; 249:205–217. [PubMed: 22889224]

Marques S, Alenquer M, Stevenson PG, Simas JP. A single CD8+ T cell epitope sets the long-term latent load of a murid herpesvirus. PLoS Pathog. 2008; 4:e1000177. [PubMed: 18846211]

Martin GS, Mannino DM, Eaton S, Moss M. The epidemiology of sepsis in the United States from 1979 through 2000. N Engl J Med. 2003; 348:1546–1554. [PubMed: 12700374]

Matsushita N, Endo Y, Sato K, Kurumizaka H, Yamashita T, Takata M, Yanagi S. Direct inhibition of TNF-alpha promoter activity by Fanconi anemia protein FANCD2. PLoS One. 2011; 6:e23324. [PubMed: 21912593]

Medzhitov R. Origin and physiological roles of inflammation. Nature. 2008; 454:428–435. [PubMed: 18650913]

Medzhitov R, Schneider DS, Soares MP. Disease tolerance as a defense strategy. Science. 2012; 335:936–941. [PubMed: 22363001]

Mizushima N, Komatsu M. Autophagy: renovation of cells and tissues. Cell. 2011; 147:728–741. [PubMed: 22078875]

Montecucco A, Biamonti G. Cellular response to etoposide treatment. Cancer Lett. 2007; 252:9–18. [PubMed: 17166655]

Nakahira K, Haspel JA, Rathinam VA, Lee SJ, Dolinay T, Lam HC, Englert JA, Rabinovitch M, Cernadas M, Kim HP, et al. Autophagy proteins regulate innate immune responses by inhibiting

the release of mitochondrial DNA mediated by the NALP3 inflammasome. Nat Immunol. 2010; 12:222–230. [PubMed: 21151103]

Raberg L, Graham AL, Read AF. Decomposing health: tolerance and resistance to parasites in animals. Philos Trans R Soc Lond B Biol Sci. 2009; 364:37–49. [PubMed: 18926971]

Raberg L, Sim D, Read AF. Disentangling genetic variation for resistance and tolerance to infectious diseases in animals. Science. 2007; 318:812–814. [PubMed: 17975068]

Rittirsch D, Huber-Lang MS, Flierl MA, Ward PA. Immunodesign of experimental sepsis by cecal ligation and puncture. Nat Protoc. 2009; 4:31–36. [PubMed: 19131954]

Russell JA. Management of sepsis. N Engl J Med. 2006; 355:1699–1713. [PubMed: 17050894]

Sauter KA, Wood LJ, Wong J, Iordanov M, Magun BE. Doxorubicin and daunorubicin induce processing and release of interleukin-1beta through activation of the NLRP3 inflammasome. Cancer Biol Ther. 2011; 11:1008–1016. [PubMed: 21464611]

Schneider DS, Ayres JS. Two ways to survive infection: what resistance and tolerance can teach us about treating infectious diseases. Nat Rev Immunol. 2008; 8:889–895. [PubMed: 18927577]

Seixas E, Gozzelino R, Chora A, Ferreira A, Silva G, Larsen R, Rebelo S, Penido C, Smith NR, Coutinho A, Soares MP. Heme oxygenase-1 affords protection against noncerebral forms of severe malaria. Proc Natl Acad Sci U S A. 2009; 106:15837–15842. [PubMed: 19706490]

Shen HM, Codogno P. Autophagy is a survival force via suppression of necrotic cell death. Exp Cell Res. 2012; 318:1304–1308. [PubMed: 22366289]

Siu WY, Lau A, Arooz T, Chow JP, Ho HT, Poon RY. Topoisomerase poisons differentially activate DNA damage checkpoints through ataxia-telangiectasia mutated-dependent and -independent mechanisms. Mol Cancer Ther. 2004; 3:621–632. [PubMed: 15141020]

Suffredini AF, Munford RS. Novel therapies for septic shock over the past 4 decades. JAMA. 2011; 306:194–199. [PubMed: 21750297]

Takeuchi O, Akira S. Pattern recognition receptors and inflammation. Cell. 2010; 140:805–820. [PubMed: 20303872]

Ulloa L, Tracey KJ. The “cytokine profile”: a code for sepsis. Trends Mol Med. 2005; 11:56–63. [PubMed: 15694867]

Valentin-Vega YA, Kastan MB. A new role for ATM: regulating mitochondrial function and mitophagy. Autophagy. 2012; 8:840–841. [PubMed: 22617444]

Vanderwerf SM, Svahn J, Olson S, Rathbun RK, Harrington C, Yates J, Keeble W, Anderson DC, Anur P, Pereira NF, et al. TLR8-dependent TNF-(alpha) overexpression in Fanconi anemia group C cells. Blood. 2009; 114:5290–5298. [PubMed: 19850743]

Weber SE, Tian H, Pirofski LA. CD8+ cells enhance resistance to pulmonary serotype 3 Streptococcus pneumoniae infection in mice. J Immunol. 2011; 186:432–442. [PubMed: 21135172]

Westbrook AM, Schiestl RH. Atm-deficient mice exhibit increased sensitivity to dextran sulfate sodium-induced colitis characterized by elevated DNA damage and persistent immune activation. Cancer Res. 2010; 70:1875–1884. [PubMed: 20179206]

Zhang X, Wan G, Berger FG, He X, Lu X. The ATM kinase induces microRNA biogenesis in the DNA damage response. Mol Cell. 2011; 41:371–383. [PubMed: 21329876]

Highlights

- Anthracyclines confer strong protection against severe sepsis.
- Anthracyclines act therapeutically by promoting disease tolerance to severe sepsis.
- DDR and autophagy are required in the lung for anthracycline-induced protection.
- ATM and FA pathways are required for protection.

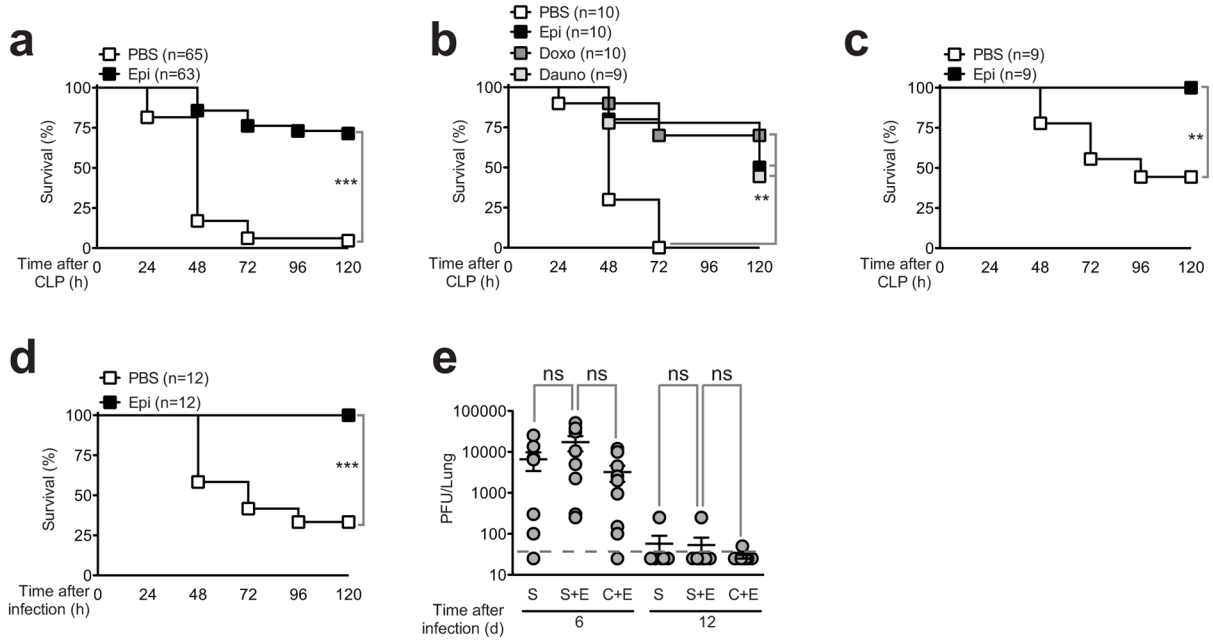

Figure 1. Epirubicin affords protection against severe sepsis

(a) Survival of C57BL/6 wild-type animals subjected to CLP treated with carrier (PBS) or epirubicin (Epi) (0.6μg/g body weight) at the time of procedure and 24 hours later. **(b)** Survival of C57BL/6 wild-type animals subjected to CLP treated with carrier (PBS), epirubicin (Epi), doxorubicin (Doxo) or daunorubicin (Dauno). Treatment schedule and doses as in (a). **(c)** Survival of NMRI mice subjected to CLP and treated with carrier (PBS) or epirubicin (Epi) as in (a). **(d)** Survival of C57BL/6 wild-type animals following intranasal inoculation of *Klebsiella pneumoniae* and treated with carrier (PBS) or epirubicin (Epi) as in (a). **(e)** Quantification of infectious viral MuHV-4 particles in lung of C57BL/6 wild-type animals previously subjected to mock CLP (S), mock CLP treated with epirubicin (S+E) or CLP treated with epirubicin (C+E). Epirubicin treatment dose and schedule as in (a). Mice were intranasally inoculated with 1000 PFU of MuHV-4 on day 3 post CLP and viral particles quantified by plaque assay at days 6 and 12 post viral infection. Each circle represents individual animals and horizontal lines indicate arithmetic means ± SEM from two independent assays. The dashed horizontal line represents the limit of detection of the assay. ns, not significant; *P<0.05; **P<0.01; ***P<0.001 (log-rank (Mantel-Cox) test for (a) to (d) and Mann-Whitney test for (e)). See also Figure S1 and Table S1.

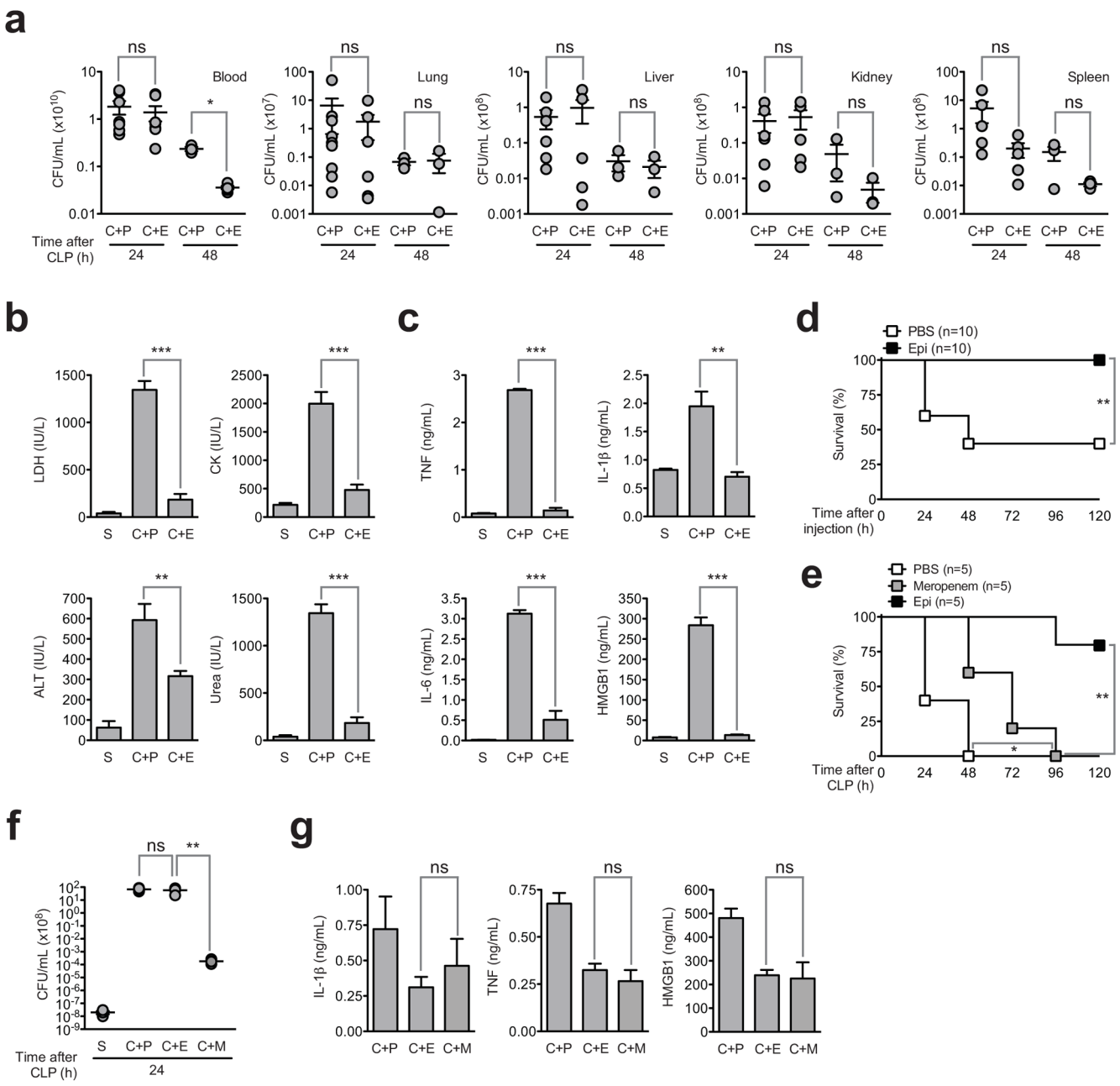

Figure 2. Epirubicin promotes disease tolerance to severe sepsis

(a) Polymicrobial load (CFUs) in blood, lung, liver, kidney and spleen, at indicated time points, of C57BL/6 animals undergoing CLP and treated with PBS (C+P) or epirubicin (C+E) (0.6μg/g body weight) at the time of procedure and 24 hours later. Each circle represents individual animals. Horizontal lines indicate arithmetic means ± SEM. **(b) and (c)** Epirubicin counteracts tissue damage and inflammation associated with CLP as assessed by (b) LDH, CK, ALT, urea and (c) TNF, IL-1β, IL-6 and HMGB1 plasma concentrations in C57BL/6 wild-type animals 24 hours after mock CLP (S) (n=2) or CLP followed by treatment with PBS (C+P) (n=5) or epirubicin (C+E) (n=7) as in (a). Results shown represent arithmetic means ± SEM from duplicate (b) or triplicate (c) readings per animal. **(d)** Survival of C57BL/6 wild-type animals following lethal LPS injection and treatment

with carrier (PBS) or epirubicin (Epi) as in (a). **(e)** Survival of C57BL/6 wild-type animals subjected to CLP treated with carrier (PBS), meropenem (40μg/g body weight/day) or epirubicin (Epi) as in (a). **(f)** CFUs in blood, at indicated time, of C57BL/6 animals undergoing mock CLP (S) or CLP followed by treatement with PBS (C+P), epirubicin (C +E) or meropenem (C+M) as in (a). Each circle represents individual animals. Horizontal lines indicate arithmetic means ± SEM. **(g)** IL-1β, TNF and HMGB1 plasma concentrations in C57BL/6 wild-type animals 24 hours after CLP followed by treatment with PBS (C+P) (n=4), epirubicin (C+E) (n=5) or meropenem (C+M) (n=5) as in (c). ns, not significant; *P<0.05; **P<0.01; ***P<0.001 (log-rank (Mantel-Cox) test for (d) and (e), Mann-Whitney test for (a) and (f), and unpaired t test for (b), (c) and (g)). See also Figure S2.

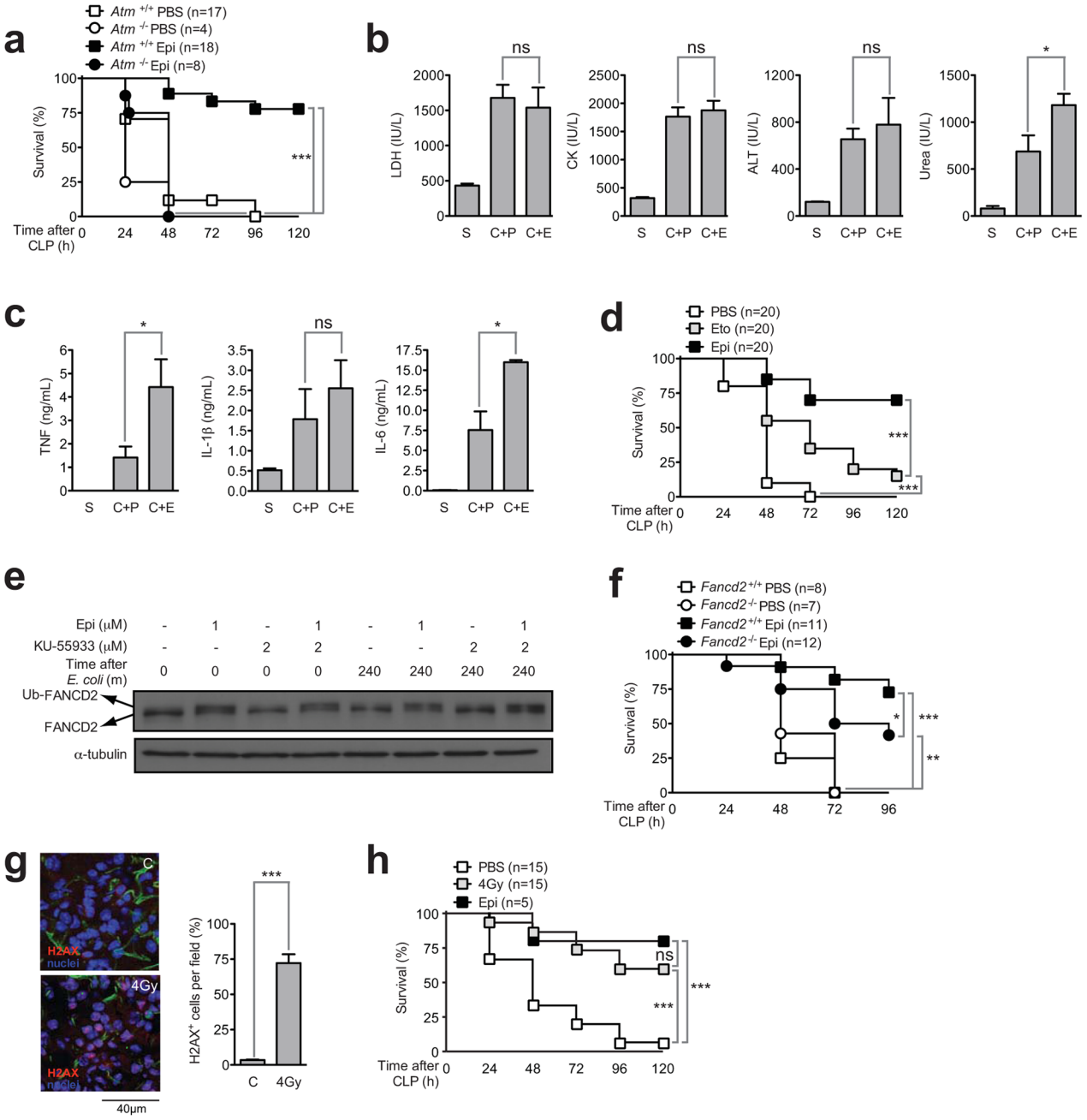

Figure 3. The protection afforded by epirubicin against severe sepsis is mediated by ATM

(a) Survival of $Atm^{+/+}$ and $Atm^{-/-}$ C57BL/6 animals subjected to CLP and treated with PBS or epirubicin (Epi) with same schedule and dose as in fig 1. **(b)** LDH, CK, ALT, urea and **(c)** TNF, IL-1β and IL-6 plasma concentrations in $Atm^{-/-}$ C57BL/6 animals 24 hours after mock CLP (S) (n=2) or CLP followed by treatment with PBS (C+P) (n=8) or epirubicin (C+E) (n=8) as in (a). Results shown represent arithmetic means ± SEM from triplicate readings per animal. **(d)** Survival of PBS-, etoposide (Eto)-, and epirubicin (Epi)-treated wild-type C57BL/6 animals undergoing CLP. Etoposide dose was 2μg/g body weight. Treatment schedule as in (a). **(e)** FANCD2 and Ub-FANCD2 protein levels by immunoblotting in THP-1 cells following *E. coli* challenge after a pre-incubation (1 hour) with carrier,

epirubicin or KU-55933 as indicated. **(f)** Survival of *Fancd2*$^{+/+}$ and *Fancd2*$^{-/-}$ animals subjected to CLP and treated with PBS or epirubicin (Epi) with same schedule and dose as in (a). **(g)** Representative sections of γH2AX staining and percentage of γH2AX^{+} cells per field (right panel) in lungs isolated 1 hour after mice were subjected to whole body γ irradiation (4 Gy). Results shown represent arithmetic means ± SD from 3 fields. **(h)** Survival of C57BL/6 wild-type animals subjected to CLP following whole body γ irradiation (4Gy) or treated with carrier (PBS) or epirubicin (Epi) as in (a). ns, not significant; *P<0.05; **P<0.01; ***P<0.001 (log-rank (Mantel-Cox) test for (a), (d), (f) and (h) and unpaired t test for (b), (c) and (g)). See also Figure S3 and Table S2.

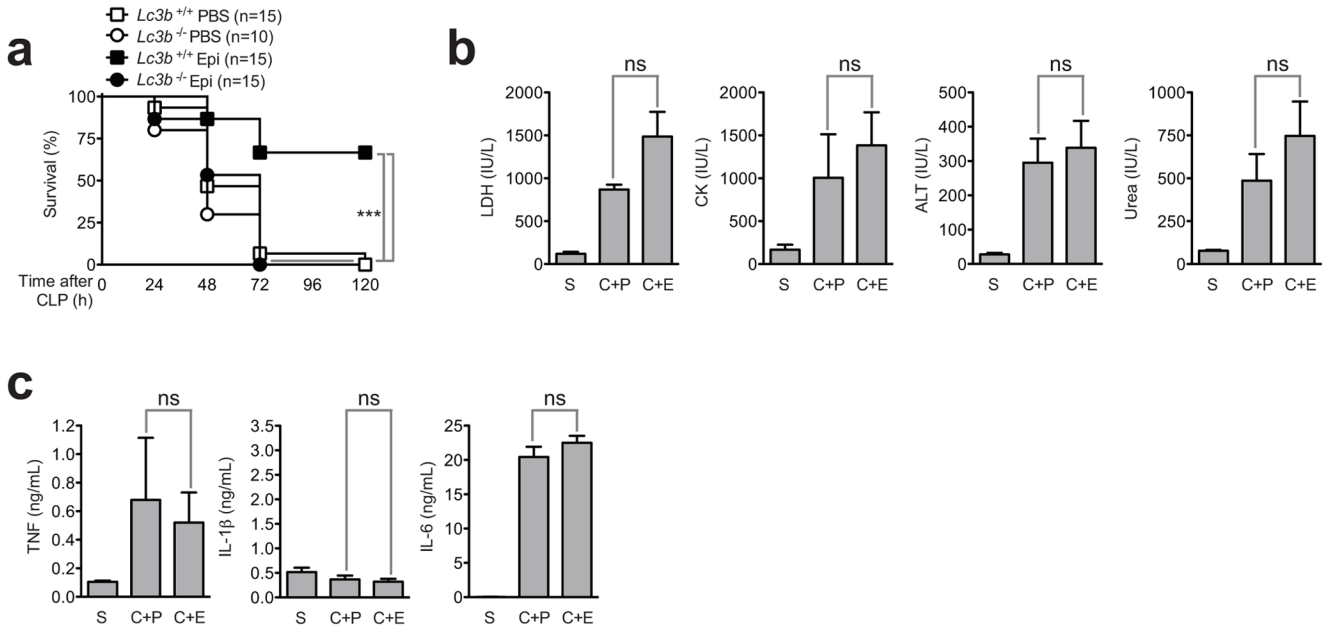

Figure 4. The ATM-dependent protection of epirubicin against severe sepsis relies on the induction of autophagy

(a) Survival of *Lc3b*$^{+/+}$ and *Lc3b*$^{-/-}$ animals subjected to CLP and treated with PBS or epirubicin (Epi) with same schedule and dose as in fig 1. **(b)** LDH, CK, ALT, urea and **(c)** TNF, IL-1β and IL-6 plasma concentrations in *Lc3b*$^{-/-}$ animals 24 hours after mock CLP (S) (n=2) or CLP followed by treatment with PBS (C+P) (n=4) or epirubicin (C+E) (n=7) as in (2b). Results shown represent arithmetic means ± SEM from triplicate readings per animal. ns, not significant; *P<0.05; **P<0.01; ***P<0.001 (log-rank (Mantel-Cox) test for (a), unpaired t test for (b) and (c)). See also Figure S4.

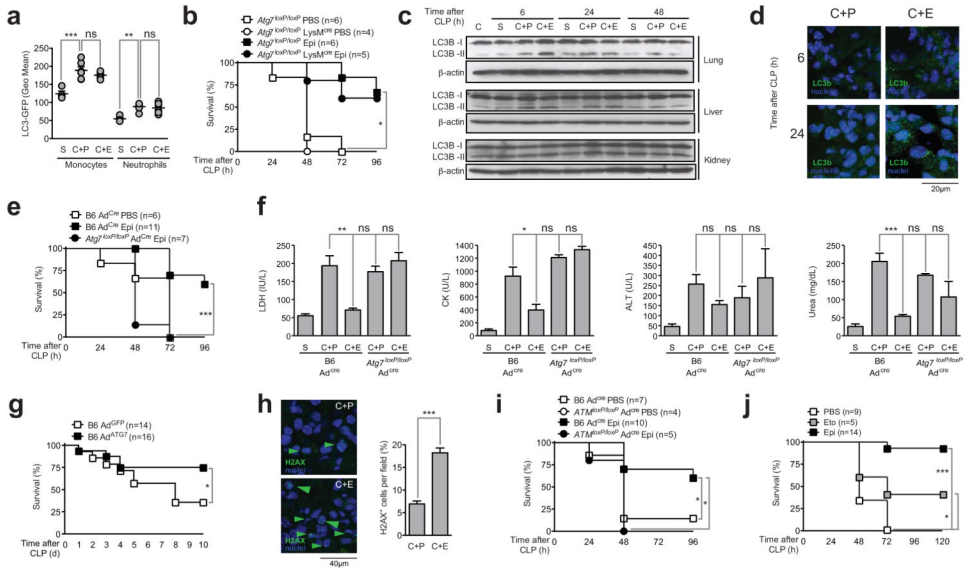

Figure 5. The protective effect of epirubicin is dependent on the activation of ATM and the autophagy pathway in the lung

(a) GFP expression in blood monocytes and neutrophils, isolated from transgenic LC3b-GFP animals, 24 hours after mice were subjected to mock CLP (S) or CLP followed by treatment with PBS (C+P) or epirubicin (C+E) (0.6μg/g body weight) at the time of procedure and 24 hours later. Each circle represents individual animals. Horizontal lines indicate arithmetic means ± SEM. **(b)** Survival of *Atg7*$^{loxP/loxP}$ and *Atg7*$^{loxP/loxP}$ *LysM*$^{cre/cre}$ mice subjected to CLP and treated with PBS or epirubicin (Epi) with same schedule and dose as in (a). **(c)** LC3B-I and LC3B-II protein levels by immunoblotting using a specific antibody against LC3B in lung, liver and kidney, isolated at the indicated times, of naïve C57BL/6 animals (C) or mice subjected to mock CLP (S) or CLP followed by treatment with PBS (C+P) or epirubicin (C+E) as in (a). **(d)** Representative sections of LC3b staining in lungs, isolated at the indicated times, of mice subjected to CLP followed by treatment with PBS (C+P) or epirubicin (C+E) as in (a). **(e)** Survival of wild-type (B6) and *Atg7*$^{loxP/loxP}$ animals subjected to CLP and treated with PBS or epirubicin (Epi) with same schedule and dose as in (b) 5 days after inhalation of adenoviral vector encoding Cre (Ad^{Cre}). **(f)** LDH, CK, ALT and urea plasma concentrations in wild-type (B6 Ad^{Cre}) and *Atg7*$^{loxP/loxP}$ Ad^{Cre} animals 24 hours after mock CLP (S) (n=2 for B6 Ad^{Cre}) or CLP followed by treatment with PBS (C+P) (n=5 for B6 Ad^{Cre} and n=2 for *Atg7*$^{loxP/loxP}$ Ad^{Cre}) or epirubicin (C+E) (n=6 for B6 Ad^{Cre} and n=3 for *Atg7*$^{loxP/loxP}$ Ad^{Cre}) as in (a). **(g)** Survival of wild-type (B6) animals subjected to CLP 4 days after inhalation of adenoviral vector encoding GFP (Ad^{GFP}) or *Atg7* (Ad^{ATG7}). **(h)** Representative sections of γH2AX staining and percentage of γH2AX^{+} cells per field (right panel) in lungs, isolated 6 hours after mice were subjected to CLP followed by treatment with PBS (C+P) or epirubicin (C +E) as in (a). Results shown represent arithmetic means ± SD from 10 fields. **(i)** Survival of wild-type (B6) and *Atm*$^{loxP/loxP}$ animals subjected to CLP and treated with PBS or epirubicin (Epi) with same schedule and dose as in (b) 5 days after inhalation of Ad^{Cre}. **(j)** Survival of C57BL/6 wild-type animals subjected to CLP treated with carrier (PBS), etoposide (40μg/g body weight/day) or epirubicin (Epi) (0.6μg/g body weight) intranasally, at the time of procedure and 24 hours later. ns, not significant; *P<0.05; **P<0.01; ***P<0.001 (log-rank (Mantel-Cox) test for (b), (e), (g), (i) and (j), Mann-Whitney test for (a), and unpaired t-test for (f) and (h) (right panel)). See also Figure S5.

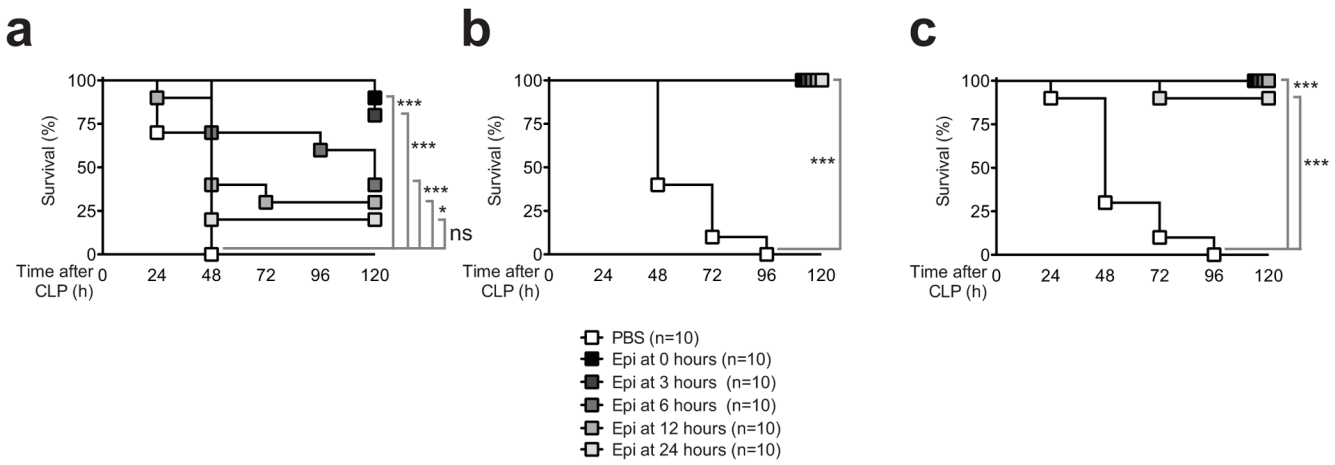

Figure 6. Epirubicin confers protection against severe sepsis in a therapeutic manner

(a) Survival of C57BL/6 wild-type animals subjected to CLP treated with PBS or epirubicin (same dose as in Figure 1) at indicated times in the absence of meropenem; **(b)** with administration of meropenem (40μg/g body weight/day) starting at the time of the procedure or **(c)** with meropenem treatment starting 12 hours after CLP. ns, not significant; *P<0.05; **P<0.01; ***P<0.001 (log-rank (Mantel-Cox)).

Original Study

Therapy-Induced Cellular Senescence Induces Epithelial-to-Mesenchymal Transition and Increases Invasiveness in Rectal Cancer

Joana Tato-Costa,[1] Sandra Casimiro,[1] Teresa Pacheco,[1] Ricardo Pires,[1,2] Afonso Fernandes,[1] Irina Alho,[1] Pedro Pereira,[1] Paulo Costa,[3] Henrique Bicha Castelo,[3] João Ferreira,[1] Luís Costa[1,2]

Abstract

We evaluated the effects of the senescence-associated secretome (SAS) in vitro and in clinical samples from patients with rectal cancer who had undergone neoadjuvant chemoradiotherapy (CRT). The effects of the SASs on colorectal cancer cells translated into increased invasiveness and induction of epithelial-to-mesenchymal transition (EMT). In the clinical samples, senescence and EMT co-occurred within a fraction of cancer cell clusters. These results could have important implications in guiding treatment after CRT.

Introduction: DNA damaging agents and ionizing radiation used in the therapy of human cancers can induce senescence of cancer cells. Senescent cells exhibit a secretory phenotype (senescence-associated secretome [SAS]) that can affect cancer cell behavior and, eventually, clinical prognosis. We assessed the effects of the SAS on the induction of epithelial-to-mesenchymal transition (EMT) in vitro and in clinical samples from patients with rectal cancer who had undergone neoadjuvant chemoradiotherapy (CRT). **Materials and Methods:** Colorectal cancer cells (HCT 116) were induced into senescence by exposure to either 5-fluorouracil (5-FU) or doxorubicin. The senescent state was confirmed by staining for senescence-associated β-galactosidase (SA-β-Gal). The paracrine effects of SASs were assessed on proliferating HCT 116 cells. The quantified parameters were cell proliferation, invasive capacity, and induction of EMT. Senescence and EMT in clinical samples were assessed by the expression levels (reverse transcriptase-quantitative polymerase chain reaction) of genes related to senescence and EMT after laser-assisted microdissection of cancer cell clusters that stained either positive or negative for SA-β-Gal. **Results:** We have shown that cultured colon cancer cells induced into senescence by exposure to 5-FU exhibit a SAS capable of paracrine induction of EMT in colon and rectal cancer cell lines and increased cell invasion in vitro. Using laser-assisted microdissection, we found that in rectal cancer samples from patients treated with neoadjuvant CRT, tumor cell niches enriched for senescent cells bookmark regions of increased mRNA expression levels of EMT-related proteins (Slug, Snail, vimentin) compared with the nearby senescent-null tumor cell niches. **Conclusion:** We have provided, first-hand, strongly suggestive evidence that senescent cancer cells emerging in the context of neoadjuvant CRT for rectal cancer influenced the tumor microenvironment by promoting EMT by way of short-range interactions.

Clinical Colorectal Cancer, Vol. ■, No. ■, 1-9

Keywords: 5-Fluorouracil, Neoadjuvant chemotherapy, Rectal cancer, Senescence-associated secretory phenotype, Therapy-induced senescence

Introduction

Distant relapse affects about 15% to 20% of patients diagnosed with locally advanced rectal cancer, despite all the therapeutic advances.[1,2] Whether diagnosed as locally advanced or at any stage in the presence of positive lymph nodes, the standard of care treatment for patients with rectal cancer has been neoadjuvant

[1]Instituto de Medicina Molecular, Faculdade de Medicina de Lisboa, Lisboa, Portugal
[2]Oncology Division, Hospital de Santa Maria, Centro Hospitalar Lisboa Norte, Lisboa, Portugal
[3]Surgery Division, Hospital de Santa Maria, Centro Hospitalar Lisboa Norte, Lisboa, Portugal

Submitted: Jul 3, 2015; Accepted: Sep 17, 2015

Address for correspondence: Luís Costa, MD, PhD, Oncology Division, Hospital de Santa Maria, Centro Hospitalar Lisboa Norte, Av. Prof. Egas Moniz, Lisboa 1649-028, Portugal
E-mail contact: luiscosta.oncology@gmail.com

1533-0028/$ - see frontmatter
http://dx.doi.org/10.1016/j.clcc.2015.09.003

chemotherapy with the thymidylate synthase inhibitor 5-fluorouracil (5-FU) and concomitant radiotherapy (chemoradiotherapy [CRT]), followed by surgery.[3,4]

It has been previously described that chemotherapy, in addition to its cytotoxic action, can induce a cellular state of irreversible proliferative arrest because of severe DNA damage, termed "therapy-induced senescence" (TIS).[5,6] Initially considered to be a phenomenon typical of normal somatic cells that lost their ability to divide and, thereby, termed "replicative senescence," it is now known that senescence can also be a response mechanism triggered by several factors, including oncogenic mutations, oxidative stress, and DNA damaging agents.[7,8]

The effect of cellular senescence in the context of cancer is not completely understood. Cell senescence can play a direct role in tumor growth inhibition, because it is an important antiproliferative mechanism.[9] In lung and breast cancer, the detection of cell senescence after neoadjuvant chemotherapy correlated positively with the response to treatment.[10,11] Also, in colorectal cancer, patients with sporadic senescent cells detected before treatment had increased susceptibility to TIS and a better response to adjuvant chemotherapy.[12] However, evidence has shown that senescent cells can also exert deleterious effects on the tissue microenvironment.[13] The so-called senescence-associated secretory phenotype (SASP) of these cells, which includes the secretion of several pro-inflammatory cytokines, epithelial growth factors, and tissue remodeling enzymes, can induce a more aggressive phenotype in nonsenescent cells in a paracrine fashion.[14] Data from studies of breast, prostate, and pancreatic cancer showed that senescent fibroblasts promoted tumor growth and progression by increasing proliferation and invasion and inducing an epithelial-to-mesenchymal transition (EMT) in premalignant and malignant cells.[15-19] It was further shown that neoadjuvant chemotherapy-induced senescence observed in patients with malignant pleural mesothelioma or lung cancer was potentially associated with a poor outcome.[20,21] Finally, senescent human prostate and breast tumor cells also have a SASP, raising the question of broader effects of SASPs on tumor behavior.[17,22] In the present study, we assessed the effects of the SASP from chemotherapy-induced senescence on induction of EMT in vitro and whether the coupling between cancer cell senescence and EMT induction was recapitulated in clinical samples from patients with rectal cancer who had undergone neoadjuvant CRT.

Materials and Methods

Cell Lines and Human Tissue Specimens

The human colon carcinoma cell lines HCT 116 and SW48 and the human rectal cancer cell line SW837 were obtained from the American Type Culture Collection (CCL-247, CCL-235, and CCL-231, respectively). HCT 116 was cultured in McCoy's 5A modified medium (Life Technologies, Carlsbad, CA) supplemented with 10% fetal bovine serum (Life Technologies), 100 U/mL penicillin/streptomycin (Life Technologies), 2 mM L-glutamine (Life Technologies), and 1% nonessential amino acids (Life Technologies). SW48 and SW837 were cultured in Dulbecco's modified Eagle medium (Life Technologies) supplemented with 10% fetal bovine serum (Life Technologies) and 100 U/mL penicillin/streptomycin (Life Technologies). All cell lines were kept at 37°C in 5% carbon dioxide. Rectal cancer specimens (n = 19) were collected during standard of care surgery from patients with rectal cancer who had or had not (controls) undergone neoadjuvant CRT, included in OCT compound (Sakura Finetek, Alphen aan den Rijn, The Netherlands), snapshot frozen in liquid nitrogen within 30 minutes of collection, and preserved at −80°C. The ethics commission of the Hospital de Santa Maria, Centro Hospitalar Lisboa Norte (Lisbon, Portugal) approved the study, and all the patients provided written informed consent.

Induction of Cell Senescence

A total of 4.0×10^4 HCT 116 cells were seeded in 60-mm diameter plates and continuously exposed to 5.0 μM 5-FU (Accord Farmacêutica Ltd, São Paulo, Brazil) or 0.5 μM doxorubicin (Sigma-Aldrich, St Louis, MO), for 7 days or 4 hours, respectively. The media with and without (controls) drugs were replaced every 48 hours. After drug removal, the cells were incubated with fresh medium. Conditioned media were collected 72 hours after drug release (senescence-associated secretome [SAS] medium). Culture media conditioned by exponentially growing (nonsenescent) cells (non-SAS medium) were collected 72 hours after seeding. The conditioned media were stored at 4°C and used within 48 hours of storage.

Cellular Assays

The detection of senescence-associated β-galactosidase (SA-β-Gal) activity in HCT 116 cells and frozen tissues was performed using the Senescence Cells Histochemical Staining Kit (Sigma-Aldrich), according to the manufacturer's instructions, followed by counterstaining with nuclear fast red (Sigma-Aldrich) and visualized in a Leica DM2500 bright field microscope (Leica Microsystems, Hannover, Germany).

Cell proliferation was assessed using the alamarBlue assay and 5-bromo-2′-deoxyuridine (BrdU) incorporation. The alamarBlue assay (Life Technologies) was performed according to the manufacturer's instructions. To determine the effect of the conditioned media on cell proliferation, HCT 116, SW837, and SW48 cells were plated in 96-well plates (2.0×10^3, 1.0×10^4, and 1.0×10^4 cells/well, respectively) and incubated for 24 hours in the presence of SAS medium or non-SAS medium. To test for BrdU incorporation, the cells induced into senescence by 5-FU or untreated control cells were exposed to 10 μM of BrdU for 24 hours or 1 hour, respectively. The cells were then fixed in 3.7% paraformaldehyde (PFA) for 10 minutes at room temperature. DNA was subsequently depurinated for 30 minutes in 4.0 N HCl, followed by a neutralization step in PBS supplemented with Tris buffer (100 mM; pH 8) for another 30 minutes. The cells were incubated with anti-BrdU antibody (1:50; clone BMC 9318; Roche, Basel, Switzerland) for 1 hour at 37°C, followed by incubation with anti-mouse Cy3 antibody (1:200; Jackson ImmunoResearch, West Grove, PA). Cover slips were mounted in VECTASHIELD with 4′,6-diamidino-2-phenylindole (DAPI; Vector Laboratories, Burlingame, CA), and visualized in a Zeiss Axiovert 200M inverted wide-field fluorescence microscope (Carl Zeiss MicroImaging GmbH, Jena, Germany). Apoptosis was assessed using the Caspase-Glo 3/7 Assay (Promega, Madison, WI), according to the manufacturer's instructions.

Figure 1 Low-Dose 5-Fluorouracil (5-FU) Induces Cellular Senescence in HCT 116 Colon Cancer Cells. (A) Detection of Senescence-Associated β-Galactosidase (SA-β-Gal) in HCT 116 Cells Not Exposed to 5-FU (Controls) or Exposed to 5-FU (5 μM) for 7 Days. Note the Increased Staining for SA-β-Gal (Blue Signal) and Enlarged Size of 5-FU–Treated Cells. (B) HCT 116 Cells Not Treated With 5-FU (Controls) or Treated With 5 μM of 5-FU for 7 Days Were Incubated With 10 μM 5-Bromo-2′-deoxyuridine (BrdU). This Showed That BrdU Incorporation by 5-FU–Treated Cells Was Residual (~6% BrdU-Positive Cells), Even After 24 Hours of BrdU Incorporation Compared With Controls (~58% of BrdU-Positive Cells After 1 Hour of Incorporation). Cells That Incorporated BrdU Show Nuclear Staining (Red Signal; White Arrows); Nuclei Were Counterstained With 4′,6-Diamidino-2-Phenylindole (DAPI) (Blue Signal); 400 Nuclei Analyzed per Sample. (C) Quantification of HCT 116 Cells by AlamarBlue Not Exposed to 5-FU (Controls) or Exposed to 5 μM of 5-FU for 7 Days. (D) Quantification of Apoptosis in HCT 116 Cells Not Exposed (Controls) or Exposed to 5-FU (5 μM) for 7 Days. Caspase-3 and -7 Activities Were Measured by a Luminescent Assay (Caspase-Glo 3/7 Assay; Promega; See "Materials and Methods"). Note That the Accumulated Apoptosis Observed During the Induction of Senescence by 5-FU Was Lower Than in Control Cultures. All Determinations Were Performed in Triplicate, and Data Are Given as Scatter Plots of the Mean ± Standard Error of Mean. **P* < .05; ***P* < .01; ****P* < .001, Unpaired *t* Test

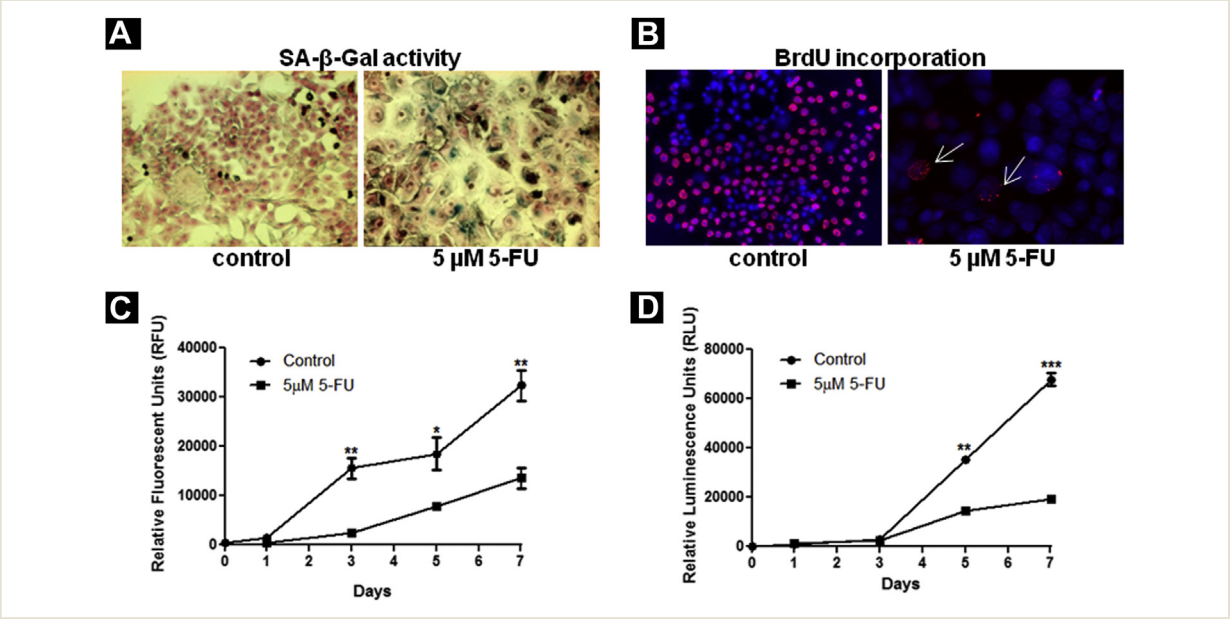

Immunofluorescence

The cell lines HCT 116, SW837, and SW48 were seeded on glass cover slips (2.0×10^5, 9.0×10^5, and 9.0×10^5 cells, respectively) in 60-mm diameter plates and continuously exposed to SAS medium or non-SAS medium for 72 hours. Next, the medium was removed, and the cells were fixed with 3.7% PFA for 10 minutes at room temperature. The cells were permeabilized with PBS/0.5% Triton X-100 for 10 minutes and then incubated with anti-E-cadherin antibody (1:1000; HECD-1, Life Technologies) for 1 hour at 37°C, followed by incubation with anti-mouse Cy3 antibody (1:200; Jackson ImmunoResearch) for 45 minutes at 37°C. The cover slips were mounted in VECTASHIELD with DAPI (Vector Laboratories), and visualized in a Zeiss Axiovert 200M inverted wide-field fluorescence microscope (Carl Zeiss MicroImaging GmbH).

Cytokine Profiling

The detection and semiquantification of cytokines present in the conditioned media were performed using the Proteome Profiler Array Human XL Cytokine Array Kit (R&D Systems) according to the manufacturer's instructions. In brief, the membranes were incubated with 500 μL of conditioned media (normalized for the total number of cells and total protein quantification, which in this case corresponded to 8 mg/mL protein, determined using the DC Protein Assay, Bio-Rad, Hercules, CA). Chemiluminescence detection was done in ChemiDoc MP (Bio-Rad). Pictures were acquired using ImageLab software, version 4.1 (Bio-Rad) and imported to ImageJ software, version 1.48 (National Institutes of Health, Bethesda, MD) for image analysis. The mean pixel density in each dot was determined by subtracting the same background value, and the average pixel density of duplicate spots was calculated.

RNA Isolation and Reverse Transcriptase Quantitative Polymerase Chain Reaction

The cell lines HCT 116, SW837, and SW48 (3.0×10^4, 9.0×10^5, and 9.0×10^5 cells, respectively) were seeded in 60-mm diameter plates and continuously exposed to SAS medium or non-SAS medium for 72 hours. The RNeasy Mini Kit (Qiagen, Valencia, CA) for total RNA isolation and DNase I (Promega) were used in accordance with the manufacturer's instructions. The RNA concentration and purity were assessed in a NanoDrop

Figure 2 Cytokines Secreted by 5- Fluorouracil (5-FU)—Induced Senescent HCT 116 Colon Cancer Cells. (A) Cytokine Screening Arrays Incubated With Either Senescence-Associated Secretome (SAS)— or Non-SAS (Control)—Conditioned Medium Obtained as Described in Materials and Methods. Note That Each of the Probed Cytokines Is Detected in Duplicate (Double-Spot) in Each Array. (B) Profiles of Mean Spot Pixel Density, Created Using ImageJ Software. (C) Quantification of Interleukin (IL)-8 in Media Conditioned for 72 Hours by Either Proliferating (Non-SAS Medium; Control) or Senescent (SAS Medium) HCT 116 Cells. Results Represent Mean ± Standard Error of Mean of Triplicate Experiments

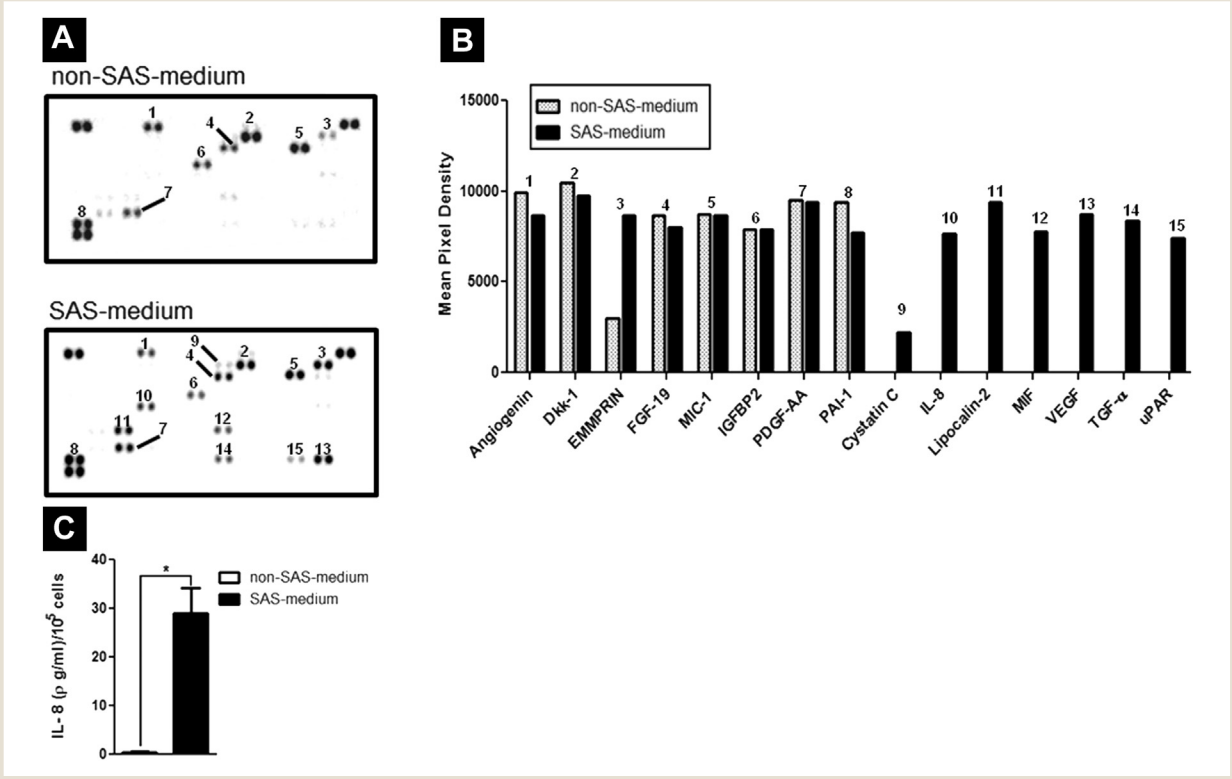

Abbreviations: EMMPRIN = extracellular matrix metalloproteinase inducer; FGF-19 = fibroblast growth factor 19; IGFBP2 = insulin-like growth factor binding protein 2; MIC-1 = macrophage inhibitory cytokine 1; MIF, macrophage migration inhibitory factor; PAI-1 = plasminogen activator inhibitor 1; PDGF-AA = platelet-derived growth factor-AA; TGF-α = transforming growth factor-α; uPAR = urokinase-type plasminogen activator receptor; VEGF = vascular endothelial growth factor.

spectrophotometer (Thermo Fisher Scientific, Waltham, MA). RNA (1 μg per sample) was reverse transcribed using the Superscript III First-Strand Synthesis System for reverse transcriptase (RT) polymerase chain reaction (PCR) with random hexamer primers (Life Technologies), according to the manufacturer's instructions. RNA extraction from the microdissected tissues was performed using the RNeasy Plus Micro kit (Quiagen) according to the manufacturer's instructions. Total RNA was reverse transcribed using the RT2Nano PreAMP cDNA Synthesis kit (Quiagen) according to the manufacturer's instructions. cDNA was amplified using semiquantitative real-time PCR (qPCR) using Power SYBR Green PCR Master Mix (Applied Biosystems, Carlsbad, CA) and specific primers in a Rotor Gene 6000 (Corbett; Quiagen). Specific primers were used for the following genes: *CDKN2A,* which codes for p16INK4a (PPH00207C); *IL-8,* coding for IL-8 (PPH00568A; Quiagen); *VIM,* coding for vimentin, forward 5′- CGAAAACACCCTGCAATCTT-3′, vimentin, reverse 5′-TCCTGGATTTCCTCTTCGTG-3′; *FN1* gene, encoding for fibronectin, forward 5′-CAGTGGGA-GACCTCGAGAAG-3′, fibronectin, reverse 5′-TCCCTCGGAA-CATCAGAAAC-3′; and *CDKN2A,* coding p21Waf1/Cip1, forward 5′- CTCAGAGGAGGCGCCATGT-3′, p21Waf1/Cip1, reverse 5′-CCATTAGCGCATCACAGTCG-3′. The genes *SNAI1, SNAI2, ZEB1,* and *GAPDH,* which encode for Snail, Slug, Zeb1, and GAPDH proteins, respectively, were amplified using previously published primers.[23] The relative mRNA expression levels were determined using the $2^{\Delta CT}$ method and normalized to the *GAPDH* housekeeping gene, using the mean value of 3 replicates.

Invasion Assay

The cell invasion assay was performed using the 24-well BD BioCoat Tumor Invasion System (BD Biosciences, San Jose, CA), according to the manufacturer's instructions. In brief, HCT 116 cells (5.0×10^4 cells/mL) were plated in the upper chambers, and SAS medium or non-SAS medium (control) was added to the lower chambers. After 24 hours of incubation at 37°C with 5% carbon dioxide, the cells in the membrane were stained with 4 μg/mL of Calcein-AM (Merck Millipore, Darmstadt, Germany) in Hank's buffered salt solution (Life Technologies) at 37°C in 5% carbon dioxide for 1 hour. Fluorescence was quantified using an Infinite200 Multimode reader (Tecan, Männedorf, Switzerland) at 494/517 nm (excitation/emission).

Figure 3 The Secretome of Senescent HCT 116 Cells Stimulates the Proliferation of Nonsenescent Cells. Quantification of HCT 116, SW48, and SW837 Cells by AlamarBlue After Incubation With Conditioned Media, Either Non–Senescence-Associated Secretome (SAS) Medium (Controls) or SAS Medium, for 24 Hours. Ratios Between Values Obtained After and Before Incubation With Conditioned Media Are Presented. All Determinations Were Performed in Triplicate, and Data Are Shown as Scatter Plots of Mean ± Standard Error of Mean. *$P < .05$ and **$P < .01$, an Unpaired *t* Test

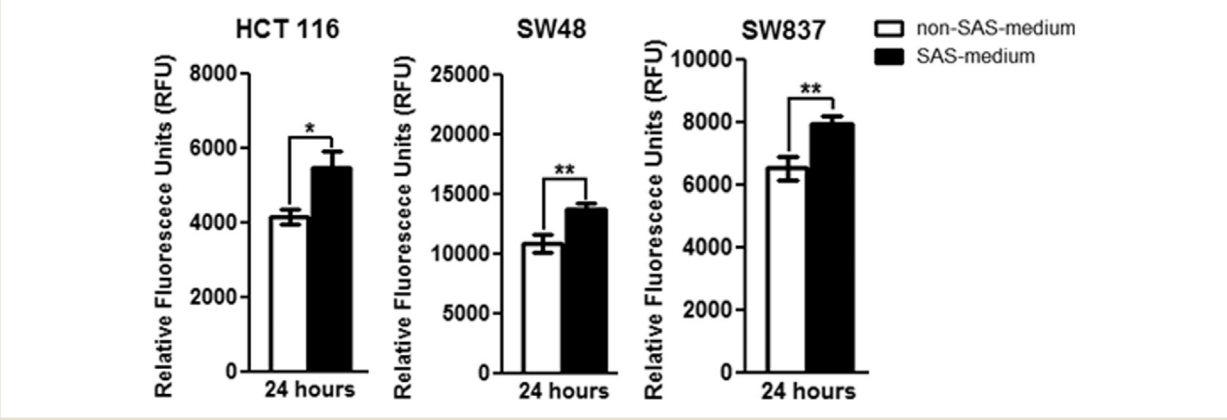

IL-8 Quantification

IL-8 in conditioned media was quantified with the Human IL-8/CXCL8 Quantikine ELISA (enzyme-linked immunosorbent assay) kit (R&D Systems), according to the manufacturer's instructions.

Laser Microdissection

Tumor cells were microdissected in a Laser PALM-Microbeam 4.2 microdissection system (Carl Zeiss MicroImaging GmbH), as previously described.[24] Sequential slides were obtained for the identification of senescent tumor cells (SA-β-Gal activity, as described) and for laser microdissection.

Statistical Analysis

The assays were performed in triplicate. The data were analyzed with GraphPad Prism software, version 5.00, for Windows (GraphPad Software, La Jolla, CA). The data are expressed as the mean ± standard error of the mean. Differences between groups were analyzed using a 2-tailed unpaired *t* test and Fisher's exact test, as appropriate. The nonparametric Mann-Whitney *U* test was used to compare 2 populations with independent observations. The level of statistical significance was set at $P < .05$.

Results

Low-Dose 5-FU Induces Cellular Senescence in HCT 116 Colorectal Cancer Cells

To address the paracrine effects of the secretome from colorectal cancer cells on their nonsenescent counterparts, we first induced cellular senescence by exposing HCT 116 colorectal cancer cells to low-dose 5-FU (5.0 μM) for 7 days. Then, we checked for the presence of senescent cells by cytochemical detection of the activity of SA-β-Gal. We observed that > 80% of the cells exposed to 5-FU displayed high levels of SA-β-Gal compared with that displayed by the control cells (Figure 1A). In agreement with the senescent state, 5-FU–treated cells displayed residual BrdU incorporation (~6% BrdU-positive cells) compared with the nontreated controls (~58% BrdU-positive cells; Figure 1B) and reduced proliferation (alamarBlue assay; $P < .05$ to $P < .01$; Figure 1C). The measurement of caspase-3 and -7 activities showed that apoptosis contributed little to the reduced cell numbers observed in the HCT 116 populations exposed to low doses of 5-FU ($P < .01$ to $P < .001$; Figure 1D). We concluded that low-dose 5-FU induced HCT 116 cells into a senescent state.

Secretome of Senescent HCT 116 Cells Stimulates Proliferation of Nonsenescent Cells

To test the paracrine effects of the SAS, we characterized the cytokine profile of culture media conditioned by HCT 116 cells induced into senescence by 5-FU, termed "SAS medium." Controls were provided by culture media conditioned by exponentially growing HCT 116 cells (see the "Materials and Methods" section). This cytokine profile, assessed using a dedicated array, showed SAS media were enriched in IL-8, TGF-α, VEGF, cystatin C, lipocalin 2 (LCN2), macrophage migration inhibitory factor, extracellular matrix metalloproteinase inducer, and urokinase-type plasminogen activator receptor (Figure 2A,B). Because IL-8 is a hallmark of SASs, we further quantified this cytokine using ELISA. The results confirmed a significant increase of IL-8 in SAS medium ($P < .05$; Figure 2C).

Analyses of cell viability using the alamarBlue assay showed that after culturing HCT 116 cells for 24 hours in presence of SAS or non-SAS media (controls), the SAS media induced a significant increase in cell proliferation ($P < .05$; Figure 3), in accordance with previously published data for other cell types.[15,16,18] To check whether this effect was cell type specific, we also tested the effects of SAS media on proliferation in a different colon cancer cell line (SW48) and in a rectal cancer cell line (SW837). These results confirmed the stimulatory effect of the SAS on the proliferation of these cell lines (Figure 3). These data suggest that the secretome of HCT 116 cells induced to senesce by exposure to 5-FU exerts a positive effect on the proliferation of cycling colorectal and rectal cancer cells.

Figure 4 The Secretome of Senescent Colon Cancer Cells Induces Epithelial-to-Mesenchymal Transition and Increases Invasiveness. (A) HCT 116, SW48, and SW837 Cells Incubated With Conditioned Media, Either Non–Senescence-Associated Secretome (SAS) (Control) or SAS-Enriched, for 72 Hours and Stained by Immunofluorescence With Anti–E-Cadherin Antibodies (Red Signal); Nuclei Were Counterstained With 4′,6-Diamidino-2-Phenylindole (DAPI) (Blue Signal). The Cellular Peripheral E-cadherin Signal Is Either Lost or Significantly Reduced in Cells Exposed to SAS Medium. (B) Cells Exposed to Conditioned Media (Non-SAS [Control] vs. SAS-Enriched) Were Analyzed by Reverse Transcriptase Quantitative Polymerase Chain Reaction for Expression of Epithelial-to-Mesenchymal Transition-Related Markers (Slug, Zeb1a, Snail, Fibronectin, and Vimentin). Expression of These Genes Was Normalized for *GAPDH* Expression. (C) The Chemoattractant Properties of Conditioned Media (Non-SAS [Control] vs. SAS-Enriched Medium) Were Monitored Using a Standard Invasion Assay (See "Materials and Methods"). Migrating Cells Were Scored by Quantification of Calcein AM-Associated Fluorescence. All Determinations Were Done in Triplicate, and Data Are Given as Scatter Plots of the Mean ± Standard Error of Mean. *$P < .05$; **$P < .01$; ***$P < .001$, Unpaired *t* Test

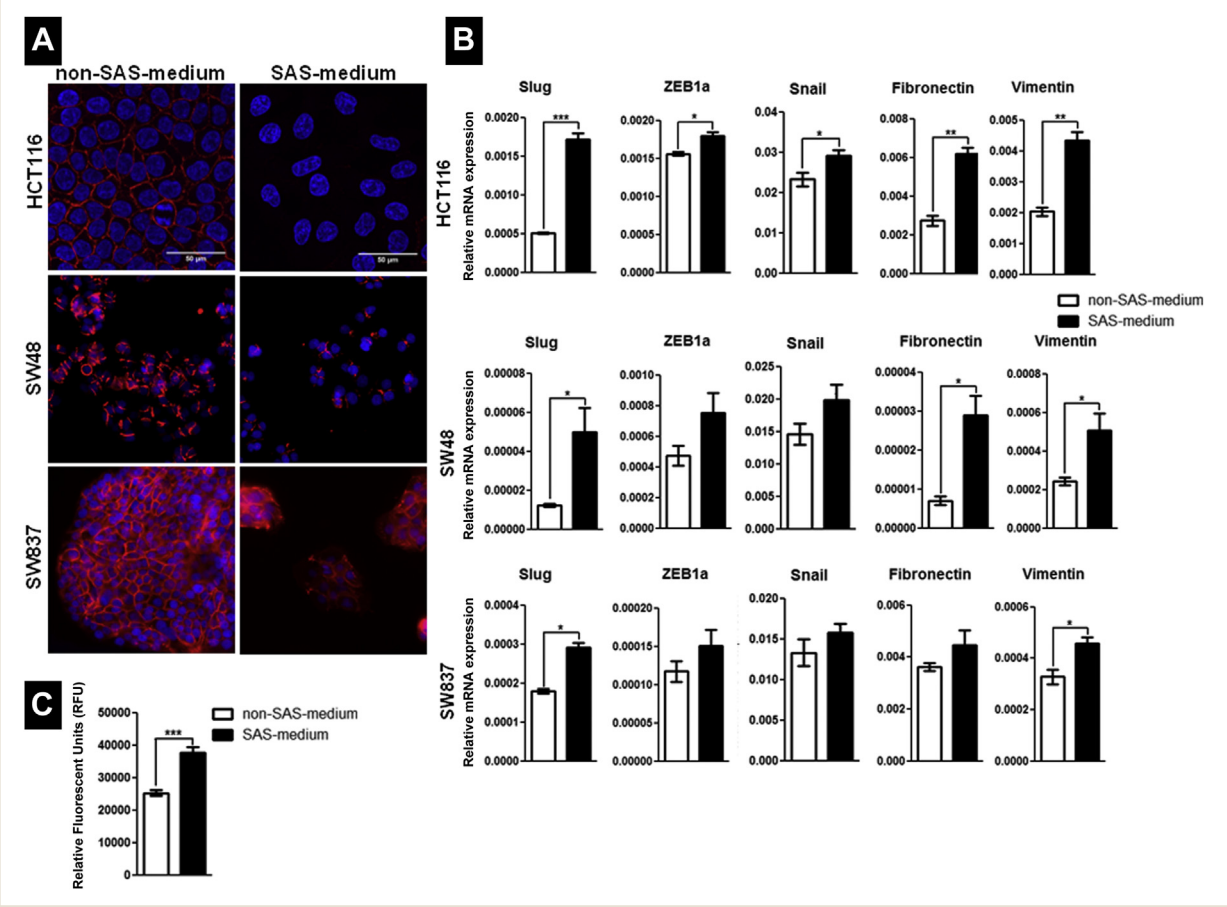

Secretome of Senescent Colon Cancer Cells Promotes EMT and Increased Invasiveness

Next, we investigated whether the SAS could affect the epithelial phenotype of proliferating colon and rectal cancer cells. We found that in contrast to incubation with non-SAS control medium, incubation with SAS medium induced loss of E-cadherin expression, as assessed by immunofluorescence with E-cadherin–specific antibodies (Figure 4A). Moreover, our results showed a significant increase ($P < .05$ to $P < .001$) in mRNA levels of Slug, ZEB1a, Snail, fibronectin, and vimentin (Figure 4B), all hallmarks of EMT in HCT 116, SW48, and SW837 cells. Also, HCT 116 cells exposed to SAS medium displayed increased invasiveness compared with control cells exposed to non-SAS conditioned medium ($P < .001$; Figure 4C).

Finally, we checked whether the observed effects of the SAS on stimulation of EMT and invasive behavior were dependent on the drug used to induce the SAS. Thus, we obtained media conditioned by HCT 116 cells that were induced into senescence by brief exposure to doxorubicin (0.5 μM, 4 hours). This treatment resulted in a proportion of senescent cells (SA-β-Gal staining, ~ 80%) similar to that obtained after exposure to 5-FU (data not shown). Also, within the constraints of the array we used, the cytokine profile of the SAS obtained from doxorubicin-induced senescent HCT 116 cells was similar to that obtained from 5-FU–induced senescent cells (Supplemental Figure 1A–C; online version). Similarly, exposure to the doxorubicin-SAS medium also induced upregulation of EMT-related genes in proliferating HCT 116 cells (Supplemental Figure 1D; online version). In summary, these data

Table 1 Patient and Tumor Characteristics

Characteristic	Neoadjuvant CRT		
	Yes (n = 7)	No (n = 12)	*P* Value
Male gender (%)	57	83	.3047[a]
Age (years)			.7553[b]
Median	70.8	68.6	
Range	50-84	43-89	
pT classification[c] (%)			.3047[a]
pT2	43	17	
pT3	57	83	
RLN involvement (%)	71	50	.6332[a]

Abbreviations: CRT = chemoradiotherapy; RLN = regional lymph nodes.
[a]Fisher's exact test.
[b]Student's *t* test.
[c]Staging according to American Joint Committee on Cancer Staging Manual, 7th edition.

have shown that in the presence of senescence-specific secretomes, colon and rectal cancer cells are induced into EMT and acquire increased invasiveness.

Neoadjuvant Chemotherapy Promotes Emergence of Senescence and EMT in Human Rectal Cancers

The previous data highlighted a relevant set of paracrine effects exerted by the SAS on target proliferating colon cancer cells (ie, induction of EMT). We then wondered whether these effects might be of more broad clinical relevance and, thus, observable in tumors from patients with rectal cancer.

Because the initial specimens collected for diagnostic purposes were routinely embedded in paraffin and, thus, did not allow for accurate detection of senescent cancer cells in untreated tumors, an assessment of the effects of CRT on the induction of cell senescence in each patient was precluded. We, therefore, selected as a model system rectal cancer samples collected at surgery from patients who had or had not undergone neoadjuvant CRT (Table 1). These 2 groups were similar concerning gender distribution, mean age, pathologic primary tumor classification (pT), and regional lymph node involvement ($P = .3047$, $P = .7553$, $P = .3047$, and $P = .6332$, respectively).

In these samples, we tested whether CRT induced senescence in tumor cells and whether the proximity to senescent cancer cells correlated with the induction of EMT. Thus, frozen rectal cancer samples from patients who had either undergone CRT (n = 7) or had not (controls; n = 12) were sectioned, and randomly chosen clusters of cancer cells were laser microdissected free of stromal components for quantitative analysis of specific mRNA using RT-qPCR.

We initially tested for the expression of genes that strongly correlate with the senescent state (ie, *p21Waf1/Cip1, p16INK4a,* and *IL-8*). Both *p21Waf1/Cip1* and *IL-8* were upregulated in the group of patients who had undergone neoadjuvant CRT ($P < .05$; Figure 5A) compared with the control (non-CRT) samples, suggesting that CRT induced cellular senescence in these tumors. Next, we analyzed the expression of the EMT-related markers, Snail, Slug, and vimentin in the same samples. These genes were significantly upregulated in tumors from patients treated with neoadjuvant CRT ($P < .05$; Figure 5A).

Subsequently, in samples from patients who had undergone neoadjuvant CRT, we obtained serial sections in which every other section was stained for SA-β-Gal and used to directly assess the presence of senescent cells in the contiguous sections (stained with cresyl violet). Staining for SA-β-Gal was detected in discrete regions of tumor tissue, and cancer cell clusters enriched with senescent cells were identified and selected (Supplemental Figure 2A; online version). These clusters, together with nearby clusters (> 700 μm), in which senescent cells were absent (controls), were laser microdissected and used for the analysis of expression of p21Waf1/Cip1 and IL-8 and of the EMT markers Snail, Slug and vimentin using RT-qPCR (Supplemental Figure 2B; online version). As expected, p21Waf1/Cip1 and IL-8 were upregulated in tumor cell clusters enriched in senescent cells (Figure 5B). More importantly, Snail, Slug, and vimentin also showed increased expression in these same tumor cell clusters, indicating that senescence and EMT co-occurred within the same microenvironment (Figure 5B). It is unlikely that senescent cells themselves were the source of increased expression of genes related to EMT, because this is not part of the drug-induced senescent phenotype. We found that the expression of Snail and vimentin was significantly lower in HCT 116 cells that reached senescence by exposure to 5-FU compared with HCT 116 cells induced into EMT ($P < .001$; Supplemental Figure 3; online version).

Discussion

Good evidence has shown that the tumor microenvironment has a role in cancer progression.[25] Recently, it was shown that in patients with rectal cancer receiving neoadjuvant therapy, the patterns of gene expression of cancer-associated fibroblasts provided predictive power for distant recurrence and prognosis. This finding supports a role for the microenvironment in rectal cancer behavior.[26] Also, the treatment of patients with cancer using DNA-damaging agents, in both neoadjuvant and curative settings, was shown to induce epithelial cancer cells into accelerated forms of senescence.[14] Senescent cells derived from either nontransformed cells or cancer cells are associated with SASs.[17] Despite the powerful paracrine effects exerted by SASs in vitro,[15-19] to what extent senescent cancer cells present within tumors influence the microenvironment and, eventually, cancer progression has remained elusive.[12,20,21]

We initially interrogated the cytokine composition of the SAS from colon cancer cells (HCT 116) induced to senesce by exposure to either 5-FU, which targets cells in the S phase and interferes with DNA repair, or to doxorubicin, a DNA-damaging drug. We have presented evidence that senescent colon cancer cells are able to consistently secrete several cytokines to high levels (eg, IL-8), irrespectively of whether senescence was induced by 5-FU or doxorubicin. In addition, we have provided evidence, for the first time, that CD147, cystatin C, LCN2, and TGF-α are also SAS-related molecules. As previously described for other cell types,[16,17,19] in 2 different colon cancer cell lines (HCT 116 and SW48) and 1 rectal cancer cell line (SW837), the paracrine effects of the SAS included increased proliferation and invasiveness and the induction of EMT, all of which correlate with aggressive cell behavior.

Figure 5 Neoadjuvant (Neo.) Chemotherapy Promotes Emergence of Senescence and Epithelial-to-Mesenchymal Transition (EMT) in Human Rectal Cancers. (A) Total RNA Was Extracted From Microdissected Clusters of Cancer Cells From Human Rectal Cancer Samples Obtained From Patients Who Had Either Received Neoadjuvant Chemoradiotherapy (Neo. CRT+; n = 7) or Not (Neo. CRT− [Controls]; n = 12) Before Surgery. Specified mRNA Were Quantified by Reverse Transcriptase Quantitative Polymerase Chain Reaction (RT-qPCR) and Normalized to *GAPDH* Expression. (B) In Rectal Cancer Samples From Patients Subjected to Neoadjuvant Chemoradiotherapy (n = 4), Cancer Cell Clusters Enriched in Senescent Cells and Clusters Located Nearby (> 700 μm) and Certified as Devoid of Senescent Cells (Controls) Were Laser Microdissected and Used for Quantification of Specific mRNA by RT-qPCR. Note the Increase in Both Senescence (p21Waf1/Cip1, Interleukin-8) and EMT Markers (Snail, Slug, Vimentin) in Tumor Areas Enriched for Senescent Cells. Whiskers Represent the Minimum and Maximum Across the Data. **P* < .05, Mann-Whitney *U* Test

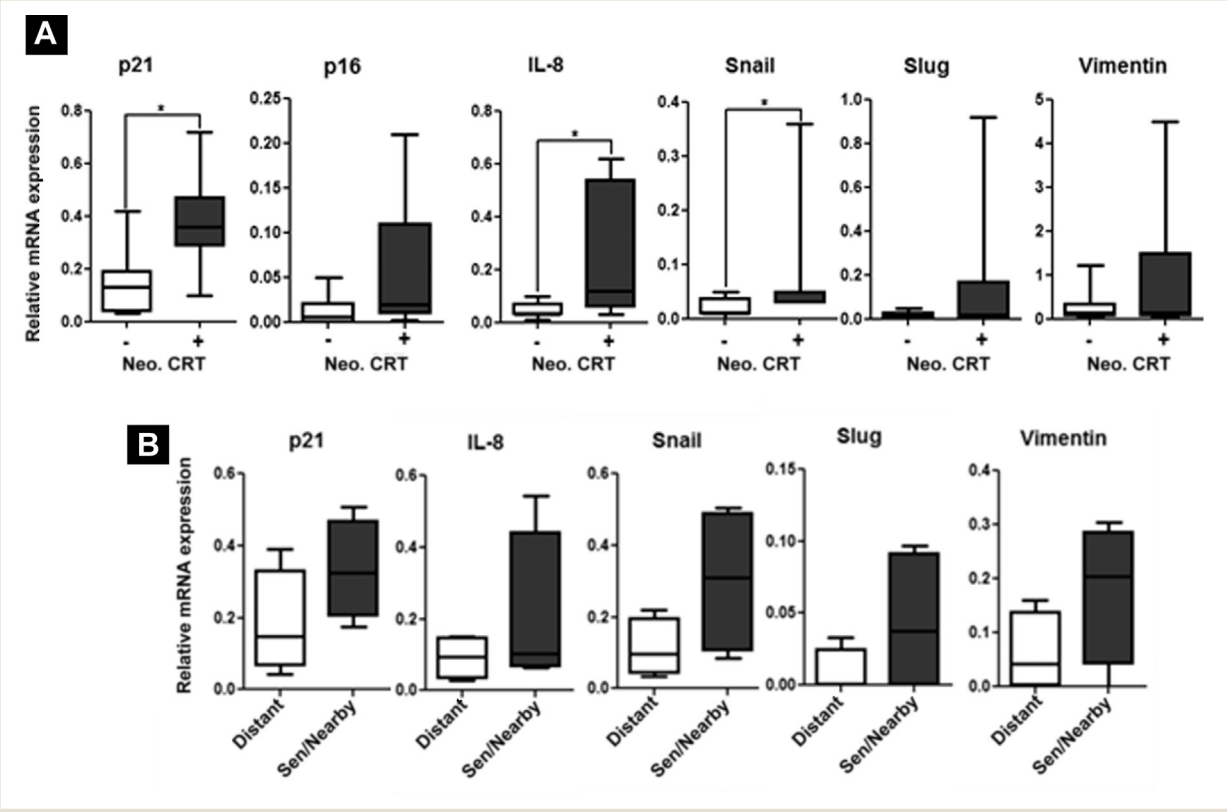

Our data also showed that, in contrast to cells undergoing EMT, senescent cells express relatively low mRNA levels of EMT markers such as Snail and vimentin, thus allowing a distinction between these 2 cellular outcomes using gene expression criteria. Given the consistent induction of EMT by SASs and the known relevance of EMT in cancer behavior, we addressed whether the paracrine effects of senescent cells, by way of the SAS, on EMT induction seen in vitro might be recapitulated in vivo, in the clinical setting. Our data showed that in tumor sections obtained from patients with rectal cancer, the senescent cells, identified by their strong staining for SA-β-Gal, were present within discrete clusters of cancer cells. Laser microdissection of these clusters and of nearby clusters devoid of senescent cells was performed and followed by RT-qPCR analysis of the senescence and EMT markers, p21Waf1/Cip1 and IL-8 and Snail, Slug, and vimentin, respectively. This showed that these genetic markers were coexpressed at greater levels in the cancer cell clusters enriched for senescent cells relative to the nearby clusters (> 700 μm) devoid of senescent cells. These data strongly suggest the co-occurrence of senescence and EMT within the same cell clusters. They are also consistent with the influence of senescent cancer cells on the induction of EMT being relatively short range and not affecting nearby niches of cancer cells.

Tumor recurrence after preoperative CRT followed by surgery with curative intent remains a major problem to successful cancer treatment, affecting 15% to 20% of patients diagnosed with locally advanced rectal cancer.[1,2] Tumor regression after neoadjuvant CRT has been used to evaluate the treatment response and prognosis.[27,28] However, the results of neoadjuvant therapy have ranged from a lack of effectiveness to complete pathologic remission. Clearly, the identification of novel predictive biomarkers of disease progression is crucial to improve adjuvant therapeutic agents and follow-up strategies.

Conclusion

Both 5-FU and doxorubicin robustly induced senescence and SASs in cultured HCT 116 cells. The effects of the SASs on the

proliferating colon and rectal cells translated into increased proliferation, invasiveness, and induction of EMT. In clinical samples from patients who had undergone neoadjuvant CRT, senescence and EMT co-occurred within a fraction of cancer cell clusters. Future studies are needed to determine whether after neoadjuvant therapy for rectal cancer, the presence of senescent cells and EMT-related changes in their microenvironment add prognostic power regarding cancer recurrence and patient survival.

Clinical Practice Points

- In patients with rectal cancer, locoregional relapse and distant metastasis are major events leading to death.
- Senescent cells exhibit a secretory phenotype that can affect cancer cell behavior and, eventually, clinical prognosis.
- We focused on therapy-induced cancer cell senescence and on the effects exerted by senescent cells on cancer cell behavior and the tumor microenvironment.
- We found that, in vitro, the secretomes of senescent cells induce invasion and EMT.
- The effects of senescent cancer cells on EMT appear to be recapitulated in clinical samples from patients with rectal cancer who had undergone neoadjuvant CRT.
- CRT induced cancer cell senescence, and senescence and EMT coexisted within the same cancer cell niches.
- The results of the present study have provided first-hand evidence that senescent cells can alter the tumor microenvironment and raises the possibility that the combined assessment of senescence and EMT could be useful in guiding treatment after CRT.

Acknowledgments

The authors acknowledge the oncology fellows Margarida Matias and Mafalda Casa-Nova for all support with clinical data collection and Pedro Gonçalo Rodrigues from the pathology division. This work was supported by the Histology and Comparative Pathology Laboratory and the Bioimaging Unit of the Instituto de Medicina Molecular for technical support. J. Tato-Costa, S. Casimiro, I. Alho, and P. Pereira were supported by fellowships from Fundação para a Ciência e Tecnologia (grants SFRH/BD/45219/2008, SFRH/BPD/34801/2007, SFRH/BD/44716/2008, and SFRH/BD/45502/2008, respectively). João Ferreira receives support from Gulbenkiam Foundation (grant 96526/2009).

Disclosure

The authors have stated that they have no conflicts of interest.

Supplemental Data

The supplemental figures accompanying this article can be found in the online version at http://dx.doi.org/10.1016/j.clcc.2015.09.003.

References

1. Sauer R, Becker H, Hohenberger W, et al. Preoperative versus postoperative chemoradiotherapy for rectal cancer. *N Engl J Med* 2004; 351:1731-40.
2. Bosset JF, Collette L, Calais G, et al. Chemotherapy with preoperative radiotherapy in rectal cancer. *N Engl J Med* 2006; 355:1114-23.
3. Longley DB, Harkin DP, Johnston PG. 5-Fluorouracil: mechanisms of action and clinical strategies. *Nat Rev Cancer* 2003; 3:330-8.
4. O'Connell MJ, Martenson JA, Wieand HS, et al. Improving adjuvant therapy for rectal cancer by combining protracted-infusion fluorouracil with radiation therapy after curative surgery. *N Engl J Med* 1994; 331:502-7.
5. Ewald JA, Desotelle JA, Wilding G, Jarrard DF. Therapy-induced senescence in cancer. *J Natl Cancer Inst* 2010; 102:1536-46.
6. Wu PC, Wang Q, Grobman L, Chu E, Wu DY. Accelerated cellular senescence in solid tumor therapy. *Exp Oncol* 2012; 34:298-305.
7. Hayflick L. The limited in vitro lifetime of human diploid cell strains. *Exp Cell Res* 1965; 37:614-36.
8. Collado M, Serrano M. The power and the promise of oncogene-induced senescence markers. *Nat Rev Cancer* 2006; 6:472-6.
9. Roninson IB. Tumor cell senescence in cancer treatment. *Cancer Res* 2003; 63: 2705-15.
10. Roberson RS, Kussick SJ, Vallieres E, Chen SY, Wu DY. Escape from therapy-induced accelerated cellular senescence in p53-null lung cancer cells and in human lung cancers. *Cancer Res* 2005; 65:2795-803.
11. te Poele RH, Okorokov AL, Jardine L, Cummings J, Joel SP. DNA damage is able to induce senescence in tumor cells in vitro and in vivo. *Cancer Res* 2002; 62: 1876-83.
12. Haugstetter AM, Loddenkemper C, Lenze D, et al. Cellular senescence predicts treatment outcome in metastasised colorectal cancer. *Br J Cancer* 2010; 103: 505-9.
13. Coppe JP, Desprez PY, Krtolica A, Campisi J. The senescence-associated secretory phenotype: the dark side of tumor suppression. *Annu Rev Pathol* 2010; 5:99-118.
14. Collado M, Serrano M. Senescence in tumours: evidence from mice and humans. *Nat Rev Cancer* 2010; 10:51-7.
15. Krtolica A, Parrinello S, Lockett S, Desprez PY, Campisi J. Senescent fibroblasts promote epithelial cell growth and tumorigenesis: a link between cancer and aging. *Proc Natl Acad Sci U S A* 2001; 98:12072-7.
16. Parrinello S, Coppe JP, Krtolica A, Campisi J. Stromal–epithelial interactions in aging and cancer: senescent fibroblasts alter epithelial cell differentiation. *J Cell Sci* 2005; 118:485-96.
17. Coppe JP, Patil CK, Rodier F, et al. Senescence-associated secretory phenotypes reveal cell-nonautonomous functions of oncogenic RAS and the p53 tumor suppressor. *PLoS Biol* 2008; 6:2853-68.
18. Bavik C, Coleman I, Dean JP, Knudsen B, Plymate S, Nelson PS. The gene expression program of prostate fibroblast senescence modulates neoplastic epithelial cell proliferation through paracrine mechanisms. *Cancer Res* 2006; 66:794-802.
19. Ohuchida K, Mizumoto K, Murakami M, et al. Radiation to stromal fibroblasts increases invasiveness of pancreatic cancer cells through tumor–stromal interactions. *Cancer Res* 2004; 64:3215-22.
20. Wang Q, Wu PC, Dong DZ, et al. Polyploidy road to therapy-induced cellular senescence and escape. *Int J Cancer* 2013; 132:1505-15.
21. Sidi R, Pasello G, Opitz I, et al. Induction of senescence markers after neoadjuvant chemotherapy of malignant pleural mesothelioma and association with clinical outcome: an exploratory analysis. *Eur J Cancer* 2011; 47:326-32.
22. Jackson JG, Pant V, Li Q, et al. p53-mediated senescence impairs the apoptotic response to chemotherapy and clinical outcome in breast cancer. *Cancer Cell* 2012; 21:793-806.
23. Yu M, Smolen GA, Zhang J, et al. A developmentally regulated inducer of EMT, LBX1, contributes to breast cancer progression. *Genes Dev* 2009; 23: 1737-42.
24. Casimiro S, Luis I, Fernandes A, et al. Analysis of a bone metastasis gene expression signature in patients with bone metastasis from solid tumors. *Clin Exp Metastasis* 2012; 29:155-64.
25. Albini A, Sporn MB. The tumour microenvironment as a target for chemoprevention. *Nat Rev Cancer* 2007; 7:139-47.
26. Saigusa S, Toiyama Y, Tanaka K, et al. Cancer-associated fibroblasts correlate with poor prognosis in rectal cancer after chemoradiotherapy. *Int J Oncol* 2011; 38: 655-63.
27. Rodel C, Martus P, Papadoupolos T, et al. Prognostic significance of tumor regression after preoperative chemoradiotherapy for rectal cancer. *J Clin Oncol* 2005; 23:8688-96.
28. Dhadda AS, Dickinson P, Zaitoun AM, Gandhi N, Bessell EM. Prognostic importance of Mandard tumour regression grade following pre-operative chemo/radiotherapy for locally advanced rectal cancer. *Eur J Cancer* 2011; 47:1138-45.

Therapy-Induced Cellular Senescence Increases Rectal Cancer Invasiveness

Supplemental Figure 1 **Cytokine Screening Array and Epithelial-to-Mesenchymal Transition (EMT) Induction by Senescence-Associated Secretome (SAS) Medium Obtained From Doxorubicin-Induced Senescent HCT 116 Colon Cancer Cells. (A) Cytokine Screening Arrays Incubated With Either SAS or Non-SAS (Controls) Media. SAS Media Were Conditioned by HCT 116 Cells Induced Into Senescence by Doxorubicin. Each of the Probed Cytokines Was Detected in Duplicate. (B) Profiles of Mean Spot Pixel Density Were Created Using ImageJ Software. (C) SAS Medium Conditioned by Senescent HCT 116 cells (Doxorubicin-Induced Senescence) Was Enriched in Interleukin (IL)-8 Relative to Control (Non-SAS) Medium. Quantifications Were Performed by Enzyme-Linked Immunosorbent Assay. (D) Expression Levels of mRNA From EMT-Related Genes in Proliferating HCT 116 cells Incubated for 72 Hours With Either SAS Medium or Non-SAS Medium (Controls). Gene Expression Was Assessed by Reverse Transcriptase Quantitative Polymerase Chain Reaction and Normalized to *GAPDH* Expression. All Determinations Were Done in Triplicate, and Data Are Presented as Scatter Plots of the Mean ± Standard Error of the Mean. *$P < .05$, Unpaired *t* Test**

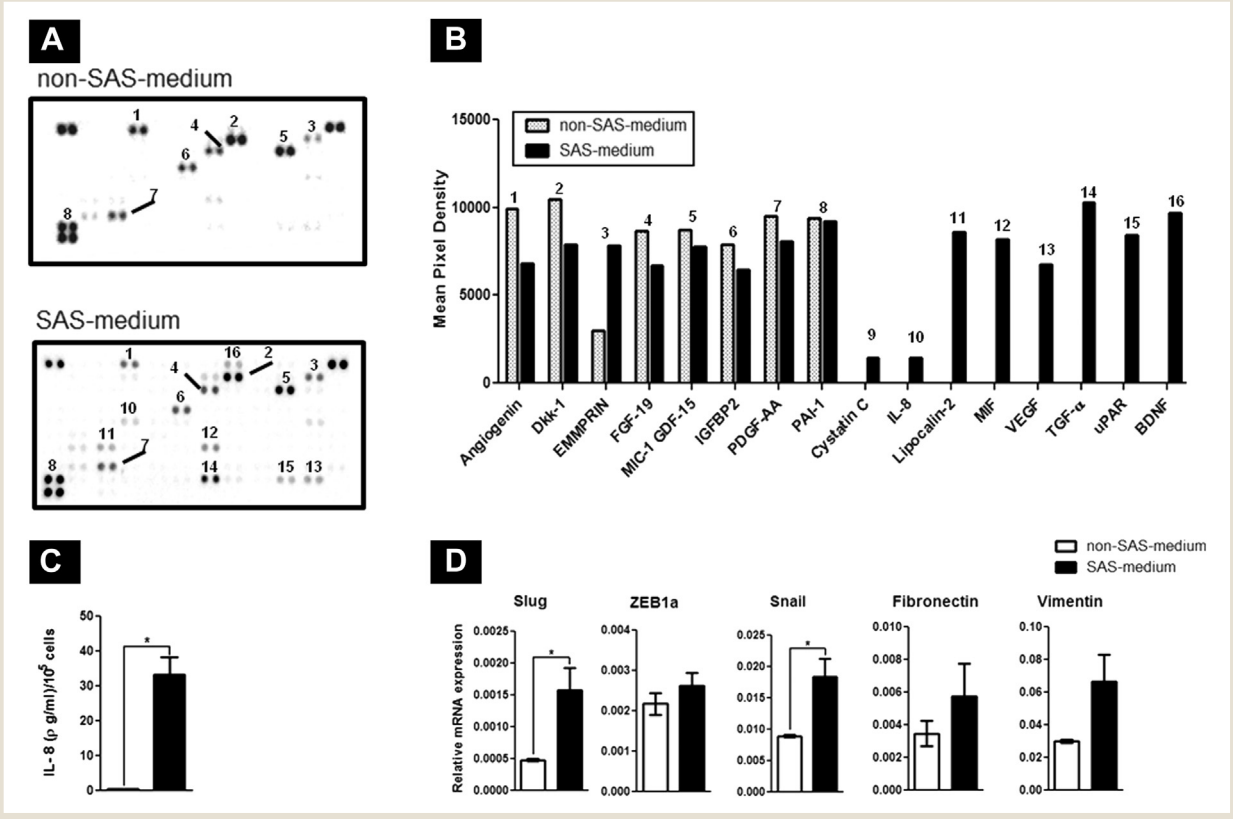

Abbreviations: EMMPRIN = extracellular matrix metalloproteinase inducer; FGF-19 = fibroblast growth factor 19; IGFBP2, insulin-like growth factor binding protein 2; MIC-1 = macrophage inhibitory cytokine 1; MIF = migration inhibitory factor; PAI-1 = plasminogen activator inhibitor 1; PDGF-AA = platelet-derived growth factor-AA; TGF-α = transforming growth factor-α; uPAR = urokinase-type plasminogen activator receptor; VEGF = vascular endothelial growth factor.

Supplemental Figure 2 Representative Sequential Frozen Sections of Human Rectal Cancer Tissue Selected for Isolation of Senescent-Positive and Senescent-Negative Epithelial Cell Populations by Laser Microdissection. (A) Section Stained for Senescence-Associated β-Galactosidase (SA-β-Gal) Activity to Identify Clusters of Cancer Cells Harboring Senescent Cells (Blue Staining; Upper Inset, Left; Arrows, Top Right) and Nearby Clusters Devoid of SA-β-Gal Staining (Lower Inset, Left; Bottom Right). Counterstaining Was With Nuclear Fast Red. (B) Contiguous Section Stained With Cresyl Violet in Which Areas Selected for Microdissection Are Delineated (Senescent-Positive, Blue Lines; Senescent-Negative, Already Laser-Ablated, Red Lines). Magnification, ×100 (A, left) and ×200 (A, Right; B)

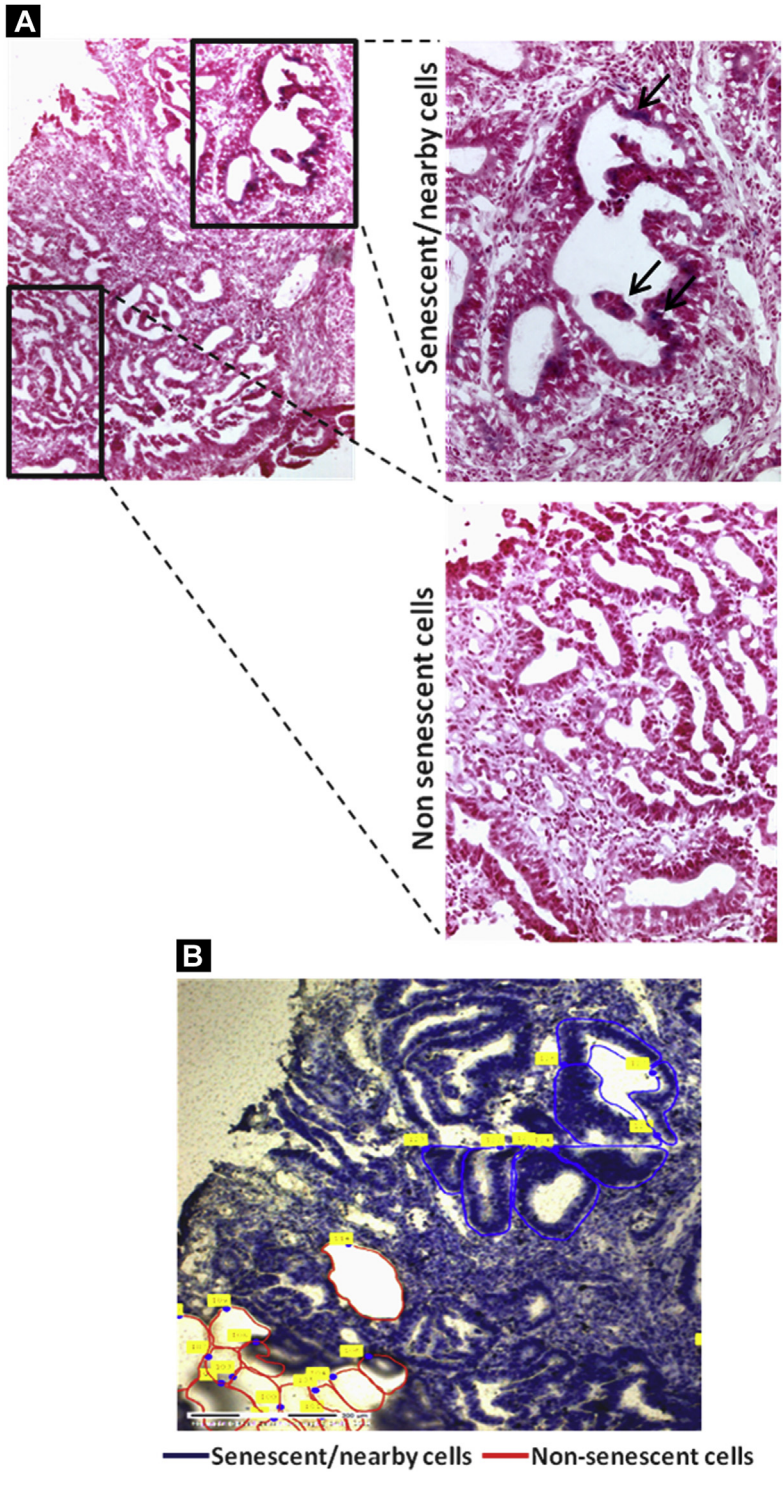

Supplemental Figure 3 Epithelial-to-Mesenchymal Transition (EMT)-Related Genes Are Poorly Expressed in Senescent Cells. Expression of Vimentin and Snail Were Assessed by Reverse Transcriptase Quantitative Polymerase Chain Reaction in HCT 116 Cells, Either Senescent or Induced Into EMT by Exposure to SAS-Enriched Medium. All Determinations Were Done in Triplicate, and Data Are Given as Scatter Plots of the Mean ± Standard Error of the Mean. ***P < .001, Unpaired t Test